

DEFECTIVE MANGANESE AND VANADIUM OXIDE NANOSHEETS FOR
ELECTROCHEMICAL SUPERCAPACITORS

BY
PENG GAO

A THESIS
SUBMITTED TO THE FACULTY OF
ALFRED UNIVERSITY

IN PARTIAL FULFILLMENT OF THE REQUIREMENTS
FOR THE DEGREE OF
DOCTOR OF PHILOSOPHY
IN
MATERIALS SCIENCE AND ENGINEERING

ALFRED, NEW YORK

AUGUST, 2018

DEFECTIVE MANGANESE AND VANADIUM OXIDE NANOSHEETS FOR
ELECTROCHEMICAL SUPERCAPACITORS

BY

PENG GAO

B.S. TIANJIN UNIVERSITY (2010)

M.S. TIANJIN UNIVERSITY (2013)

SIGNATURE OF AUTHOR _____

APPROVED BY _____

SCOTT T. MISTURE, ADVISOR

DOREEN D. EDWARDS, ADVISORY COMMITTEE

S.K. SUNDARAM, ADVISORY COMMITTEE

DAWEI LIU, ADVISORY COMMITTEE

CHAIR, ORAL THESIS DEFENSE

ACCEPTED BY _____

ALASTAIR N. CORMACK, DEAN
KAZUO INAMORI SCHOOL OF ENGINEERING

ACCEPTED BY _____

JAY CERIO, DEAN OF GRADUATE
AND CONTINUING STUDIES
ALFRED UNIVERSITY

Alfred University theses are copyright protected and may be used for education or personal research only. Reproduction or distribution in part or whole is prohibited without written permission from the author.

Signature page may be viewed at Scholes Library, New York State College of Ceramics, Alfred University, Alfred, New York.

ACKNOWLEDGMENTS

Working towards a Ph.D degree for nearly 5 years is really a wonderful journey, filled with success and failure, happiness and bitterness, joys and tears. It is definitely not possible for me to complete the Ph.D study at Alfred University without the help and support of many people. First and foremost, I would like to give my deepest thanks to my academic advisor Dr. Scott T. Misture, who offers me constant academic challenges and guidance throughout my Ph.D study, which made me a qualified materials scientist. I would also like to thank my committee members, Dr. Doreen D. Edwards, Dr. S.K. Sundaram, and Dr. Dawei Liu, for spending time in discussing my thesis work and effective instructions. Particularly, I would give my sincere appreciation to Dr. Dawei Liu, who has given me selfless help and strong support during all my research and future academic careers. Additionally, I would like to express my gratitude to all my friends for their friendship and companionship, especially my best friend Yuxuan Gong. This material is based upon work supported by the National Science Foundation under Grant No. DMR-1409102. The author gratefully acknowledges the financial support of the National Science Foundation. This research used resources of the Advanced Photon Source (APS), a U.S. Department of Energy (DOE) Office of Science User Facility operated for the DOE Office of Science by Argonne National Laboratory under Contract No. DE-AC02-06CH11357. This work is also based upon research conducted at the Cornell High Energy Synchrotron Source (CHESS) which is supported by the National Science Foundation under award DMR-1332208. We are indebted to Karena Chapman, Kevin Beyer, Olaf Borkiewicz, and Kamila M. Wiaderek at APS, as well as Rong Hong, Peter Ko, Kenneth Finkelstein and Christopher Pollock at CHESS, for their valuable guidance in high-energy X-ray measurements. Last but not least, I would like to thank my beloved parents and my wife Jiaofeng Yang, who support me unconditionally during my study at Alfred University.

TABLE OF CONTENTS

	Page
Acknowledgments	iii
Table of Contents	iv
List of Tables	viii
List of Figures	ix
Abstract	xix
CHAPTER I. INTRODUCTION AND LITERATURE REVIEW	1
1.1 Fundamentals of electrochemical energy storage	1
1.2 Energy storage mechanisms of electrochemical supercapacitors	4
1.2.1 Electrical double-layer capacitors	5
1.2.2 Pseudocapacitors	7
1.2.3 Extrinsic pseudocapacitors	8
1.3 Commonly used electrode materials for electrochemical supercapacitors	9
1.3.1 Carbon-based materials	9
1.3.2 Conductive polymers	12
1.3.3 Transition metal oxides	14
1.3.3.1 Ruthenium oxide	14
1.3.3.2 Manganese oxide	15
1.3.3.3 Vanadium oxide	18
1.3.3.4 Other transition metal oxides	21
1.4 Fabrication methods for making supercapacitor electrodes	22
1.5 Initiatives of using 2-D layered δ -MnO ₂ and VO ₂ (B) nanosheets as supercapacitor electrodes	25
1.5.1 Advantages of using 2-D layered δ -MnO ₂ and VO ₂ (B) nanosheets as supercapacitor electrodes	25
1.5.2 Commonly used approaches to fabricate 2-D layered δ -MnO ₂ and VO ₂ (B) nanosheets	29
1.6 Motivation of incorporating structural defects into the transition metal oxides as a promising way to improve their charge storage properties	33
1.6.1 Commonly used approaches to improve the electrode properties of transition metal oxides	33
1.6.2 A novel strategy to improve the charge storage properties of transition metal oxides by intentionally introducing structural defects	34
1.7 Probable ways of intentionally incorporating structural defects into transition metal oxides	37
1.8 Commonly used techniques for detecting the structural defects and alkali cation intercalation mechanism during charge/discharge process	40

1.8.1 X-ray Absorption Spectroscopy (XAS)	41
1.8.2 X-ray Scattering and Pair Distribution Function (PDF) analysis	42
1.8.3 Raman Spectroscopy	44
1.8.4 Other detection techniques.....	46
CHAPTER II. THE CRITICAL ROLE OF ACID TREATMENT INDUCED POINT DEFECTS IN IMPROVING THE SPECIFIC CAPACITANCE OF 2-D BIRNESSITE δ-MNO₂ NANOSHEETS	48
2.1 Introduction	49
2.2 Materials and Methods	51
2.2.1 Chemicals and reagents	51
2.2.2 Fabrication of δ -MnO ₂ nanostructures.....	51
2.2.3 Characterization of the samples	53
2.2.4 Electrochemical measurements.....	54
2.3 Results and Discussion	56
2.3.1 Phases and microstructures of parent K _x MnO ₂ and protonated H _x MnO ₂	56
2.3.2 Characterization of the exfoliated δ -MnO ₂ nanosheets.....	58
2.3.3 Investigation of the δ -MnO ₂ nanosheets flocculation/reassembly processes.....	59
2.3.4 Phases and microstructures of the reassembled δ -MnO ₂ nanostructures	61
2.3.5 Oxidation states determination of the protonated and reassembled δ -MnO ₂ nanosheets	68
2.3.6 Defects structure characterization of the protonated and reassembled δ -MnO ₂ nanosheets	73
2.3.7 Investigation of supercapacitor electrodes preparation methods for obtaining optimized charge storage properties.....	77
2.3.8 Electrochemical measurements of the protonated and reassembled δ -MnO ₂ nanosheets	82
2.4 Summary: effects of defects on capacitance.....	88
CHAPTER III. INVESTIGATION OF THE CHARGE STORAGE MECHANISMS OF DEFECTIVE δ-MNO₂ NANOSHEETS USED AS SUPERCAPACITOR ELECTRODES	89
3.1 Introduction	89
3.2 Materials and Methods	92
3.2.1 Chemicals and reagents	92
3.2.2 Preparation of carbon and binder-free MnO ₂ nanosheet electrodes by electrophoretic deposition method.....	92
3.2.3 pH equilibration of the as-deposited MnO ₂ nanosheet electrodes and interrupted electrochemical cycling.....	93
3.2.4 Characterization of the samples	94
3.2.5 Electrochemical measurements.....	96

3.3	Results and Discussion	98
3.3.1	Investigation of the electrophoretic deposition process to make carbon and binder free δ -MnO ₂ nanosheet electrodes	98
3.3.2	Characterization of the EPD prepared binder-free electrodes charge/discharged with different electrolytes	102
3.3.3	Electrochemical comparison of the EPD prepared δ -MnO ₂ nanosheet electrodes that are equilibrated in different pH environment	105
3.3.4	<i>Ex-situ</i> Raman spectroscopy of charge/discharged δ -MnO ₂ nanosheet electrodes equilibrated in different pH environment	108
3.3.5	<i>In-situ</i> XANES spectroscopy of δ -MnO ₂ nanosheet electrodes equilibrated in different pH environment	111
3.3.6	<i>In-situ</i> X-ray diffraction, scattering and PDF analysis of pH = 2 equilibrated δ -MnO ₂ nanosheet electrodes	117
3.4	Summary: investigation of the charge storage mechanism of defective δ -MnO ₂	119
CHAPTER IV. MN DOPED VO₂(B) NANOSHEETS.....		121
4.1	Introduction	121
4.2	Materials and Methods	124
4.2.1	Chemicals and reagents	124
4.2.2	Preparation of VO ₂ (B) and Mn-doped VO ₂ (B) nanosheets	124
4.2.3	Preparation of VO ₂ (A) nanobelts	125
4.2.4	Characterization of the samples	125
4.2.5	Electrochemical measurements	126
4.3	Results and Discussion	128
4.3.1	Investigation of the hydrothermal reaction conditions to prepare the VO ₂ (B) nanosheets	128
4.3.2	Effects of different pH equilibration on structures, morphologies and charge storage properties of the hydrothermally prepared VO ₂ (B) nanosheets	132
4.3.3	Phases and microstructures of the hydrothermally prepared pure and Mn-doped VO ₂ (B) nanosheets	135
4.3.4	Determination of oxidation states of the hydrothermally prepared pure and Mn-doped VO ₂ (B) nanosheets	141
4.3.5	Phase composition and local structure characterization of the hydrothermally prepared pure and Mn-doped VO ₂ (B) nanosheets	143
4.3.6	Electrochemical measurements of the hydrothermally prepared pure and Mn-doped VO ₂ (B) nanosheets	146
4.4	Summary: Mn doped VO ₂ (B) nanosheets	156
SUMMARY AND CONCLUSIONS		158
FUTURE WORK		160
REFERENCES.....		161

**APPENDIX I. CUSTOM ELECTROCHEMICAL CELL FOR IN-SITU
MEASUREMENTS..... 183**

LIST OF TABLES

	Page
Table I. Estimation of Surface Frenkel Defect Concentration.	77
Table II. Summary Findings of Defects and Electrochemistry in δ -MnO ₂ Electrodes.....	87
Table III. Various Hydrothermal Reaction Conditions that have been Investigated to Prepare VO ₂ (B) Nanosheets	128

LIST OF FIGURES

	Page
Figure 1. (a) Cyclic voltammetry for RuO ₂ in 1 M H ₂ SO ₄ solution exhibiting typical mirror-image symmetry. (b) Cyclic voltammetry for Pb-PbCl ₂ battery electrode showing typical irreversibility.....	2
Figure 2. Comparison of charge and discharge behavior for capacitor and battery.	3
Figure 3. Ragone plot for various electrochemical energy storage devices.....	4
Figure 4. Construction of the electrode/electrolyte interface.....	6
Figure 5. The effect of crystallite size on the discharge curve of LiCoO ₂	9
Figure 6. (a) Cyclic voltammetry curves of carbon nanotube based supercapacitor electrode at different scan rates; (b) galvanostatic charge-discharge curves at a constant current density of 0.5 A/g.	10
Figure 7. (a) TEM image of the purified carbon nanotubes, (b) cyclic voltammetry of the carbon nanotube thin films cycled from 0 to 1 V at 500 mV/s scan rate.....	12
Figure 8. (a) SEM images of graphene nanosheets (scale bar: 10 μm), (b) Ragone plot of graphene supercapacitor.	12
Figure 9. (a) The SEM image of PANI on stainless-steel substrate, and (b) cyclic voltammetry curves of as-prepared PANI electrode under different scan rates.	13
Figure 10. (a) The SEM image of PPy film on polished graphite plate, and (b) cycle stability of PPy film obtained at 5 mA/cm ²	14
Figure 11. Typical cyclic voltammetry curves of MnO ₂ based electrodes cycled in 1 M Na ₂ SO ₄ electrolyte at a scan rate of 5 mV/s.	16
Figure 12. Crystal structures of (a) α, (b) β, (c) γ, and (d) δ MnO ₂	17
Figure 13. Crystal structure of V ₂ O ₅	19

Figure 14. (a, b) SEM images of V_2O_5 architecture constructed from nanosheets, (c) XRD patterns, indicating the differences between the layered structures of the 3-D V_2O_5 architecture, the stacked V_2O_5 film, and the bulk V_2O_5 crystal, (d) capacitance comparison of the as-prepared samples at different scan rates.	19
Figure 15. Crystal structure of $VO_2(B)$	20
Figure 16. (a, b) SEM images of $VO_2(B)$ nanoflowers on 3D graphene networks, (c) cyclic voltammetry curves of the as prepared samples, and (d) areal specific capacitance as a function of current density.	21
Figure 17. (a, b) The SEM images of MnO_2 nanotube arrays, (c) CV curves of MnO_2 nanotube array electrode at scan rate of 20 mV/s, and (d) mass-specific capacitance and area-specific capacitance as function of cycle number.	24
Figure 18. Schematic illustration of electrophoretic deposition process: (a) Cathodic EPD and (b) anodic EPD.	24
Figure 19. SEM images of (a) pristine layered $K_{0.45}MnO_2$, (b) Li^+ -layered MnO_2 , (c) Na^+ -layered MnO_2 , and (d) K^+ -layered MnO_2	26
Figure 20. (a) Specific capacitance comparison of the different electrodes underwent 500 electrochemical cycles. (b) Comparison of specific capacitance, ionic conductivity, and BET surface area of different MnO_2 polymorphs.	27
Figure 21. (a) SEM image of N-doped graphene- $VO_2(B)$ nanosheet-built 3-D flower hybrid, (b) cycling performance at a current density of 50 mAh/g.	28
Figure 22. Experimental procedures of making the δ - MnO_2 nanosheets from its bulk crystalline phase.	29
Figure 23. The typical SEM morphologies of δ - MnO_2 nanosheets prepared by (a) hydrothermal method, (b) electrodeposition method, and (c) wet chemistry method.	31
Figure 24. (a) HRTEM image of the $VO_2(B)$ nanosheets prepared by hydrothermal method, (b) TEM image of pure $VO_2(B)$ nanosheets, and (c) High-magnification SEM image of the flower-like $VO_2(B)$ samples.	32
Figure 25. Schematic illustration shows the formation process of $VO_2(B)$ ultrathin nanosheets: (a) bulk $VO_2(B)$, (b) lithiated $VO_2(B)$, (c) hydrated $VO_2(B)$, and (d) single layers $VO_2(B)$	33

Figure 26. Schematic diagrams of cation-deficient MnO ₂ phases viewed along the [001] direction illustrating two different defect configurations: (a) γ -MnO ₂ intergrowth structure with chain-like vacancy clustering and (b) ϵ -MnO ₂ with point defects.	35
Figure 27. Schematic diagrams showing (a) substitution of divalent O ²⁻ anions with monovalent F ⁻ and OH ⁻ anions resulting the formation of cationic Ti ⁴⁺ vacancies, and (b) the aliovalent doping of Mn cations in V ₂ O ₅ structure through a two-step transformation process.	38
Figure 28. Short-range and long-range order structure of a δ -MnO ₂ monolayer.	40
Figure 29. (a) EXAFS data on the hollow and solid γ -Fe ₂ O ₃ NPs (bulk γ -Fe ₂ O ₃ was used as a reference), (b) Voltage curve at the first discharge state (up to ~3.5 Li ⁺ insertion) versus metallic Li counter electrode, (c) XANES spectra measured at eight points depicted in the voltage profile shown in (b), and (d) The Fe oxidation state obtained from XANES plots shown in (c).	42
Figure 30. (a) Experimental PDFs for δ -MnO ₂ synthesized as a function of pH. (b) Best-fit PDF profiles up to 8.5 Å calculated for a model containing 17% vacancies. (c)-(e) Best-fit PDF profiles up to 7 Å calculated for a chalcophanite model (Fig. 6d).	44
Figure 31. (a) The schematic diagram of the operando Raman spectroscopic test for pseudocapacitive δ -MnO ₂ thin-film electrode. (b-d) Raman spectroscopic evolution of pseudocapacitive MnO ₂ thin film cycled between 0 and 0.7 V in (a) 2 M LiNO ₃ , (b) 2 M NaNO ₃ , and (c) 2 M KNO ₃ aqueous electrolyte.	45
Figure 32. (a) High-resolution TEM image of a Ti _{0.78} □ _{0.22} O _{1.12} F _{0.40} (OH) _{0.48} particle. (b) atomic-resolution image of anatase crystal oriented along the [001] axis. (c) colored high-resolution TEM image with a profile plot of a line of atoms.	46
Figure 33. Typical synthesis procedures for making 3-D porous δ -MnO ₂ nanosheet assemblies with controlled defect content.	52
Figure 34. SEM images of (a) pristine K _x MnO ₂ , and (b) protonated H _x MnO ₂ . Scale bars, 500 nm. XRD patterns of (c) pristine K _x MnO ₂ , and (d) protonated H _x MnO ₂ . Data collected on APS 11-ID-B.	57

Figure 35. (a) Energy dispersive spectrum of the protonated H_xMnO_2 , and (b) XPS survey scan of the protonated H_xMnO_2	57
Figure 36. (a) The photo image of the exfoliated δ - MnO_2 nanosheets stabilized in suspension, (b) SEM image and (c) bright-field TEM image of exfoliated δ - MnO_2 nanosheets, (d) AFM image of MnO_2 nanosheets on Si wafer, (e) the height profile along the line shown in the AFM image in (d). Scale bar, 50 nm (b-c).....	58
Figure 37. SEM images of reassembled δ - MnO_2 nanostructures flocculated by (a) adding 6N HCl solution to the suspension all at once while stirring to reach pH = 2, and (b) adding 6N HCl solution to the suspension at a constant rate of 1 mL/min while stirring to reach pH = 2. Scale bar, 500 nm (a-b).....	59
Figure 38. The SEM images of (a) H^+ , (b) Li^+ , and (c) Na^+ flocculated δ - MnO_2 nanostructures. Scale bar, 500 nm (a-c).....	60
Figure 39. SEM images of reassembled MnO_2 nanostructures treated in (a) pH = 2 and (b) pH = 4 solution for 24 h. (c) high-magnification SEM image of reassembled MnO_2 nanostructures treated in pH = 2 solution for 24 h. Scale bar, 500 nm (a-b); 50 nm (c).	62
Figure 40. XRD patterns of (a) protonated MnO_2 , (b) reassembled MnO_2 treated in pH = 4 solution for 24 h, (c) reassembled MnO_2 treated in pH = 2 solution for 24 h. Data collected on APS 11-ID-B.	63
Figure 41. Comparison of the experimental PDF (reassembled MnO_2 , pH = 2) and the PDF calculated for a single δ - MnO_2 sheet confirms the δ - MnO_2 motif is maintained in the exfoliated and reassembled nanosheet floccs.	63
Figure 42. The typical N_2 adsorption-desorption isotherms of (a) protonated MnO_2 , (b) reassembled MnO_2 treated in pH = 2 solution for 24 h, (c) reassembled MnO_2 treated in pH = 4 solution for 24 h.	64
Figure 43. TGA curves of (a) protonated MnO_2 , (b) reassembled MnO_2 treated in pH = 2 solution for 24 h, (c) reassembled MnO_2 treated in pH = 4 solution for 24 h.....	65
Figure 44. FTIR spectra of (a) protonated MnO_2 ; (b) reassembled MnO_2 treated in pH = 4 solution for 24 h; (c) reassembled MnO_2 treated in pH = 2 solution for 24 h (inset shows the structure of the TBAOH molecule).	66

Figure 45. XPS spectra of reassembled MnO ₂ treated in pH = 2 solution for 24 h. (a) XPS survey scan, (b) high resolution XPS N 1s and C 1s spectrum.	67
Figure 46. FTIR spectra of reassembled MnO ₂ treated in pH = 4 solution for 24 h, (a) before and (b) after one CV cycling in 1M Na ₂ SO ₄ electrolyte at 50 mV/s scan rate.	68
Figure 47. XPS spectra in the (a) Mn 2p, and (b) Mn 3s regions corresponding to (A) protonated MnO ₂ , (B) reassembled MnO ₂ treated in pH = 4 solution for 24 h, (C) reassembled MnO ₂ treated in pH = 2 solution for 24 h.	70
Figure 48. X-ray absorption measurements of the as-prepared three samples and reference Mn oxide materials. (a) XANES spectra of reference materials MnO, Mn ₃ O ₄ , Mn ₂ O ₃ and MnO ₂ . (b) XANES spectra of protonated MnO ₂ , pH = 2 and 4 treated reassembled MnO ₂ . The reference materials of Mn ₂ O ₃ and MnO ₂ from panel (a) are also shown for ease comparison. (c) First derivative curves corresponding to the samples shown in panel (b). (d) Average oxidation state of Mn for the samples and standards derived from the K-edge energy.	72
Figure 49. High-energy X-ray scattering and experimental PDF data. (a) I(Q) and (b) F(Q) for the pH = 2 and pH = 4 treated MnO ₂ nanosheets assemblies, and (c) G(r) for the pH-treated samples, protonated MnO ₂ (H _x MnO ₂), and parent phases (K _x MnO ₂)..	74
Figure 50. Empirical analysis of δ-MnO ₂ PDF. δ-MnO ₂ equilibrated at pH = 2 is shown here.	76
Figure 51. Typical SEM morphology of reassembled δ-MnO ₂ nanostructure drop-cast on Ni foils substrate.	78
Figure 52. Cyclic voltammetry curves for the reassembled δ-MnO ₂ nanostructure drop-cast on Ni foil substrate at a scan rate of 100 mV/s.	78
Figure 53. Galvanostatic charge-discharge curves of (a) 80 wt.% MnO ₂ -15 wt.% carbon black-5 wt.% PVDF, (b) 80 wt.% MnO ₂ -10 wt.% carbon black-10 wt.% PVDF, (c) 75 wt.% MnO ₂ -20 wt.% carbon black-5 wt.% PVDF, and (d) 70 wt.% MnO ₂ -20 wt.% carbon black-10 wt.% PVDF.	80
Figure 54. Comparison of specific capacitance for (a) 80 wt.% MnO ₂ -15 wt.% carbon black-5 wt.% PVDF, (b) 75 wt.% MnO ₂ -20 wt.% carbon black-5 wt.% PVDF, (c) 80 wt.% MnO ₂ -10 wt.% carbon black-10 wt.% PVDF, and (d) 70 wt.% MnO ₂ -20 wt.% carbon black-10 wt.% PVDF as a function of current density.	80

- Figure 55.** The galvanostatic charge-discharge curves of (a) 0.32 mg/cm², (b) 0.8 mg/cm², (c) 1.28 mg/cm², (d) 2.08 mg/cm², and (e) 3.04 mg/cm² MnO₂ mass loading. (f) Comparison of specific capacitance for the electrodes with different MnO₂ mass loading as a function of current density. 82
- Figure 56.** Electrochemical testing results: (a) CV curves for the samples at 50 mV/s scan rate; (b), (c), and (d) galvanostatic charge-discharge curves of the pH = 2, 4 and H_xMnO₂ samples; (e) comparison of specific capacitance for the samples as a function of current density; and (f) cycle stability at constant current density of 5 A/g between 0 and 1 V. 84
- Figure 57.** Electrochemical impedance spectroscopy of protonated and reassembled δ-MnO₂ electrodes. (a) Nyquist plots of the samples in the frequency range of 0.1 Hz - 100 kHz at an open circuit potential of 5 mV (inset shows the electrical equivalent circuit used for fitting the impedance spectra); and (b) comparison of the charge transfer resistance among the three samples (values obtained from the fitted data). 86
- Figure 58.** Typical procedures for making binder-free electrodes by EPD method, pH equilibration and interrupted electrochemical cycling. 94
- Figure 59.** Photographs of the δ-MnO₂ nanosheet assemblies on different substrates prepared by electrophoretic deposition (EPD). (a) Ni foil, (b) Au-coated Kapton[®], and (c) glassy carbon foil. 99
- Figure 60.** (a) Cross-sectional image of the MnO₂ nanosheet assemblies on Ni foil substrate prepared by EPD; (b) typical SEM morphology of MnO₂ nanosheets on substrates prepared by EPD. Scale bar, 50 μm (a), 500 nm (b). 99
- Figure 61.** Typical SEM images of MnO₂ nanosheet assemblies on Ni foil substrate prepared by EPD with different deposition time (mass loading). (a) 2 min (0.2 mg), (b) 4 min (0.4 mg), (c) 6 min (0.6 mg), and (d) 10 min (1.0 mg). Scale bar, 200 nm (a), 1 μm (b-d). 100
- Figure 62.** Specific capacitances of the EPD prepared binder-free MnO₂ nanosheet electrodes on Ni foil substrates with different deposition time. The capacitance of MnO₂ nanosheet floccs measured by mixing with carbon black and binder is also included for ease comparison. 101
- Figure 63.** CV comparison of the EPD prepared MnO₂ nanosheet electrodes cycled in (a) 1M Na₂SO₄, (b) 2M KNO₃, and (c) 1M Rb₂SO₄ electrolytes at 10 mV/s scan rate. 103

Figure 64. Typical SEM image of MnO ₂ nanosheet floccs electrophoretic deposited on the Ni foil substrate and fully charged with potassium ions at 1 mV/s scan rate. Scale bar, 1 μm.	105
Figure 65. Energy dispersive spectrum of the MnO ₂ nanosheet floccs electrophoretic deposited on Ni foil substrate (a) fully charged and (b) fully discharged with potassium ions.....	105
Figure 66. (a) Typical CV curves and (b) specific capacitance comparison of MnO ₂ nanosheet floccs deposited on Au-coated Kapton [®] tapes and equilibrated at pH = 2 for different hours.	107
Figure 67. Typical CV curves of the MnO ₂ nanosheet floccs deposited on Au-coated Kapton [®] tapes and equilibrated at (a) pH = 2, and (b) pH = 4 solution for 24 h. (c) Specific capacitance comparison of the two samples.....	108
Figure 68. <i>Ex-situ</i> Raman spectroscopy of the MnO ₂ nanosheet floccs deposited on glassy carbon foils, equilibrated at (a) pH = 2, and (b) pH = 4 HNO ₃ solution for 24 h and interrupted at different charge states during electrochemical cycling.	110
Figure 69. Raman scattering spectra of (a) hollandite MnO ₂ , (b) coronadite MnO ₂ , (c) romanechite MnO ₂ , (d) todorokite MnO ₂ , (e) birnessite MnO ₂ , (f) pyrolusite MnO ₂ , and (g) ramsdellite MnO ₂	111
Figure 70. (a) XANES spectra of reference materials MnO, Mn ₃ O ₄ , LiMn ₂ O ₄ and MnO ₂ . (b) Relationship between K-edge energy and Mn oxidation state (standards) for determining oxidation state of Mn in the samples.....	112
Figure 71. <i>In-situ</i> XANES spectra and calculated Mn oxidation states obtained at fully discharged and fully charged states for (a, b) pH = 2, (c, d) pH = 4, and (e, f) pH = 9 equilibrated MnO ₂ nanosheet electrodes. Figures (b, d, and f) also show the comparison of Mn oxidation states variation measured from XANES data and predicted from electrochemical CV loop.	114
Figure 72. Mn oxidation state change comparison upon charge/discharge of pH = 2, 4 and 9 equilibrated MnO ₂ nanosheet electrodes.....	115
Figure 73. Curve fitting of O 1s XPS spectra of MnO ₂ nanosheet floccs equilibrated at (a) pH = 2, and (b) pH = 4 solution for 24 h.	116

Figure 74. (a-c) <i>In-situ</i> X-ray diffraction and (d) PDF data of pH = 2 equilibrated MnO ₂ nanosheet electrodes upon repeated charge/discharge.	118
Figure 75. Typical synthesis procedures for making pure and Mn-doped VO ₂ (B) nanosheet.....	125
Figure 76. Typical XRD patterns of the hydrothermally prepared vanadium oxide nanostructures. (a) 0.2 g V ₂ O ₅ + 25 mL H ₂ O + 5 mL 30 wt.% H ₂ O ₂ , 180 °C, 12 h; (b) 0.36 g V ₂ O ₅ + 30 mL H ₂ O + 5 mL 30 wt.% H ₂ O ₂ , 190 °C, 12 h; (c) 0.18 g V ₂ O ₅ + 10 mL H ₂ O + 10 mL 30 wt.% H ₂ O ₂ + 10 mL IPA, 170 °C, 24 h; (d) 0.09 g V ₂ O ₅ + 5 mL H ₂ O + 5 mL 30 wt.% H ₂ O ₂ + 5 mL IPA, 180 °C, 6 h; (e) 0.05 g V ₂ O ₅ + 5 mL H ₂ O + 10 mL 30 wt.% H ₂ O ₂ + 10 mL IPA, 180 °C, 6 h.....	130
Figure 77. SEM images of hydrothermally prepared vanadium oxide nanostructures. (a) 0.2 g V ₂ O ₅ + 25 mL H ₂ O + 5 mL 30 wt.% H ₂ O ₂ , 180 °C, 12 h; (b) 0.36 g V ₂ O ₅ + 30 mL H ₂ O + 5 mL 30 wt.% H ₂ O ₂ , 190 °C, 12 h; (c) 0.18 g V ₂ O ₅ + 10 mL H ₂ O + 10 mL 30 wt.% H ₂ O ₂ + 10 mL IPA, 170 °C, 24 h; (d) 0.09 g V ₂ O ₅ + 5 mL H ₂ O + 5 mL 30 wt.% H ₂ O ₂ + 5 mL IPA, 180 °C, 6 h; (e) 0.05 g V ₂ O ₅ + 5 mL H ₂ O + 10 mL 30 wt.% H ₂ O ₂ + 10 mL IPA, 180 °C, 6 h. Scale bar, 2 μm (a), 1 μm (b), 500 nm (c-d), 200 nm (e).....	131
Figure 78. Typical XRD patterns of the hydrothermally prepared VO ₂ (B) nanosheets equilibrated at pH = 2, 6 and 9 solution for 24 h.	133
Figure 79. Typical SEM images of the hydrothermally prepared VO ₂ (B) nanosheets equilibrated at (a) pH = 2, (b) pH = 6, and (c) pH = 9 solution for 24 h. Scale bar, 200 nm (a), 500 nm (b-c).	133
Figure 80. (a) Galvanostatic charge-discharge curves of pH = 2, 6 and 9 equilibrated VO ₂ (B) nanosheets at 0.5 A/g current density; (b) Comparison of specific capacitance for the samples as a function of current density.....	134
Figure 81. Typical SEM images of the pure VO ₂ (B) (a, c) and Mn-doped VO ₂ (B) (b, d) nanosheets prepared by hydrothermal method and dried in oven overnight. Scale bar, 500 nm (a-b), 200 nm (c-d).....	136
Figure 82. The energy dispersive spectrum of (a) VO ₂ (B) and (b) Mn-doped VO ₂ (B) nanosheets. The inset table shows the quantification of each element present in Mn-doped VO ₂ (B) nanosheets.	137
Figure 83. XRD patterns of (a) pure VO ₂ (B) and (b) Mn-doped VO ₂ (B) nanosheets. Data collected on CHESS F2 station.	138

Figure 84. TGA curves of (a) pure and (b) Mn-doped VO ₂ (B) nanosheets.....	140
Figure 85. XRD patterns of (a) VO ₂ (B) and (b) Mn-doped VO ₂ (B) nanosheets after TGA in air to 600 °C.....	140
Figure 86. XPS survey scan of (a) pure and (b) Mn-doped VO ₂ (B) nanosheets	141
Figure 87. Curve fitting of the V 2p _{3/2} XPS spectra of (a) pure VO ₂ (B) and (b) Mn-doped VO ₂ (B) nanosheets; (c) comparison of the relative ratio of V ⁵⁺ and V ⁴⁺ in pure and Mn-doped VO ₂ (B) nanosheets; (d) XPS spectra in the Mn 2p regions of Mn-doped VO ₂ (B)	142
Figure 88. Pair distribution functions (PDFs or G(r) s) of (a) pure VO ₂ (B) and (b) Mn-doped VO ₂ (B) nanosheets over 1.34 – 90 Å r range.....	144
Figure 89. Comparison of the experimental Pair Distribution Functions (PDF) G(r) over low r regions (1 – 7 Å) of pure and Mn-doped VO ₂ (B) nanosheets.	146
Figure 90. (a) Cyclic voltammetry comparison of the pure and Mn-doped VO ₂ (B) nanosheets measured in 1M Na ₂ SO ₄ electrolyte solution at a potential window of 0-0.8 V with 20 mV/s scan rate; (b) variation of specific capacitance as a function of scan rate for both samples; (c) Galvanostatic charge-discharge curves of pure and Mn-doped VO ₂ (B) nanosheets in 1M Na ₂ SO ₄ electrolyte solution at 0.2 A/g current density; (d) comparison of specific capacitance for both samples as a function of current density.	148
Figure 91. Cyclic voltammetry curves for (a) VO ₂ (B) and (b) Mn-doped VO ₂ (B) nanosheets in 1M Na ₂ SO ₄ electrolyte at various scan rates.....	149
Figure 92. Galvanostatic charge-discharge curves for (a) VO ₂ (B) and (b) Mn-doped VO ₂ (B) nanosheets in 1M Na ₂ SO ₄ electrolyte solution at different current densities.....	149
Figure 93. (a) The XRD pattern and (b) SEM image of the hydrothermally prepared VO ₂ (A) . Scale bar, 500 nm. (c) Cyclic voltammetry curves for VO ₂ (A) in 1M Na ₂ SO ₄ electrolyte at various scan rates. (d) Specific capacitance comparison of VO ₂ (A), VO ₂ (B) and Mn-doped VO ₂ (B) at 2 mV/s scan rate.....	150
Figure 94. Variation of log (i) vs. log (v) for power law fitted at various potentials for (a) VO ₂ (B) and (b) Mn-doped VO ₂ (B) nanosheets; (c) b-value for the pure and Mn-doped VO ₂ (B) nanosheets plotted as a function of potentials for cathodic scans.....	153

Figure 95. (a) Nyquist plots of the pure and Mn-doped VO₂(B) nanosheets in the frequency range of 0.01 Hz-100 kHz at an open circuit potential of 5 mV (inset shows the electrical equivalent circuit used for fitting the impedance spectra); (b) comparison of the charge transfer resistance of the as-prepared two samples (values obtained from the fitted data)..... 154

Figure 96. Cycling stability of pure and Mn-doped VO₂(B) nanosheets at a constant current density of 5 A/g between 0 and 0.8 V. 155

Figure 97. Photo images of custom electrochemical cell for *in-situ* measurements..... 183

Figure 98. Dimensions of the custom electrochemical cell. 184

Figure 99. The configuration and thickness of the glassy carbon electrode, the active material, the electrolyte and the Kapton[®] window in the cell..... 185

ABSTRACT

Electrochemical supercapacitors, which can provide higher power density than batteries and higher energy density than electrostatic capacitors, have received great attention in recent years as promising alternative energy storage devices. δ -MnO₂ and VO₂ nanosheets are considered as most promising electrode materials, due to their low cost, environmental friendliness, and large capacitance. Especially, their layered structures can provide high-speed pathways for the intercalation of protons or alkali cations during electrochemical cycling, which leads to excellent charge storage capability. While a lot of effort has been devoted to improve the electrode performance by microstructure control or load the samples on conducting materials, new intrinsic approaches are urgently needed to realize more and faster charge storage.

In this study, a new strategy has been proposed to increase the capacitance of δ -MnO₂ and VO₂ nanosheets by intentionally creating defects (such as cation vacancies) in their lattice structures. δ -MnO₂ nanosheets are prepared by exfoliating the parent crystals, and then flocculated under carefully controlled experimental conditions. The obtained 3-D porous assemblies with 150 m²/g specific surface area are equilibrated in varied pH, in order to create charged defect pairs we term ‘surface Frenkel Defects’. The XANES data demonstrates an increase of the Mn³⁺/Mn⁴⁺ ratio with decreasing pH equilibration values. The X-ray scattering and PDF analysis shows that the Mn surface Frenkel defect content reaches 26.5 % for the nanosheet assemblies equilibrated at pH = 2 and 19.9 % for the pH = 4 sample, indicating that equilibration at lower pH leads to the formation of more Mn vacancies in the reassembled δ -MnO₂ nanostructures. The electrochemical results show that the specific capacitance increased from about 200 F/g (pH = 4) to over 300 F/g (pH = 2) by intentional introduction of ~30 % surface Frenkel defects, while at the same time the charge transfer resistance decreased from ~15 Ω to ~3 Ω , indicating direct correlation of Mn cation defects with specific capacitance. The alkali cation intercalation mechanism has also been investigated through *in-situ* X-ray PDF and XANES measurements. The *in-situ* XRD and PDF data show reversible expansion/contraction of the nanosheet layers upon charge/discharge, as well as unchanged interlayer spacing during cycling. The *in-situ* XANES data exhibits a reversible shift of the absorption edge to lower energies for different pH equilibrated samples when decreasing the applied potentials, indicating the reduction of Mn⁴⁺ to Mn³⁺ and confirms that the Faradaic redox reaction is the main charge storage mechanism in the defective MnO₂ nanosheet system. A slower reduction of Mn for the MnO₂ nanosheets with higher defect content has been observed when comparing the oxidation state derived from XANES and that calculated from cyclic voltammetry, emphasizing the important role of defects in the charge storage process without affecting the Mn oxidation states. The pure and Mn-doped VO₂(B) nanosheets have been prepared by hydrothermal methods. Mn incorporation leads to porous and more open structures, which facilitates sodium ion intercalation and thereby greatly improves its charge storage performance. In general, this work provides a new way to the design next generation electrochemical supercapacitors through controlling the defect structures of layered transition metal oxide nanosheets.

CHAPTER I. INTRODUCTION AND LITERATURE REVIEW

1.1 Fundamentals of electrochemical energy storage

In the past decades, the need for development of alternative energy conversion and storage systems has increased dramatically due to the rapid global economic growth, the environmental issues and the depletion of fossil fuels. In most application areas, batteries and electrochemical supercapacitors have become the most effective and practical technologies for electrochemical energy conversion and storage, and represent the two fundamental electrical energy storage mechanisms. In batteries, the electrical energy is stored as potential chemical energy, which requires Faradaic oxidation and reduction of electrochemically active materials that can release charges and perform electrical work when they flow between two electrodes with different potentials.¹ In contrast, capacitors (especially the electrical double layer capacitors) usually exhibit a non-Faradaic electrical energy storage process, which is based on charge separation at the electrode/electrolyte interface.²

The main differences between these two typical energy storage approaches can be summarized as follows:

- i. Different reversibility arises between the Faradaic and non-Faradaic systems. For energy storage in batteries with Faradaic reactions, chemical interconversions of the anode and cathode materials always happen, usually accompanied with phase changes. Thus, the charge and discharge processes often involve irreversibility in interconversion of electrode materials, and the cycle life is usually restricted to less than one thousand cycles. In contrast, the capacitors usually have almost unlimited cyclability upon charge/discharge, since no chemical or phase changes are involved.
- ii. The energy densities that can be achieved with capacitors are substantially smaller than those with batteries. For example, the charge stored in double layer capacitors per atom of active surface area is only about 10-20% of that involved with battery redox materials.¹ However, the power density of capacitors is much

better than that of batteries, due to their fast surface absorption process without sluggish ion diffusion and phase changes that usually happen in batteries.

- iii. The charge and discharge behavior evaluated by cyclic voltammetry is different. As shown in Figure 1, the charge/discharge processes of capacitors are nearly mirror images of each other, given that no diffusion controlled processes are involved, and therefore the CV curves usually exhibit rectangular shapes. In contrast, the charge/discharge processes in battery are rarely reversible, and a different potential range is needed for the active material oxidation and reduction. Thus the CV curves are asymmetric and no mirror-image shape is manifested. This is also a fundamental way to distinguish capacitor and battery behavior.

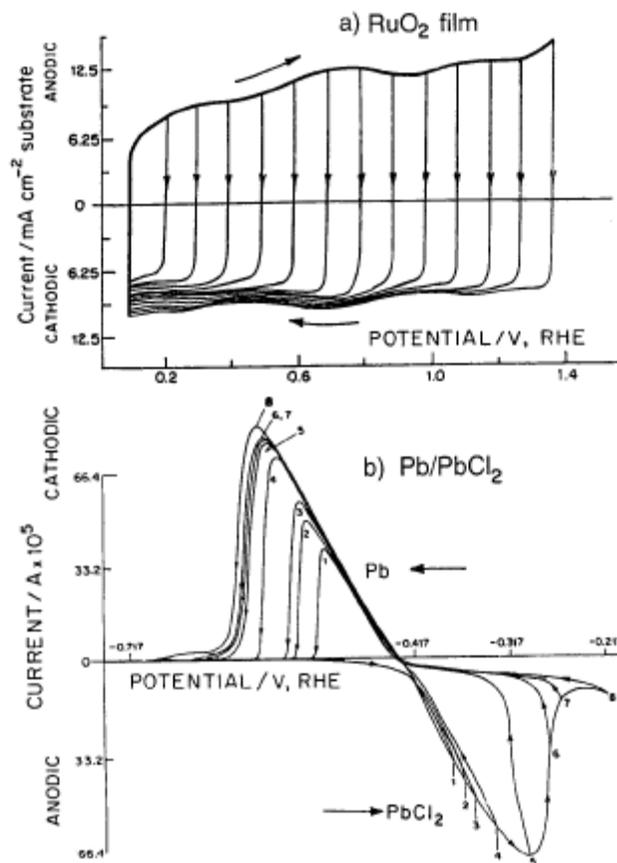


Figure 1. (a) Cyclic voltammetry for RuO₂ in 1 M H₂SO₄ solution exhibiting typical mirror-image symmetry. (b) Cyclic voltammetry for Pb-PbCl₂ battery electrode showing typical irreversibility. From Conway.¹

iv. The charge and discharge curves of capacitor and battery are also different. As shown in Figure 2, for an ideal capacitor, the voltage declines linearly with the extent of charge, while for an ideal battery, the voltage will remain constant as long as the two phases co-exist. Thus the presence of voltage plateau in galvanostatic experiments always indicates battery behavior.³ From a thermodynamic perspective, when charging a double-layer capacitor, every added additional charge has to do electrical work against the charge density that has already accumulated on the interface, thus continuously increasing the potential difference. However, when charging a battery, as long as the two phases of the active materials co-exist, the thermodynamic potential is independent of the charge already added, and therefore the potential difference is ideally constant.¹

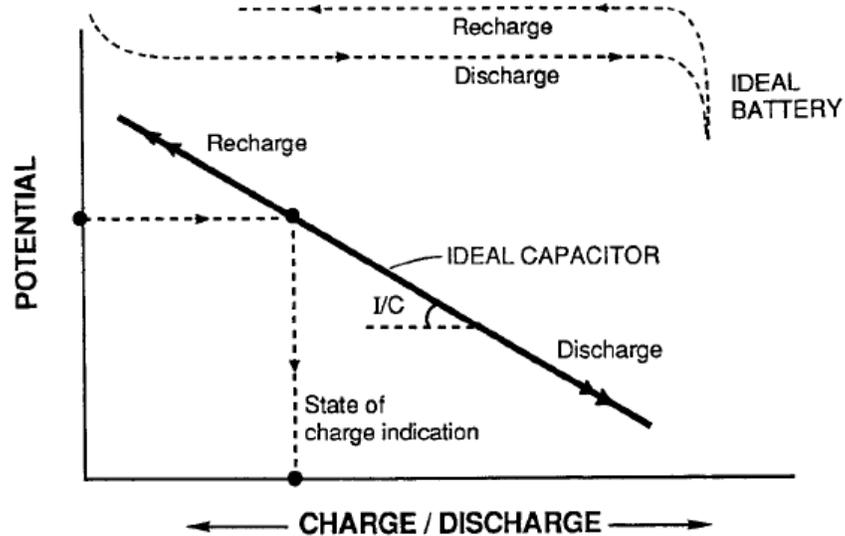


Figure 2. Comparison of charge and discharge behavior for capacitor and battery. From Conway.¹

In general, each electrochemical energy storage mechanism has its own advantages and disadvantages, and it needs to be emphasized that until now scientists have not found a way to completely substitute one with another. However, researchers have achieved some new progress recently. Figure 3 shows a Ragone plot for the most important electrochemical energy storage systems, illustrating their relationship between power and

energy density. Clearly, in between the traditional capacitors and batteries, there emerged another energy storage system, named electrochemical supercapacitors or pseudocapacitors, which can provide both high power density and reasonably high energy density, thus have attracted much attention in recent years and become very promising candidates and may serve as a versatile solution to various emerging energy applications.

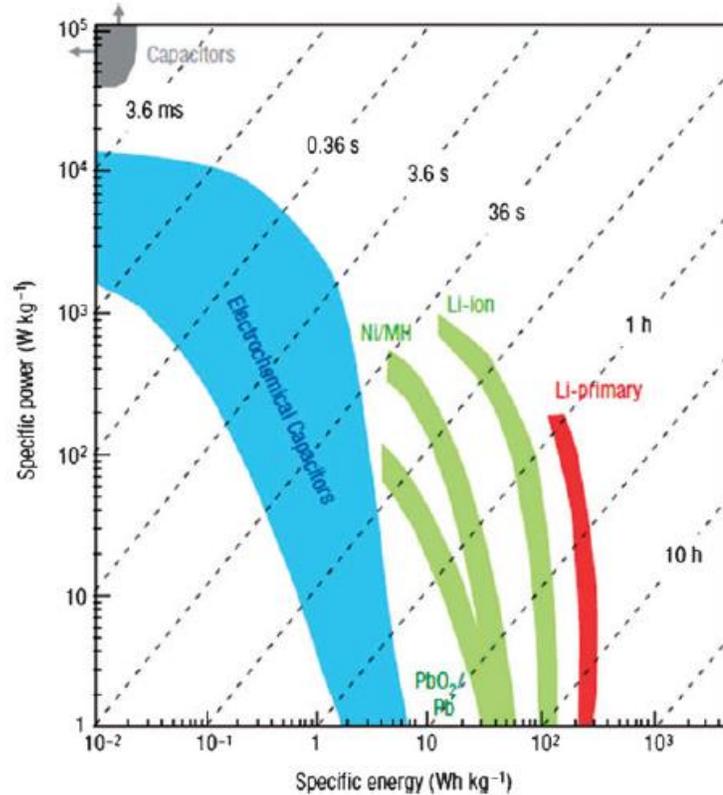


Figure 3. Ragone plot (specific power vs. specific energy) for various electrochemical energy storage devices. From Wei, *et al.*²

1.2 Energy storage mechanisms of electrochemical supercapacitors

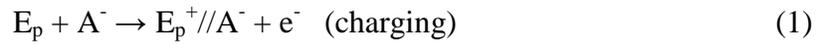
Typically speaking, the electrochemical supercapacitors can be classified into two types based on their different charge storage mechanisms: (i) electrical double-layer capacitor (EDLC), which is based on the non-Faradaic charge separation at the electrode/electrolyte interface, and (ii) pseudocapacitor, which depends on the Faradaic redox reactions of the electroactive materials that occur in the electrode materials.⁴⁻⁷

1.2.1 Electrical double-layer capacitors

In an electrical double-layer capacitor, the energy is stored in electrode/electrolyte interface in an electrostatic way, which arises from the electrostatic charge accumulation at the interface. During the whole process, an excess or deficit of electrical charges is accumulated on the electrode surfaces, and the electrolyte ions with counterbalancing charges are accumulated on the electrolyte side to meet the electro-neutrality. Specifically speaking, the electrons moved from the negative electrode to the positive electrode through an external load when charging, meanwhile the cations move towards the negative electrode and the anions move towards the positive electrode in electrolyte. The reverse processes happen when discharge. Therefore, no chemical reactions or phase changes are involved in the whole charge/discharge process, no charge transfer across the electrode/electrolyte interface, and no ion exchange between the electrode and electrolyte.

The electrochemical processes for charge and discharge can be described as follows.

For the positive electrode:



For the negative electrode:



Where E_p and E_n represent the positive and negative electrode surfaces, A^- and C^+ represent anion and cation in electrolyte, and // represents electrode/electrolyte interface.

Overall, the charge and discharge processes can be expressed as follows:



The double-layer structure at the electrode/electrolyte interlayer is also shown in Figure 4. When a voltage is applied, the electrode will generate two layers of polarized ions. One is in the lattice structure of the electrode surface, and the other one is the solvated electrolyte ions with opposite polarity (which is named outer Helmholtz layer). These two layers are separated at the electrode/electrolyte interface by a monolayer of solvent molecules, which is called the inner Helmholtz layer. Thus, the electrical double-layer typically store electrical charges in a conventional capacitor fashion, which consists of two layers of polarized ions and separated by a monolayer of solvent molecules that is serving as a molecular dielectric.

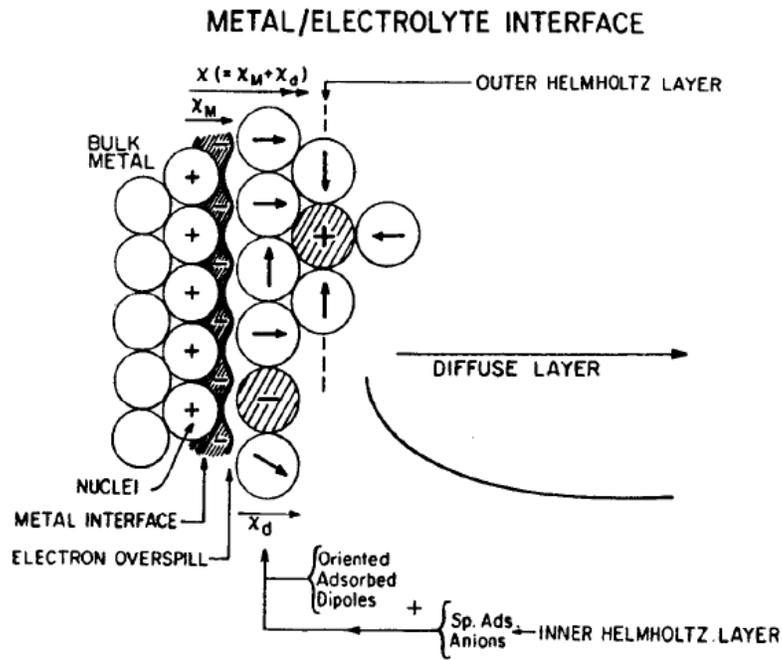


Figure 4. Construction of the electrode/electrolyte interface showing its surface double-layer structure. χ_M and χ_d are the intrinsic surface potentials of the metal and adsorbed dipoles, respectively. From Conway.¹

The double-layer capacitance can usually be calculated by using the following Equation¹:

$$C = A\epsilon/4\pi d \quad (7)$$

Where C is the capacitance, A is the electrode surface area, ϵ is the electrolyte dielectric constant, and d is the thickness of double-layer. Since the double-layer is usually composed of one monolayer solvent molecules, which has typical thickness on the range of a few angstroms (0.3-0.8 nm), thus the double-layer supercapacitors usually have much larger capacitance compared with conventional capacitors.^{8,9}

1.2.2 Pseudocapacitors

Unlike the double-layer capacitor, pseudocapacitors exhibit different charge storage mechanism. The most distinct feature of pseudocapacitors is its Faradaic origin. When a voltage is applied, fast and reversible faradaic redox reactions will take place on the surface of electrode materials, accompanied with charge transfer between electrode and electrolyte across the double layer.^{4,10} This is similar to charge and discharge processes in batteries. However, the adsorbed ion has no chemical reaction with the electrode active materials, therefore only charge transfer process happens. Such capacitance originates due to specific thermodynamic conditions, that the electrode potential (V) is a continuous function of the charge (q) acquired, thus a derivative dq/dV is obtained and can be measured as capacitance.¹ This is also the reason why such capacitance is referred as pseudocapacitance, because it originates in a quite different way compared with the traditional double-layer capacitors. The ability of electrode materials to accomplish pseudocapacitance is usually determined by the chemical affinity of the electrode materials to the adsorbed ions, the structure and porosity of the electrode materials, the presence of redox centers and intercalation possibility.

The Faradaic pseudocapacitive reactions can take place both on the surface and in the bulk (usually near the surface) of the electrode. Take the example of MnO_2 , the pseudocapacitive charge storage mechanism can be described as follows.^{11,12}

For the surface Faradaic redox reaction only involve the surface adsorption of electrolyte cations ($\text{C}^+ = \text{H}^+, \text{Li}^+, \text{Na}^+$ and K^+):



For the bulk Faradaic redox reaction that involve intercalation and deintercalation of electrolyte cations ($C^+ = H^+, Li^+, Na^+$ and K^+) into the bulk of MnO_2 :



It has been demonstrated that compared with double-layer capacitance, pseudocapacitors usually exhibit much higher capacitance per unit area, because¹ (i) the pseudocapacitive reactions take place with de-solvated electrolyte ions, which are much smaller than the solvated ions that used in generating double-layer capacitance, and (ii) pseudocapacitive reactions can take place both on the surface and in the bulk near the surface, thus larger capacitance values can be obtained. The disadvantages of pseudocapacitors are (i) they usually exhibit relatively lower power density compared with EDLCs because of the sluggish Faradaic processes, and (ii) the lack of long-term cyclability (similar to batteries), due to the redox reactions occurred at the electrodes.¹³

1.2.3 Extrinsic pseudocapacitors

Extrinsic pseudocapacitance has recently emerged as a subclassification of pseudocapacitive materials that host ion intercalation but are engineered to short length scales to reduce diffusion distances such that the discharge behavior becomes linear and no structural phase changes occur.^{14,15} In contrast to the so-called “intrinsic” pseudocapacitive materials, which exhibit typical capacitive charge storage properties in a wide range of particle sizes and morphologies, the “extrinsic” pseudocapacitive materials usually do not exhibit pseudocapacitance in bulk state because of phase transformation during ion intercalation. However, when increasing their surface area, the exposure of more active surface adsorption sites and decrease of diffusion distances will lead to improved high-rate performance and suppression of phase transformation.¹⁵ Therefore, pseudocapacitance can emerge as a result of nanostructure engineering that leads to more exposed surface adsorption sites or high ion intercalation rates, and the typical flat discharge curve for battery materials will change to a sloping one that is usually observed for pseudocapacitive materials.

A typical example of “extrinsic” pseudocapacitance is shown in Figure 5. It can be clearly seen that the bulk LiCoO_2 exhibits a typical voltage plateau at about 3.9 V during lithium intercalation. With decreasing the particle sizes, the voltage plateau gradually decreases. Especially when the particle size is reduced to 6 nm, the nanosized material exhibits an almost linear discharge curve in the whole intercalation range, which clearly demonstrate that nanostructure engineering can lead to large percent of active surface adsorption sites and high-speed diffusion pathways, which finally results in the change of charge and discharge behaviour compared with their bulk counterpart.¹⁶

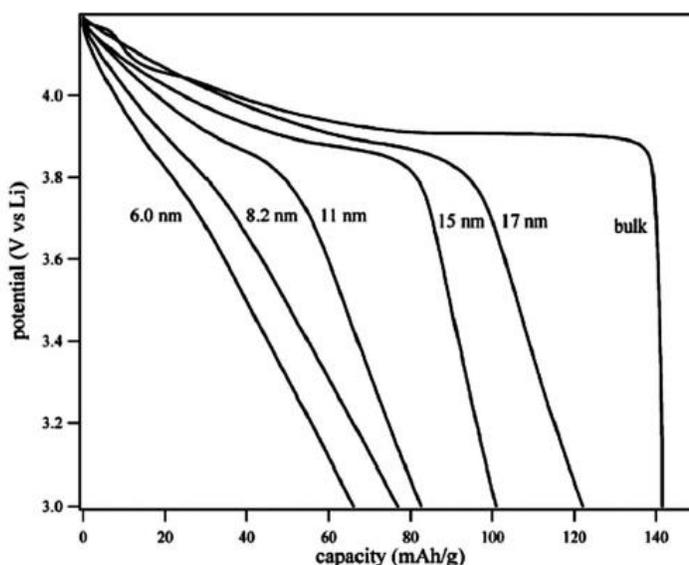


Figure 5. The effect of crystallite size on the discharge curve of LiCoO_2 . From Okubo, *et al.*¹⁶

1.3 Commonly used electrode materials for electrochemical supercapacitors

Generally speaking, electrode materials of the electrochemical supercapacitors can be classified into three categories: (1) carbon-based materials,¹⁷⁻²⁰ (2) conductive polymers,^{6,21-23} and (3) transition metal oxides.²⁴⁻³¹

1.3.1 Carbon-based materials

Carbon based materials are considered promising electrode material candidates for industrial application because of their distinctive advantages, such as high abundance, non-toxicity, good stability and electronic conductivity, high surface area, and low cost.³²

The carbon materials mainly store charges in the electrical double-layer at the electrode/electrolyte interface, and no redox reaction involved, thus can be classified as electrical double-layer capacitors. This can also be understood from their typical cyclic voltammetry and galvanostatic charge-discharge curves. Figure 6 shows the typical electrochemical measurement results of carbon nanotube-based supercapacitor electrodes. The cyclic voltammetry curves exhibit typical rectangular shape, and the galvanostatic charge-discharge profiles exhibit triangular symmetrical distribution, which indicate characteristic of EDLC capacitive properties.³³

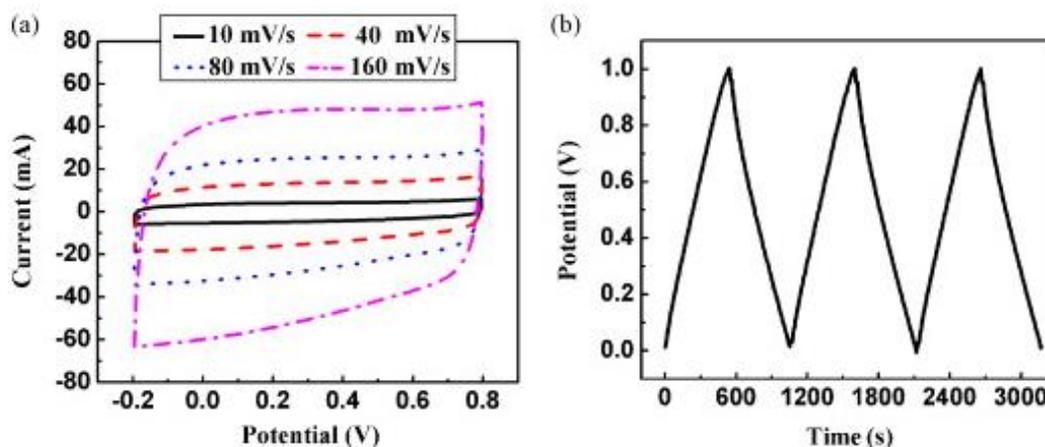


Figure 6. (a) Cyclic voltammetry curves of carbon nanotube based supercapacitor electrode at different scan rates; (b) galvanostatic charge-discharge curves at a constant current density of 0.5 A/g. From Li, *et al.*³³

Since the carbon-based materials mainly exhibit double-layer capacitance, which depends on the surface adsorption of the electrolyte ions, the capacitance mainly depends on the surface area that can be accessed by the electrolyte ions. Good electrical conductivity, appropriate pore shape and pore-size distribution are also important factors that can influence the specific capacitance.^{1,4} In general, good carbon-based supercapacitor electrodes should always have high and accessible surface area, porous structures with appropriate pore shape and size distribution that can promote the fast electrolyte ions adsorption, as well we good electrical conductivity.

Typical carbon materials include activated carbon, carbon nanotubes, graphene, etc. Among them, activated carbon is the most extensively investigated material due to its low

cost, high surface area and high electrical conductivity. For example, Zhi *et al*¹⁸ have prepared activated carbon electrodes by utilizing waste tires as the precursor. Through adjust the processing parameters, they can tailor the physical properties (such as porosity) of the resulting activated carbon and tune the electrode performance. Their results showed that the capacitance is mainly controlled by the micropore volume, whereas the rate capability is mainly dominated by the mesopores/micropore volume ratio.

Carbon nanotubes are another commonly used electrode materials for making double-layer capacitors, owing to their high surface area, good chemical stability and electronic conductivity, as well as unique internal structures. For example, Pan *et al*³⁴ have prepared multi-walled carbon nanotubes via chemical vapor deposition, and making the electrodes on nickel foils by electrophoretic deposition method. The TEM image in Figure 7(a) indicates an open porous structure with high accessible surface area, and the cyclic voltammetry curves in Figure 7(b) shows a good cyclability with no degradation observed. The calculated capacitance is 21 F/g, with a power density of ~20 kW/kg.

Graphene is another outstanding candidate for making supercapacitor electrodes, owing to its unique two dimensional nanosheet structure, extremely high surface area, excellent electrical conductivity and high strength.^{35,36} Therefore, people can usually achieve high capacitance by using graphene to construct supercapacitor electrodes. For example, Liu *et al*³⁷ have prepared graphene based supercapacitor electrodes. From Figure 8(a) it can be seen that a mesoporous structure can be obtained due to the curved graphene sheet morphology. The Ragone plot shown in Figure 8(b) indicates that a high energy density of 67.7 Wh/kg can be obtained (equivalent to that of a Ni metal hydride battery), but the supercapacitor can be charged and discharged in seconds or minutes.

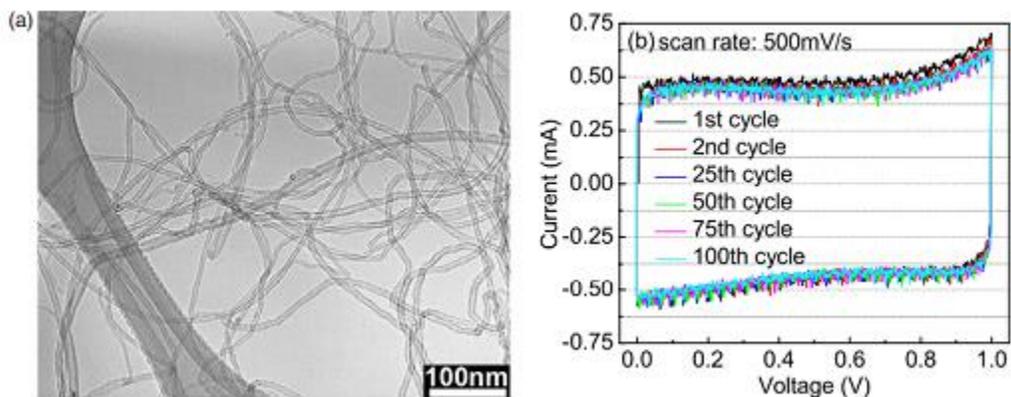


Figure 7. (a) TEM image of the purified carbon nanotubes, (b) cyclic voltammetry of the carbon nanotube thin films cycled from 0 to 1 V at 500 mV/s scan rate. From Du, *et al.*³⁴

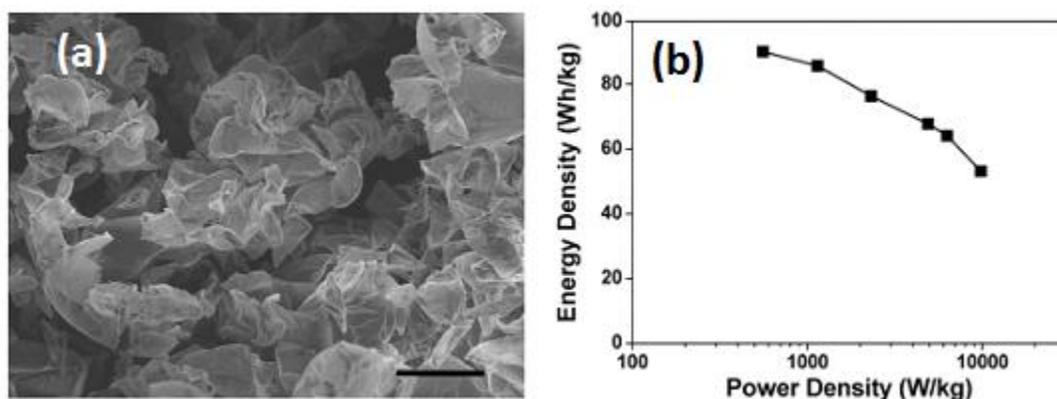


Figure 8. (a) SEM images of graphene nanosheets (scale bar: 10 μm), (b) Ragone plot of graphene supercapacitor. From Liu, *et al.*³⁷

1.3.2 Conductive polymers

Conductive polymers can be classified as pseudocapacitors, because they mainly offer capacitance through redox processes. The possibility of introducing positive or negative charge centers on electronically conjugated polymer chains through electrochemical redox reaction makes them viable candidate materials for supercapacitors.¹ The conductive polymers can be charged positively or negatively, accompanied with ion insertion to balance the injected charges. The redox reactions usually happen throughout the entire bulk instead of just on the surface.³⁸ Such charge and discharge processes are also highly reversible since no phase changes are involved.¹ Due to many advantages of conductive polymers, including high conductivity, high voltage window, high capacity and reversibility, environmental friendliness and low

cost,³⁹⁻⁴² more and more works have been done to investigate the possibility of using conductive polymers as pseudocapacitor electrodes.

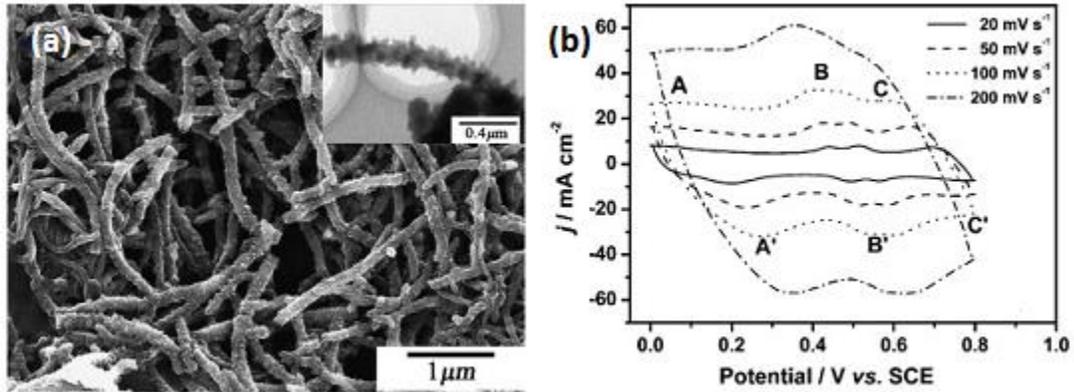


Figure 9. (a) The SEM image of PANI on stainless-steel substrate, and (b) cyclic voltammetry curves of as-prepared PANI electrode under different scan rates. From Li, *et al.*⁴³

The most commonly investigated conductive polymers used as supercapacitor electrode materials are polyaniline (PANI) and polypyrrol (PPy). A lot of papers can be found from recent years. Li *et al.*⁴³ have prepared PANI fiber (as shown in Figure 9(a)) on stainless steel substrate. The cyclic voltammetry measurement in 1 M H₂SO₄ electrolyte shown in Figure 9(b) demonstrates a high specific capacitance of 418 F/g at 20 mV/s scan rate. Sharma *et al.*⁴⁴ have prepared PPy film on graphite plate by using a novel pulsed polymerization method, with its morphology shown in Figure 10(a). The obtained electrode exhibits very high specific capacitance and excellent cycle stability, as shown in Figure 10(b). Besides, other commonly used conductive polymers serve as supercapacitor electrodes are polythiophene (PTh),^{45,46} poly(3,4-ethylene-dioxythiophene) (PEDOT),^{47,48} etc.

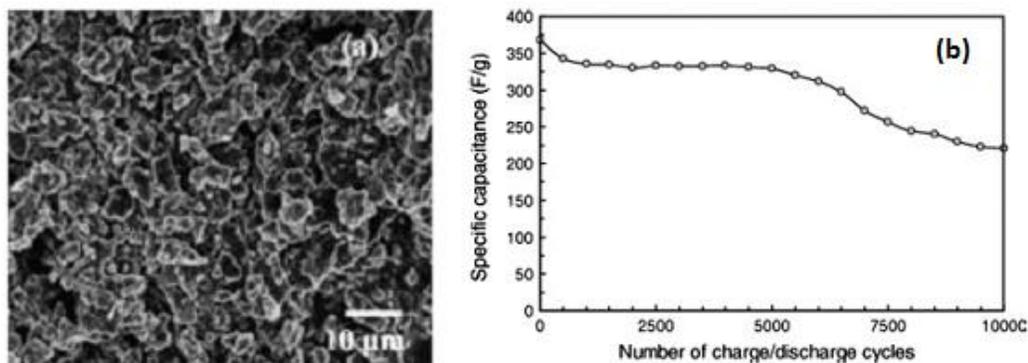


Figure 10. (a) The SEM image of PPy film on polished graphite plate, and (b) cycle stability of PPy film obtained at 5 mA/cm^2 . From Sharma, *et al.*⁴⁴

1.3.3 Transition metal oxides

Transition metal oxides are considered as most promising next generation electrochemical supercapacitor electrode materials, since they can provide higher energy density than conventional carbon-based double-layer capacitors, and also better electrochemical stability than conductive polymer-based materials. The charge storage mechanism in transition metal oxides is pseudocapacitive, which mainly involve electrochemical faradaic redox reactions within appropriate voltage windows, but also exhibit some double-layer capacitance.^{4,49} The general prerequisites for transition metal oxides to be used as electrochemical supercapacitor electrodes are: (1) the metal must have at least two oxidation states that can coexist within a continuous voltage range, with no phase change or irreversible structure change, (2) the transition metal oxide itself must be electronically conductive, and (3) the protons or alkali cations should be absorbed on the oxide surface or intercalate into their lattice easily during charge and discharge.^{1,4} Until now, the most extensively investigated materials include ruthenium oxide, manganese oxide, vanadium oxide, and so on.

1.3.3.1 Ruthenium oxide

Among all transition metal oxides, ruthenium oxide is the first and most extensively studied candidate, due to its wide potential window, high proton conductivity, extremely high specific capacitance, long cycle life, good electrical conductivity, and high rate capability.^{50,51} The charge storage mechanism of ruthenium oxide in acidic electrolyte

can be expressed in Equation (10), the electron transfer is accompanied with proton adsorption on the surface of RuO₂, and the Ru oxidation state is changed correspondingly.⁵²⁻⁵⁴



Several factors can affect the electrochemical behavior of ruthenium oxide, including:

(1) Surface area. The higher the surface area, the more active redox centers can be provided, and thus more capacitance can be obtained.⁵⁵

(2) Water content in the structure. Proton exchange is a critical process for charge storage as shown in Equation (10), and the hydrogen atoms can move much more efficiently in hydrous samples, thus the presence of water will promote the proton diffusion and thereby increase the capacitive behavior.^{56,57}

(3) Crystallinity. Generally speaking, amorphous samples with disordered structures can help improving the capacitance, because the redox reactions not only happened on the surface but also occurred in the bulk.⁵⁵ In contrast, a well crystallized sample will prevent proton intercalation into the bulk of the sample due to diffusion limitation, thus leading to inferior capacitance.

(4) Particle size. Smaller particle size can help shorten the diffusion distance and thereby facilitate the proton intercalation into the bulk, leading to more active sites and improved specific capacitance.^{58,59}

1.3.3.2 Manganese oxide

Although ruthenium oxide exhibits remarkably high specific capacitance and several other advantages, however, its drawbacks, such as high cost, low abundance, and especially environmental harmfulness, limit its commercialization as supercapacitor electrodes.⁶⁰ Thus, researchers have put significant effort trying to find cheaper and more environmentally friendly metal oxide materials that show similar electrochemical behavior to ruthenium oxide. After the early report by Goodenough in 1999,⁶¹ manganese oxide, with many advantages such as low cost, environmentally friendliness, as well as

high theoretical capacitance of 1370 F/g,^{12,62-64} has attracted much attention in recent years and is considered as a very promising alternative material for electrochemical supercapacitor applications.

The capacitance of manganese oxides also mainly comes from pseudocapacitance, which is originate from the reversible redox reactions of Mn, as well as the intercalation/de-intercalation of electrolyte cations. The mechanism can be generally expressed as shown in Equations (8) and (9). Unlike many metal oxide pseudocapacitors that exhibit redox peaks in CV curves, the manganese oxide based electrodes always exhibit typical rectangular shaped CV curves (as shown in Figure 11) despite the redox nature of energy storage, which is analogous to the non-faradaic energy storage mechanism. This is because the electrodes are charged and discharged at a pseudo-constant rate over the whole voltammetric cycle.²⁵

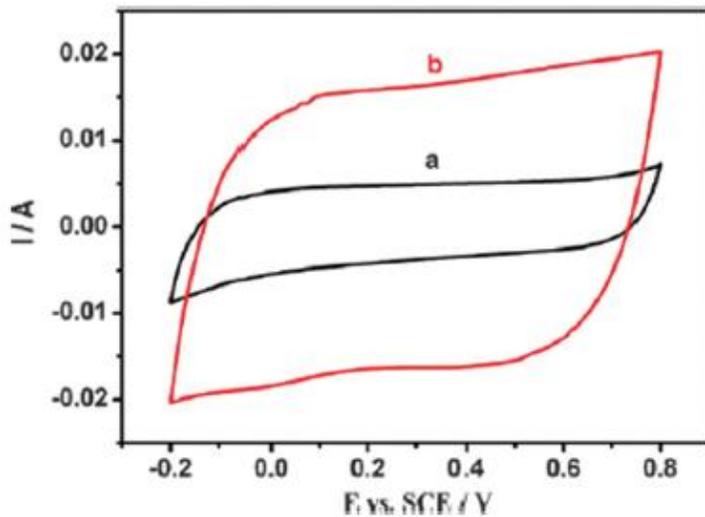


Figure 11. Typical cyclic voltammetry curves of MnO₂ based electrodes cycled in 1 M Na₂SO₄ electrolyte at a scan rate of 5 mV/s. From Xu, *et al.*⁶⁵

The specific capacitance of manganese oxide electrodes can be affected by many factors. For example, different crystallinity can lead to different capacitance. The high crystallinity can give rise to high electrical conductivity, but the alkali cation intercalation will be limited. The lower crystallinity may result from distorted structures and lack of long range periodicity, which enable exposure of more surface absorption sites and thus facilitate the ion absorption. However, the samples with low crystallinity typically exhibit

low electrical conductivity. Thus, there is a trade-off between high electrical conductivity and more absorption of alkali cations.

The crystal structure is another important factor that can affect the specific capacitance. As shown in Figure 12, MnO_2 can crystallize into several crystallographic structures, and different structures show different MnO_6 octahedra linkages. Since the pseudocapacitance mainly depends on the proton or alkali cation intercalation, only those structures with sufficient diffusion pathways can lead to good capacitive properties. Devaraj *et al*⁶⁶ have measured the capacitance of different MnO_2 crystal structures, and the results indicate that the capacitance strongly depends on the structure, and it decreases in the following order: $\delta = \alpha > \gamma > \beta$.

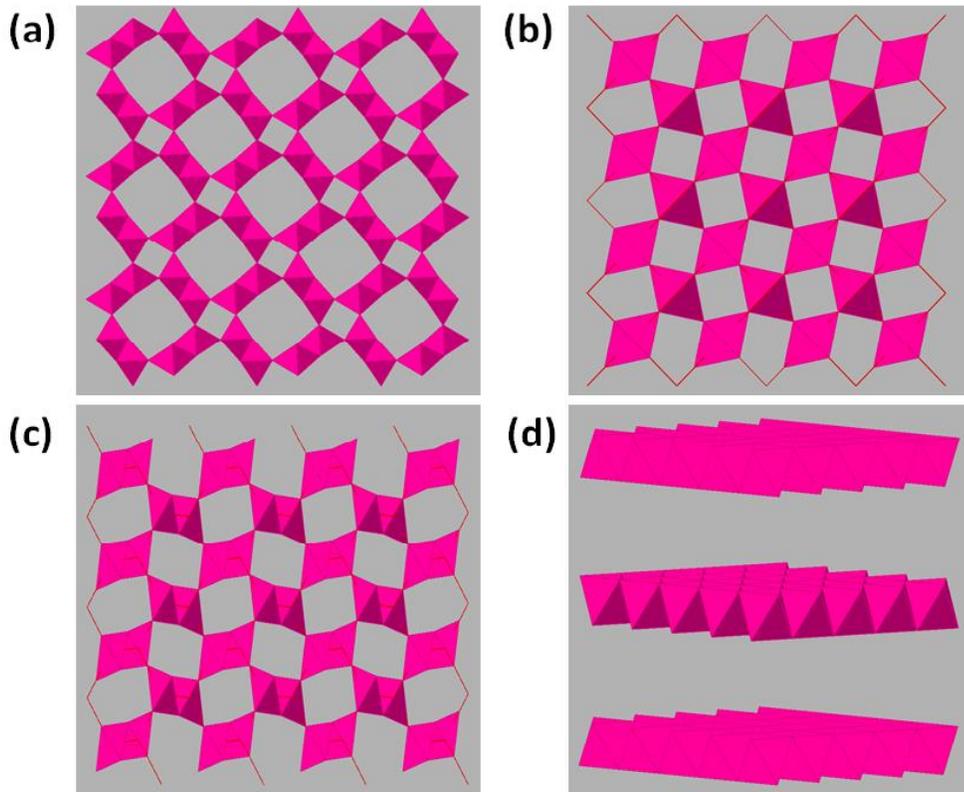


Figure 12. Crystal structures of (a) α , (b) β , (c) γ , and (d) δ MnO_2 .

Morphology and surface area are also very important factors that affect the specific capacitance. There is no doubt that the capacitance will increase with the increase of surface area and the formation of porous structures, since the large surface area will

provide more active adsorption sites and the porous structures will definitely facilitate the ion intercalation process.

The electrical conductivity of the electrode materials is critical in improving the capacitive performance, since the electrical conductivity of manganese oxide is typically poor. Therefore great efforts have been devoted to improving the electrical conductivity through incorporation of other metal atoms into manganese oxide compounds.⁶⁷⁻⁶⁹ Another way of improving the electronic conductivity is by tuning the defect chemistry, such as changing the oxidation states of Mn, or introducing cation/anion vacancies. Also, depositing a thin layer onto a porous electronically conductive substrate with large surface area has also been confirmed as a way to improve the electrochemical performance.⁷⁰

1.3.3.3 Vanadium oxide

Vanadium oxides have emerged in recent years as potential electrochemical supercapacitor electrodes, due to their variable oxidation states that can provide much wider potential window and much higher capacities, along with other advantages such as low cost, abundant resources, and easy synthesis.^{71,72} After the first report of using V_2O_5 for charge storage by Whittingham *et al.*,⁷³ more and more works have been done in recent years, with V_2O_5 and $VO_2(B)$ having been the most extensively investigated.

V_2O_5 is a favorable candidate for supercapacitor electrodes due to its accessible layered structure, which is shown in Figure 13. The orthorhombic V_2O_5 consists of distorted VO_6 octahedral building blocks linked together to form the layered anisotropic structure.⁷⁴ Adjacent layers are stacked together via weak van der Waals interactions, which make it possible to exfoliate the single layer from the bulk, and then assemble 3-D porous nanostructures. Zhu *et al.*⁷⁵ prepared 3-D V_2O_5 nanostructures using a freeze drying method, which exhibit porous nanostructures as shown in Figure 14(a-b). The obtained V_2O_5 electrode has a surface area of $133 \text{ m}^2/\text{g}$, and exhibits excellent electrochemical charge storage properties, including high capacitance of 451 F/g and 90% capacitance retention after 4000 cycles. The challenge for V_2O_5 is its low conductivity. In order to address this issue, doping with other elements⁷⁶ or using conductive substrates⁷⁷ can be used as effective methods.

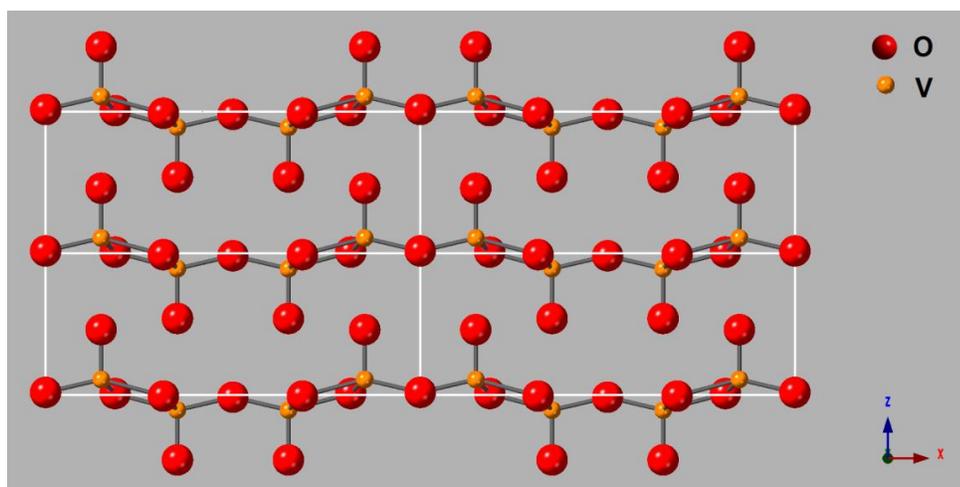


Figure 13. Crystal structure of V_2O_5 .

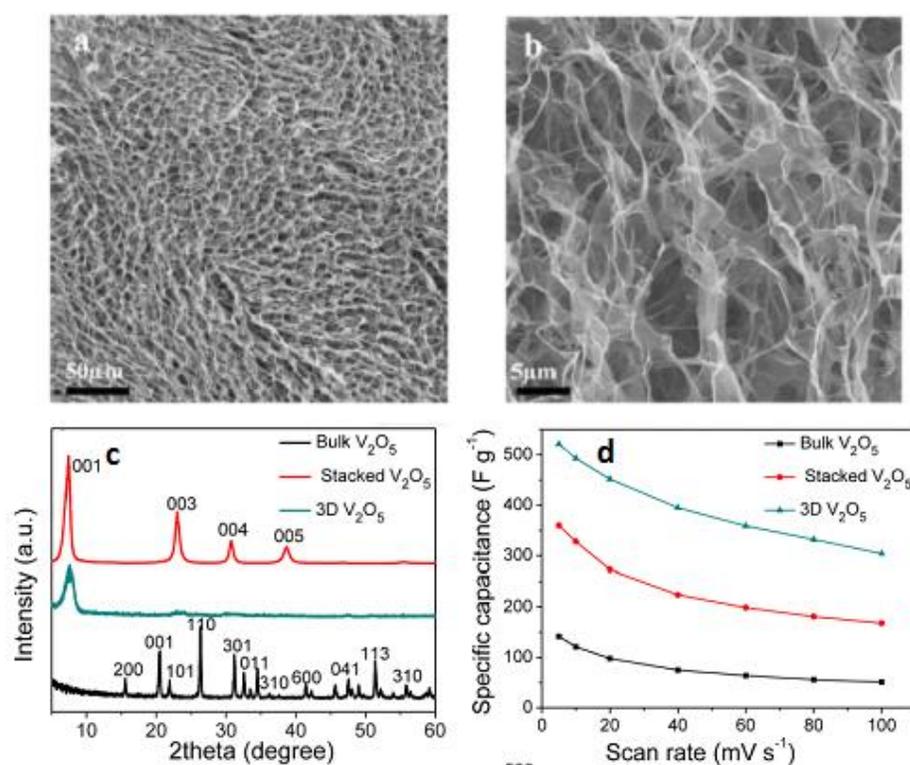


Figure 14. (a, b) SEM images of V_2O_5 architecture constructed from nanosheets, (c) XRD patterns, indicating the differences between the layered structures of the 3-D V_2O_5 architecture, the stacked V_2O_5 film, and the bulk V_2O_5 crystal, (d) capacitance comparison of the as-prepared samples at different scan rates. From Zhu, *et al.*⁷⁵

$\text{VO}_2(\text{B})$, a metastable monoclinic polymorph, is also a promising electrode materials for pseudocapacitors. The crystal structure of $\text{VO}_2(\text{B})$ is shown in Figure 15, which is comprised of distorted VO_6 octahedra that are edge sharing. Each sheet is linked to adjacent sheets by corner sharing in c-direction.⁷⁸ Unlike the other polymorphs of vanadium oxide, the corner and edge sharing structure of $\text{VO}_2(\text{B})$ is resistant to lattice shearing during alkali cation intercalation, thus leading to a quite stable structure during electrochemical cycling. The $\text{VO}_2(\text{B})$ nanosheets are usually prepared using the hydrothermal method, which can be very fast and ease realization of mass production.

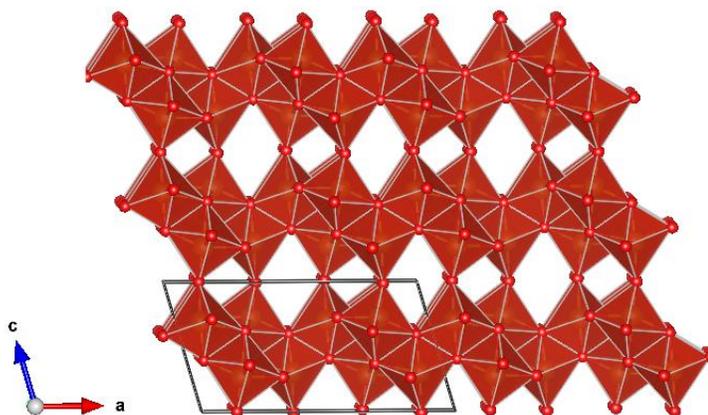


Figure 15. Crystal structure of $\text{VO}_2(\text{B})$.

Several studies have investigated the charge storage properties of $\text{VO}_2(\text{B})$ nanosheets. Wang *et al*⁷⁹ have prepared interconnected $\text{VO}_2(\text{B})$ nanoflowers uniformly grown on 3-D graphene networks, as shown in Figure 16(a-b). The hybrid produced an improved area specific capacitance of 466 mF/cm^2 , a capacitance retention of 63.5% after 3000 cycles, and exhibits superior supercapacitor properties. Rahman *et al*⁸⁰ prepared a novel $\text{VO}_2(\text{B})$ -multiwall carbon nanotube (MWCNT) composite with a sheet-like morphology by a simple *in-situ* hydrothermal process. The nanosheets are grown together in the form of bundles composed of numerous nanosheets, each with a smooth surface and a typical length of 300-500 nm, width of 50-150 nm, and thickness of 10-50 nm. The electrochemical results indicate improved lithium ion storage properties. Wang *et al*⁸¹ have prepared $\text{VO}_2(\text{B})$ nanosheets by a liquid-phase exfoliation from $\text{VO}_2(\text{B})$ bulk.

Compared with the bulk counterpart, the exfoliated nanosheets exhibit enhanced lithium ion storage properties.

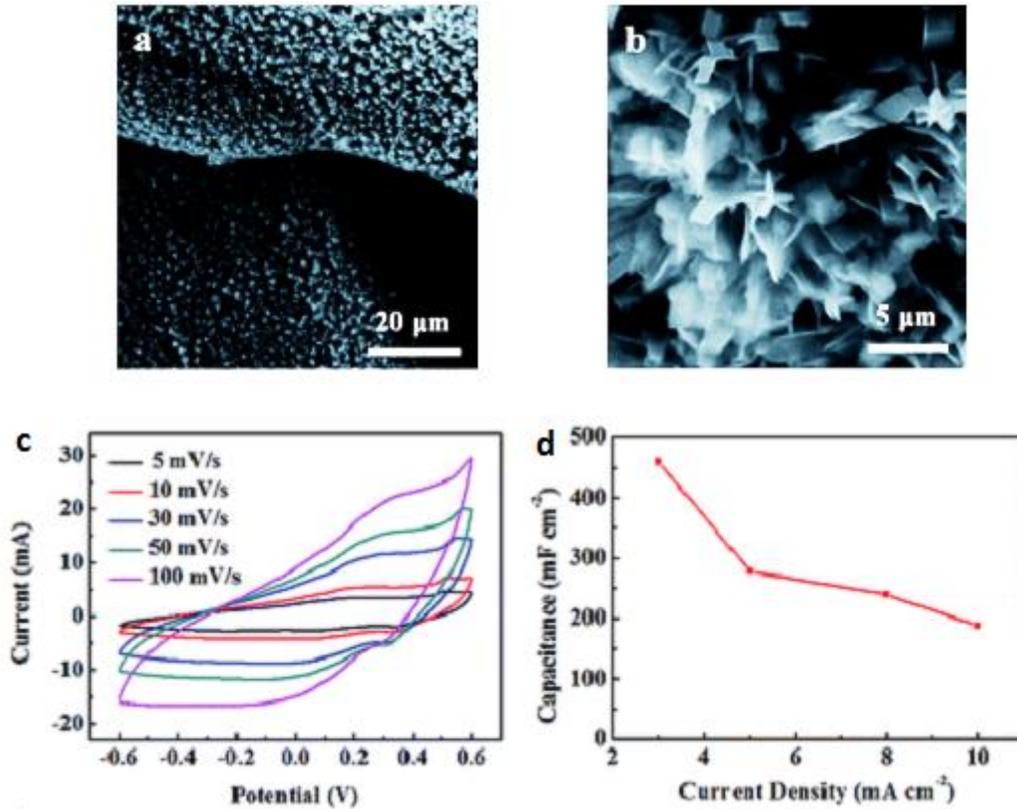


Figure 16. (a, b) SEM images of VO₂(B) nanoflowers on 3D graphene networks, (c) cyclic voltammetry curves of the as prepared samples, and (d) areal specific capacitance as a function of current density. From Wang, *et al.*⁷⁹

1.3.3.4 Other transition metal oxides

Several other transition metal oxides have also been investigated as potential candidates for the application of pseudocapacitor electrodes. For example, Shivakumara *et al.*³¹ prepared porous flower-like α -Fe₂O₃ nanostructures by an ethylene glycol mediated self-assembly process. The obtained electrode possesses a discharge capacitance of 127 F/g at 1 A/g current density, and 80% capacitance retention after 1000 cycles. Kim *et al.*²⁶ have synthesized NiO nanostructures with three distinct morphologies by a sol-gel method and studied their morphology-dependent supercapacitor properties. The NiO nanoflowers with a distinctive 3-D network and the highest pore volume shows the best supercapacitor properties, indicating that forming a 3-D network is a

straightforward way of improving the electrochemical properties of a supercapacitor. Rao *et al*²⁷ prepared ultralayered Co_3O_4 structures with high porosity by a homogeneous precipitation process under hydrothermal conditions. The as-prepared samples exhibit rectangular 2-D flake morphology with micrometer length, and the charge-discharge study shows that the material can deliver very high specific capacitance of 548 F/g at a current density of 8 A/g and retains 66% of capacitance at 32 A/g. Rajeswari *et al*³⁰ have prepared 1-D MoO_2 nanorods by thermal decomposition of tetrabutylammonium hexamolybdate in an inert atmosphere. The galvanostatic charge-discharge studies show that a specific capacitance of 140 F/g can be achieved in 1 M H_2SO_4 solution. Ren *et al*⁸² prepared hollow SnO_2 microspheres via chemically induced self-assembly in hydrothermal environment. The obtained sample exhibits high specific capacitance of 663 F/g, which can be attributed to the high specific surface area and hollow structure of SnO_2 microspheres.

1.4 Fabrication methods for making supercapacitor electrodes

Developing appropriate ways to fabricate the supercapacitor electrodes is typically very important to get good performance, especially when tested using three electrodes system in the lab. One of the most commonly used approaches can be described as follows. First, the active material is mixed with binders and conductive additives in a desired ratio to obtain homogeneous slurry. Then, the slurry is spread onto a conductive substrate (such as nickel foil, aluminum foil, stainless steel, etc.). Finally, the as-obtained electrode will be dried to evaporate the solvent and therefore achieve a uniform coating layer. The slurry can be spread onto substrates either by hand, or using a tape-casting machine. The critical point is to choose the appropriate ratio of active material, binder and conductive additives, and make sure they are homogeneously mixed together.

Another technique to make binder-free electrode is sol-gel dip-coating method. A stable colloidal suspension consisting active material is first prepared by the sol-gel method, and a thin film can be directly obtained on conductive substrates through “dip-coating” or “drop-coating” methods. Finally, the thin film is calcined at various temperatures to get the desired electrodes.^{11,83} The calcination temperature is critical in forming the desired morphology and porosity of the thin films, which will lead to

different capacitive properties. The film thickness is also very important, since the electrical conductivity is usually decreased dramatically with increasing the film thickness (especially for the transition metal oxides), and only the top thin layer is involved in the redox reactions.⁸⁴

Anodic electrochemical deposition is also a facile way to prepare binder-free electrodes. The whole setup usually involves the target precursor salt, a voltage source, and two electrodes. When an electric field is applied, the charged reactive species will diffuse onto the electrode surface through the electrolyte, and then oxidize and deposit to form a thin film. Xia *et al*⁸⁵ have prepared highly ordered MnO₂ nanotube arrays via electrochemical deposition method on porous alumina template, which are shown in Figure 17(a-b). The electrochemical results show that the as-prepared electrode possesses a high specific capacitance of 320 F/g, as well as good rate capability and cycle stability. The deposition parameters, such as applied voltage, time, temperature, precursor concentration, etc., usually need to be adjusted, in order to achieve 3-D porous nanostructures with large surface area and appropriate thickness, which will finally lead to enhanced supercapacitor performance.

Another effective way to make binder-free electrodes is electrophoretic deposition (EPD). The process can be simply illustrated in Figure 18.⁸⁶ Typically speaking, the charged particles are first dispersed or suspended in a liquid medium. Then with the application of an electric field, the charged particles will be attracted to and deposited onto a conductive substrate of opposite charge. The particles can be either positively or negatively charged, and therefore the deposition can happen on either cathode or anode, respectively. The principal driving force for EPD is the charge on the particles and the electrophoretic mobility of the particles in the solvent under the applied electric field. However, one intrinsic disadvantage of EPD is that the water cannot be used as liquid medium, since the application of high voltage will lead to the evolution of oxygen and hydrogen at the electrode surface and therefore affect the quality of the deposited film. The main factors that can affect the deposition process include applied voltage or current density, the precursor concentration, the suspension stability, as well as the charges on the particles. Therefore, in order to get a thin film with porous structure, the above-mentioned parameters need to be precisely manipulated. Several works have been done in

recent years.⁸⁷⁻⁹⁰ which make the EPD method an effective way to prepare binder-free electrodes for supercapacitor applications.

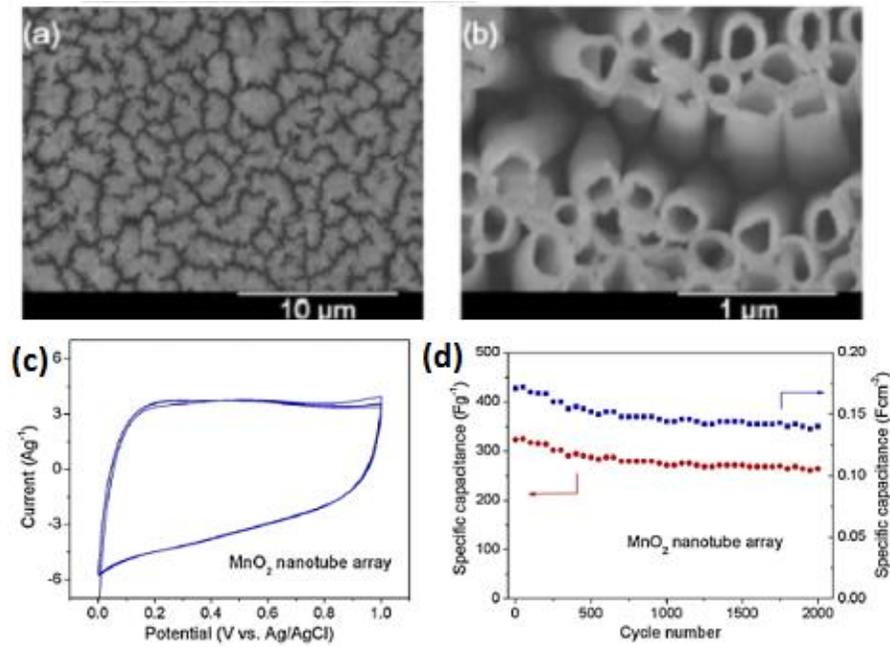


Figure 17. (a, b) The SEM images of MnO₂ nanotube arrays, (c) CV curves of MnO₂ nanotube array electrode at scan rate of 20 mV/s, and (d) mass-specific capacitance and area-specific capacitance as function of cycle number. From Xia, *et al.*⁸⁵

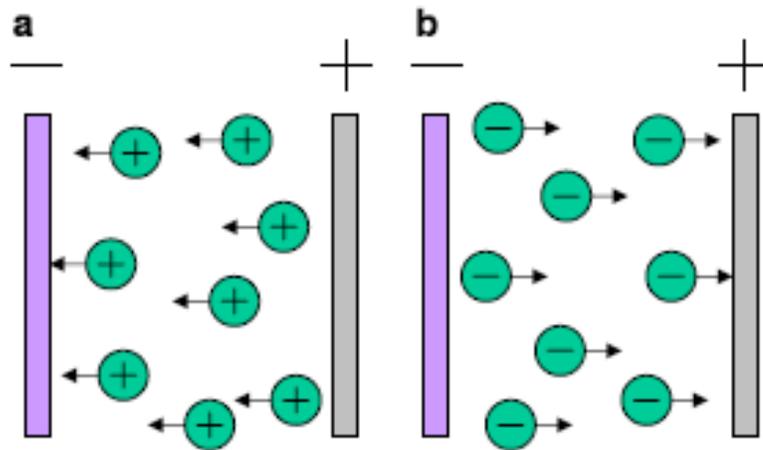


Figure 18. Schematic illustration of electrophoretic deposition process: (a) Cathodic EPD and (b) anodic EPD. From Besra, *et al.*⁸⁶

1.5 Initiatives of using 2-D layered δ -MnO₂ and VO₂(B) nanosheets as supercapacitor electrodes

After the first discovery of single-layer graphene in 2004 by Novoselov and Geim,⁹¹ the two-dimensional (2-D) layered nanomaterials with atomic thickness have attracted extensive attention, due to their unique and fascinating properties and inspirational applications such as catalysis, sensing, photovoltaics, and energy storage.⁹²⁻⁹⁵

1.5.1 Advantages of using 2-D layered δ -MnO₂ and VO₂(B) nanosheets as supercapacitor electrodes

As shown in Figure 12, there are several polymorphs of MnO₂, and each one has a distinctive structure. These structures are different in the way MnO₆ octahedra are linked together, and thereby they possess tunnels and interlayers with gaps of different magnitude. It can be seen that the α , β and γ phases possess 1-D tunnel in their structures, the δ -phase is a 2-D layered material, and the λ -phase exhibits a 3-D spinel structure. Since the pseudocapacitive properties mainly depend on the intercalation/de-intercalation of protons or cations in MnO₂, only structures with sufficient gaps/channels that can facilitate fast ion diffusion and accommodate as many as these ions are useful for enhanced supercapacitive properties.

Compared with the polymorphs that possess tunnel structures, the 2-D layered MnO₂ nanosheets are more promising for the application in energy storage devices because of the following advantages:²⁵

(1) The open and large interlayer spaces enable sufficient contact between the electrolyte and material surface, which will provide high-speed pathways for the ion intercalation process.

(2) The layered structures can also help relax the electrochemical strains induced by the ion intercalation and redox changes of the constituent cations, which can greatly increase the structure stability and cyclability.

The δ -MnO₂ nanosheet composed of edge-sharing MnO₆ octahedra, and the individual nanosheets are separated from each other by water molecules and different cations located in the interlayer region.^{96,97} Although the bulk layered crystals are composed of hundreds of single sheets compactly stacked together, which typically

exhibit small surface area and poor supercapacitor performance, when exfoliated to single- or few-layer nanosheets and then re-assembled together, porous nanostructures with large surface area can always be obtained (as shown in Figure 19). Moreover, the single-layer oxide nanosheet can provide effectively 100% surface without “bulk” component, thus can greatly help minimizing the diffusion barriers within the oxide during charge/discharge processes. Therefore, with the combination of 3-D porous nanostructures that can provide enormous numbers of surface adsorption sites, and the large and open interlayer gallery that can promote fast ion intercalation, the 2-D layered δ -MnO₂ nanosheets are considered a most promising candidate for making supercapacitor electrodes.

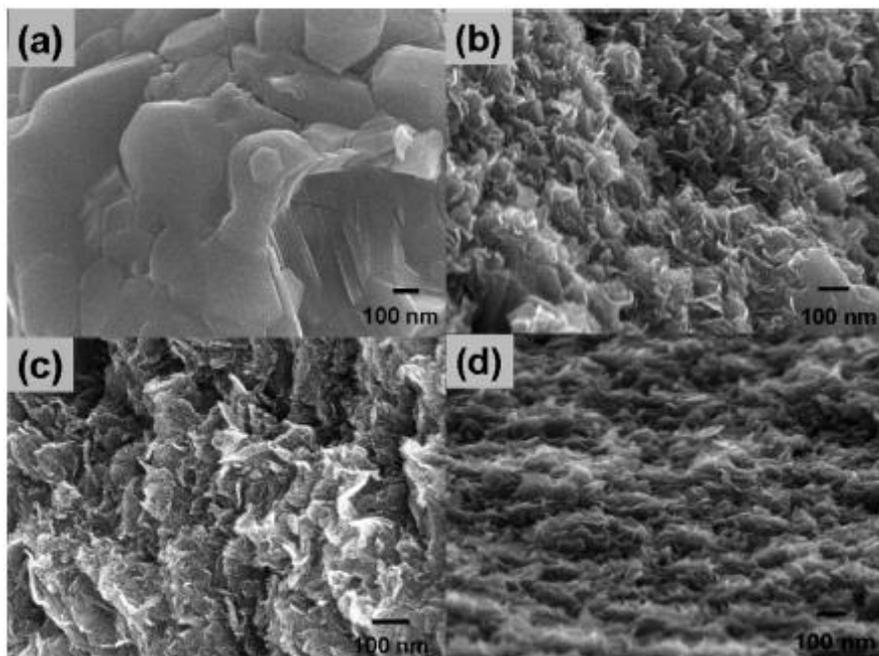


Figure 19. SEM images of (a) pristine layered K_{0.45}MnO₂, (b) Li⁺-layered MnO₂, (c) Na⁺-layered MnO₂, and (d) K⁺-layered MnO₂. From Song, *et al.*⁹⁸

Devaraj *et al.*⁶⁶ have prepared various MnO₂ polymorphs and evaluated their capacitive properties. Their results show that the measured specific capacitance strongly depends on the crystallographic structures. The β -MnO₂ is unsuitable for capacitor applications because of its narrow (1×1) tunnels that cannot accommodate cations during the charge/discharge process. In contrast, the layered δ -MnO₂ nanosheet exhibits high

specific capacitance values due to its large interlayer separation. Ghodbane *et al*⁹⁹ have also prepared a series of MnO₂ allotropic phases, and compared their capacitive properties, with the results shown in Figure 20. Other than the spinal phase of MnO₂, which possesses much larger surface area that leads to enhanced specific capacitance, the 2-D layered birnessite exhibits higher capacitance than all other polymorphs. Their results also indicate that the increased cavity size results in the improvement of the electrochemical performance.

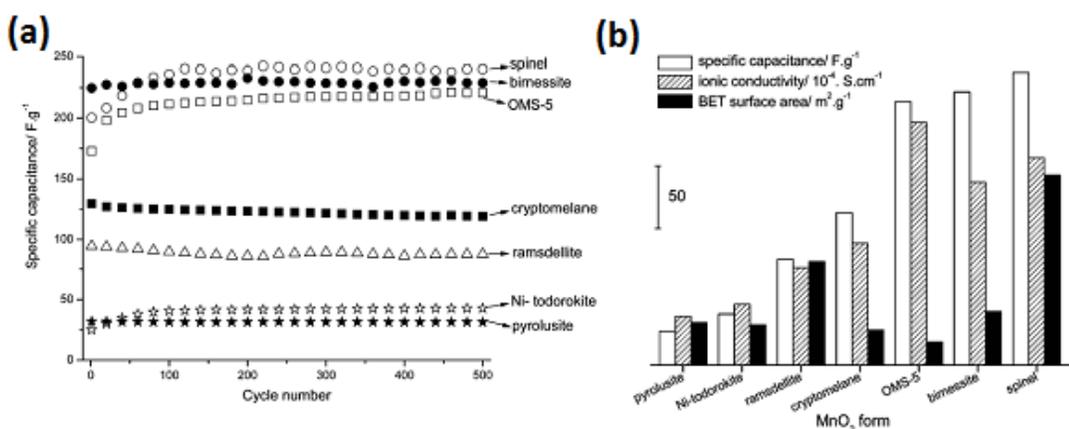


Figure 20. (a) Specific capacitance comparison of the different electrodes underwent 500 electrochemical cycles. (b) Comparison of specific capacitance, ionic conductivity, and BET surface area of different MnO₂ polymorphs. From Ghodbane, *et al*.⁹⁹

Similar to birnessite δ -MnO₂, the VO₂(B) also exhibits certain advantages compared with other polymorphs when used as supercapacitor electrodes. There are four polymorphs of VO₂, including the most stable phase VO₂(R) with the rutile structure, the monoclinic VO₂(R) with a slightly distorted rutile structure, the tetragonal phase VO₂(A), and the metastable phase VO₂(B) with monoclinic structure.¹⁰⁰ As described in section 1.3.3.3, the crystal structure of VO₂(B) is comprised of distorted VO₆ octahedra that are edge sharing. Each sheet is linked to adjacent sheets by corner sharing along the c-direction, and it possesses perovskite-like cavities.⁷⁸ The cation diffusion is usually parallel to the [010] crystal orientation. Since the cation insertion usually leads to uniaxial expansion of the perovskite-like cavities, and the edge sharing of the octahedra is along the lattice expansion direction, thus, there is an increased resistance to V-O bond

cleavage during cation intercalation, which finally leads to a stable structure during electrochemical cycling compared with other polymorphs.¹⁰¹

Recently, various nanostructures of VO₂(B) have been prepared, such as 0-D nanoparticles,¹⁰² 1-D nanorods¹⁰³ and nanowires,¹⁰⁴ etc. However, poor electrochemical performance has always been observed for samples with these morphologies, which may be due to the easier agglomeration and collapse of the nanostructures.¹⁰⁵ Therefore, the preparation of 2-D nanosheets, assembled 3-D nanostructures, has received great attention due to their enhanced capacitance and cycle stability. For example, Nethravathi *et al*¹⁰¹ have prepared N-doped graphene-VO₂(B) nanosheets through hydrothermal reactions (as shown in Figure 21(a)). The as-prepared sample exhibits large capacity, high rate capability, and excellent cycling stability when used as lithium ion batteries. Rahman *et al*⁸⁰ prepared VO₂(B)-multiwall carbon nanotube composite with a sheet-like morphology. The as-prepared electrodes exhibit capacity retention of 92% after 100 cycles, which is due to the fact that the composite can prevent aggregation of the active materials and also accommodates large volume variation.

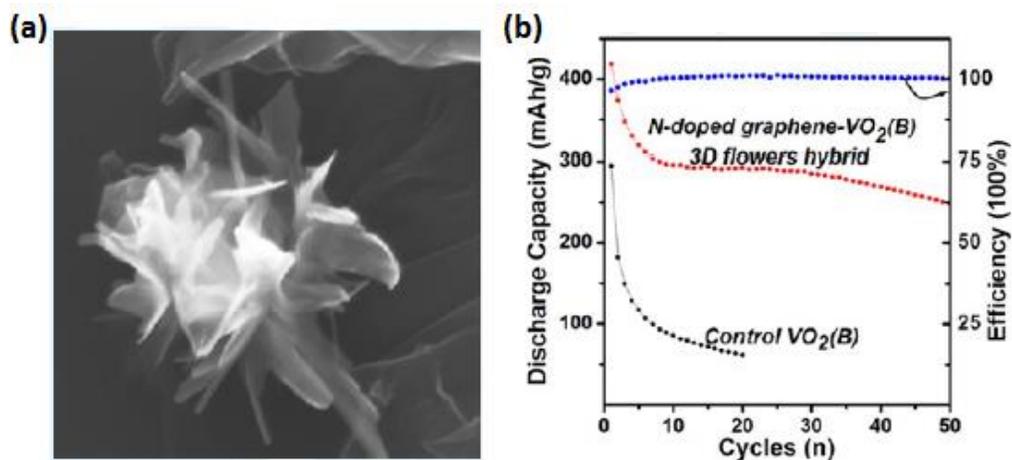


Figure 21. (a) SEM image of N-doped graphene-VO₂(B) nanosheet-built 3-D flower hybrid, (b) cycling performance at a current density of 50 mAh/g. From Nethravathi, *et al*.¹⁰¹

1.5.2 Commonly used approaches to fabricate 2-D layered $\delta\text{-MnO}_2$ and $\text{VO}_2(\text{B})$ nanosheets

Inspired by the exfoliation of layered graphite, metal oxide nanosheets can also be prepared by exfoliating a layered compound into single layers or few layers. Thus, one of the most widely used methods for preparing $\delta\text{-MnO}_2$ nanosheets is described as follows: high temperature solid-state reaction to prepare the parent bulk layered phase, ion-exchange of the interlayer alkali metal ions with protons, and exfoliation with large organic molecules (TBAOH, TMAOH, etc.).^{106,107} The exfoliated 2-D nanosheets are usually stabilized in the colloidal suspension. Because of the negative surface charge of these exfoliated $\delta\text{-MnO}_2$ nanosheets, they can be reassembled with introduction of cationic species, leading to the formation of highly porous 3-D nanostructures with tailored pore size and surface morphologies.^{98,108} The overall procedures are shown in Figure 22.¹⁰⁹

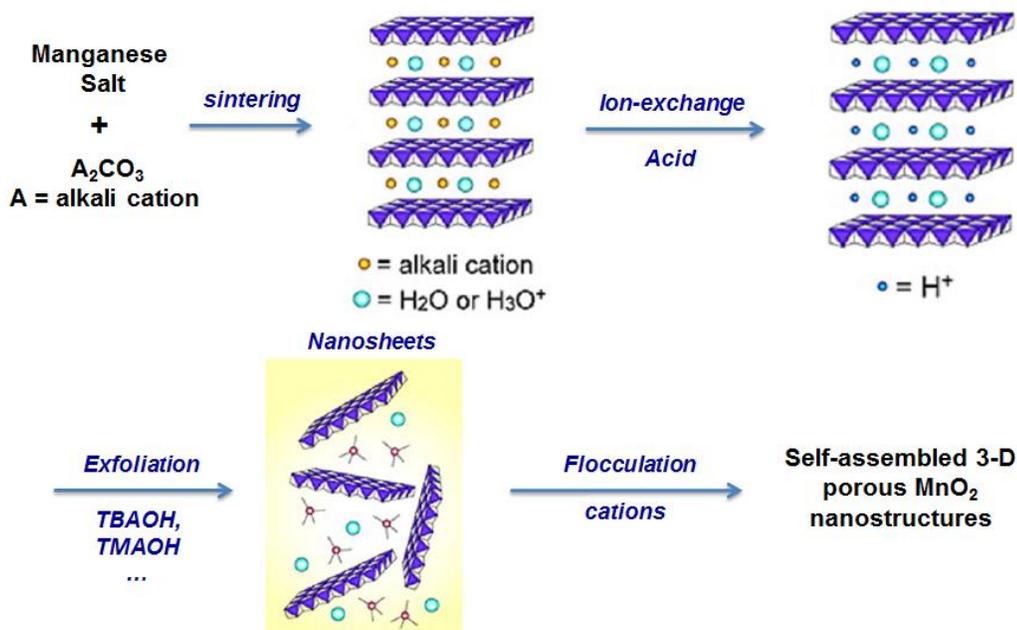


Figure 22. Experimental procedures of making the $\delta\text{-MnO}_2$ nanosheets from its bulk crystalline phase. From Kai, *et al.*¹⁰⁹

A lot of published papers have reported the successful preparation of exfoliated $\delta\text{-MnO}_2$ nanosheets and the reassembled 3-D porous nanostructures with large surface area.

Sasaki *et al*¹⁰⁶ have investigated the exfoliation process of the layered manganese oxide upon contact with aqueous TBA ions. They found that the $\text{H}_{0.13}\text{MnO}_2 \cdot 0.7\text{H}_2\text{O}$ underwent various reactions including intercalation, osmotic swelling, and delamination into single sheets, which depending on the TBA concentration. Hwang *et al*⁹⁸ have successfully prepared the porous assembly via flocculation of the exfoliated MnO_2 nanosheets with alkali metal cations. The as-prepared samples exhibit mesoporous structures with large surface area (50-70 m^2/g) and good supercapacitor properties. Our group has also synthesized $\delta\text{-MnO}_2$ nanosheets via exfoliation with TBAOH under ultrasonication, and flocculation with acid. The observation of porous structures after reassembly highlights the usefulness of our ultrasonic-assisted exfoliation and flocculation procedures, where the exfoliation rate is greatly enhanced compared with most other reported procedures.²⁵

Except the method mentioned above, other commonly used approaches for making $\delta\text{-MnO}_2$ nanosheets include hydrothermal preparation, electrodeposition, wet chemistry method, etc. For example, Zhang *et al*¹¹⁰ have synthesized hierarchical porous nanostructures assembled from ultrathin birnessite-type MnO_2 nanosheets through a rapid hydrothermal method without using any template and surfactant. The SEM image in Figure 23(a) demonstrates that the products are composed of many ultrathin nanosheets with core-corona structure. Liu *et al*¹¹¹ have directly grown MnO_2 nanosheet arrays on Ni foam current collectors using one-step electrodeposition method. The obtained samples exhibit well defined mesoporous structures, as shown in Figure 23(b). The as-deposited MnO_2 nanosheets exhibit an average thickness of 20-25 nm with a pore size ranging from 2 to 8 nm. Sinha *et al*¹¹² reported the nucleation and growth of $\delta\text{-MnO}_2$ nanosheets using a simple wet chemical reaction at low temperature. The obtained samples exhibit typical sheet-like morphology as shown in Figure 23(c), demonstrating the usefulness of the wet chemistry method.

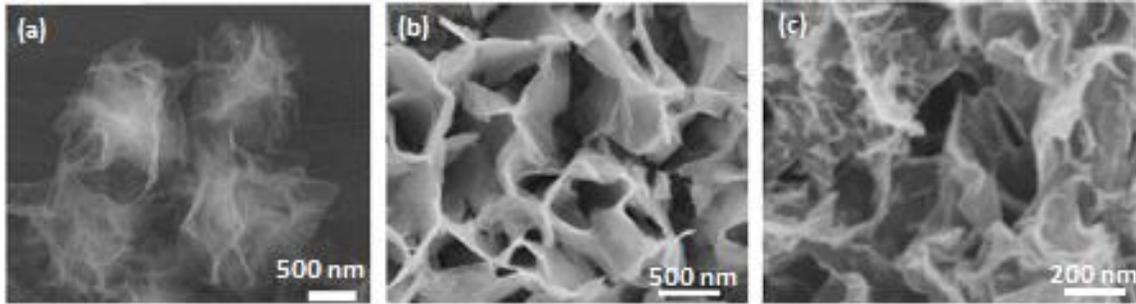


Figure 23. The typical SEM morphologies of δ -MnO₂ nanosheets prepared by (a) hydrothermal method, from Zhang, *et al.*,¹¹⁰ (b) electrodeposition method, from Liu, *et al.*,¹¹¹ and (c) wet chemistry method. From Sinha, *et al.*¹¹²

Unlike the versatile preparation methods for δ -MnO₂ nanosheets that have been developed, most of the VO₂(B) nanosheets are generally synthesized via hydrothermal reactions according to recently published papers. Through adjusting the hydrothermal reaction conditions, various nanostructures with desired morphologies assembled from VO₂(B) nanosheets can be easily obtained. Liang *et al.*¹¹³ have prepared ultra-large (over 100 μ m) VO₂(B) nanosheets with an exceptionally small thickness of only 2–5 nm, as shown in Figure 24(a), through a facile template-free hydrothermal synthesis approach. Mai *et al.*¹¹⁴ have investigated the influence of PVP and PEG on structures and surface morphologies during hydrothermal reactions, and has successfully prepared pure thin VO₂(B) nanosheets as shown in Figure 24(b). Zhang *et al.*¹¹⁵ have successfully prepared flowerlike VO₂(B) nanostructures assembled from single-crystalline nanosheets via a facile hydrothermal method using PVP as a capping reagent, with the typical morphology shown in Figure 24(c). They have also investigated the crystal growth mechanism, which was dominated by nucleation and growth, self-assembly, and Ostwald ripening. Several other papers have also reported the successful preparation of VO₂(B) nanosheets with desired morphologies, which confirm the effectiveness of the hydrothermal synthesis method.

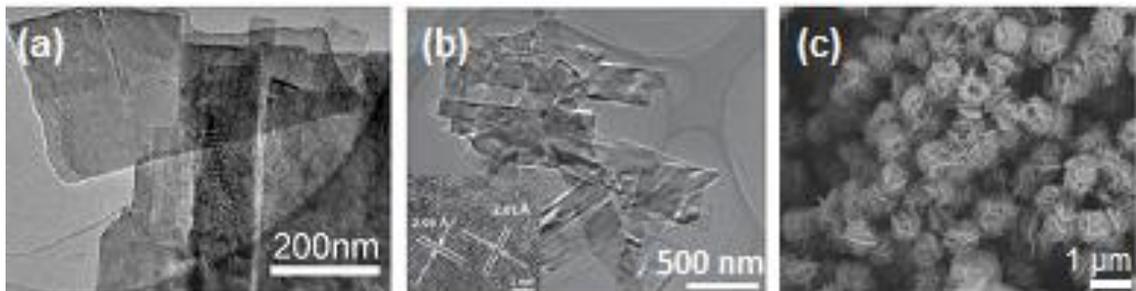


Figure 24. (a) HRTEM image of the VO₂(B) nanosheets prepared by hydrothermal method, from Liang, *et al.*,¹¹³ (b) TEM image of pure VO₂(B) nanosheets, from Mai, *et al.*,¹¹⁴ and (c) High-magnification SEM image of the flower-like VO₂(B) samples. From Zhang, *et al.*¹¹⁵

Recently, Liu *et al.*¹¹⁶ have proposed a room-temperature intercalation-deintercalation strategy to obtain ultrathin nanosheets exfoliated from layered materials. The schematic diagram is shown in Figure 25. The key point of this method is successive insertion of lithium ions and larger molecules, which will efficiently enlarge the interplanar distance and thereby weaken their strong covalent interactions. Specifically speaking, the bulk VO₂(B) is prepared by hydrothermal method. Then the bulk product was dispersed in deionized water by ultrasonication and stirred with LiCl for 24 hours. After lithiation, the solid intermediate was washed with deionized water sufficiently to remove the LiCl adsorbed on the VO₂(B) surface. Finally, single layers of VO₂(B) nanosheets can be exfoliated from the solid intermediates in DMF/H₂O (V/V=1:1) solution under ultrasonication for 5 hours. The TEM image shows a large-area and nearly transparent ultrathin VO₂(B) nanosheet with lateral dimensions of ca. 200-500 nm. The AFM results indicate the large 2-D nanosheets exhibit a height of ca. 0.62 nm, which matches well with the theoretical thickness of 0.615 nm for VO₂(B) single layers along the [001] direction, indicating the successful exfoliation of single-layer VO₂(B) nanosheet. Therefore, this work provides a new scalable strategy of making single-layer VO₂(B) nanosheet.

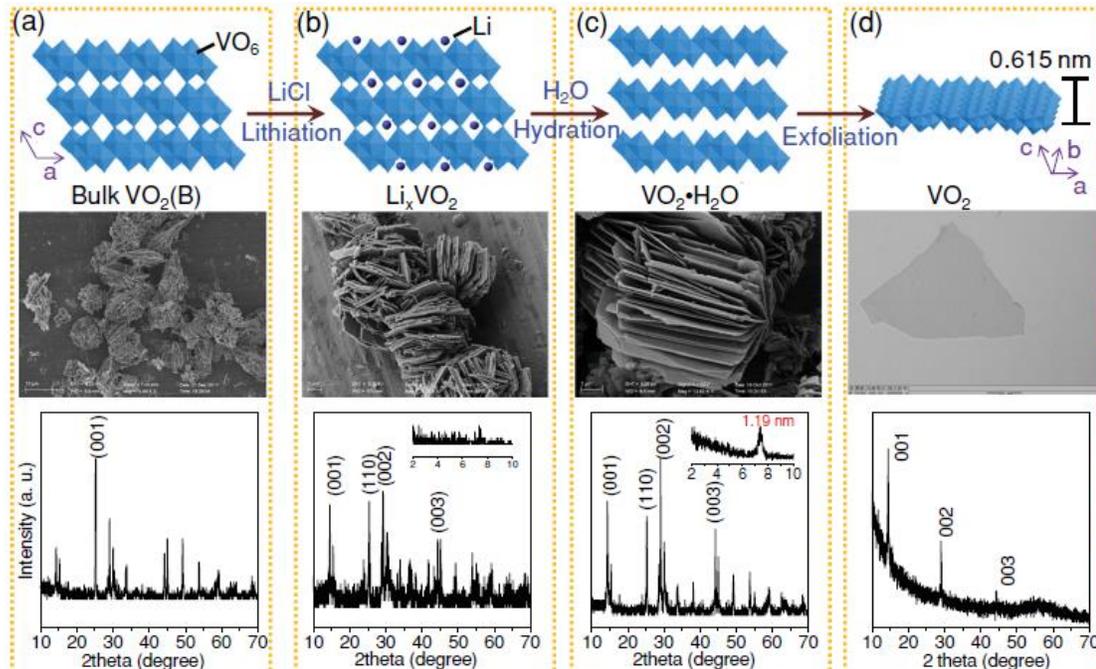


Figure 25. Schematic illustration shows the formation process of $\text{VO}_2(\text{B})$ ultrathin nanosheets: (a) bulk $\text{VO}_2(\text{B})$, (b) lithiated $\text{VO}_2(\text{B})$, (c) hydrated $\text{VO}_2(\text{B})$, and (d) single layers $\text{VO}_2(\text{B})$. From Liu, *et al.*¹¹⁶

1.6 Motivations of incorporating structural defects into the transition metal oxides as a promising way to improve their charge storage properties

The performance of electrochemical charge storage devices is largely determined by the physicochemical properties of the active electrode materials, such as morphologies, porosity, crystal structures, electrical conductivity, etc. While most works in the past decades have been focused on developing nanomaterials with large surface areas, or mixing the metal oxides with conductive materials to improve the electrical conductivity, a new strategy, which is mainly depends on the intentional introduction of atomic scale structural defects into the host lattice, has emerged in recent years and attracted more and more attention as an effective and alternative way to further improve the charge storage properties.

1.6.1 Commonly used approaches to improve the electrode properties of transition metal oxides

The most commonly used way to improve the electrode properties is by microstructure/morphology control, in order to create large surface area for alkali cation

adsorption. Since the pseudocapacitance mainly depends on the surface adsorption and redox reactions, increasing the surface area will definitely leads to enhanced charge storage properties. For example, Huang *et al*¹¹⁷ have prepared mesoporous nanotubes assembled from interwoven ultrathin birnessite MnO₂ nanosheets, which delivered a specific capacitance of 365 F/g with capacitance retention of 90.4 % after 3000 cycles. Zhang *et al*¹¹⁵ synthesized flower-like VO₂(B) nanostructures assembled from single nanosheets via hydrothermal reactions. The as-prepared samples exhibit improved electrochemical properties with the first discharge capacity reaching 74.9 mAh/g. They also reported that the morphologies had a critical influence on the electrochemical intercalation properties with lithium ions.

Another effective way to improve the electrode performance is by loading the oxides on conducting materials, since the low electrical conductivity is always a major limitation for their application. For example, Peng *et al*¹¹⁸ have synthesized planer supercapacitors based on hybrid nanostructures of ultrathin 2-D MnO₂/graphene nanosheets, which exhibit high specific capacitance of 208 F/g at 10 A/g current density and excellent rate capability. Nethravathi *et al*¹⁰¹ have prepared N-doped graphene/VO₂(B) nanosheets. When used in lithium ion batteries, the as-prepared samples exhibit large capacity, high rate capability, and excellent cycling stability, which can be attributed to the excellent electronic conductivity associated with the N-doped graphene, short diffusion length for lithium ions related to ultrathin nanosheets, and improved charge transfer due to the anchoring of the VO₂(B) flowers to graphene.

1.6.2 A novel strategy to improve the charge storage properties of transition metal oxides by intentionally introducing structural defects

Other than the above mentioned methods, another strategy to improve the charge storage properties is to deliberately incorporate atomic scale defects into the lattice structure of transition metal oxides. The structural defects usually include cation vacancies, anion vacancies, doping defects, local structure distortion, etc. The defects can either serve as extra host sites for proton or alkali cations, or facilitate the proton/alkali cation diffusion during charge/discharge process, which provide a facile and new way for the design of next generation energy storage devices.¹¹⁹ The first comprehensive studies

to correlate structural defects with charge storage properties were published by Ruetschi in the mid-1980s for intergrowth MnO₂ phases.¹²⁰⁻¹²² All MnO₂ materials were produced from an aqueous phase either by electrolysis or by chemical oxidation-precipitation, which contain cation vacancies intrinsically. The cation vacancy concentration depends on several parameters, including deposition/precipitation rate, pH, Mn²⁺ in aqueous solution, partial water vapor pressure, and temperature. They found that the cation vacancies can lowering the activation energy for proton transport through the lattice, thus enhance the thermodynamic reactivity of the materials. It is also more favorable for the electrochemical intercalation of electrolyte cations near the vacancies, which leads to enhanced rate capability in defective MnO₂ phases for electrochemical intercalation/deintercalation.

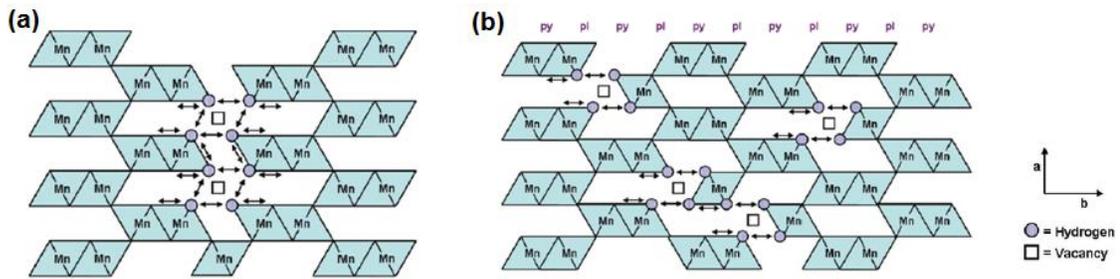


Figure 26. Schematic diagrams of cation-deficient MnO₂ phases viewed along the [001] direction illustrating two different defect configurations: (a) γ -MnO₂ intergrowth structure with chain-like vacancy clustering and (b) ϵ -MnO₂ with point defects. Arrows depict some possible proton-transport pathways associated with cation-vacant sites.

From Ruetschi, *et al.*¹²²

Following this pioneering study, more works have been conducted to intentionally introduce structural defects into different transition metal oxides, in order to investigate the relation between structural defects and charge storage properties. Pernet *et al.*¹²³ have done some related work in the early 1990s for maghemite, a cation deficient form of Fe₃O₄. They found that the cation vacancies can accommodate up to ~0.25 mol Li ions per formula unit. Thus, the cation deficient γ -Fe₂O₃ can serve as a platform for making electrodes that possess enhanced charge storage properties. Bonil *et al.*¹²⁴ have prepared hollow iron oxide nanoparticles with very high cation vacancy content (up to 44 %) recently. *In situ* studies show that a large amount of lithium ions can intercalate into

hollow iron oxide NPs without structural charge, due to the extra Fe vacancies surrounded by protonated oxygen groups. The vacancies can provide an additional 221 mAh/g capacity, meaning that cation vacancies are responsible for the enhanced capacity in the conversion reactions. They have further demonstrated that the hollow γ -Fe₂O₃ nanoparticles with large amounts of cation vacancies can also serve as host sites for the fast Na⁺ ion intercalation.¹²⁵ Thus, the cation vacancies are efficient for both lithium and sodium charge storage during the intercalation /deintercalation process. Li *et al*¹²⁶ prepared defective TiO₂ anatase nanoparticles by mild solvothermal process, which contain large amounts of cation vacancies (up to 22 %). When used for lithium ion batteries, the defective TiO₂ exhibits higher capacity and better rate capability, especially at high current densities. Kim *et al*¹²⁷ have prepared reduced α -MoO_{3-x} and compared it with fully oxidized α -MoO₃. The introduction of oxygen vacancies leads to a larger interlayer spacing, which promotes faster charge storage kinetics and enables the α -MoO₃ structure to be retained during lithium ion insertion and removal. This research highlights the importance of incorporating oxygen vacancies into transition metal oxides as a strategy for increasing the charge storage kinetics of redox-active materials. Yu *et al*¹²⁸ have synthesized Mn-doped V₂O₅ by sol-gel process with Mn²⁺ directly added during sol preparation. The XPS results show co-existence of V⁴⁺ and V⁵⁺ in Mn-doped sample, and the formation of oxygen vacancies due to Mn²⁺ substitution. Both the lower valence vanadium ions and oxygen vacancies can help increase the film's conductivity. The electrochemical results also indicate enhanced discharge capacities with much improved cyclic stability for the Mn-doped samples. Coustier *et al*⁷⁶ have prepared Cu and Ag doped V₂O₅. They found that the electrical conductivity of V₂O₅ increases by two to three orders of magnitude with increasing doping contents. The doped sample exhibits high intercalation rate and almost no capacity fading after more than 450 cycles.

In general, it can be summarized that the presence of structural defects may provide the following advantages:

(1) Lowering the activation energy and thus promotes the proton or alkali cation intercalation/deintercalation process.

(2) Serve as extra host sites for alkali cation intercalation, thus provides much higher capacitance.

(3) Increase the electrical conductivity and promote the charge transfer process, which improve the electrode kinetics.

(4) Alleviating the electrochemical strain during electrochemical cycling, thus enabling excellent rate capability.

1.7 Methods to intentionally incorporate structural defects into transition metal oxides

There are several ways for tailoring the defect structure in transition metal oxides including replace the constituent cations or anions with aliovalent substitutes, treating the oxides at temperatures in defect inducing atmosphere, equilibrating the oxides in different transition metal ion solutions or in acid environment with different pH values, as well as preparing the metal oxides with porous structures and high surface-to-volume ratio to amplify the effects of surface defects.

Doping is the most commonly used way to tune the defect structure and enhances the properties of the oxides. The replacement of constituent cations/anions with aliovalent dopants not only increases the cation/anion vacancy content, but may also increase the cell volume of the host lattice, thus provides new intercalation sites, facilitates the diffusion of alkali cations, and also improves the electronic conductivity. Benjamin *et al*¹²⁹ have prepared defective γ -Fe₂O₃ by replacing a fraction of Fe³⁺ with highly oxidized Mo⁶⁺ to generate cation vacancies. The Mo-substituted γ -Fe₂O₃ exhibits about three times higher cation vacancy content compared with the original γ -Fe₂O₃. Li *et al*¹²⁶ have synthesized defective anatase TiO₂ by substituting the divalent O²⁻ anions with monovalent F⁻ and OH⁻ anions, as shown in Figure 27(a). For every four substitutions of oxygen ions by monovalent anions, one cationic vacancy is created. The cation vacancy content can be controlled by reaction temperature. Zeng *et al*¹³⁰ prepared Mn-doped V₂O₅ lithium-ion battery cathode material by using a layered compound, vanadium (III) jarosite, as the precursor, and Mn²⁺ as the dopant, which is shown in Figure 27(b). The uniform aliovalent doping of the larger Mn²⁺ cations into the V₂O₅ structure increases the cell volume, which facilitates the Li⁺ ion diffusion, and introduces oxygen vacancies that improve the electronic conductivity.

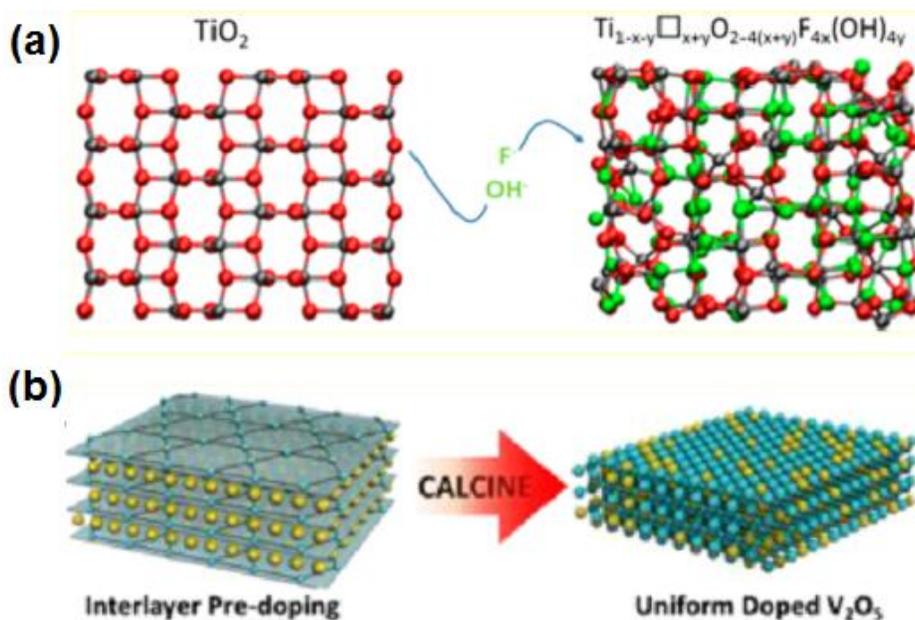


Figure 27. Schematic diagrams showing (a) substitution of divalent O^{2-} anions with monovalent F^- and OH^- anions resulting the formation of cationic Ti^{4+} vacancies, from Li, *et al.*,¹²⁶ and (b) the aliovalent doping of Mn cations in V_2O_5 structure through a two-step transformation process. From Zeng, *et al.*¹³⁰

Another useful way to create structural defects is by treating the oxides at temperatures in defect inducing atmospheres. As reported by Swider-Lyons *et al.*¹³¹, proton-compensated cation vacancies can be created in V_2O_5 powders under controlled temperature and atmosphere. The effects can be further enhanced by making samples with large surface area, thus more cation vacancies will be exposed to the electrolyte during the charge storage process. Shin *et al.*¹³² have reported oxygen-deficient $TiO_{2-\delta}$ nanoparticles prepared by hydrogen reduction. The H_2 thermally treated $TiO_{2-\delta}$ nanoparticles showed greatly improved lithium storage properties because of the increase of the electronic conductivity. They also systematically investigated the effects of oxygen vacancies and electronic charge carrier concentration on the overall lithium storage performance, which revealed that the well-balanced Li^+/e^- transport is the key factor for high-performance TiO_2 anodes.

Equilibrating the oxides in different transition metal ion solutions can also help generate structural defects (such as cation vacancies), especially for δ - MnO_2 . For example, Grangeon *et al.*¹³³ have equilibrated the synthetic δ - MnO_2 at pH = 5 or 7, and

then reacted with Zn to produce Zn-sorbed δ -MnO₂. The sorption of Zn into the interlayer causes the departure of layer Mn³⁺, leading to the formation of new reactive layer vacancies. Another similar and facile way for creating cation vacancies that emerged in recent years is by equilibrating the oxides in acid environment with low pH values. This has been confirmed to be very effective for generating cation vacancies in birnessite δ -MnO₂ by Manceau *et al.*¹³⁴ They have prepared a suspension of Na-saturated δ -MnO₂, and then equilibrated at pH = 10, 6 and 3 for different times. Figure 28 shows the typical short-range and long-range ordered structure of a δ -MnO₂ monolayer, which contains Mn vacancies and surface coordinated Mn³⁺. Their results indicate that lowering the pH from 10 to 6 and then to 3 increase the vacancies from 0.08 to 0.15 and to 0.21 per layer octahedron. Therefore, lower pH treatment can lead to the formation of more Mn vacancies. Similar results have also been observed by Abdulaeva *et al.*¹³⁵ They found that the cation-deficient perovskites Ln_{2/3}TiO₃ (Ln = La, Nd) can be obtained by leaching of Ln³⁺ ions from HLnTiO₄ in acid solution. The right product can only be obtained under appropriate conditions. Ln_{2/3}TiO₃ will dissolve at higher HCl concentration and the reaction will not occur at lower HCl concentration.

In a scaling approach, preparing materials with high surface area will also leads to the formation of more defects because the increased fraction of surface sites favors the formation of structural defects. For example, Li *et al.*¹³⁶ have prepared vanadium pentoxide aerogels with high surface area (196 m²/g) and ultrathin nanofiber (~10 nm) morphology through a sol-gel method followed by a freeze-drying process. The enhanced performance of this cation-deficient V₂O₅ can be related to the aerogel-like nanoarchitectures, since the aerogels are considered as “all-surface” materials and contain a high concentration of structural defects. Gao *et al.*²⁵ have compared the effects of surface morphologies on the formation of cation vacancies in δ -MnO₂ nanosheets. The results show that the formation of Mn vacancies is more favorable in high-surface area nanosheet assemblies, with steric limitations reducing the extent of the reactions in well-crystalline birnessites.

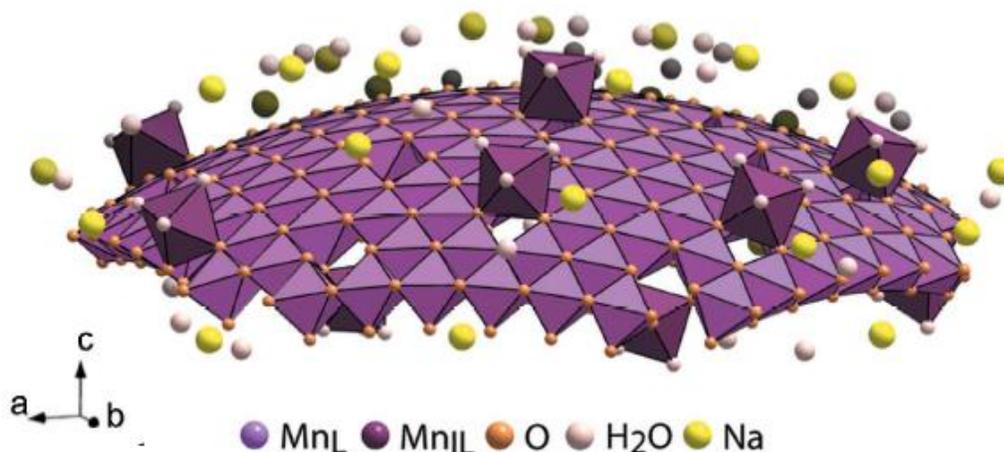


Figure 28. Short-range and long-range order structure of a δ - MnO_2 monolayer. The octahedral layer contains 79 at.% Mn^{4+} and 11 at.% Mn^{3+} (Mn_L), and 10 % vacancies which for the most part (8 %) are capped by an interlayer Mn^{3+} octahedron (Mn_{IL}). The Mn_{IL} octahedra share three corners with the three surface O atoms surrounding a vacancy, and complete their coordination with three interlayer water molecules. The layer charge deficit created by Mn^{4+} vacancies and Mn_L^{3+} for Mn_L^{4+} substitutions is compensated by 8 at.% Mn_{IL}^{3+} , 27 at.% Na^+ and H^+ (not represented). The interlayer also contains water molecules weakly bonded to Na. From Manceau, *et al.*¹³⁴

1.8 Commonly used techniques for detecting the structural defects and alkali cation intercalation mechanism during charge/discharge process

As discussed in section 1.6.2, the first studies correlate the cation vacancies with charge storage properties were published by Ruetschi for γ - MnO_2 . The Ruetschi cation vacancy fraction can be calculated by using a series of equations based on the structural water and total manganese content as described in many published papers.^{137,138} Although this traditional method based on the potentiometric titration is simple and easily realized in the laboratory, it can only provide a rough estimate of the cation vacancy content with low accuracy. Also, the defects are typically considered as local structures and cannot be simply characterized by traditional tools such as XRD and SEM, etc. Therefore, more advanced and sophisticated techniques are needed to investigate the defect structures, as well as for elucidating the charge storage mechanisms.

1.8.1 X-ray Absorption Spectroscopy (XAS)

In recent years, X-ray Absorption Spectroscopy, including X-ray Absorption Near Edge Structure (XANES) and Extended X-ray Absorption Fine Structure (EXAFS), have been widely used to understand the structural and electronic changes of many transition metal oxides. By using XANES, we are able to investigate the oxidation state change accurately. In EXAFS, we can determine the number and species of the near neighbor atoms, and their distance from the designated atom, from the oscillatory part of the absorption coefficient above the absorption edge. Thus, this technique is very sensitive, powerful and effective in detecting the local defect structures, oxidation state change, as well as surface coordination variations.

Bonil *et al*¹²⁴ have prepared hollow γ -Fe₂O₃ nanoparticles, and investigated the Li⁺ intercalation process during electrochemical cycling by synchrotron X-ray absorption techniques. The EXAFS data (Figure 29(a)) shows that the hollow γ -Fe₂O₃ has significantly lower signals at the Fe-Fe distance (2-3.5 Å) compared to gamma Fe₂O₃, and that the solid γ -Fe₂O₃ has similar intensity comparing to the bulk γ -Fe₂O₃, indicating the presence of a large amount of Fe vacancies in the hollow γ -Fe₂O₃. The XANES data (Figure 29(c-d)) shows no oxidation state change of Fe during the initial stage of Li⁺ intercalation, indicating that the protonated oxygen sites around cation vacancies can accumulate the charges upon Li⁺ intercalation without affecting the oxidation state of Fe until the filling of the vacancies is complete. They further studied the intercalation of Na⁺ ions into structural defects in hollow γ -Fe₂O₃.¹²⁵ Both the XANES and EXAFS data confirm the intercalation of ~1.4 Na⁺ ions into structural defects. Slower reduction of the Fe ions during Na⁺ intercalation was also found by using XANES, indicating that the protonated oxygen sites around cation vacancies may serve as the charge storage sites during Na⁺ intercalation.

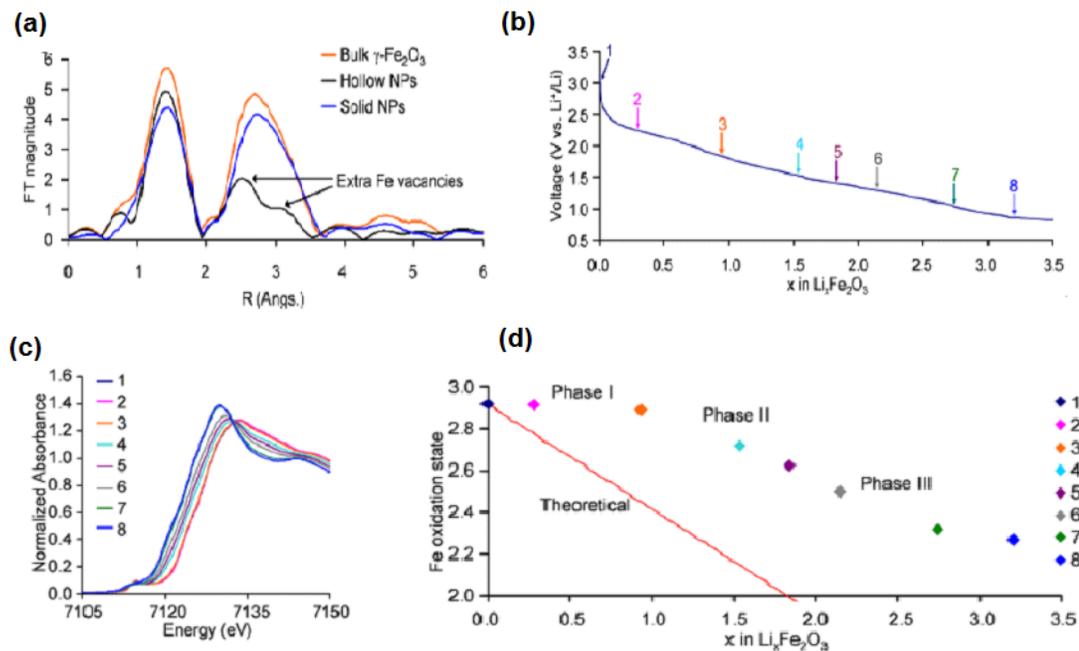


Figure 29. (a) EXAFS data on the hollow and solid $\gamma\text{-Fe}_2\text{O}_3$ NPs (bulk $\gamma\text{-Fe}_2\text{O}_3$ was used as a reference), (b) Voltage curve at the first discharge state (up to $\sim 3.5 \text{ Li}^+$ insertion) versus metallic Li counter electrode, (c) XANES spectra measured at eight points depicted in the voltage profile shown in (b), and (d) The Fe oxidation state obtained from XANES plots shown in (c). From Bonil, *et al.*¹²⁴

1.8.2 X-ray Scattering and Pair Distribution Function (PDF) analysis

Another powerful technique for detecting the local defect structure in nanomaterials, especially the materials without long-range order, is X-ray scattering and pair distribution function analysis. While diffraction techniques only consider the Bragg peaks, the PDF method utilizes information of both the Bragg peaks and the diffuse scattering buried in-between the Bragg peaks. So it requires accurate determination of the diffuse and background intensities.¹³⁹ Compared with EXAFS, the X-ray PDF analysis can provide not only the local structure variation but also covers the full range of atom-atom distances, and is free of Debye-Waller effects. Therefore, it can provide more reliable distances beyond the first coordination shell and with higher resolution. The r value of each peak in PDF function corresponds to different interatomic distances, and the peak area is related to the relative number of those distances. Therefore, the local structure variation accompanied with defect formation can be accurately determined by direct observation of the presence of new peaks, shifts of the peak positions, and changes

of the peak intensities. Through fitting the experimental data with a model, more detailed information about the defect structure can be obtained.

Manceau's group¹³⁴ has done pioneering work on the pH-dependent structure of δ - MnO_2 by using high energy X-ray scattering and PDF analysis, and their results are shown in Figure 30. The Mn ions migrate from layer to interlayer sites at acidic pH, leading to the formation of Mn vacancy with higher content, as reflected from the decreased Mn_L - Mn_L correlation with decreasing pH. Besides, the Mn_L - Mn_{IL} correlation increases when the pH decreases, indicating the coordination of MnO_6 octahedra above or below cation vacancies. Our group²⁵ has done some similar experiments, and our results are consistent with the model of Manceau *et al.*¹³⁴ We have also observed an increase in Mn vacancy content with decreasing pH, as well as the appearance of a PDF peak at a distance not found in the δ - MnO_2 structure, which corresponds to Mn_L - Mn_{IL} . The increase in concentration of Mn vacancies by 30 % between different pH equilibrated samples supports the hypothesis that increased proton sorption at the MnO_2 surface in more acidic electrolytes expels more in-plane Mn, and therefore leads to the formation of more Mn vacancies. Li *et al.*¹²⁶ investigated F^- and OH^- substituted TiO_2 by PDF analysis. The refinement of Ti site occupancy yields ca. 74 %, which implies the presence of large amounts of cation vacancies. The electrochemical measurements revealed improved charge storage capacity, indicating that the cation vacancies act as additional lithium hosting sites within the anatase framework. Jiang *et al.*¹⁴⁰ has investigated the local structures of Mn- and La-substituted BiFeO_3 by synchrotron X-ray scattering and PDF analysis. They found that both La and Mn doping induce strong local structural disorder, which can be observed by the decreased peak intensity and smearing of several peaks from the extracted PDF data.

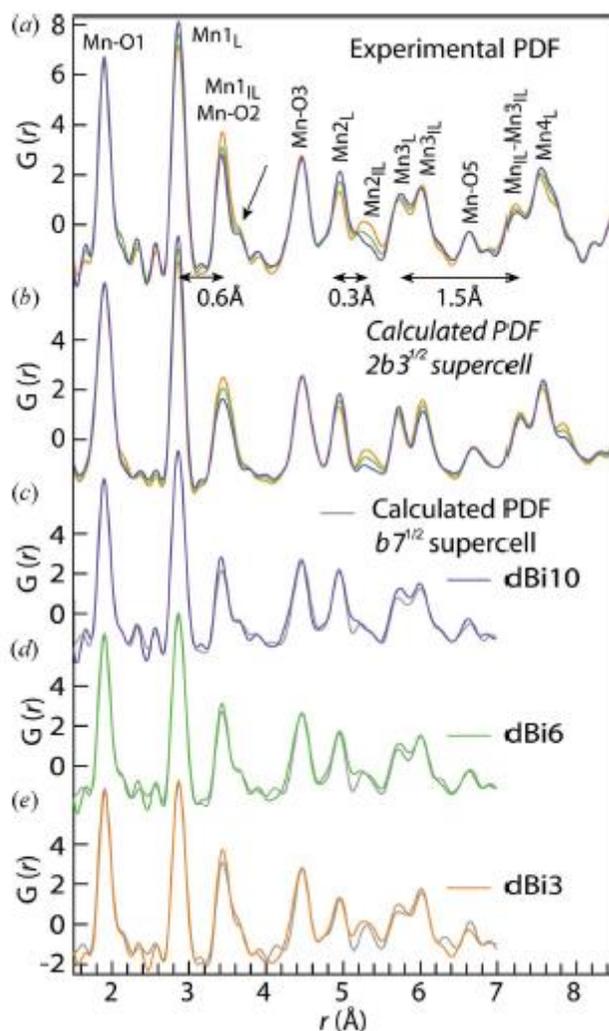


Figure 30. (a) Experimental PDFs for δ -MnO₂ synthesized as a function of pH, showing the reverse variation of the Mn-Mn_L and Mn-Mn_{IL} pairs as a result of the layer-to-interlayer migration of Mn_L at acidic pH. (b) Best-fit PDF profiles up to 8.5 Å calculated for a model containing 17% vacancies. (c)-(e) Best-fit PDF profiles up to 7 Å calculated for a chalcophanite model. This model reproduces the short-range relaxation of the Mn-Mn and Mn-O distances around vacancies. From Manceau, *et al.*¹³⁴

1.8.3 Raman Spectroscopy

Raman spectroscopy can also provide valuable information for detecting the crystal structure change. Based on the inelastic scattering between photon and phonons, it is an excellent technique for studying the structure of amorphous and nanomaterials due to its high sensitivity to the lattice vibration and short range order. Typically when used for probing the charge storage process in batteries/supercapacitors, the lattice changes induced by ion intercalation/deintercalation or redox reactions during charge/discharge

process can be monitored, especially by *in-situ*/operando Raman measurements, thereby offering direct correlations between the state of charge/discharge and the crystal phases of the electrode materials.

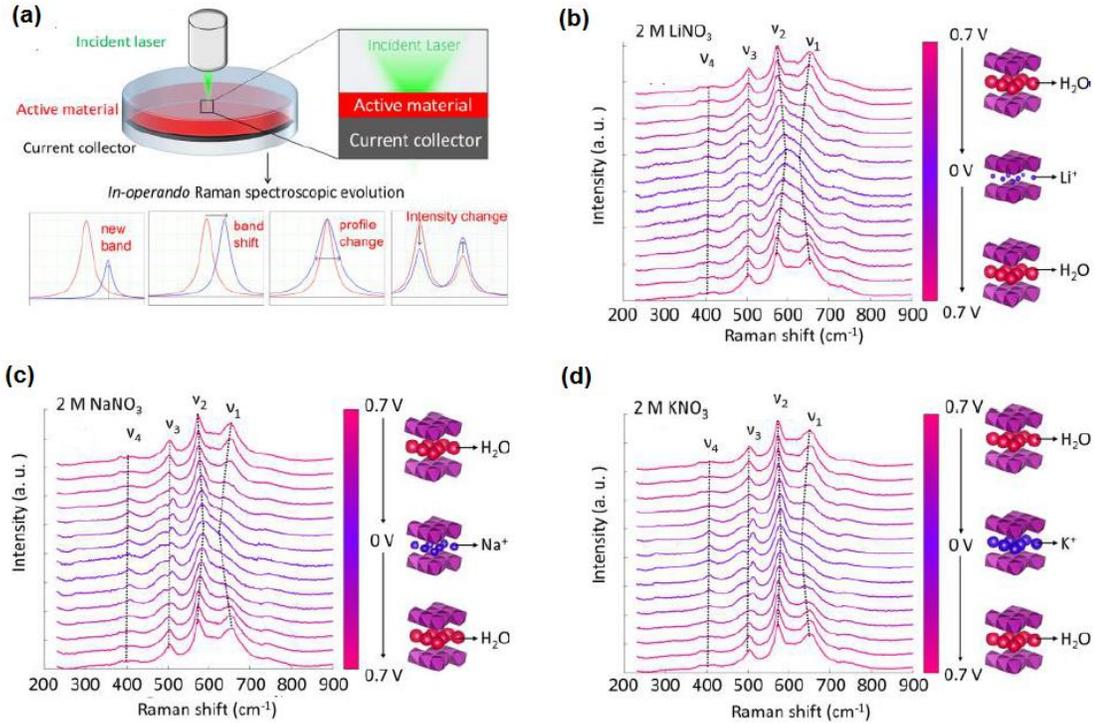


Figure 31. (a) The schematic diagram of the operando Raman spectroscopic test for pseudocapacitive δ -MnO₂ thin-film electrode. (b-d) Raman spectroscopic evolution of pseudocapacitive MnO₂ thin film cycled between 0 and 0.7 V in (a) 2 M LiNO₃, (b) 2 M NaNO₃, and (c) 2 M KNO₃ aqueous electrolyte. From Chen, *et al.*¹⁴¹

Cheng *et al.*¹⁴² used operando Raman spectroscopy to monitor the phase changes of α -Mn_{0.98}O₂ during the charge/discharge process. They found that α -Mn_{0.98}O₂ changes to the mixed phase of Na-MnO₂ and Mn₃O₄ immediately when immersed in Na₂SO₄ solution. Besides, the charge storage mechanism is more complex than previously considered. H⁺, Na⁺, and even Mn²⁺ ions may be involved in the energy storage process. Chen *et al.*¹⁴¹ probed the structural changes of a thin-film MnO₂ electrode during cycling using operando Raman spectroscopy. Their primary results are shown in Figure 31. Through studying the changes of spectral features (e.g., band, position, width, and intensity) under different conditions (charge and discharge) in different electrolytes, they got a better insight into the cation incorporation and charge storage mechanism. This can

further help relates the cation-size effects to their electrochemical charge storage properties.

1.8.4 Other detection techniques

Other than above mentioned approaches, several different techniques are also used to detect local structural defects. Koketsu *et al.*¹⁴³ have prepared anatase TiO₂ with high concentrations of titanium vacancies, which is achieved through the partial substitution of oxide ions by monovalent anions, such as fluoride and hydroxide groups. The atomic-resolution TEM images, shown in Figure 32, allow direct visualization of the titanium vacancies. The variation in atomic column intensity observed on the high-resolution image (Figure 32(b)) corresponds to a variation in the Ti atomic occupations, and thereby directly indicates the presence of vacancies. The intensity variation and dark contrast between atomic columns are further emphasized in the colored image and in the line profile in Figure 32(c).

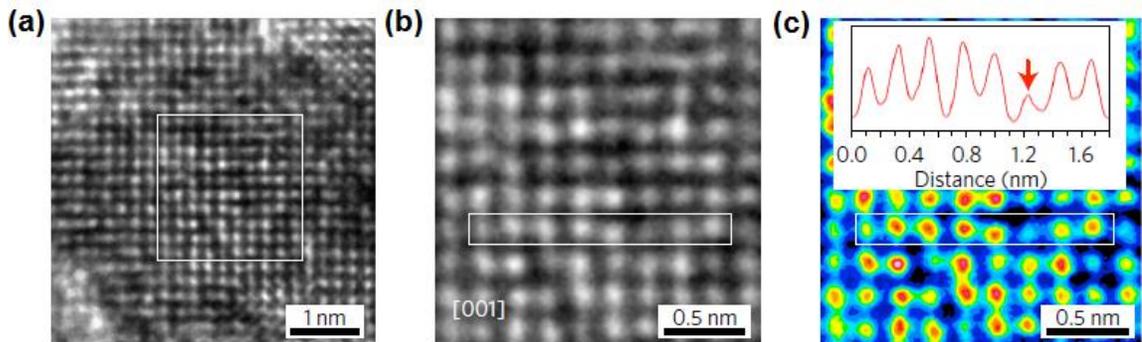


Figure 32. (a) High-resolution TEM image of a Ti_{0.78}□_{0.22}O_{1.12}F_{0.40}(OH)_{0.48} nanoparticle. (b) atomic-resolution image of anatase crystal oriented along the [001] axis. (c) colored high-resolution TEM image with a profile plot of a line of atoms (white rectangle), which exhibit a clear intensity variation both of atomic columns and dark patches in between.

From Koketsu, *et al.*¹⁴³

Li *et al.*¹²⁶ have also prepared anatase TiO₂ with high concentrations of titanium vacancies obtained through substitution of divalent O²⁻ with monovalent F⁻ and OH⁻. They have detected the local structural defects by using solid-state ¹⁹F NMR spectroscopy, which reveals that the fluoride ions can accommodate up to three different

environments, depending on Ti and vacancies, with a preferential location close to vacancies.

Ariza *et al*¹⁴⁴ have investigated the lithium extraction/reinsertion mechanism and the role of protons in a lithium-rich manganese oxide ($\text{Li}_{1.6}\text{Mn}_{1.6}\text{O}_4$) by using inelastic neutron scattering (INS) spectroscopy, a technique that is very sensitive to protons. Their results show the presence of hydroxyls and structural water in the delithiated sample, and the water may be located in the lamellar-like regions of the defect structure. When the lithium is reinserted, most of the hydroxyls are removed, but some protons still remain in the structure mainly as structural water. The INS results confirmed that the extraction of protons and reinsertion of Li^+ is more effective in $\text{Li}_{1.6}\text{Mn}_{1.6}\text{O}_4$, which is in agreement with its improved lithium uptake properties.

CHAPTER II. THE CRITICAL ROLE OF ACID TREATMENT INDUCED POINT DEFECTS IN IMPROVING THE SPECIFIC CAPACITANCE OF 2-D BIRNESSITE δ -MNO₂ NANOSHEETS

Disclaimer: This chapter was published in the journal “Nature Communications” titled “The critical role of point defects in improving the specific capacitance of δ -MnO₂ nanosheets” with many co-authors. Peng Gao, Peter Metz, Trevyn Hey, Yuxuan Gong, Dawei Liu, Doreen D. Edwards, and Scott T. Misture work in Alfred University, Jane Y. Howe works at Hitachi High-technologies Inc., and Rong Huang works at the Cornell High Energy Synchrotron Source at Cornell University. Scott T. Misture, Dawei Liu and Doreen D. Edwards conceived the research. Peng Gao and Trevyn Hey synthesized the materials. Peng Gao performed the electrochemical measurements. Peter Metz and Scott T. Misture performed the X-ray scattering measurements. Peng Gao and Rong Huang performed the XANES measurements. Yuxuan Gong performed the XPS measurements. Trevyn Hey performed the AFM measurements. Jane Y. Howe performed the TEM measurements. Peng Gao, Peter Metz and Trevyn Hey performed the material characterization. All authors discussed and analyzed the data. Peng Gao, Peter Metz and Scott T. Misture wrote the paper. Most of the text in this chapter is taken verbatim from this paper.

2.1 Introduction

Manganese dioxide (MnO_2) in its many forms has been the subject of much study for electrochemical supercapacitor applications. The birnessite form of MnO_2 ($\delta\text{-MnO}_2$), comprising stacked sheets of edge-shared MnO_6 octahedra with interlayer alkali ions,^{96,97} has been studied for some time and shows both double-layer and Faradaic charge storage.^{145,146} The two-dimensional $\delta\text{-MnO}_2$ generally exhibits improved capacitance and rate behavior compared to other polymorphs because the interlayer galleries provide high-speed pathways for diffusion of protons or alkali cations during the charge and discharge processes.^{147,148} However, the low electrical conductivity of $\delta\text{-MnO}_2$ (10^{-5} to 10^{-6} S/cm) has greatly limited its application, prompting study of composite electrodes containing graphene,^{118,149} carbon nanotubes,^{150,151} carbon fibers,^{152,153} and so on. In addition, nanostructuring has been employed to improve the surface area and capacitance, for example by growing nanoneedles,¹⁵⁴ nanoflowers,¹⁵⁵ nanoparticles¹⁵⁶ and so on.

In recent years, intentional creation of cation vacancies has been explored to increase the charge storage capacitance of transition metal oxides, where cation vacancies provide additional cation intercalation sites.¹¹⁹ The first studies correlating cation vacancies and charge storage properties were published in the mid-1980s for intergrowth $\gamma\text{-MnO}_2$ phases.¹²⁰⁻¹²² As discussed in Chapter I, cation vacancy content may be controlled via several approaches, and can be quite large in some cases. For example, Li *et al*¹²⁶ modified anatase TiO_2 with monovalent F^- and OH^- anions to form up to 22 at % Ti vacancies for additional Li storage. Similarly, Koo *et al*^{124,125} transformed Fe_3O_4 (spinel) into hollow $\gamma\text{-Fe}_2\text{O}_3$ rods containing up to 44 % vacant iron sites, and show that Li and Na ion intercalation is possible without structural phase transformation.

Little work on the formation of cation vacancies in $\delta\text{-MnO}_2$ nanosheets has been reported to date, but extensive study of the important role of birnessite-like MnO_2 in photosynthesis, ion sorption and other bio- and geochemical processes provides rich literature on its behavior in aqueous environments.¹⁵⁷ Recently, Manceau *et al*,¹³⁴ building from many earlier works on Mn oxidation state in K-birnessites,^{158,159} systematically investigated the effects of pH on cation vacancy content in phyllosulfate nanoparticles. Their approach exploited high-energy X-ray scattering (HEXS) to perform pair distribution function (PDF) analysis, truncation rod analysis, and

simulations using the Debye equation to show that lower pH causes migration of Mn from the MnO₂ nanosheet to the sheet surface. Thus, the authors were able to quantify Mn vacancies in the nanosheets and Mn³⁺ cations displaced to the interlayers. Later work by Marafatto and coworkers¹⁵⁷ employed sub-picosecond optical and X-ray absorption spectroscopy to track the mechanisms of Mn reduction under illumination to quantify the effects of different interlayer cations on MnO₂ photo-reduction rates. Their results support the Mn redox reaction mechanism proposed by Manceau *et al.*,¹³⁴ including displacement of the Mn³⁺ cation to the interlayer gallery.

In this chapter, we exfoliate and reassemble δ -MnO₂ nanosheets to form 3-D mesoporous pseudocapacitive electrodes with controlled concentration of Mn point defects and Mn^{3+/4+} ratios. The nanosheet reassembly and electrode fabrication processes have been investigated. The as-prepared samples have been characterized systematically using various techniques, including SEM, TEM, AFM, XRD, TGA, FT-IR, BET, XPS, XANES, X-ray scattering and PDF analysis. Electrochemical and high energy X-ray scattering measurements provide direct evidence that intentional Mn ion defects and Mn reduction synergistically improve supercapacitor performance. The 3-D assembly and defect control represent straightforward and industrially-scalable approaches to improving specific capacitance.

2.2 Materials and Methods

2.2.1 Chemicals and reagents

Manganese carbonate (MnCO_3), potassium carbonate (K_2CO_3), sodium sulfate (Na_2SO_4), lithium sulfate (Li_2SO_4), sulfuric acid (H_2SO_4), acetylene black, poly(vinylidene fluoride) (PVDF) and nickel foil (Ni foil) were purchased from Alfa Aesar. 6N hydrochloric acid (HCl) solution and sodium hydroxide (NaOH) were obtained from Fisher Scientific. The tetrabutylammonium hydroxide solution (TBAOH, 40 wt. % in H_2O) and N-methyl-2-pyrrolidone (NMP) were purchased from Sigma-Aldrich. All reagents were used as received without further purification.

2.2.2 Fabrication of $\delta\text{-MnO}_2$ nanostructures

Powder synthesis included mixing MnCO_3 and K_2CO_3 powders in a molar ratio of 40 : 9, by milling in isopropyl alcohol for 10 minutes using a McCrone Micronizing Mill (McCrone Group, USA) with alumina media. The resulting suspension was dried on a hot plate for 30 min at 60 °C and then calcined in alumina crucible at 800 °C for 24 h in air. 0.5 g of the resulting layered K_xMnO_2 was then proton ion-exchanged in HCl solution (1 mol/L, 45 mL) in an ultrasonic bath at room temperature for 4 h. The ion exchange process was repeated two additional times, followed by washing with DI water and air drying.

In order to obtain the exfoliated MnO_2 nanosheets, 0.35 g protonated H_xMnO_2 was equilibrated with 32.5 mL aqueous TBAOH solution (30 mL H_2O + 2.5 mL 40 wt. % TBAOH) for 4 h in an ultrasonic bath at room temperature. The resulting suspension was centrifuged at 10,000 rpm for 10 min. to separate the remaining bulk H_xMnO_2 from the nanosheet suspension. Self-assembly of the nanosheets in the colloidal suspension was typically achieved by adding 6N HCl solution to the suspension at a constant rate of 1 mL/min while stirring to reach pH = 2, resulting in flocculation to form high surface area 3-D porous structures. The flocculation (reassembly) process has also been investigated systematically by adding different cations (H^+ , Li^+ , Na^+) and using different methods (immediately adding vs. titration), in order to optimize the flocculation procedures.

Mn defects and redox were controlled by equilibrating the assembled nanosheets at target pH values by increasing the pH from 2 upwards using 1 mol/L NaOH additions and stirring for 24 h. Dry nanosheet assemblies were finally obtained by washing, centrifugation (Sorvall Legend X1 Centrifuge, Thermo Scientific, USA, the powders were centrifuged at 12,000 rpm for 10 min.), rinsing in 2-propanol and drying overnight at room temperature. Typically speaking, 8-10 mg MnO₂ floccs can be obtained from 100 mL nanosheet suspension. Thus, 3-D porous MnO₂ nanostructures assembled from ultrathin 2-D δ-MnO₂ nanosheets with controlled defect content were obtained. The protonated bulk H_xMnO₂ without exfoliation was also electrochemically tested, for the purpose of comparison with the 3-D assembled nanosheets. The overall procedures for making δ-MnO₂ nanosheets and the reassembled 3-D porous nanostructures can be summarized as follows (Figure 33).

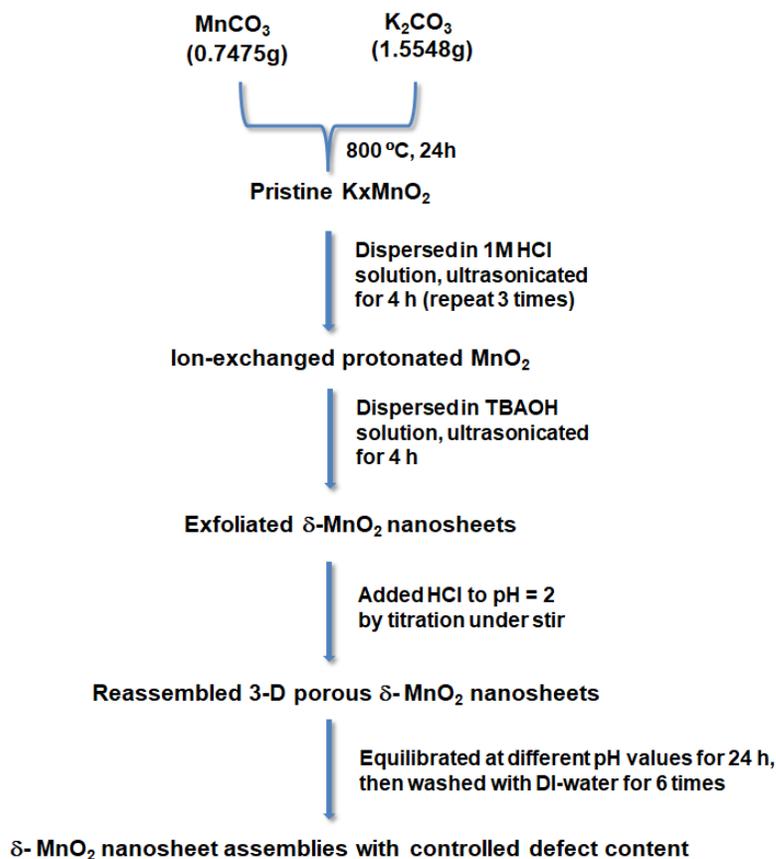


Figure 33. Typical synthesis procedures for making 3-D porous δ-MnO₂ nanosheet assemblies with controlled defect content.

2.2.3 Characterization of the samples

Microstructures were studied using scanning electron microscopy (SEM, FEI Quanta 200) at 20 kV. Energy dispersive spectroscopy (EDS) was carried out using a FEI EDAX system equipped with a silicon-drift detector. Transmission electron microscopy and high-resolution SEM were carried out using a Hitachi HF-3300 TEM/STEM (The images were obtained by Jane Y. Howe at Hitachi High-Technologies Canada, Inc.). The STEM unit has a secondary-electron detector, which allows simultaneous high-resolution SEM and TEM imaging at 300 kV. The thickness and crystallite dimension of the exfoliated MnO₂ nanosheets were probed by multimode atomic force microscope (AFM, Bruker Dimension Icon®) in tapping mode using antimony doped silicon tips (The images were taken by Trevyn Hey at Binghamton University). The exfoliated nanosheets were electrostatically attached to a clean silicon wafer by drying the nanosheet suspension, and imaged in air.

Thermogravimetric analysis (TGA) was performed using a TA Instruments SQT-Q600 DTA/TGA under flowing air with a heating rate of 10 °C/min, in order to investigate the presence of water and organic compounds in the interlayer region of MnO₂ nanosheets. The presence of any functional groups from organic compounds was also probed with IR spectroscopy (Nicolet 6700 FT-IR Spectrometer, USA). The specific surface area and porosity were examined by nitrogen adsorption and desorption isotherms collected at 77 K using a Micromeritics TriStar II 3020 system. The local chemical environment of the samples was characterized using a PHI Quantera X-ray photoelectron spectrometer (XPS) equipped with Al K α radiation.

Mn K-edge X-ray absorption near-edge spectroscopy measurements were carried out at the bending magnet beamline F3 at the Cornell High Energy Synchrotron Source (CHESS). Data were collected at room temperature in fluorescence mode using a Hitachi vortex 4-element silicon drift detector. All spectra were calibrated using the spectrum of Mn metal foil, and the software package ATHENA was used for analysis.¹⁶⁰

The Mn vacancy content in δ -MnO₂ samples was determined using high energy X-ray scattering and PDF analysis, with data collected at the Advanced Photon Source on beamline 11-ID-B using the rapid-acquisition PDF geometry.¹⁶¹ Data sets were collected using standard 1 mm Kapton capillaries in Debye-Scherrer geometry, Si <311>

monochromated primary beam at 58.66 keV, and a silicon flat plate area detector. Scattering data for PDF extraction were collected over a Q-range of 0.4 - 24.5 Å⁻¹, and the powder diffraction data for all samples was collected over a Q-range of 0.2 - 9.0 Å⁻¹. 2-D X-ray diffraction data were integrated to 1-D using FIT2D,¹⁶² after appropriately calibrating detector deviations from orthogonality and masking invalid pixels. CeO₂ was used as the calibration standard for detector geometry. Meanwhile, CeO₂ and Ni were used to evaluate the instrument response function. The PDF data was reduced using PDFgetX2,¹⁶³ which includes the appropriate corrections for inelastic scattering and energy-dependent detector response, in addition to experimental background and absorption corrections, amongst others. Most of the PDF data acquisition and analysis were conducted by Peter Metz.^{164,165}

2.2.4 Electrochemical measurements

Two different ways have been investigated to make the supercapacitor working electrodes. The first attempt is to directly deposit the dispersed δ-MnO₂ nanostructures from suspension onto substrates. The other method, which was mainly used in this work, is by mixing the active material, acetylene black and PVDF in NMP solution. After stirring for 6 h, the homogeneous slurry was spread onto a Ni foil substrate with an area of 1 cm², and then heated at 100 °C for 2 h to evaporate the solvent and obtain the electrode. The effects of different ratio (active material, acetylene black and PVDF) and mass loading of MnO₂ on electrochemical performance have been investigated. The typical loading of the active material on the working electrode was in the range of 0.5-0.6 mg/cm².

The capacitive performance was measured using a CHI 650E electrochemical analyzer (CHI, USA) with a conventional three-electrode cell. Ag/AgCl and platinum wire were used as the reference and auxiliary electrodes, respectively, with 1 M Na₂SO₄ aqueous electrolyte. Cyclic voltammetry scans were carried out from 0 to 1 V at a scan rate of 50 mV/s. Galvanostatic charge-discharge was measured at different constant current densities from 0.2 to 10 A/g. Electrochemical impedance spectroscopy (EIS) was performed in the frequency range of 0.1 Hz - 100 kHz at an open circuit potential of 5

mV. EIS data was fitted to an electrical equivalent circuit model using ZsimpWin (Version 3.21, EChem Software) software.

2.3 Results and Discussion

2.3.1 Phases and microstructures of parent K_xMnO_2 and protonated H_xMnO_2

The morphologies of pristine K_xMnO_2 , and its protonated form, H_xMnO_2 , are shown in Figure 34(a-b). It can be seen that the K_xMnO_2 and H_xMnO_2 particles are platy, with lateral dimensions in the range of one micron, and that proton exchange does not alter the grain morphology. The synchrotron diffraction data for the parent K_xMnO_2 is shown in Figure 34(c). While laboratory diffraction data tends to reveal little besides the $00l$ reflections ($Q < 2 \text{ \AA}^{-1}$), high energy X-rays with high brilliance reveal more of the characteristic features and hkl bands at larger scattering vectors. The Rietveld refinement reveals that the as-synthesized parent material is layered birnessite, primarily exhibiting the monoclinic polytype with less than 10 wt.% of the rhombohedral polytype and no additional crystalline phases. The two birnessite polytypes differ only in regard to intersheet ordering, which is sensitive to the type and quantity of interlayer species present. The resulting protonated phase should therefore be insensitive to the polytypism observed. Figure 34(d) shows the X-ray diffraction pattern for protonated MnO_2 , demonstrating that phase purity was also achieved after the ion-exchange process.

The removal of potassium ions from the interlayer region in parent K_xMnO_2 after proton exchanging three times has been confirmed by energy dispersive spectroscopy and XPS survey scans, which are shown in Figure 35. From Figure 35(a), the spectrum indicates negligible potassium quantities, and the carbon signal is an artifact of the carbon tape used to prepare the powder mount. Quantification of the potassium according to the inset table in Figure 35(a) reveals substantially less than 1 % residual K of the whole sample. This has been further confirmed by the XPS spectra shown in Figure 35(b). The survey scan demonstrates the absence of potassium peak, which would be located at the binding energy of 292 eV. The XPS survey scan also shows a complete absence of any signal from Al ions, thus giving a good confidence that no contamination by the Al_2O_3 milling media was encountered.

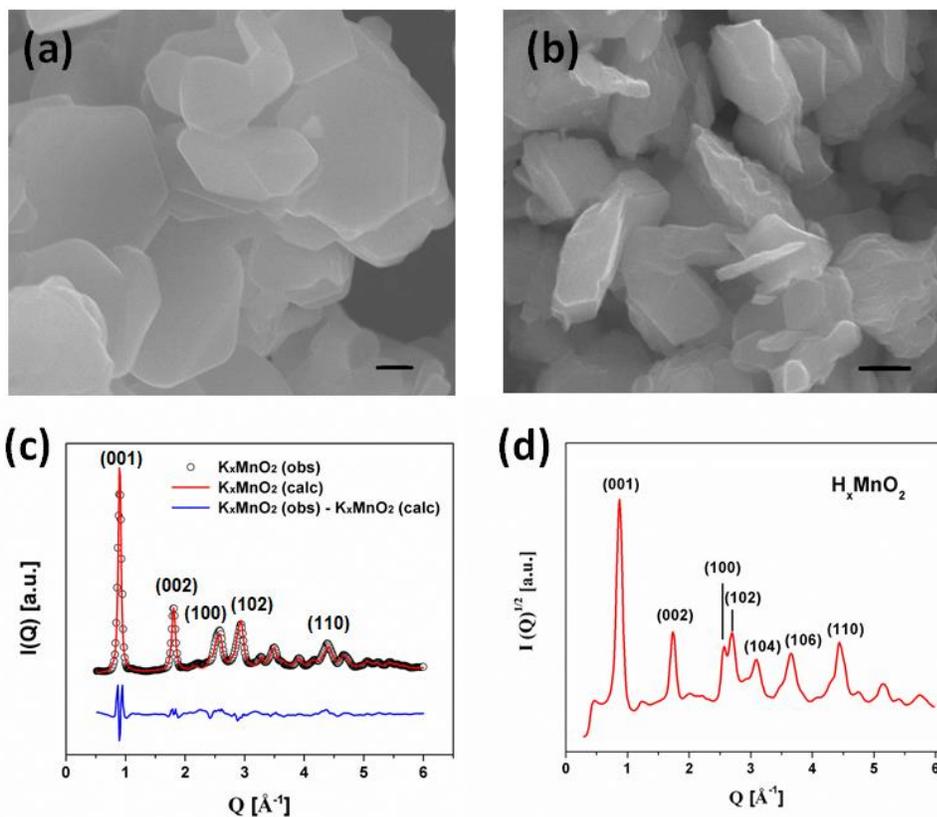


Figure 34. SEM images of (a) pristine K_xMnO_2 , and (b) protonated H_xMnO_2 . Scale bars, 500 nm. XRD patterns¹⁶⁴ of (c) pristine K_xMnO_2 , the Rietveld refinement ($R_{wp} = 13\%$) of the diffraction pattern reveals a mixture of monoclinic (C2/m, 91 %) and rhombohedral (R-3m, 9 %) birnessite polytypes, and (d) protonated H_xMnO_2 . Data collected on APS 11-ID-B.

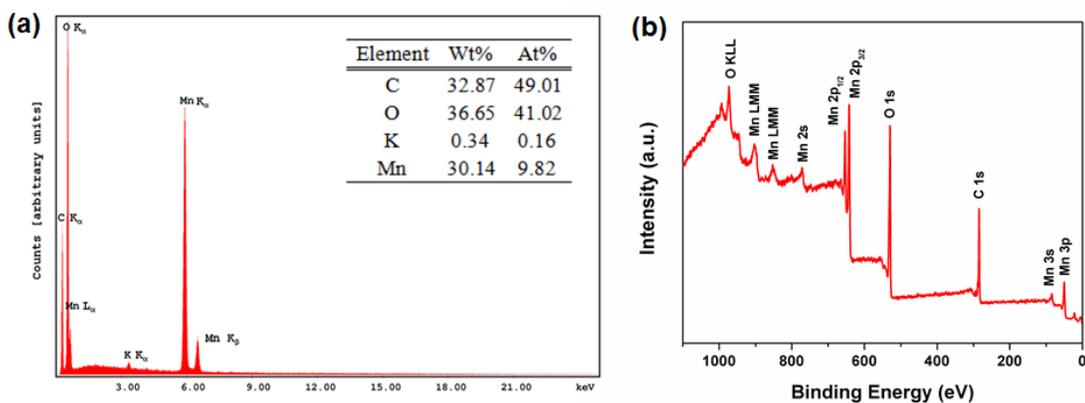


Figure 35. (a) Energy dispersive spectrum of the protonated H_xMnO_2 , and (b) XPS survey scan of the protonated H_xMnO_2 .

2.3.2 Characterization of the exfoliated δ -MnO₂ nanosheets

The final nanosheet in the colloidal suspension is shown in Figure 36(a). The obtained transparent colloidal suspension is stable for several months without apparent observation of deposits, demonstrating the effectiveness of ultrasonic-assisted exfoliation process, where the exfoliation rate is greatly enhanced compared with other reported procedures.^{106,107} High-magnification SEM and TEM images shown in Figure 36(b-c) demonstrate that the sheets are generally flat, with some scrolling at the edges. The AFM image (Figure 36(d)) also displays nanosheet fragments with flat surfaces and thickness of 3-4 nanosheets, suggesting that some of the nanosheets exfoliate into bunches or restacks to a small extent upon drying.

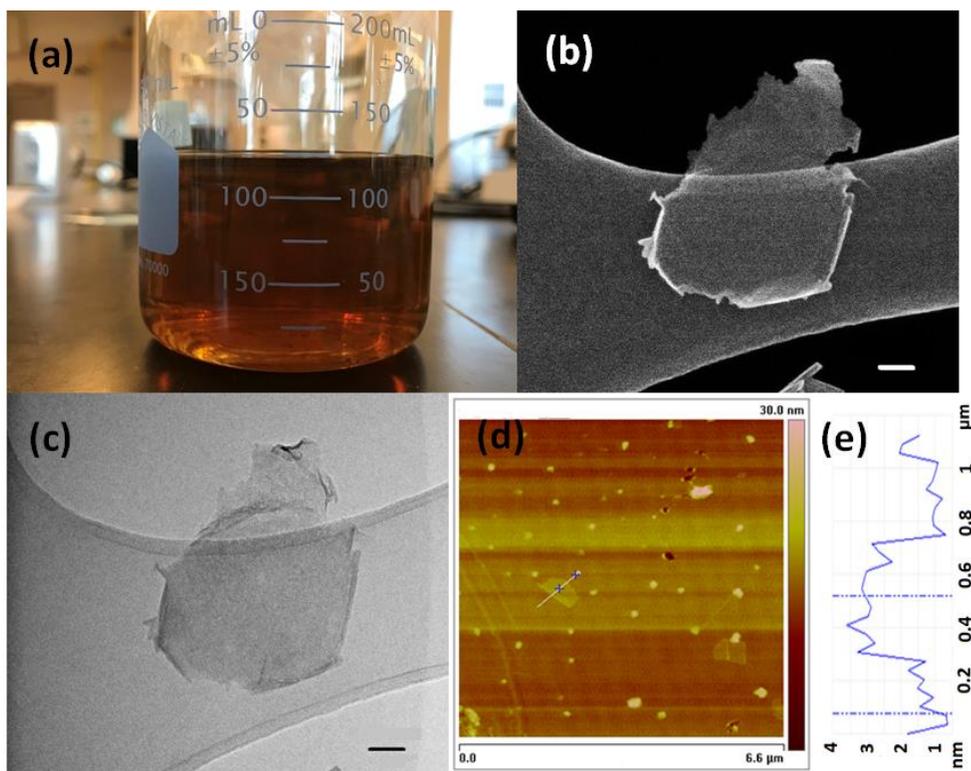


Figure 36. (a) The photo image of the exfoliated δ -MnO₂ nanosheets stabilized in suspension, (b) SEM image and (c) bright-field TEM image of exfoliated δ -MnO₂ nanosheets, (d) AFM image of MnO₂ nanosheets on Si wafer, (e) the height profile along the line shown in the AFM image in (d). Scale bar, 50 nm (b-c).

2.3.3 Investigation of the δ -MnO₂ nanosheets flocculation/reassembly processes

The reassembly of δ -MnO₂ nanosheets is usually realized by introducing cation guest species into the nanosheet suspension. This is because the surface of the as-prepared δ -MnO₂ nanosheets is usually negatively charged, therefore the introduction of cationic species will lead to spontaneous attraction of dispersed nanosheets, and finally results in the formation of reassembled particles. Moreover, the flocculation/reassembly processes need to be carefully controlled, in order to get desired 3-D porous nanostructures. In this work, we have studied the influences of different cations (H⁺, Li⁺, Na⁺) and different methods (immediately adding vs. titration) on morphologies of the obtained floccs, in order to optimize the flocculation/reassembly procedures.

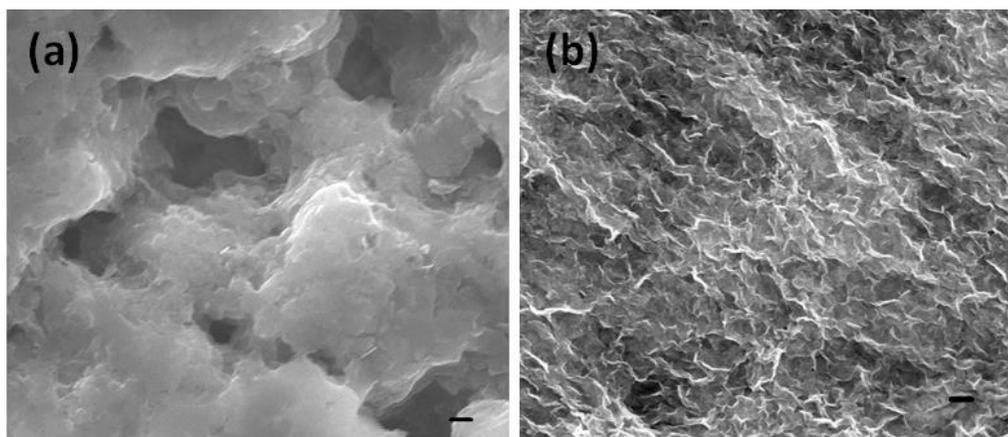


Figure 37. SEM images of reassembled δ -MnO₂ nanostructures flocculated by (a) adding 6N HCl solution to the suspension all at once while stirring to reach pH = 2, and (b) adding 6N HCl solution to the suspension at a constant rate of 1 mL/min while stirring to reach pH = 2. Scale bar, 500 nm (a-b).

Figure 37 shows the comparison of two reassembled samples that are flocculated by (a) directly adding H⁺ to the suspension within short time while stirring to reach pH = 2 (immediately adding), and (b) adding H⁺ to the suspension at a constant rate of 1 mL/min while stirring to reach pH = 2 (titration). Clearly it can be seen that when all the protons are added into the suspension without using titration method (as shown in Figure 37(a)), the nanosheets are simply restacked together, forming bulk crystals with less porosity. In contrast, when the protons are added into the nanosheet suspension at a constant slow rate, the floccs exhibit 3-D porous nanostructures, which is shown in

Figure 37(b). The formation of different morphologies can be simply illustrated as follows. When all the protons are added into the suspension within seconds, the presence of large amount of cationic species within short time makes it easier and kinetically favorable for the negatively charged nanosheets stack together, thus leading to the formation of densely packed structures with less porosity. However, when protons are added into the suspension slowly, the nanosheets are more likely to form the small fluffy agglomerates each time the protons are added and then quickly dispersed under stirring. Finally the fluffy agglomerates will reassemble together and leading to the formation of 3-D porous nanostructures. Since the porous nanostructures with large surface area can promote the absorption and intercalation of alkali cations, which is critical for improving the supercapacitor electrode's performance, thus it can be concluded that the cationic species are better to be added into the nanosheet suspension at a slow constant rate by using titration method.

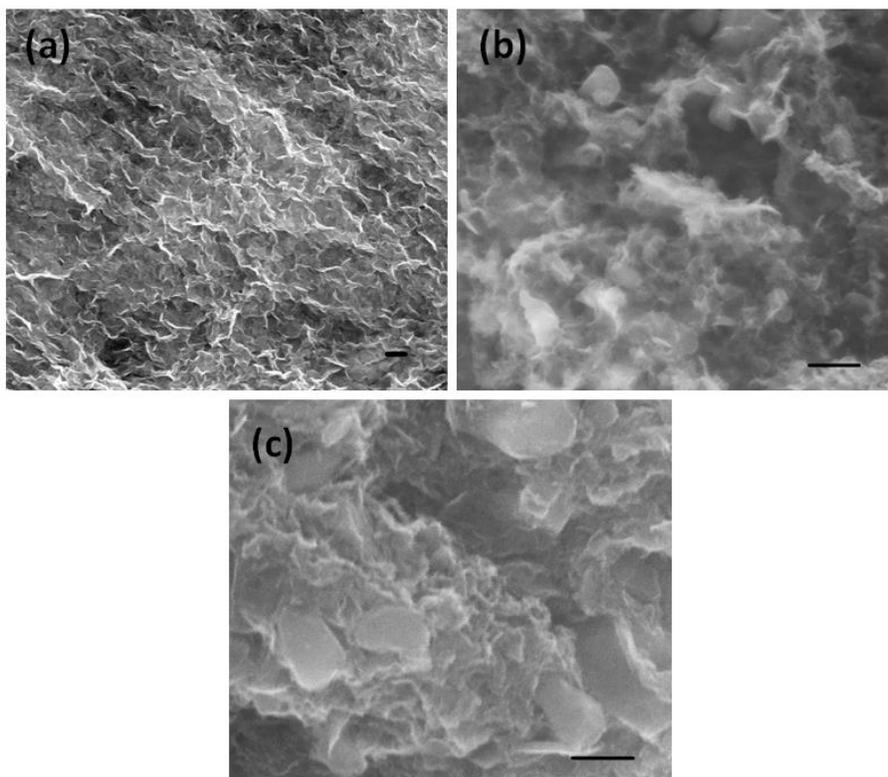


Figure 38. The SEM images of (a) H^+ , (b) Li^+ , and (c) Na^+ flocculated $\delta\text{-MnO}_2$ nanostructures. Scale bar, 500 nm (a-c).

The effects of different cationic species (H^+ , Li^+ and Na^+) on surface morphologies of the reassembled δ - MnO_2 nanostructures have also been investigated, with the results shown in Figure 38. All cations are added into the suspension at the same rate under stirring. The addition of protons is finished when the pH value reached 2, and the addition of Li^+ and Na^+ ions are stopped when no apparent color change of the suspension was observed. Although the quality of the SEM images is not good, all the three samples still look porous, indicating that the use of different cationic species has no apparent influence on the morphologies of the reassembled nanostructures. Since we will equilibrate the reassembled nanostructures in acid environment in the following experiments to introduce defects, and in order to avoid introducing unwanted species (such as Li^+ , Na^+ , etc.), we decided to use H^+ to flocculate the δ - MnO_2 nanosheets during the reassembly process.

2.3.4 Phases and microstructures of the reassembled δ - MnO_2 nanostructures

The SEM images of flocculated δ - MnO_2 nanostructures, followed by equilibration at pH = 2 and 4 solutions for 24 h, are shown in Figure 39(a) and (b). It can be clearly seen that both samples exhibit 3-D porous nanostructures and equilibration at different pH values have no apparent influence on their morphologies. The high-magnification SEM image shown in Figure 39(c) demonstrates the presence of scrolling at the edges, which is consistent with the TEM images and has been noted in other nanosheet studies.^{166,167} The observation of porous structures after reassembly highlights the usefulness of our ultrasonic-assisted exfoliation and titration-based flocculation procedures, where the exfoliation rate is greatly enhanced without sacrificing the porous nanostructures.

The X-ray diffraction patterns (Figure 40) for reassembled MnO_2 (the XRD pattern for protonated MnO_2 has also been included for comparison) demonstrate that phase purity was achieved during synthesis and that exfoliation and reassembly yields complex nanostructures as evidenced by peak broadening and asymmetry. After reassembly of the nanosheets, in-plane $hk0$ reflections remain discernible, indicating that the crystalline nature of the 2-D sheets is preserved. Further, the derived PDF is consistent both with literature¹⁶⁸ and the calculated PDF of a single δ - MnO_2 nanosheet (Figure 41); further

confirming the δ -MnO₂ nanosheet motif is maintained. The broadening of the 00 l basal reflections shows that although some sheet-to-sheet restacking occurs, the stacks are on the order of only 3-4 nm (estimated using the Scherrer equation), which is consistent with the AFM results. Shifts of the basal reflections result from increased water content in the reassembled nanosheet floccules compare to the proton-exchanged form.

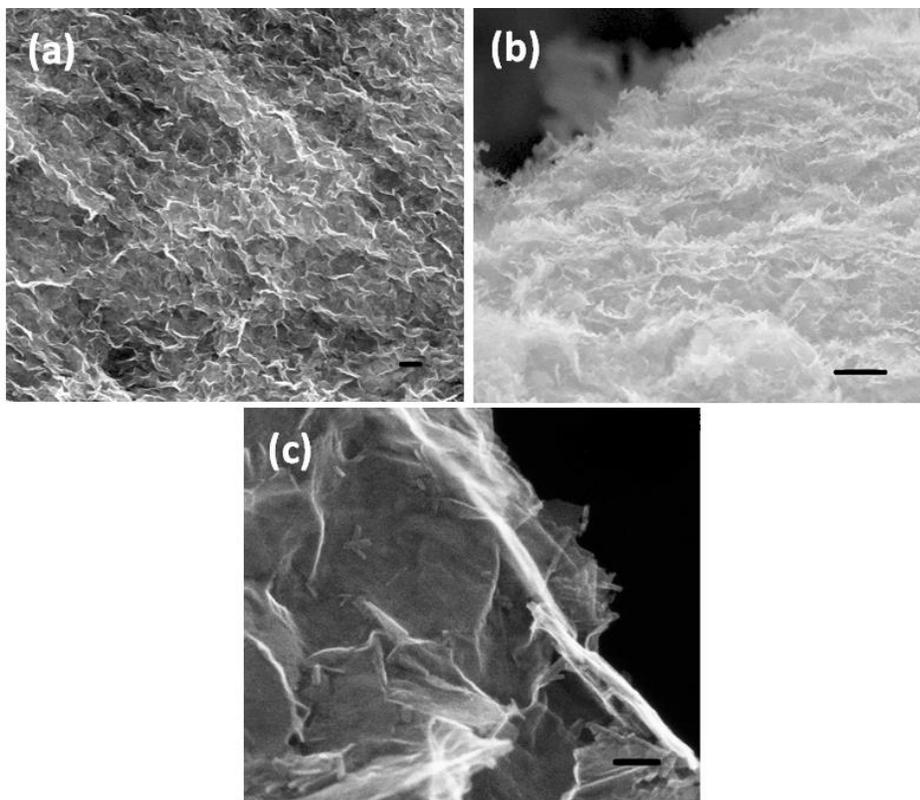


Figure 39. SEM images of reassembled MnO₂ nanostructures treated in (a) pH = 2 and (b) pH = 4 solution for 24 h. (c) high-magnification SEM image of reassembled MnO₂ nanostructures treated in pH = 2 solution for 24 h. Scale bar, 500 nm (a-b); 50 nm (c).

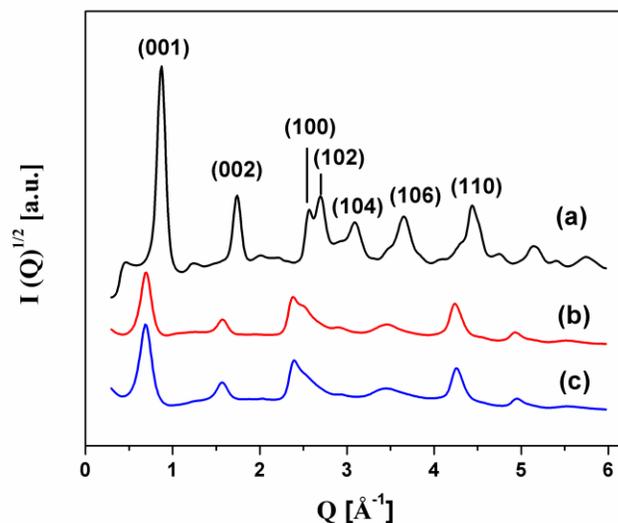


Figure 40. XRD patterns of (a) protonated MnO_2 , (b) reassembled MnO_2 treated in $\text{pH} = 4$ solution for 24 h, (c) reassembled MnO_2 treated in $\text{pH} = 2$ solution for 24 h. Data collected on APS 11-ID-B.

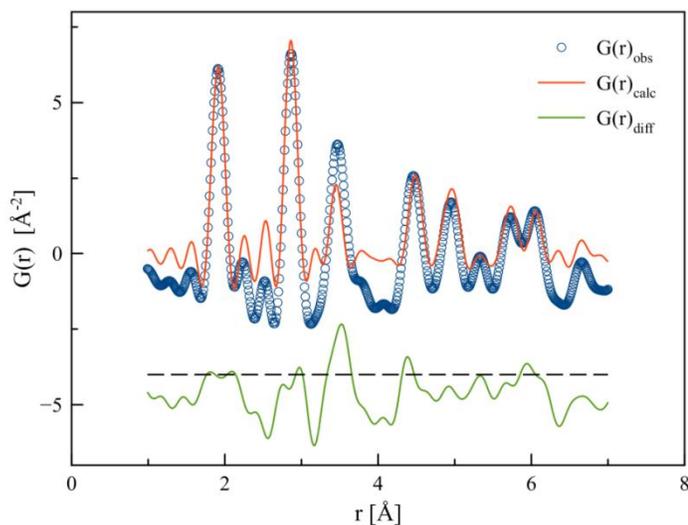


Figure 41. Comparison of the experimental PDF (reassembled MnO_2 , $\text{pH} = 2$) and the PDF calculated for a single $\delta\text{-MnO}_2$ sheet confirms the $\delta\text{-MnO}_2$ motif is maintained in the exfoliated and reassembled nanosheet floccs.¹⁶⁴

Nitrogen adsorption-desorption isotherms were used to quantify the specific surface area (SSA) of all specimens, and the results are shown in Figure 42. While protonated MnO_2 showed no evidence of mesopores, both reassembled MnO_2 nanostructures show

typical type IV isotherms (IUPAC classification) with distinct H3-type hysteresis loops, a result of open slit-like mesopores.¹⁶⁹ The Brunauer Emmet and Teller (BET) specific surface areas (SSA) were $120 \pm 0.4 \text{ m}^2/\text{g}$ for the pH = 2 sample and $144 \pm 1 \text{ m}^2/\text{g}$ for the pH = 4 sample, and only $4.5 \pm 0.1 \text{ m}^2/\text{g}$ for H_xMnO_2 , where the former values are roughly double the surface areas reported by Song *et al*⁹⁸ for reassembled oxide nanosheets.

Together, the XRD, BET and microscopy shown above indicate that the reassembled nanosheets have macro and mesopores, with the mesoporosity arising due to loose agglomeration of randomly oriented sheet clusters. The extent of exfoliation and/or restacking, typical sheet thicknesses determined by AFM and average crystallinity in the sheet stacking direction as determined by XRD are similar or better for our MnO_2 specimens than those reported recently for MnO_2 , TiO_2 , Co_3O_4 , ZnO , and WO_3 .¹⁶⁷ Therefore, the typical structures in Figure 39(a) are of the form of edge-to-face assembled nanosheet booklets, with “wall thicknesses” of up to 4 nm. The high specific surface area of the MnO_2 nanosheet assemblies facilitates infiltration of the electrolyte into the porous electrode to enhance the specific capacitance.^{3,15}

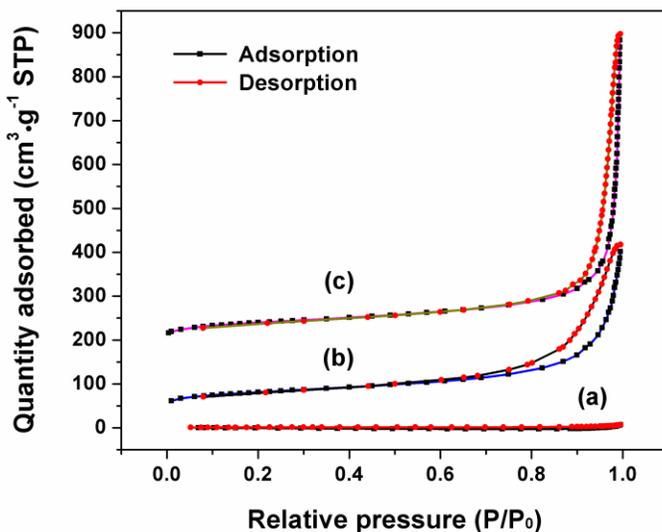


Figure 42. The typical N_2 adsorption-desorption isotherms of (a) protonated MnO_2 , (b) reassembled MnO_2 treated in pH = 2 solution for 24 h, (c) reassembled MnO_2 treated in pH = 4 solution for 24 h. Curves (b) and (c) are offset by 50 and 200 $\text{cm}^3 \cdot \text{g}^{-1}$ STP respectively.

During soft chemical processing, the surface and interlayer tetrabutyl ammonium hydroxide (TBAOH) and water content may vary with processing conditions. Figure 43 shows the thermogravimetric analysis of the protonated, pH = 2 and pH = 4 samples. Clearly it indicates 9.5 wt.% H₂O for H_xMnO₂ dried at 60°C (0.5 H₂O per MnO₂ formula unit), 12.3 wt.% (0.7 H₂O per MnO₂ formula unit) for the pH = 2 nanosheet assembly, and 15.5 wt.% (0.9 H₂O per MnO₂ formula unit) for the pH = 4 sample. The slightly higher water content in the pH = 4 vs. pH = 2 sample is a result of its slightly larger surface area.

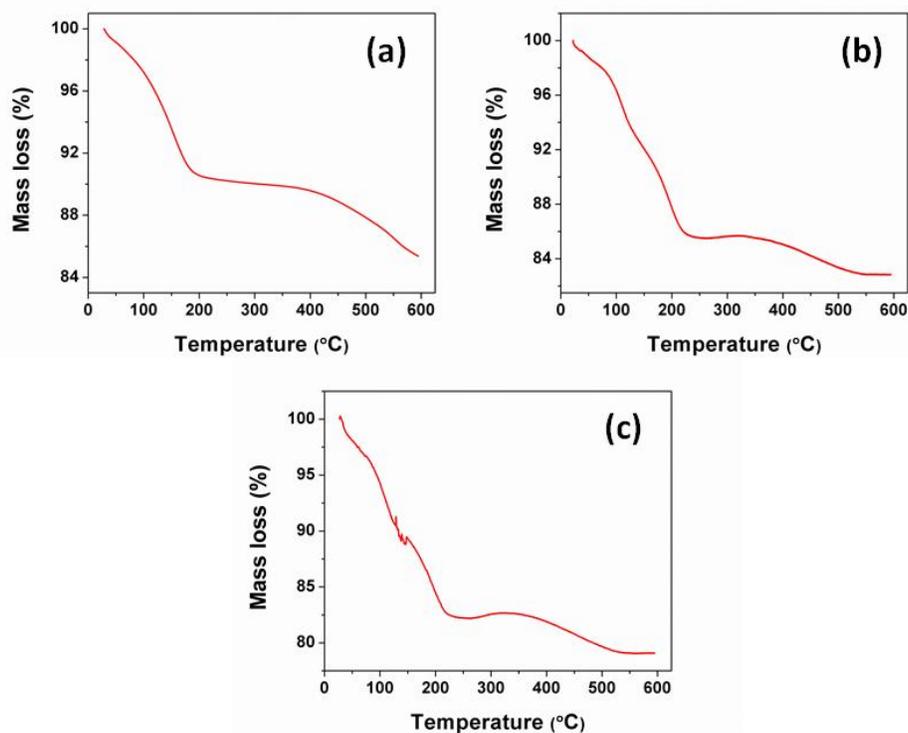


Figure 43. TGA curves of (a) protonated MnO₂, (b) reassembled MnO₂ treated in pH = 2 solution for 24 h, (c) reassembled MnO₂ treated in pH = 4 solution for 24 h.

The presence of structural water usually enables rapid proton or alkali cation transport within the interlayer, which is beneficial for increasing the charge storage properties.¹⁵ The presence of residual TBAOH in the reassembled samples was indicated by a small mass loss (~3 %, corresponding to 0.01 TBAOH per MnO₂ formula unit). Since one tetrabutylammonium molecule occupies an area of ~60 Å², and one MnO₂ unit

cell gives an surface area of 7 \AA^2 , therefore the surface coverage of residual TBAOH on MnO_2 nanosheet is about 9 % in the temperature region of 200-400 °C.^{170,171} At 400-600 °C all the samples show another mass loss corresponding to the evolution of oxygen from the lattice, leading to the formation of Mn_3O_4 ,¹⁷² and loss of structural hydroxyls.¹⁷³

Infrared (IR) spectroscopy (Figure 44) and X-ray photoelectron spectroscopy (XPS) (Figure 45) were also used to detect remnant TBAOH in the nanosheet assemblies after processing. As shown in Figure 44, all the sharp bands near 2980 cm^{-1} belong to C-H stretching vibrations in TBAOH molecules. Direct observation of nitrogen via the C-N vibration is apparent in a broad IR band near $2000 - 2300 \text{ cm}^{-1}$ while the bands in the $950 - 1300 \text{ cm}^{-1}$ region correspond to the C-N stretching vibration. The bands located at 1560 and 1600 cm^{-1} are a result of the N-H stretching vibration, and that at 1385 cm^{-1} is related to the N-O stretching vibration.¹⁷⁴⁻¹⁷⁷

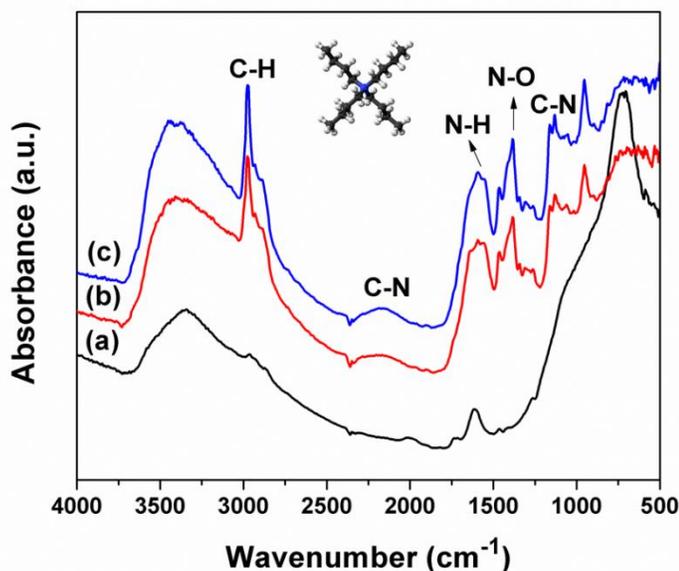


Figure 44. FTIR spectra of (a) protonated MnO_2 ; (b) reassembled MnO_2 treated in pH = 4 solution for 24 h; (c) reassembled MnO_2 treated in pH = 2 solution for 24 h (inset shows the structure of the TBAOH molecule).

The presence of residual TBAOH in the reassembled samples has also been confirmed by using the XPS survey scan (Figure 45(a)), which we can clearly see the N 1s peak coming from the TBAOH molecules. Besides, the non-symmetrical C 1s peak shape shown in Figure 45(b), as well as the presence of the small peak located at around

288 eV that can be attributed to carbon bounded to nitrogen,¹⁷⁸ also confirmed the existence of TBAOH after exfoliation and flocculation processes.

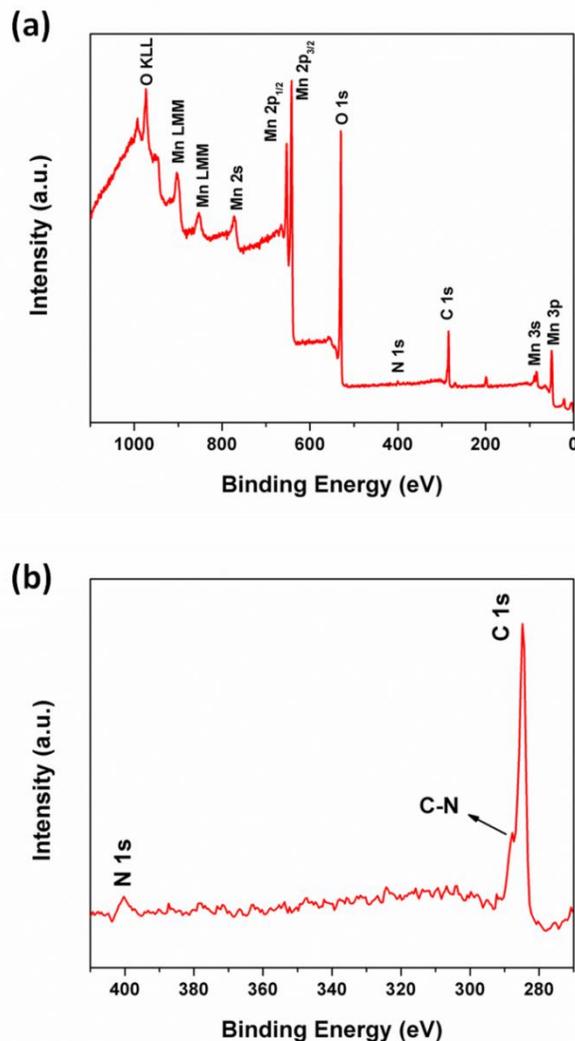


Figure 45. XPS spectra of reassembled MnO₂ treated in pH = 2 solution for 24 h. (a) XPS survey scan, (b) high resolution XPS N 1s and C 1s spectrum.

From the above TGA, FTIR and XPS analysis it can be seen that even after sufficient rinsing, the TBAOH molecules used for exfoliating the δ -MnO₂ nanosheets still existed in the reassembled nanostructures. The potential effects of the remaining TBAOH molecules on the electrochemical performance have also been discussed. Figure 46 shows the infrared spectra of reassembled MnO₂ treated in pH = 4 solution for 24 h, before and after one CV cycling in 1M Na₂SO₄ electrolyte at 50 mV/s scan rate. It can be

seen that the TBAOH is removed from the nanosheet assemblies after one charge-discharge cycle, since the IR bands corresponding to the TBAOH molecules have almost disappeared after cycling. Therefore, although it is not possible to completely remove the TBAOH molecules from the nanosheet assemblies by washing, its small surface coverage (~9 %, determined by TGA analysis and the geometry of the TBAOH molecules) and easy extraction during the first electrochemical cycle together suggest that it has limited if any influence on the measured electrochemical performance.

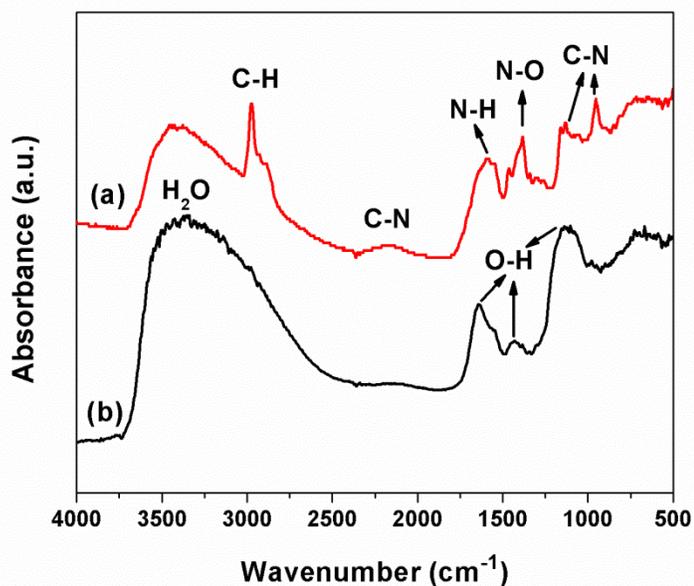


Figure 46. FTIR spectra of reassembled MnO_2 treated in pH = 4 solution for 24 h, (a) before and (b) after one CV cycling in 1M Na_2SO_4 electrolyte at 50 mV/s scan rate.

2.3.5 Oxidation states determination of the protonated and reassembled $\delta\text{-MnO}_2$ nanostructures

In order to determine the oxidation states of the Mn ions in all samples (protonated MnO_2 , pH = 2 and 4 equilibrated reassembled MnO_2), we have first employed X-ray photoelectron spectroscopy (XPS). As shown in Figure 47, the Mn 2p region mainly consists of a spin-orbit doublet corresponding to the Mn $2p_{1/2}$ and Mn $2p_{3/2}$ states around the binding energy of 653.0 and 642.0 eV. Generally speaking, the binding energy values can be used to roughly estimate the oxidation state of manganese. According to the literature, binding energy values of 642.0 eV are usually assigned to Mn^{4+} , 641.0 eV to

Mn³⁺, and 640.0 eV to Mn²⁺.^{179,180} Since the main Mn 2p_{3/2} peak for all samples is located between 642.0 and 641.0 eV, and the shape of the Mn 2p_{3/2} peaks is obviously not symmetrical, which implies the coexistence of Mn³⁺ and Mn⁴⁺ in the MnO₂ nanosheets. Moreover, studies of Biesinger *et al*¹⁸¹ showed that multiple peaks resolved under the Mn 2p spectrum can represent a single oxidation state. Thus, due to the complexity of oxidation states in Mn 2p spectrum as well as the lack of standardization, it is difficult to determine the manganese oxidation state only from the Mn 2p_{3/2} peak.

The splitting of Mn 3s peaks is often used to determine the oxidation state of Mn,¹⁸²⁻¹⁸⁴ where the electrons exchange interaction upon photoelectron ejection defines the magnitude of the splitting. The separation of peak energies for the electron exchange in the 3s-3d level of Mn is described by Equation (11).

$$\Delta E = (2S + 1) K [3s, 3d] \quad (11)$$

where ΔE is the separation of peak energies. S is the total spin of unpaired electrons in the 3s and 3d levels in the final states and $K [3s, 3d]$ is the exchange integral between 3s-3d energy levels. Based on the above theory, lower valence of Mn will lead to wider splitting of the 3s peaks. Therefore, we are able to qualitatively compare the Mn³⁺ content in the three samples through study the Mn 3s peak energy separation as shown in Figure 47(b). The ΔE values obtained are 4.8 eV for the protonated MnO₂, 4.9 eV for the pH = 4 treated reassembled MnO₂, and 5.2 eV for the pH = 2 treated reassembled MnO₂. The results indicate that lower pH treatment of the reassembled MnO₂ nanostructures can lead to the formation of more Mn³⁺ in the MnO₂ nanosheet. The protonated MnO₂ exhibits a lower Mn³⁺ content compared with both the pH = 2 and 4 samples, despite being treated at lower pH. This apparent contradiction results from steric effects in the crystalline H_xMnO₂ that inhibit Mn occupation of the interlayer galleries.

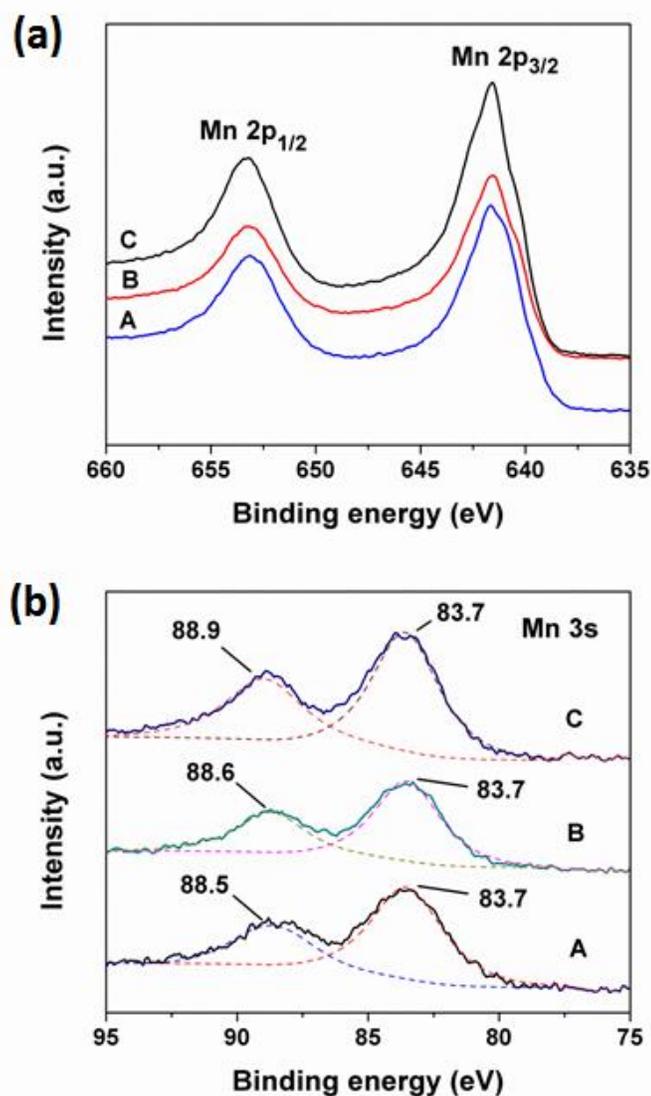


Figure 47. XPS spectra in the (a) Mn 2p, and (b) Mn 3s regions corresponding to (A) protonated MnO₂, (B) reassembled MnO₂ treated in pH = 4 solution for 24 h, (C) reassembled MnO₂ treated in pH = 2 solution for 24 h.

The oxidation state of the Mn ions in all samples was further investigated by using Mn K-edge X-ray absorption near-edge spectroscopy (XANES). The data were collected at Cornell High Energy Synchrotron Source (CHESS) at Cornell University, and the results are shown in Figure 48. Figure 48(a) shows the spectra of standard materials including MnO, Mn₃O₄, Mn₂O₃ and MnO₂. The XANES spectra of the H_xMnO₂, pH = 2 and 4 nanosheet assemblies, and reference materials Mn₂O₃ and MnO₂ are shown in Figure 48(b). The line profiles are characterized by features that correspond to a pre-edge

range with two weak broad peaks at 6540-6545 eV, a main-edge range that has one inflection point A, and the resonance peak range B.^{98,185} The weak pre-edge peaks P and P' correspond to the dipole-forbidden $1s \rightarrow 3d$ transition.¹⁷² All three samples exhibit higher intensity of peak P' than for peak P, but the peak P' is less intense as compared with the β -MnO₂ reference. This observation confirms the existence of mixed oxidation states of Mn³⁺/Mn⁴⁺ in the samples. Also, the higher intensity ratio of P' to P for H_xMnO₂ compared with the pH = 2 and 4 samples indicates that it has less Mn³⁺, because the relative intensity of the peaks P'/P is proportional to the average oxidation state.¹⁷²

The main absorption range can be assigned to the dipole-allowed $1s \rightarrow 4p$ transition. The associated edge energy is usually taken as the energy of the peak in the first derivative, which corresponds to the inflection point of the main edge in the XANES spectra (Figure 48(c)). Clearly, the main absorption edge (A) progressively shifts to lower energies with decreasing pH, implying lower pH progressively reduces Mn to the trivalent state. Also, the presence of the intense peak B for the nanosheet assemblies indicates that they are mainly comprised of edge-shared MnO₆ octahedra.¹⁸⁶ This observation further confirms that the δ -MnO₂ lattice is not dissolved by equilibration in HCl at pH as low as 1.

The average oxidation state (AOS) of Mn was determined by establishing a linear relationship between the K-edge energy and Mn oxidation state (Figure 48(d)). The AOS of Mn is 3.59 for H_xMnO₂, 3.36 for the pH = 4 MnO₂ nanosheet assembly, and 3.24 for the pH = 2 variant. The dependence of Mn valence on pH generally follows that reported earlier by Manceau and coworkers¹³⁴ for bulk Na-saturated δ -MnO₂ (birnessite) powders, where the Mn AOS varied from 3.81 at pH = 9 to 3.69 for pH = 3.

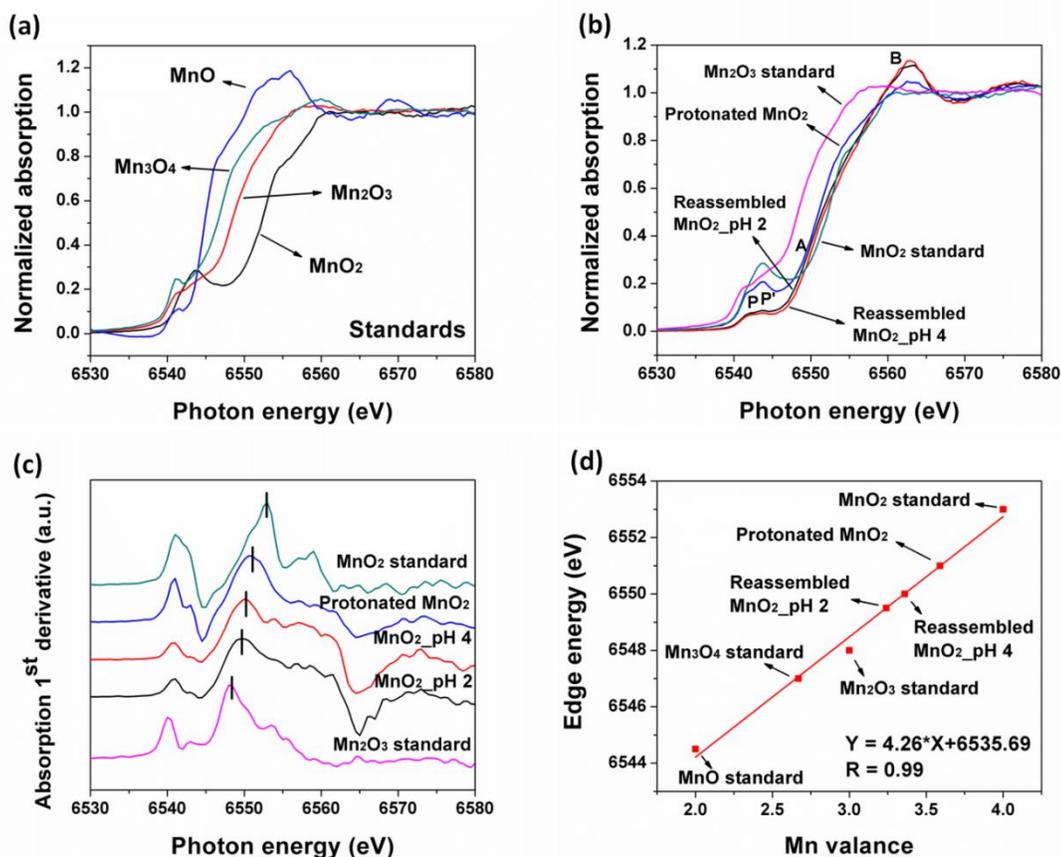


Figure 48. X-ray absorption measurements of the as-prepared three samples and reference Mn oxide materials. (a) XANES spectra of reference materials MnO, Mn₃O₄, Mn₂O₃ and MnO₂. (b) XANES spectra of protonated MnO₂, pH = 2 and 4 treated reassembled MnO₂. The reference materials of Mn₂O₃ and MnO₂ from panel (a) are also shown for ease comparison. (c) First derivative curves corresponding to the samples shown in panel (b). (d) Average oxidation state of Mn for the samples and standards derived from the K-edge energy.

For the alkali-free MnO₂ samples studied herein, we also find that treating the exfoliated MnO₂ assemblies at lower pH increases the Mn reduction to a greater extent than found for crystalline Na_xMnO₂ by Manceau and coworkers.¹³⁴ Furthermore, we find competing steric and thermodynamic effects by comparison of the proton-exchanged H_xMnO₂ to the exfoliated and re-assembled variants. The AOS of H_xMnO₂ treated at pH < 1 is 3.59, whereas the exfoliated samples treated at higher pH have AOS values of 3.36 (pH = 4) and 3.24 (pH = 2). We attribute the lesser extent of Mn reduction in crystalline H_xMnO₂ to steric hindrance by the interlayer galleries which are crowded with protons and water. This has the two-fold effect of hindering access of aqueous H₃O⁺ to reducible

Mn^{4+} , and of preventing displacement of Mn^{3+} to the sheet surface. Indeed, earlier work by Gaillot *et al*¹⁵⁸ noted that during thermal reduction of $\text{Mn}^{4+} \xrightarrow{350\text{ }^\circ\text{C}} \text{Mn}^{3+}$ in crystalline K-birnessite, Mn vacancies were not formed despite the unfavorable in-sheet lattice strain due to Jahn-Teller distortions inherent to Mn^{3+} . The interactions of neighboring in-plane Mn^{3+} and Mn^{4+} sites therefore contributes both strain and electrostatic-driven components to the energetics of $\delta\text{-MnO}_2$ defect equilibration.

2.3.6 Defects structure characterization of the protonated and reassembled $\delta\text{-MnO}_2$ nanostructures

High energy X-ray scattering and pair distribution function analysis were undertaken to further characterize the defects formed in soft chemically reduced MnO_2 nanosheets, with the specific goal of correlating the quantity of Mn point defects with Mn reduction and electrochemical performance. PDF analysis probes not only the local atomic bonding motifs but also intermediate and long-range order, thus making it an appropriate tool for investigating the structures of poorly-crystalline materials and nanoparticles that yield diffraction patterns with large amounts of diffuse scattering.¹⁶⁸

The observed scattered intensity, the reduced structure function $F(Q)$ and the associated PDF for the reassembled nanosheets are shown in Figure 49. We focus our attention on two PDF correlation peaks: the in-plane Mn-Mn peak at 2.89 Å and the Mn- Mn_{surf}^{ooo} distance at 3.45 Å (Figure 50(a)). Two notable advantages of the PDF method are that these two Mn correlations are unique in the alkali-free $\delta\text{-MnO}_2$ structure (Figure 50(b)) and that the integrated area of a PDF peak represents the number density of that specific correlation type.¹³⁹ We leverage these facts to obtain useful estimates of Mn vacancy concentrations in lieu of developing complete structure models, which are notably difficult for these material systems.^{165,187}

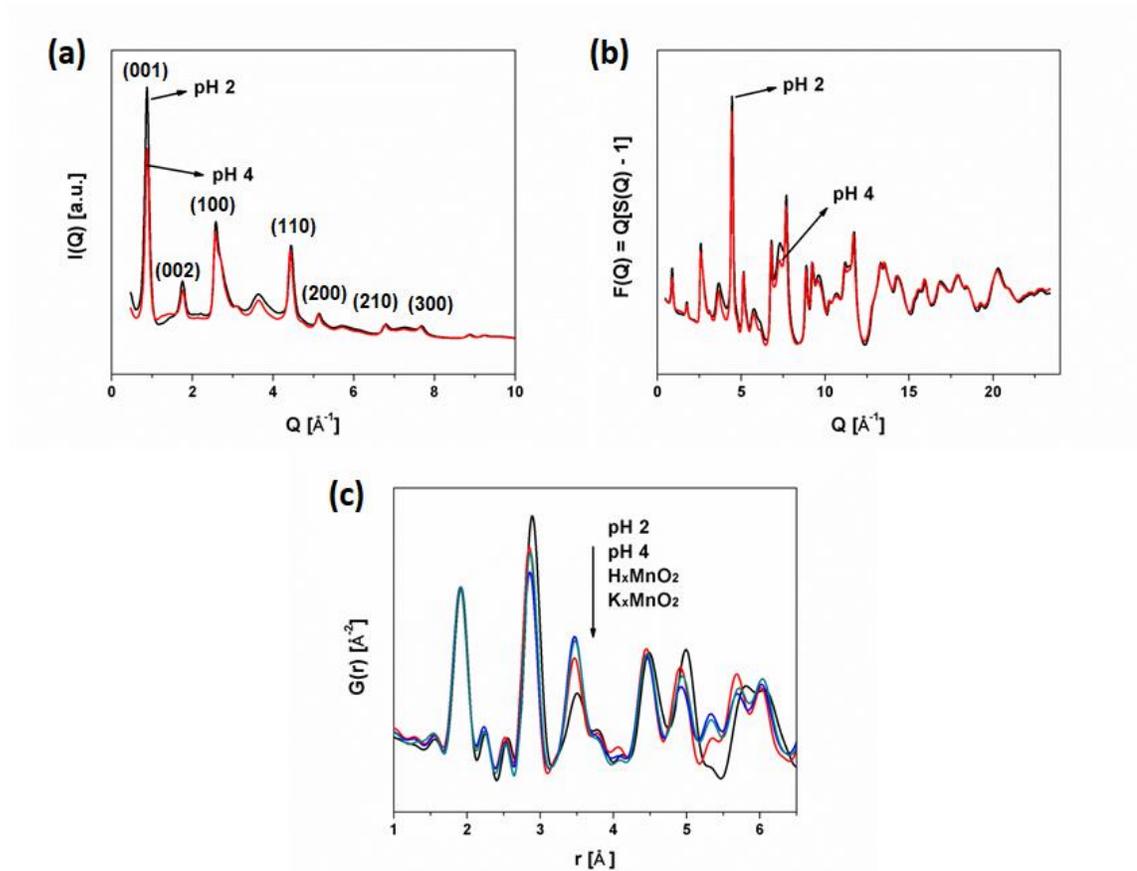


Figure 49. High-energy X-ray scattering and experimental PDF data. (a) $I(Q)$ and (b) $F(Q)$ for the pH = 2 and pH = 4 treated MnO_2 nanosheets assemblies, and (c) $G(r)$ for the pH-treated samples, protonated MnO_2 (H_xMnO_2), and parent phases (K_xMnO_2). The basal reflections evident in $I(Q < 2 \text{\AA}^{-1})$ indicate a measure of restacking. The variation in intensity as a function of pH indicates a variation in the interlayer structure attributable to either surface water or Mn. The inverse trends in the Mn-Mn peak (2.89 \AA) and Mn-Mn^{II} peak (3.45 \AA) as a function of pH support the Mn³⁺ displacement model recommended by Manceau *et al.*¹³⁴

In order to compare the PDF with respect to different samples, we have normalized our data to the amplitude of the 1.9 \AA Mn-O peak. This choice is based on the implicit assumption that all Mn ions are coordinated in a six-fold environment. We further assume that the intrinsic V_{Mn}''' population in the parent phase K_xMnO_2 is on the order of parts per million, which will be negligible compared to the percent-level vacancies in the MnO_2 nanostructures. Consequently, the relative in-plane Mn concentration can be calculated according to the following equation:

$$\frac{[Mn]_i}{[Mn]^0} = \frac{A_i}{A^0} \text{ or } [Mn]_i = \frac{A_i}{A^0} \quad (12)$$

Where the superscript ⁰ denotes quantities in K_xMnO_2 , the subscript _i denotes quantities for a derivative sample, and $[Mn]^0$ is taken as 1. The absolute accuracy of the values obtained using Equation (12) will be influenced by the correlations between interlayer water or hydroxyl pairs which perturb the low-r PDF region, leading to overestimation of the Mn_{surf}^{oo} content.¹⁶⁸ While there is notable difficulty in absolute quantification of Mn defects in these materials, this method should provide reasonable relative quantification in the derived nanosheet assemblies. Although estimation of error is not possible with this empirical approach, a percent level of uncertainty is expected for the calculated Mn concentrations.

As shown in Figure 50(a), the V_{Mn}''' concentration, which is equivalent to the Mn_{surf}^{oo} concentration, is then is $1 - [Mn]_i$ in fractional units. Here we define this type of defect as a “surface Frenkel” defect, where displacement of the in-plane Mn to the nanosheet surface is reminiscent of the Frenkel defect vacancy-interstitial pair. The results of our analysis are summarized in Table I. Consistent with the model of Manceau *et al.*,¹³⁴ we observe an increase in $[V_{Mn}''']$ with decreasing pH as well as the appearance of a PDF peak at a distance not found in the δ - MnO_2 structure which corresponds to $Mn - Mn_{surf}^{oo}$. The increase in concentration of surface Frenkel defects by approximately 30 % between the pH = 4 and pH = 2 samples supports the hypothesis that increased proton sorption at the MnO_2 surface in more acidic electrolytes expels more in-plane Mn leading to the formation of more Mn vacancies.

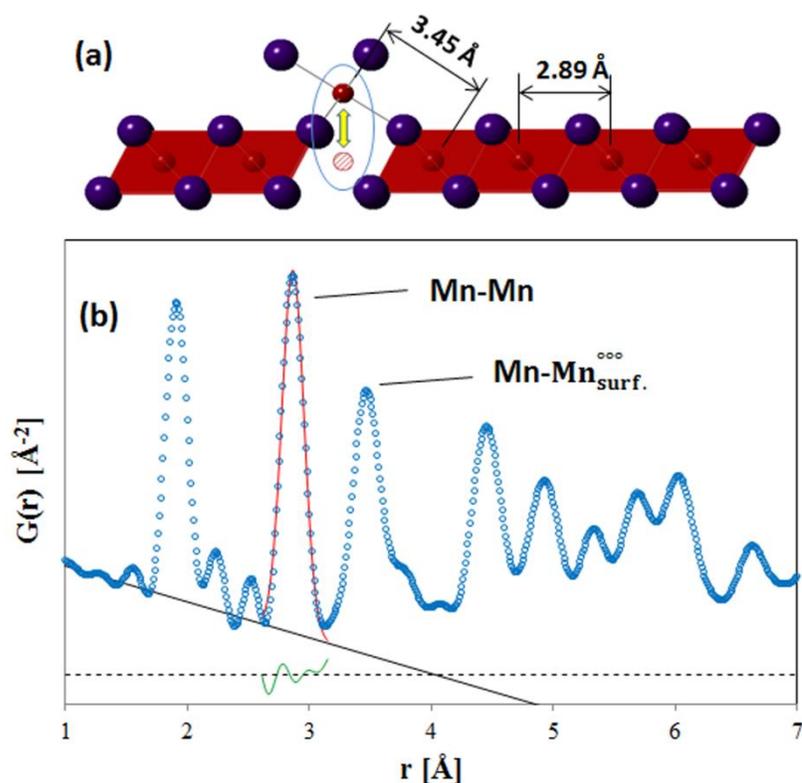


Figure 50. Empirical analysis of $\delta\text{-MnO}_2$ PDF. Using the resolved in-plane Mn-Mn correlation peak (a) we can empirically estimate the Mn surface Frenkel (circled) concentration using a Gaussian peak and linear baseline, (b) The PDF amplitude is normalized to the Mn-O correlation peak; therefore the ratio of nanosheet Mn-Mn to K_xMnO_2 Mn-Mn peak areas represents the fractional Mn-occupancy of the nanosheet assembly. $\delta\text{-MnO}_2$ equilibrated at $\text{pH} = 2$ is shown here.

As noted for the Mn valence, the PDF analysis likewise shows an apparent contradiction in the surface Frenkel defect content of the crystalline H_xMnO_2 when compared to the defect content of the $\text{pH} = 2$ and 4 samples. As shown in Table I, while the protonated form H_xMnO_2 is equilibrated at $\text{pH} < 1$, its defect concentration (18.3 %) is smaller than that in the $\text{pH} = 2$ sample (26.5 %) and is even smaller than that of the $\text{pH} = 4$ sample (19.9 %). As noted earlier, previous work shows that Mn^{3+} , with its Jahn-Teller distortion, may be accommodated in MnO_2 sheets in crystalline birnessites.¹⁸⁸ Our calculation based on XANES data shows that $\sim 2/3$, $1/2$, and $1/4$ of the Mn ions remaining in the nanosheets are reduced to Mn^{3+} for the $\text{pH} = 2$, 4, and H_xMnO_2 samples, respectively. The PDF and XANES analyses are therefore complementary in

demonstrating that surface Frenkel defects and Mn reduction are more favorable in high surface area nanosheet assemblies, with steric limitations reducing the extent of the reactions in well-crystalline birnessites.

Table I. Estimation of Surface Frenkel Defect Concentration.

Data Set	Center [Å]	Height [arb.]	Area [arb.]	FWHM [Å]	Mn-vac. [%]
Pristine MnO ₂	2.897	15.988	3.461	0.203	N/A
Protonated MnO ₂	2.858	13.896	2.826	0.191	18.3
Resembled MnO ₂ - pH 4	2.876	13.810	2.772	0.189	19.9
Resembled MnO ₂ - pH 2	2.867	12.335	2.544	0.194	26.5

*Gaussian parameters for the Mn-Mn in-sheet PDF peak corresponding to different samples extracted using Fityk.¹⁸⁹ Peak area is normalized to the Mn vacancy content of the parent phase K_xMnO₂ with the assumption that the intrinsic [V_{Mn}'''] population is on the order of parts per million in the high temperature crystalline phase.

2.3.7 Investigation of supercapacitor electrodes preparation methods for obtaining optimized charge storage properties

As the first step, we have tried the “drop-casting” method to prepare supercapacitor electrodes. The nickel foil substrates were first washed under ultrasonication in ethanol and water successively. Next, the reassembled δ-MnO₂ particles were dispersed in a mixed solution comprised of water and isopropanol, followed by ultrasonication for 2 h. Finally, different amounts of the corresponding suspension was cast onto the Ni foil surface and dried in air.

The typical SEM morphology of reassembled δ-MnO₂ nanostructure drop-cast on Ni foil substrates is shown in Figure 51. Not much difference has been observed for the drop-cast sample and reassembled nanostructures, indicating that the drop-casting process has little effect on the porous structures of the flocculated nanosheets. However, the electrochemical test result, shown in Figure 52, indicates that the specific capacitance of the drop-cast electrode is only in the range of 30-40 F/g, which is much smaller than most reported MnO₂ nanostructures that have similar morphologies and surface areas. This can be attributed to the following reasons: the deposited nanosheets are likely to

form larger agglomerates and distribute non-uniformly on the Ni foil substrates, thus exhibit smaller surface area and less active surface adsorption sites. Also, the MnO_2 exhibits poor electrical conductivity, thus leading to sluggish electrode kinetics. In addition, the poor contact between the nanosheet assemblies and the substrates may lead to large charge transfer resistance, which results bad electrochemical performance. Therefore, the above results indicate that the drop-casting method is not an appropriate way to make supercapacitor electrodes with good charge storage performance.

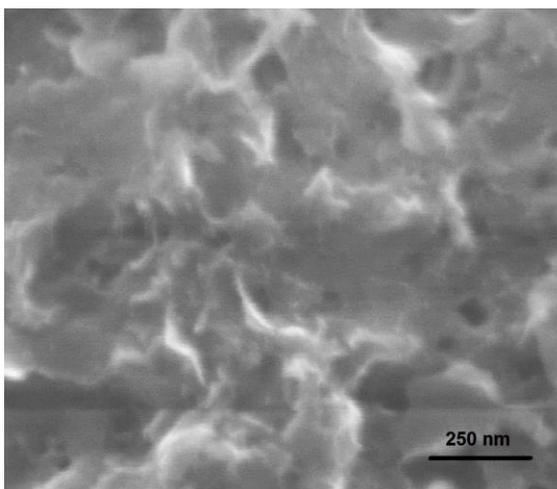


Figure 51. Typical SEM morphology of reassembled $\delta\text{-MnO}_2$ nanostructure drop-cast on Ni foils substrate.

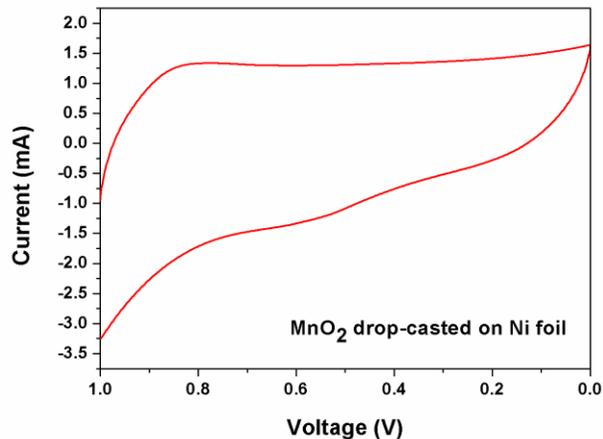


Figure 52. Cyclic voltammety curves for the reassembled $\delta\text{-MnO}_2$ nanostructure drop-cast on Ni foil substrate at a scan rate of 100 mV/s.

Another method of making supercapacitor electrodes has also been investigated, since the above mentioned “drop-casting” is not a promising way to obtain superior electrochemical performance. Specifically speaking, we mix the active material, acetylene black and PVDF in NMP solution. After stirring for 6 h, the homogeneous slurry was spread onto a Ni foil substrate with an area of 1 cm^2 , and then heated at $100 \text{ }^\circ\text{C}$ for 2 h to evaporate the solvent and obtain the electrode. The carbon black is used to increase the electrical conductivity of the electrode film, and the PVDF is a commonly used binder. In order to achieve optimized electrochemical response, we have discussed the influence of different amount of active material, carbon black and PVDF on the specific capacitance.

Figure 53 shows the galvanostatic charge-discharge curves for four electrodes with different mass ratios of MnO_2 , carbon black and PVDF, and their measured specific capacitances under different current densities are shown in Figure 54. Apparently, the electrode made with 80 wt.% MnO_2 , 15 wt.% carbon black, and 5 wt.% PVDF exhibits the largest capacitance. At 0.2 A/g current density, its specific capacitance reaches 224 F/g , which is larger than that of the electrode made with 75 wt.% MnO_2 -20 wt.% carbon black-5 wt.% PVDF, and almost double the specific capacitance of the electrodes prepared with 80 wt.% MnO_2 -10 wt.% carbon black-10 wt.% PVDF and 70 wt.% MnO_2 -20 wt.% carbon black-10 wt.% PVDF. Comparison of Figure 54(a) and (b) indicates that the replacement of 5 wt.% carbon black with MnO_2 can help greatly increases the specific capacitance, which is due to the large pseudocapacitance contributed by the MnO_2 . Comparison of Figure 54(a) and (c) also shows that the presence of large amount of PVDF is detrimental to the electrode performance, mainly because of its low electrical conductivity. Thus, the optimized electrochemical response can only be obtained by deliberately tuning the mass ratio of MnO_2 , carbon black and PVDF. Since the electrode prepared with 80 wt.% MnO_2 -15 wt.% carbon black-5 wt.% PVDF shows the largest specific capacitance, therefore we use this mass ratio to make the supercapacitor electrodes for the rest of this research work.

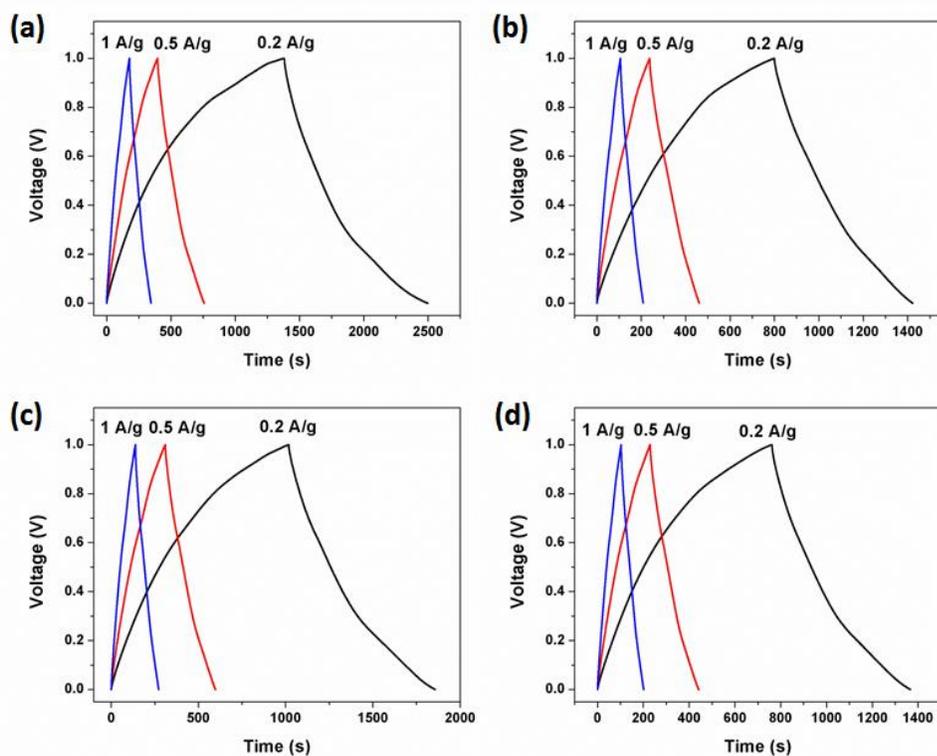


Figure 53. Galvanostatic charge-discharge curves of (a) 80 wt.% MnO₂-15 wt.% carbon black-5 wt.% PVDF, (b) 80 wt.% MnO₂-10 wt.% carbon black-10 wt.% PVDF, (c) 75 wt.% MnO₂-20 wt.% carbon black-5 wt.% PVDF, and (d) 70 wt.% MnO₂-20 wt.% carbon black-10 wt.% PVDF.

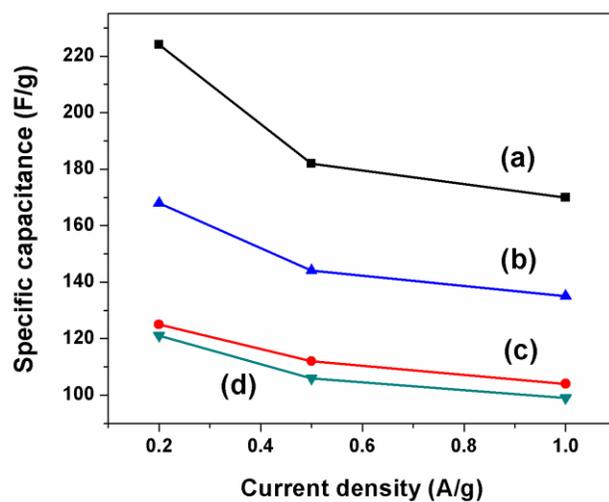


Figure 54. Comparison of specific capacitance for (a) 80 wt.% MnO₂-15 wt.% carbon black-5 wt.% PVDF, (b) 75 wt.% MnO₂-20 wt.% carbon black-5 wt.% PVDF, (c) 80 wt.% MnO₂-10 wt.% carbon black-10 wt.% PVDF, and (d) 70 wt.% MnO₂-20 wt.% carbon black-10 wt.% PVDF as a function of current density.

We have also investigated the influence of different MnO₂ mass loading on its specific capacitance. Figure 55 (a-e) shows the galvanostatic charge-discharge curves of the as-prepared electrodes with 0.32 – 3.04 mg/cm² MnO₂ mass loading and Figure 55(f) shows the comparison of their calculated specific capacitances. Clearly with decreasing the mass loading of MnO₂ nanostructures, their corresponding specific capacitance increases dramatically, especially when the mass loading of MnO₂ nanostructures less than 1 mg/cm². This is mainly because the MnO₂ exhibits poor electrical conductivity, and the electrochemical charge storage process usually happens on or near the surface. Therefore, as the film thickness goes up, more active material in electrode becomes inactive, meanwhile the poor electrical conductivity of the MnO₂ limits the charge transfer process, thus leading to inferior charge storage properties on a gravimetric basis. Therefore, for the rest of this research work, the amount of active material on the Ni foil electrodes has been fixed to 0.5-0.6 mg/cm², in order to obtain the best charge storage properties.

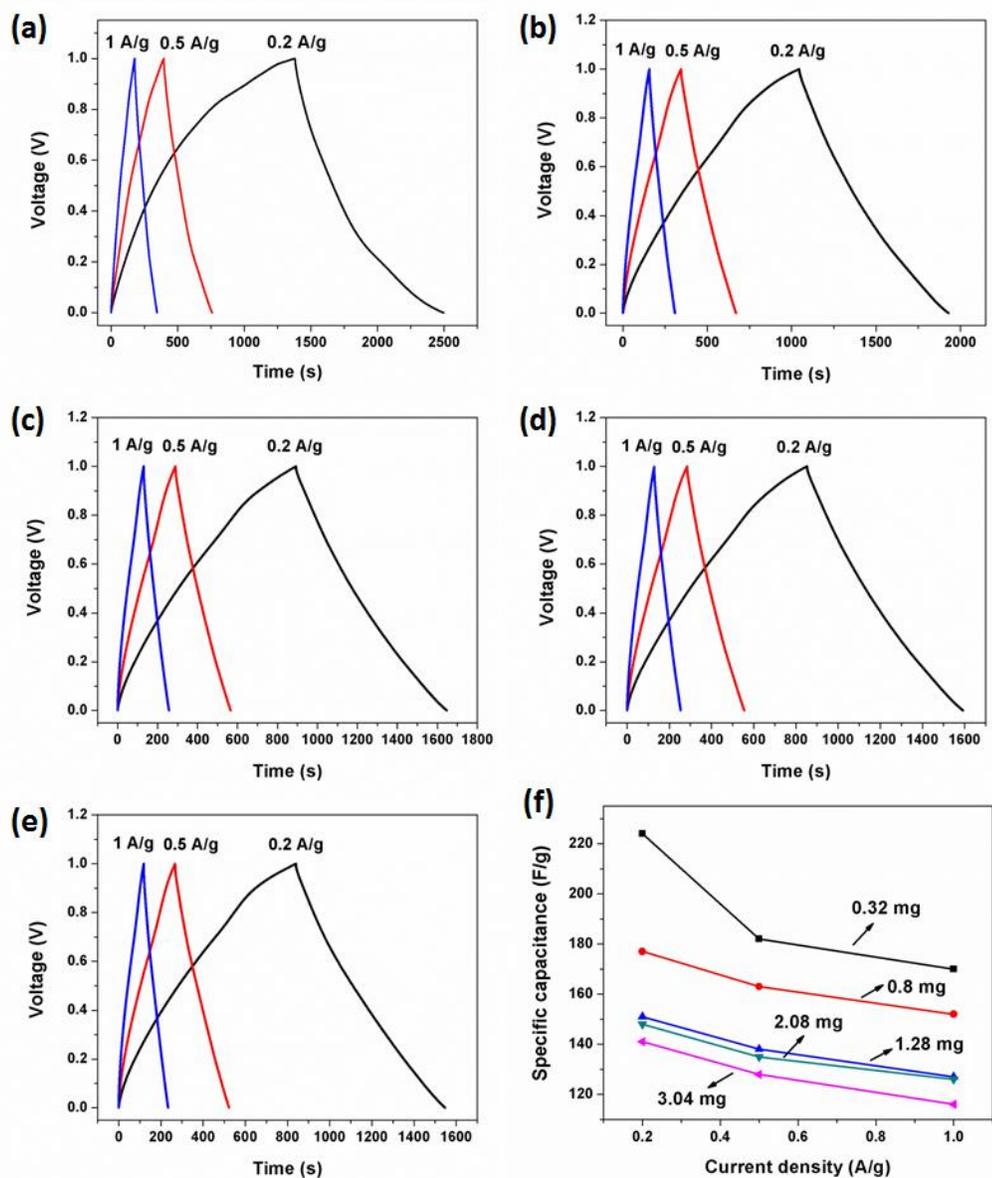


Figure 55. The galvanostatic charge-discharge curves of (a) 0.32 mg/cm², (b) 0.8 mg/cm², (c) 1.28 mg/cm², (d) 2.08 mg/cm², and (e) 3.04 mg/cm² MnO₂ mass loading. (f) Comparison of specific capacitance for the electrodes with different MnO₂ mass loading as a function of current density.

2.3.8 Electrochemical measurements of the protonated and reassembled δ -MnO₂ nanostructures

In order to investigate the role of point defects (Mn vacancies) on charge storage properties when used as supercapacitor electrodes, we have performed electrochemical measurements on the protonated and different pH equilibrated reassembled δ -MnO₂

nanosheets. As shown in Figure 56(a), the cyclic voltammetry (CV) curves for all three samples exhibit largely rectangular shapes in the potential window from 0 to 1 V, which indicates capacitive behavior. The absence of clear redox peaks for protonated and pH = 4 samples implies that the electrodes are charged and discharged at a pseudo-constant rate over the whole voltammetric cycle. However, the presence of broad redox peaks for the pH = 2 sample indicates that ion intercalation is an active and detectable charge storage mechanism for this specimen. Combined with the X-ray PDF analysis, the marked increase in Mn surface Frenkel defects with decreasing pH appears to enhance the intercalation reaction. This is also reflected in Figure 56(b-d), which shows the galvanostatic charge-discharge curves for the samples between 0 and 1 V under different current densities. The potential does not linearly change with time, a behavior typical for pseudocapacitive materials that involve redox reactions.

The specific capacitance of the electrode measured by the galvanostatic discharge method can be calculated as:

$$C = \frac{I\Delta t}{\Delta V m} \quad (13)$$

where C (F/g) is the specific capacitance, I (A) is the constant discharge current, Δt (s) is the discharge time, ΔV (V) is the potential window, and m (g) is the mass of the active material in the electrode. The specific capacitances of the three samples obtained at different current densities are summarized in Figure 56(e). At 0.2 A/g, the specific capacitance is 306 F/g for the pH = 2 sample, 209 F/g for the pH = 4 sample, and 103 F/g for crystalline H_xMnO_2 . With increasing current density, the specific capacitance decreases gradually for all the three samples.

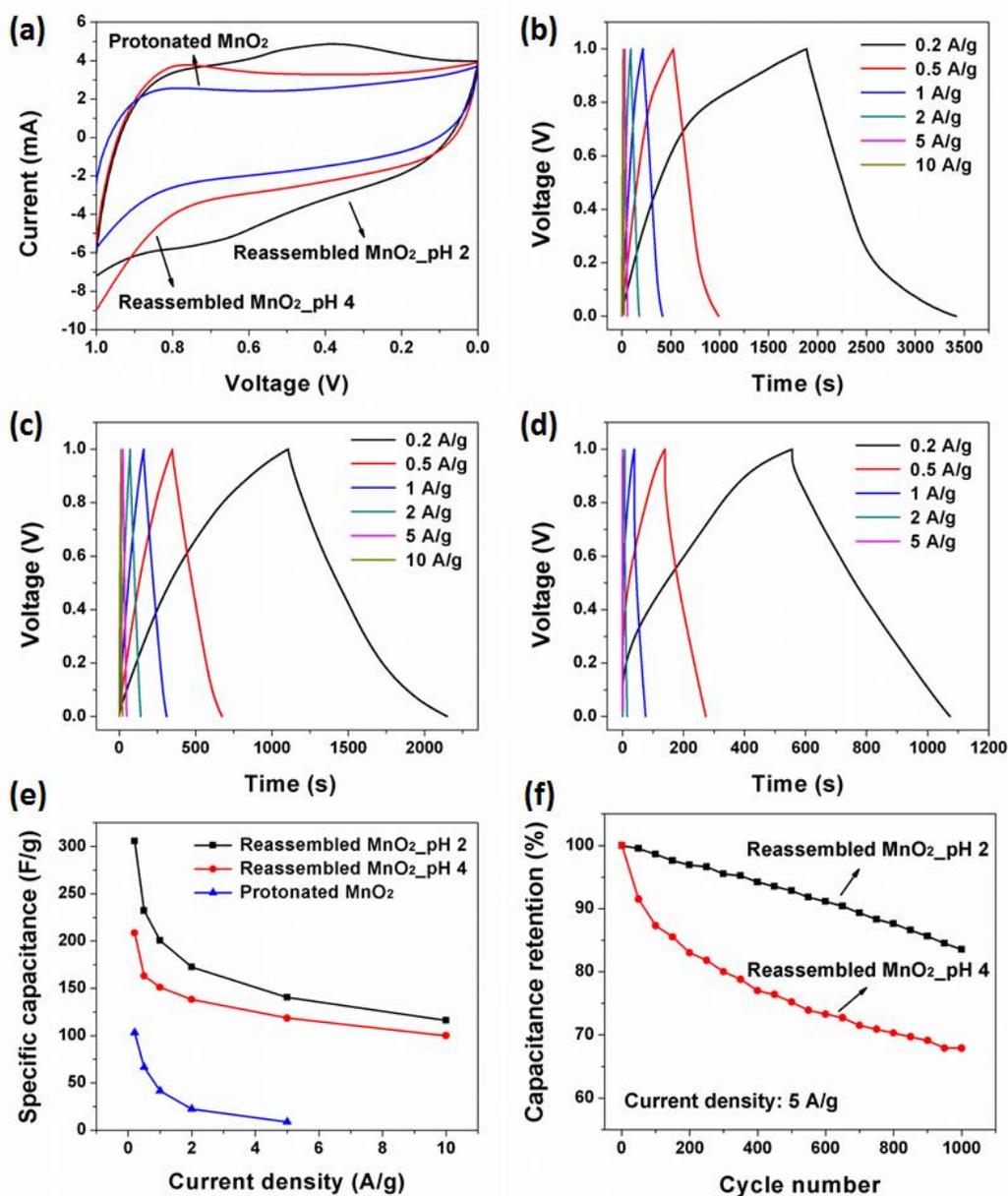


Figure 56. Electrochemical testing results: (a) CV curves for the samples at 50 mV/s scan rate; (b), (c), and (d) galvanostatic charge-discharge curves of the pH = 2, 4 and H_xMnO₂ samples; (e) comparison of specific capacitance for the samples as a function of current density; and (f) cycle stability at constant current density of 5 A/g between 0 and 1 V.

The defect chemistry also has an impact on cycling stability, demonstrated using the pH = 2 and 4 nanosheet assemblies, which is shown in Figure 56(f). After 1000 charge-discharge cycles using a very high current density of 5 A/g (2.5 mA/cm), the pH = 2 sample shows good stability, retaining 83 % of its initial specific capacitance. In

contrast, the pH = 4 sample retains only 68 % of its initial capacitance. Our results are promising when compared to earlier work, for example for MnO₂ nanostructures which retain ~92 % of the initial capacity after 1000 cycles when using a current density 5 times smaller.⁹⁸

Electrochemical impedance spectroscopy (EIS) was employed to measure the charge transfer resistance of each electrode with the results shown in Figure 57(a). All plots exhibit a straight line in the low frequency region and a single semicircle in the high frequency region, indicating a diffusion-limited step in the low frequency region and a charge transfer limited step in the high frequency region.¹⁹⁰ The Nyquist plots were further modeled and interpreted by using an appropriate electrical equivalent circuit, which is shown in the inset in Figure 57(a). R_s is a combined resistance including ionic resistance of the electrolyte, intrinsic resistance of the substrate and contact resistance at the active material/current collector interface. R_{ct} is the charge transfer resistance caused by the Faradaic reaction. Z_w is the Warburg resistance which is related to ion diffusion in the electrolyte, CPE is a constant phase element and C_L is the limit capacitance.¹⁹¹⁻¹⁹³ The calculated charge transfer resistances (R_{ct}) extracted from the high frequency range were 23, 15 and 3 Ω for the H_xMnO₂, pH = 4 and pH = 2 samples, respectively, as shown in Figure 57(b).

Table II summarizes the characteristics of the electrodes and their properties, showing several clear trends. Firstly, the XPS and XANES studies, combined with quantification of surface Frenkel defects, demonstrate that the Mn^{3+/4+} ratio in the nanosheets trends with pH treatment. More specifically, Mn⁴⁺ → Mn³⁺ reduction does not only result in formation of surface Frenkel defects but some of the Mn within the sheets is reduced to the trivalent state. As calculated based on the data in Table 2, approximately 2/3, 1/2, and 1/4 of the Mn ions remaining in the nanosheets are reduced to Mn³⁺ for the pH = 2, 4, and H_xMnO₂ samples, respectively.

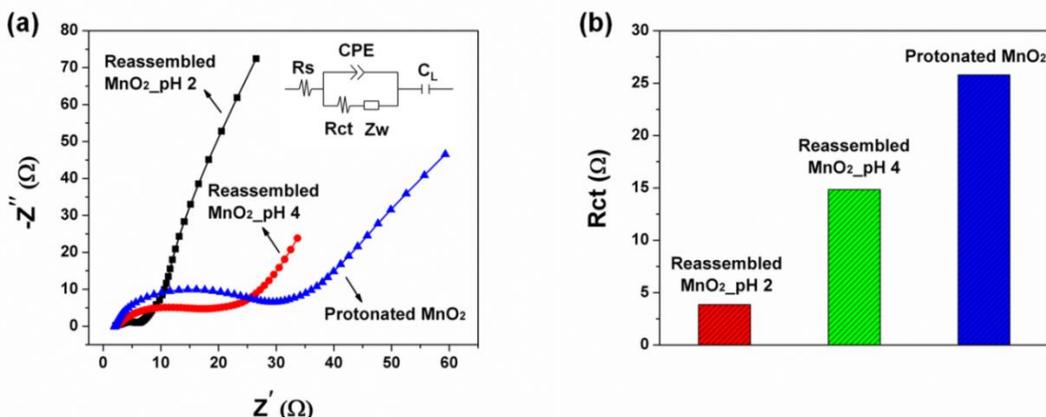


Figure 57. Electrochemical impedance spectroscopy of protonated and reassembled δ - MnO_2 electrodes. (a) Nyquist plots of the samples in the frequency range of 0.1 Hz - 100 kHz at an open circuit potential of 5 mV (inset shows the electrical equivalent circuit used for fitting the impedance spectra); and (b) comparison of the charge transfer resistance among the three samples (values obtained from the fitted data).

It has also been found out that the specific capacitance for the reassembled nanosheets correlates with the surface Frenkel defect population and Mn^{3+} content, as well as charge transfer resistance. For example, the surface areas of the pH = 2 and 4 samples are similar, but the sample treated at pH = 2 has 50 % higher capacitance, 47 % more Na^+ ion intercalation, $\times 5$ smaller charge transfer resistance, with 33 % more surface Frenkel defects, highlighting the importance of the cation defects on Na^+ ion intercalation.

The surface Frenkel defect provides two likely intercalation sites: the Mn ion vacancy, which is accessible from one side of the nanosheet; and the undercoordinated MnO_6 surface octahedron on the opposite side of the nanosheet (Figure 50(a)). In parallel, the defect reaction provides a large concentration of Mn^{3+} cations, which can presumably participate in polaron hopping conduction, thus improving electrical conductivity and charge transfer efficiency.^{2,194} We speculate that there exists some synergistic effect of the defect content and Mn redox that together define the charge transfer resistance and specific capacitance, which may explain the Na^+ ion intercalation mechanism in the defective δ - MnO_2 nanosheets and the improved charge storage properties. The electrochemical cycling behaviors also suggest it is likely that steric effects such as local distortions in the nanosheets around vacancies are active in relieving

electrochemical strains that occur during cycling, and thus define to a large extent the specific capacitance.

Table II. Summary Findings of Defects and Electrochemistry in δ -MnO₂ Electrodes.

Samples	AOS	[Mn ³⁺] (%)	[Mn ⁴⁺] (%)	[V _{Mn}] (%)	S.S.A (m ² /g)	C _p (F/g)	R _{ct} (Ω)	Na:Mn (fract.)
Reassembled MnO ₂ - pH 2	3.24	76	24	26.5	120	306	3	0.28
Reassembled MnO ₂ - pH 4	3.36	64	36	19.9	144	209	15	0.19
Protonated MnO ₂	3.59	41	59	18.3	4.5	103	23	0.09

* Comparison of defect structures and electrochemical supercapacitor properties of bulk protonated H_xMnO₂ and MnO₂ nanosheet assemblies.

2.4 Summary: effects of defects on capacitance

3-D porous nanostructures built from 2-D δ -MnO₂ nanosheets are an environmentally friendly and industrially scalable class of supercapacitor electrode material. While both the electrochemistry and defects of this material have been studied, the role of defects in improving the energy storage density of these materials has not been addressed. In this part of the research work, we have successfully prepared δ -MnO₂ nanosheet assemblies with 150 m²/g specific surface area by exfoliation of crystalline K_xMnO₂ and subsequent reassembly. The flocculation/reassembly processes have been systematically investigated, in order to get desired 3-D porous nanostructures with large surface area. Equilibrating the reassembled nanosheets in varied pH controls the extent of Mn⁴⁺ → Mn³⁺ reduction as well as creating charged defect pairs we term “surface Frenkel defects” comprising a Mn vacancy within the sheet and a six-fold coordinated Mn³⁺ site on the surface of the nanosheet. The XPS and XANES data indicate an increase of the Mn³⁺/Mn⁴⁺ ratio with decreasing pH equilibration values. The X-ray scattering and PDF analysis also shows that the Mn surface Frenkel defect content reaches 26.5 % for the nanosheet assemblies equilibrated at pH = 2 and 19.9 % for the pH = 4 sample, indicating that equilibration at lower pH environment leads to the formation of more Mn vacancies in the reassembled δ -MnO₂ nanostructures.

Different methods of preparing supercapacitor electrodes have been studied and the optimized approach has been obtained by mixing the active material with carbon black and PVDF in a certain mass ratio. The effect of film thickness on the electrochemical performance has also been discussed. The electrochemical results of pH = 2 and 4 equilibrated δ -MnO₂ nanosheet assemblies indicate direct correlation of Mn cation defects with specific capacitance. The specific capacitance increased from about 200 F/g (pH = 4) to over 300 F/g (pH = 2) by intentional introduction of ~30 % surface Frenkel defects, while at the same time the charge transfer resistance decreased from ~15 Ω to ~3 Ω . The presence of more Mn vacancies also leads to improved cycling stability. Therefore, it is now clear that Mn surface Frenkel defects in δ -MnO₂ nanosheets increase Na⁺ ion intercalation by providing new, low energy intercalation sites.

CHAPTER III. INVESTIGATION OF THE CHARGE STORAGE MECHANISMS OF DEFECTIVE δ -MnO₂ NANOSHEETS USED AS SUPERCAPACITOR ELECTRODES

3.1 Introduction

Defective transition metal oxide nanostructures, with large amounts of cation vacancies introduced into the lattice structure either by pH equilibration^{25,134} or by aliovalent cation/anion doping method,^{126,129} has been reported effective in improving their charge storage properties compared with the defect-free oxides. As discussed in Chapter II, the Mn surface Frenkel defect content reaches 26.5 % for the δ -MnO₂ nanosheet assemblies equilibrated at pH = 2 and 19.9 % for the pH = 4 sample, meanwhile the specific capacitance increased from about 200 F/g (pH = 4) to over 300 F/g (pH = 2) by intentional introduction of ~30 % more surface Frenkel defects, and the charge transfer resistance decreased from ~15 Ω to ~3 Ω . Thus the above experimental results clearly demonstrate a correlation between the quantity of defects in our 2-D δ -MnO₂ nanosheet electrode system and the quantity of Na⁺ electrochemically inserted. These correlations unambiguously imply that there is a structural feature of the defective δ -MnO₂ nanosheet that can promote alkali cation intercalation and Faradaic charge storage process. Therefore, understanding this link will help to enable rational design of pseudocapacitive materials with larger specific energy density.

Generally speaking, several techniques, including synchrotron-based X-ray diffraction, X-ray scattering and PDF analysis, X-ray absorption spectroscopy, as well as Raman spectroscopy, are always needed and commonly used as effective tools to probe the local structure variation and oxidation states change during electrochemical cycling. *Ex-situ* measurements of the charge/discharged electrodes or the *in-situ*/operando characterization of the electrodes during electrochemical cycling all shed light on the alkali cation intercalation and charge storage process. Several reported works in recent years have discussed the effects of defects on cation intercalation in certain transition

metal oxide nanostructures used as battery/supercapacitor electrodes, which paves the way for using these advanced techniques to elucidate the charge storage mechanisms.

Bonil *et al*¹²⁴ have prepared hollow iron oxide nanoparticles with very high concentration of cation vacancies. *In-situ* XRD results indicate that the lithium ions are intercalated into octahedral Fe vacancies, leading to slightly enlarged lattice spacing without affecting the overall structure. The *in-situ* XANES measurements demonstrate significantly lower rate of reduction of iron cations as compared to the theoretical one. Thus, the *in-situ* studies reveal that the presence of a large amount of Fe vacancies leads to the intercalation of lithium ions without structural change and reduction of iron cations. Koketsu *et al*¹⁴³ synthesized cation-deficient anatase TiO₂ through aliovalent doping with F. The introduction of titanium vacancies provides a thermodynamically favorable driving force to insert multivalent cations, and act as microstructural voids which can accommodate Mg²⁺/Al³⁺. *Ex-situ* PDF analysis of magnesiated/de-magnesiated electrodes show only slight changes upon electrochemical intercalation, emphasizing a robust host framework undergoes only slight structural changes. The lattice constants obtained at each charge state from the PDF refinements show a negligible variation, indicating “zero-strain” behaviour during repeated cycling and thereby high mechanical stability. Kuo *et al*¹⁸⁵ have designed a three-electrode based electrochemical cell for *in-situ* synchrotron XRD analysis of MnO₂, and they found that the (100) peak shifts toward a lower angle during the cathodic scan, suggesting lattice expansion, and reversibly shifts back to the original position during the anodic scan. Thus they concluded that the observed lattice expansion indicates involvement of intercalation or insertion of cations into the bulk of the oxide structure rather than merely on the surface. Chen *et al*¹⁴¹ investigated the charge storage mechanism of MnO₂ by probing the structural changes using operando Raman spectroscopy, and the band features are quantitatively correlated with the charge states. No new bands were observed, indicating no new phases formed during the electrochemical cycling process. The change of Raman band positions implies the replacement of water molecules with alkali cations, and the decreased band intensity indicates increased local structural disorder. Thus, the local structural variation during electrochemical charge/discharge process can be well related to the change of Raman band features, and leading to a better understanding of the charge storage mechanism.

Last but not trivial, it is necessary to mention that the nature of the electrodes is critical for the X-ray scattering measurements at synchrotron facility. In most published papers, the working electrode is prepared by mixing the active material with carbon black and binder. The useful data from active material can be obtained by subtracting the carbon and binder scattering signals from the total signal. However, this is only workable when the amount of active material is large enough and thus the obtained signal is strong enough for accurate subtraction. In our case, the mass of active material within the incident beam is typically around several micrograms, meaning that the scattering signal from the active material is usually overwhelmed by that from carbon and binder, making it almost impossible to correctly subtract the scattering data from the active materials. Therefore, the preparation of carbon and binder-free electrodes is necessary for the *in-situ* X-ray scattering measurements.

In this chapter, the work includes first developing an electrophoretic deposition (EPD) method to prepare binder-free δ -MnO₂ nanosheet electrodes on various substrates. The deposition conditions have been investigated, in order to get optimized electrochemical response. Next, *ex-situ* Raman spectra, collected on several identical MnO₂ nanosheet electrodes interrupted at different charge states, show increased local structural distortion upon cation intercalation during the cathodic process. The *in-situ* XRD and PDF data, measured using our custom electrochemical cell, demonstrate reversible expansion/contraction of the nanosheet layers upon charge/discharge, as well as unchanged interlayer spacing during cycling (which is also revealed from the Raman spectroscopy). Finally, the *in-situ* XANES spectra clearly shows reversible reduction/oxidation of Mn upon charge/discharge, confirms that the Faradaic redox reaction is a major charge storage mechanism in the defective MnO₂ nanosheet system. However, a slower reduction rate of Mn cations as compared to the theoretical one upon charge has been observed for the MnO₂ nanosheets with higher defect content, implying that a large amount of Mn vacancies in the MnO₂ nanosheets may serve as new intercalation sites for potassium ions intercalation without change of Mn oxidation state.

3.2 Materials and Methods

3.2.1 Chemicals and reagents

Nickel foil (Ni foil, 0.127 mm thickness, 99+% purity), sodium sulfate (Na_2SO_4 , $\geq 99.0\%$ purity), potassium nitrate (KNO_3 , $\geq 99.0\%$ purity), and rubidium sulfate (Rb_2SO_4 , 99.0% purity) were obtained from Alfa Aesar. Absolute ethanol (anhydrous, 200 proof) and nitric acid (HNO_3 , 70 wt.%) solution were purchased from Fisher Scientific. Kapton[®] tape was obtained from Cole-Parmer Instrument Company. Glassy carbon foil (SIGRADUR[®] K, 100 μm thickness, 1 \times 1.5 cm) was purchased from HTW Hochtemperatur-Werkstoffe RmbH Company. All reagents were used as received without further purification.

3.2.2 Preparation of carbon and binder-free MnO_2 nanosheet electrodes by electrophoretic deposition method

The δ - MnO_2 nanosheet floccs were prepared by using the same method shown in Chapter II. In order to obtain the EPD precursor solution, first, the 70 wt.% HNO_3 solution was diluted with DI water to make 1M HNO_3 solution. Then five drops of the diluted 1M HNO_3 solution and 2 mg of the as-prepared δ - MnO_2 nanosheet floccs (reassembled nanosheets, washed and dried) were added into 20 mL absolute ethanol solution in a centrifuge tube. After ultrasonication for 30 min, a brown color suspension was formed, with δ - MnO_2 nanosheet floccs homogeneously dispersed and stable for 1-2 hours. For the EPD substrates, we used Ni foil (commercial, 2 cm \times 1 cm \times 0.127 mm), Au-coated Kapton[®] tape (self-made, 2 cm \times 1 cm \times 0.1 mm), and glassy carbon foil (commercial, 1.5 cm \times 1 cm \times 0.1 mm). The Au-coated Kapton[®] electrode was prepared by sputter-coating a thin layer of Au (Cressington sputter coater, 120 s operating time) onto the folded Kapton[®] tape surface, which forms a conductive path and thus can be used as EPD substrate and supercapacitor electrodes. No pre-treatments are needed when the Au-coated Kapton[®] tape and glassy carbon foil are used as substrates, however, the Ni foil substrate was ultrasonicated in nitric acid solution for 40 min, in order to get a rough surface and thereby facilitate the deposition process.

The typical electrophoretic deposition procedure for preparing the carbon and binder free electrodes can be described as follows. A two-electrode set-up, consisting an above-mentioned substrate (cathode) and a platinum electrode (anode), immersed in the MnO₂ precursor suspension in a small beaker (10 mL capacity) with a distance separation of 1 cm, was employed for the electrophoresis. The EPD was carried out by applying a constant potential of 50 V at room temperature. Various deposition times (2, 4, 6, and 10 min) were employed to study the effect of deposited MnO₂ film thickness on its electrochemical response. Thermal treatment of the deposited films was conducted at 100 °C for 2 h in air immediately following the deposition process.

3.2.3 pH equilibration of the as-deposited MnO₂ nanosheet electrodes and interrupted electrochemical cycling

The surface Frenkel defects were introduced by equilibrating the as-deposited MnO₂ nanosheet electrodes in different pH solutions, instead of equilibrating the nanosheet floccs before the EPD process. This is because the preparation of EPD precursor usually involves addition of certain amount acid under ultrasonication, which may affect the MnO₂ nanosheets' original defect structure. Therefore, in order to avoid such influence, we choose to equilibrate the electrodes after EPD rather than treat the floccs before the deposition. In a typical procedure, the as-deposited MnO₂ nanosheet electrodes were immersed in different pH solutions, with the film on substrate surface totally covered. After 24 h equilibration, the electrodes were rinsed with DI water several times and then dried in air for further use.

After pH equilibration, the as-prepared electrodes were then electrochemically cycled and interrupted at different charge states, for the *ex-situ* Raman measurements detecting local structure variation verses charge states. This was accomplished by using a three-electrode cell. Ag/AgCl and platinum wire were used as the reference and auxiliary electrodes, respectively, with different aqueous electrolyte (Na₂SO₄, KNO₃, and Rb₂SO₄). Three full CV cycles at very low scan rate (1 mV/s) were typically applied to the working electrodes, and then interrupted at different charge states. Finally the *post-situ* charged binder-free electrodes were rinsed with deionized water thoroughly and then dried in air

for *ex-situ* characterization. The overall procedures for making binder-free electrodes, pH equilibration and interrupted cycling can be summarized as follows (Figure 58).

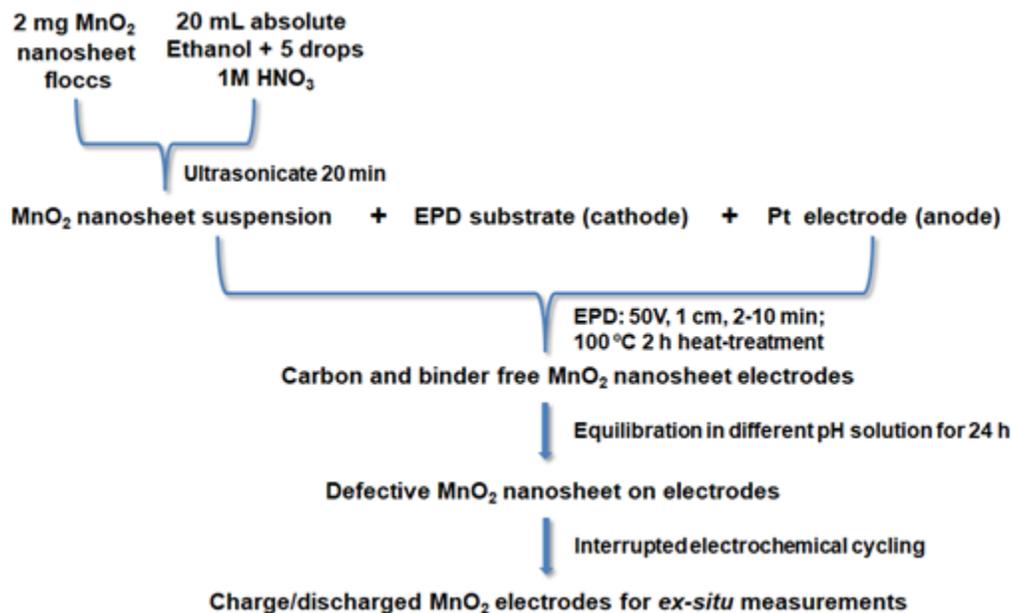


Figure 58. Typical procedures for making binder-free electrodes by EPD method, pH equilibration and interrupted electrochemical cycling.

3.2.4 Characterization of the samples

As-prepared samples were characterized by powder X-ray diffraction (XRD) using a Bruker D8 diffractometer with a Lynxeye detector and Cu K α radiation ($\lambda = 0.15418$ nm) over 5-80° 2 θ range. Microstructures were studied using scanning electron microscopy (SEM, FEI Quanta 200) at 20 kV. Energy dispersive spectroscopy (EDS) was carried out using a FEI EDAX system equipped with a silicon-drift detector.

The *ex-situ* Raman spectroscopy of charge/discharged δ -MnO₂ nanosheet electrodes on glassy carbon electrodes interrupted at different charge states was performed with a confocal Raman microscope WITec Alpha 300 system at room temperature with a 488 nm wavelength incident laser light and a 20 X Zeiss objective. For all the measurements the laser power was set to as low as 40 μ W, in order to make sure no phase transformation of δ -MnO₂ would be induced by high power laser. Typically speaking, all images were constructed by collecting spectra on 50 points from a line scan with 1 μ m step size. The data acquisition at each point was done at integration times of 5 s, along

with 10 accumulations, which has been proven to be sufficient to obtain high quality spectra even the low laser power was used. All data were processed using the WITec Project 5.0 software.

The *in-situ* high energy X-ray diffraction and scattering measurements of the defective δ -MnO₂ nanosheets on glassy carbon electrodes under electrochemical cycling was performed at the beamline 11-ID-B of APS at the Argonne National Laboratory by using our custom electrochemical cell. The detailed description and pictures of the cell can be found in Appendix I. Generally speaking, the cell comprised of 2-part housing which are made from steel plates, sealed with an O-ring and secured together by hex bolts. It contains a top reservoir which accommodates both the reference and counter electrodes, and the two sides in the bottom parts were perforated in order to allow the X-ray beam passes through the cell. Kapton[®] foil was used as the window for the X-ray beam entrance port, and the glassy carbon working electrode acted as the window for the beam exit port which is secured with Kapton[®] tape. The thickness of the electrolyte between the Kapton[®] window and glassy carbon working electrode is ~140 μ m, which is thin enough to minimize the electrolyte scattering effect. The whole cell was designed to be mounted on a kinematic top plate that is available at the beamline and therefore can be controlled to move easily. Data sets were collected in Debye-Scherrer geometry, with Si<311> monochromated primary beam at 58.66 keV, and a silicon flat plate area detector. CeO₂ was used as the calibration standard for detector geometry. The detector-to-sample distance was fixed at 20 cm for collection of proper data for PDF analysis and changed to 95 cm for rapid requisition of the X-ray diffraction pattern. The 2-D X-ray scattering data were integrated to 1-D using FIT2D,¹⁶² after appropriately calibrating detector deviations from orthogonality and masking invalid pixels. Contributions from the cell, the electrolyte, the air and the windows have also been obtained at the same conditions for subtracting the MnO₂ signal. The PDF data was reduced using PDFgetX3,¹⁹⁵ which includes the appropriate corrections for inelastic scattering and energy-dependent detector response, in addition to experimental background and absorption corrections, amongst others.

The *in-situ* X-ray absorption near edge spectroscopy (XANES) measurements were carried out at the beamline C1 at the Cornell High Energy Synchrotron Source (CHESS)

using the same custom electrochemical cell as described above. The glassy carbon foils were used as electrode substrates for the measurements. All spectra were collected at room temperature in transmission mode, and calibrated using the spectrum of Mn metal foil. Commercially available manganese oxides (MnO, Mn₃O₄, LiMn₂O₄ and MnO₂) were also measured as standards and used to extract the linear relationship between the K-edge energy and Mn oxidation state. The software package PyMca and ATHENA has been used for data analysis. The absorption edge energies were taken as the half-height of the edge step for all samples.

3.2.5 Electrochemical measurements

The electrophoretic deposited δ -MnO₂ nanosheets on Ni foils, Au-coated Kapton[®] tapes and glassy carbon foils were used as working electrodes. The loading of the active material on the working electrode was typically controlled in the range of 0.4-0.5 mg/cm². The capacitive performance was measured using a CHI 650E electrochemical analyzer (CHI, USA) with a conventional three-electrode cell. Ag/AgCl and platinum wire were used as the reference and auxiliary electrodes, respectively, with 2 M KNO₃, (or 1 M Na₂SO₄, 1 M Rb₂SO₄) aqueous electrolyte. Cyclic voltammetry scans were carried out from 0 to 0.8 V at various scan rates. Galvanostatic charge-discharge was also measured from 0 to 0.8 V at different constant current densities.

In order to prepare the electrodes electrochemically cycled and interrupted at different charge states for *ex-situ* characterization, cyclic voltammetry scans in the voltage range from 0.8 (fully discharged) to 0 V (fully charged) were used to charge the δ -MnO₂ nanosheets. Slow scan rate of 1 mV/s was applied, which will enable intercalation of alkali cations as much as possible. Three full consecutive CV cycles (scanned from 0.8 to 0 V, then back to 0.8 V) were applied to the working electrodes, and then stopped at 0.8, 0.4 and 0 V in the fourth CV loop which represent the fully-discharged, half-charged (discharged) and fully-charged states. The cathodic scan from 0.8 to 0 V represents charging the electrodes and the anodic scan from 0 to 0.8 V represents discharging the electrodes. The charge/discharged electrodes were then washed with deionized water thoroughly and finally dried in air for the *ex-situ* characterization. For the *in-situ* measurements, same electrochemical cycling conditions

were applied, except that the custom electrochemical cell has been used, which can fit into the beamline and enable simultaneous detection of structure variation or Mn oxidation state change upon cycling.

3.3 Results and discussion

3.3.1 Investigation of the electrophoretic deposition process to make carbon and binder free δ -MnO₂ nanosheet electrodes

As discussed in the Introduction, the preparation of carbon and binder-free electrodes is necessary for the *in-situ* X-ray scattering measurements, in order to correctly subtract the scattering data from the active materials. The first step we have tried is by using the “drop-casting” method, which is a simple way to make working electrodes. However, as discussed in Chapter 2.3.7, the as-prepared electrodes typically exhibit inferior electrochemical response along with small specific capacitance, thus leading to the conclusion that the “drop-casting” is not an appropriate way to make binder-free electrodes.

Another commonly used approach to make the binder-free electrodes is “electrophoretic deposition,” which has been reported effective in making electrodes that could achieve good electrochemical response.¹⁹⁶⁻²⁰⁰ In the EPD process, absolute ethanol was used as the electrolyte, in order to prevent hydrolysis under high applied voltage (50 V). 1 M HNO₃ was added to tune the charge on the MnO₂ flocs and increase the conductivity of the suspension. Ni foil, gold-coated Kapton[®] and glassy carbon foil were used as substrates. The optimal deposition condition was obtained by varying the amount of MnO₂ flocs in suspension, the pH, deposition voltage, substrate-electrode distance, and time, with the optimized values specified in Chapter 3.2.2.

The photo images shown in Figure 59 indicate that the MnO₂ nanosheet assemblies can be successfully deposited onto several substrates (Ni foil, Au-coated Kapton[®] tape, and glassy carbon foil), which confirm the effectiveness and versatility of the EPD process we have developed. The dark brown film on the bottom represents the deposited MnO₂ nanosheet assemblies, which are uniformly covered on the surface of different substrates. It was also found that the film stick very well to all substrates, with no film detachment observed after repeated washing and electrochemical cycling, demonstrating good attachment and contact between the deposited film and substrates. Figure 60(a) shows the cross-section of the MnO₂ nanosheet assembly on Ni foil substrate, indicating a uniform thickness of ~10 μ m. The typical morphology shown in Figure 60(b)

demonstrates that the porous structure of MnO₂ nanosheet assemblies can be well maintained throughout the EPD process. Thus, the SEM images further confirm the success of employing EPD method to prepare binder-free MnO₂ nanosheet electrodes without destroying their porous nanostructures.

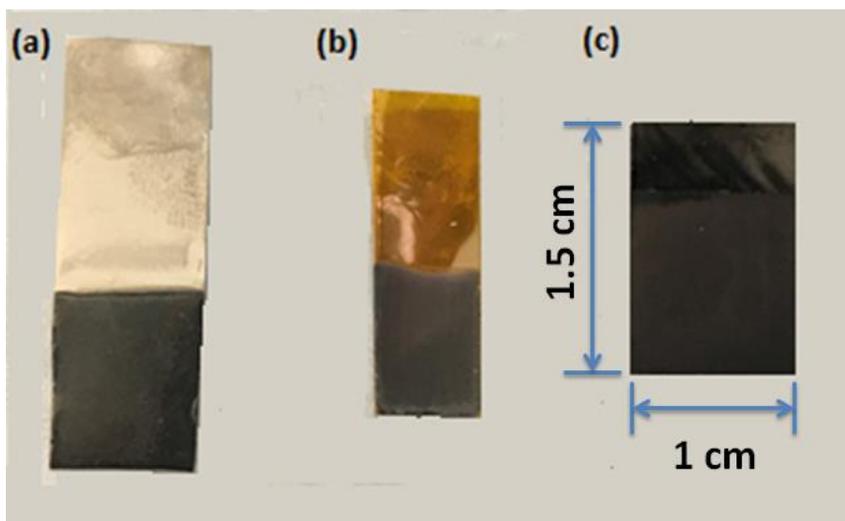


Figure 59. Photographs of the δ -MnO₂ nanosheet assemblies on different substrates prepared by electrophoretic deposition (EPD). (a) Ni foil, (b) Au-coated Kapton[®], and (c) glassy carbon foil.

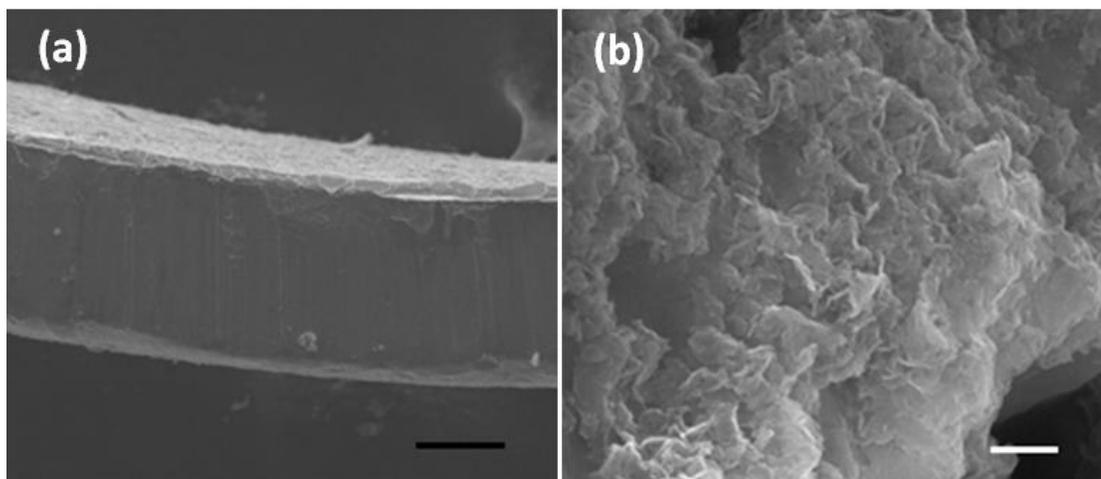


Figure 60. (a) Cross-sectional image of the MnO₂ nanosheet assemblies on Ni foil substrate prepared by EPD; (b) typical SEM morphology of MnO₂ nanosheets on substrates prepared by EPD. Scale bar, 50 μ m (a), 500 nm (b).

We have further investigated the effects of deposition time on the MnO_2 film's morphology and electrochemical response. With fixed deposition area, the mass loading and film thickness are directly proportional to the deposition time. Therefore, the longer deposition time employed, the more MnO_2 nanosheet floccs can be deposited onto the substrate surface and the thicker film will be obtained. In our experiments, 2, 4, 6, and 10 min deposition time are used for investigation, with the deposition area fixed at 1 cm^2 , the applied voltage fixed at 50 V, and the two electrodes distance fixed at 1 cm. The amount of deposited MnO_2 was determined by comparing the mass difference of the substrate before and after EPD process. Our results show that the mass loadings of MnO_2 are 0.2, 0.4, 0.6 and 1.0 mg corresponding to 2, 4, 6, and 10 min deposition time, further confirms that longer deposition time leads to higher mass loading and thereby thicker films on the substrates.

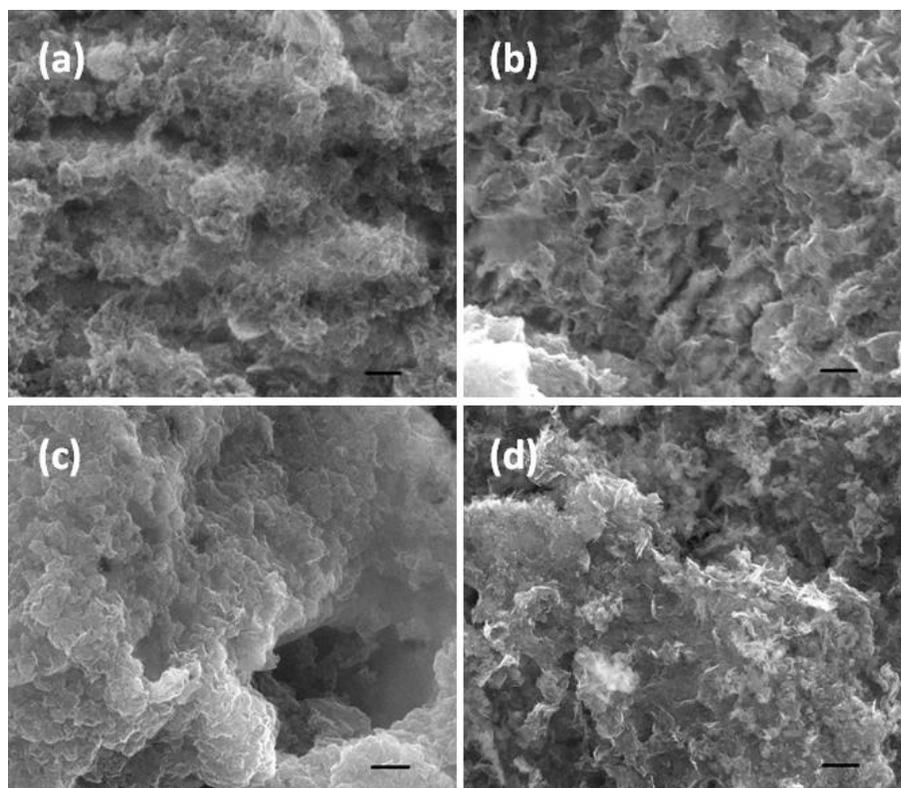


Figure 61. Typical SEM images of MnO_2 nanosheet assemblies on Ni foil substrate prepared by EPD with different deposition time (mass loading). (a) 2 min (0.2 mg), (b) 4 min (0.4 mg), (c) 6 min (0.6 mg), and (d) 10 min (1.0 mg). Scale bar, 200 nm (a), $1 \mu\text{m}$ (b-d).

The typical SEM images of MnO₂ nanosheet assemblies on Ni foil substrates prepared by EPD with different deposition time are shown in Figure 61. Clearly it can be seen that the porous nanostructures of MnO₂ nanosheet assemblies can be well maintained for all the four electrodes, indicating that the different deposition time has almost no influence on the deposited films' morphology. Further evaluation of their specific capacitance was obtained by galvanostatic charge-discharge measurements (0.2 A/g applied current density), with the results shown in Figure 62. A clear trend can be observed. With decreasing the mass loading, the specific capacitance increased from ~100 F/g (1 mg/cm² loading) to over 300 F/g (0.2 mg/cm² loading). Since all electrodes exhibit similar surface morphologies, the dramatic difference of the specific capacitance can be attributed to their different film thickness. Because of the poor electrical conductivity of MnO₂, thinner films usually exhibit faster electron charge transfer processes, thus leading to much enhanced charge storage properties.

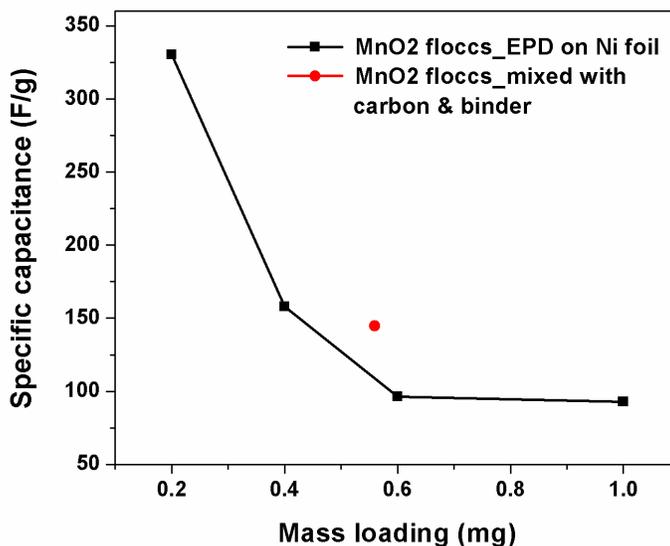


Figure 62. Specific capacitances of the EPD prepared binder-free MnO₂ nanosheet electrodes on Ni foil substrates with different deposition time. The capacitance of MnO₂ nanosheet floccs measured by mixing with carbon black and binder is also included for ease comparison. The galvanostatic charge-discharge measurements have been used to measure the specific capacitance for all samples at 0.2 A/g current density.

We have also compared the specific capacitance of MnO₂ nanosheet floccs prepared by EPD and commonly used method (mixed with carbon black and binder). As shown in

Figure 62, the electrodes prepared using EPD have capacitance comparable to electrodes prepared with binder and carbon. This result further confirms that the electrophoretic deposition we have developed can be used as an effective and facile method to prepare carbon- and binder-free electrodes on various substrates without deteriorate their electrochemical response.

As shown in Figure 62 and discussed above, with decreasing the mass loading of MnO_2 nanosheet on substrate (i.e. decrease the deposition time), much higher capacitance can be achieved. So from the charge storage perspective, smaller mass loading would be a better option when making the EPD electrodes. However, when considering the X-ray scattering experiments, the more samples we put in the X-ray beam, the stronger signals from MnO_2 can be obtained. Thus, higher mass loading is preferred in this case. Therefore, as a tradeoff of the electrochemical performance and the X-ray scattering experiments, the electrodes are typically prepared with $0.4\text{-}0.5\text{ mg/cm}^2$ mass loading, which shows not only good electrochemical response but also strong enough scattering signals that can be used to detect local structure variations.

3.3.2 Characterization of the EPD prepared binder-free electrodes charge/discharged with different electrolytes

Electrochemical cycling of the EPD prepared binder-free electrodes in different electrolytes (Na^+ , K^+ and Rb^+) was undertaken, in order to determine if the electrochemical behavior of the heavier cations was similar to that of Na^+ ion cycling. The goal was selection of a stronger X-ray scatterer than Na^+ , which is the typical electrolyte cation we used in our previous electrochemical measurements. In order to keep the same ionic strength, $1\text{M Na}_2\text{SO}_4$, 2M KNO_3 and $1\text{M Rb}_2\text{SO}_4$ aqueous solutions have been used as the electrolytes. Several identical electrodes have been prepared on Ni foil substrates by EPD method, which was then cycled in above mentioned electrolytes by cyclic voltammetry to compare their electrochemical response.

The typical cyclic voltammetry curves of EPD prepared MnO_2 nanosheet electrodes cycled in $1\text{M Na}_2\text{SO}_4$, 2M KNO_3 and $1\text{M Rb}_2\text{SO}_4$ electrolytes at 10 mV/s scan rate are shown in Figure 63. Clearly it can be seen that the CV curves for electrodes cycled in Na_2SO_4 and KNO_3 electrolytes (Figure 63(a) and (b)) exhibit similar quasi-rectangular

shapes in the potential window from 0 to 1 V, which indicates capacitive behavior. The presence of broad redox peaks in both CV curves indicate that the intercalation pseudocapacitive charge storage process occurred when both ions (Na^+ and K^+) are used as electrolytes. Similar CV curve enclosed area also demonstrates similar capacitance that can be achieved with both electrolytes. Thus the above results show that K^+ ion can be used as an alternative electrolyte to replace Na^+ ion, giving rise to the same charge storage process and similar capacitance.

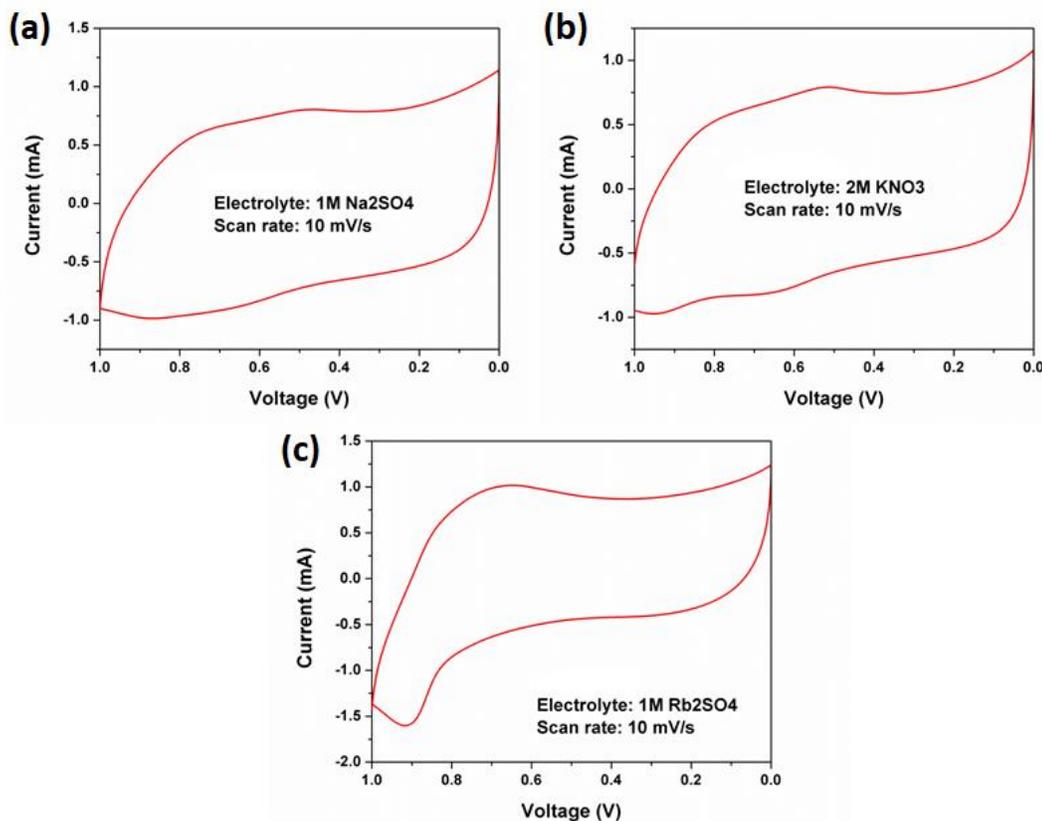


Figure 63. CV comparison of the EPD prepared MnO_2 nanosheet electrodes cycled in (a) 1M Na_2SO_4 , (b) 2M KNO_3 , and (c) 1M Rb_2SO_4 electrolytes at 10 mV/s scan rate.

In contrast, when 1M Rb_2SO_4 was used as the electrolyte, a different CV curve shape (Figure 63(c)) has been observed compared with the electrodes cycled in Na_2SO_4 and KNO_3 electrolytes. A broad peak in the potential range from 0.8 to 1 V during anodic scan has been observed, and its origin cannot be identified. The absence of clear redox peaks in the potential range from 0 to 0.8 V implies that the electrodes are charged and

discharged at a pseudo-constant rate, without apparent pseudocapacitive reaction observed. Thus, different charge storage process may present when Rb^+ ion was used as electrolyte. The above results clearly show that the EPD prepared electrodes only exhibit normal and similar electrochemical behavior when using Na^+ and K^+ ions as charge carriers, therefore we chose the K^+ ion as the electrolyte cation for the experiments.

Further characterization of the EPD prepared MnO_2 nanosheet electrodes that are fully charged/discharged with K^+ ions has been performed, in order to elucidate the morphology change and amount of potassium ions intercalated during charging process. A typical SEM image of MnO_2 nanosheet floccs electrophoretically deposited on Ni foil substrate that is fully charged with potassium ions at 1 mV/s scan rate is shown in Figure 64. Compared with the uncharged ones (shown in Figure 61), no apparent morphology difference is observed. The porous nanostructures are still well maintained, without obvious agglomeration or detachment of the nanosheets from the substrate, indicating that electrochemical cycling at very slow scan rate has little effect on the morphology of deposited MnO_2 nanosheet assemblies.

Energy dispersive spectra of MnO_2 nanosheet floccs deposited on Ni foil substrate that are fully charged/discharged with potassium ions were also obtained, with the results shown in Figure 65. For the fully charged sample, the potassium peaks can be clearly observed, which confirms the intercalation of K^+ ions during the charge process. When the electrode was fully discharged, the significantly decreased potassium peak intensity indicates de-intercalation of K^+ ions during the discharge process. The K^+ content estimated from the EDS results are ~15.2 % and ~4.6 % corresponding to fully charged and fully discharged samples. The presence of small amount of K^+ in the fully discharged sample indicates that not all of the K^+ ions are able to de-intercalate from the MnO_2 nanosheet during the discharge process at 1 mV/s scan rate. In general, the above EDS results demonstrate that the potassium ions can be intercalated into the electrodes during the charge process, which further confirms the effectiveness of the EPD method we have developed to make the binder-free supercapacitor electrodes.

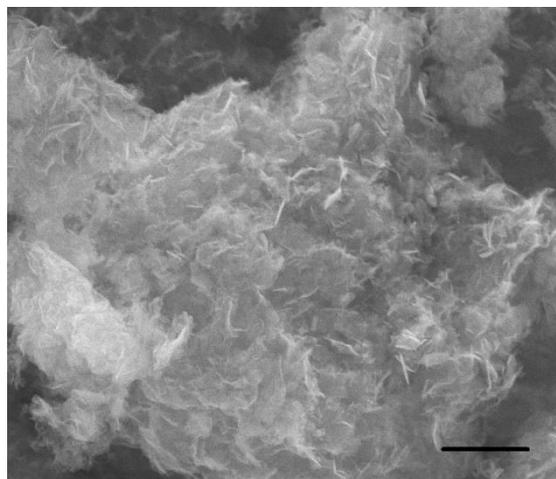


Figure 64. Typical SEM image of MnO₂ nanosheet floccs electrophoretic deposited on the Ni foil substrate and fully charged with potassium ions at 1 mV/s scan rate. Scale bar, 1 μ m.

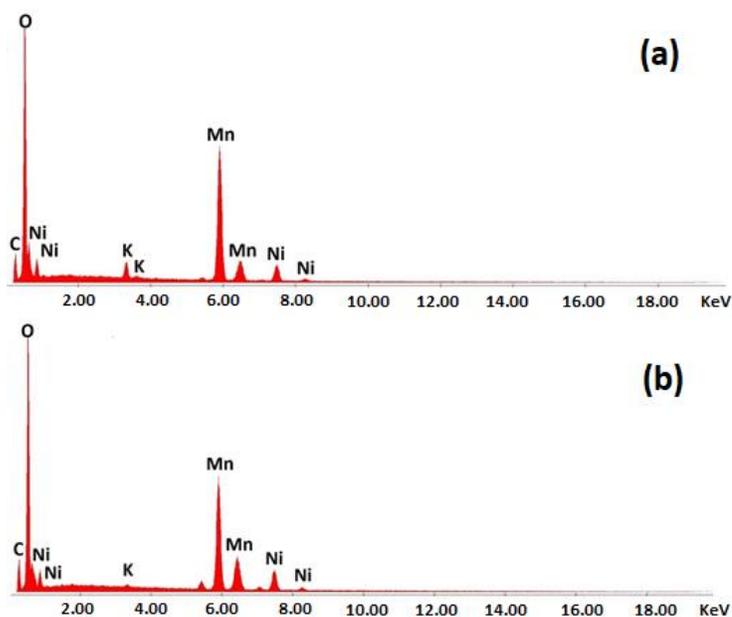


Figure 65. Energy dispersive spectra of the MnO₂ nanosheet floccs electrophoretic deposited on Ni foil substrate (a) fully charged and (b) fully discharged with potassium ions.

3.3.3 Electrochemical comparison of the EPD prepared δ -MnO₂ nanosheet electrodes that are equilibrated in different pH environment

As discussed in section 3.2.3, the involvement of acid during the preparation of the EPD precursor may affect the MnO₂ nanosheets' defect structure. In order to avoid the potential influence, the surface Frenkel defects were introduced by equilibrating the as-

deposited MnO₂ nanosheet electrodes in different pH solutions, instead of equilibrating the nanosheet floccs before the EPD process. The effects of different equilibrating acids, the different equilibration time, and different equilibrating pH values on the film's stability and electrode's electrochemical performance will be described below. All electrodes investigated were prepared using Au-coated Kapton[®] substrate.

First, we have tried to equilibrate the MnO₂ electrodes in pH = 2 and 4 solutions for 24 h, with the pH values adjusted by different acids (HNO₃, H₂SO₄ and HCl). It was found that when HCl was used to adjust the solution pH, the films show no signs of detachment or dissolution after equilibration at both pH values and stick well to the substrate. However, when H₂SO₄ and HNO₃ were used for pH treatment, only equilibration at pH = 4 leads to intact films, whereas equilibration at pH = 2 for 24 h results in detachment of the MnO₂ floccs from the substrates. The above results indicate that HCl would be appropriate to adjust the pH values, since it shows no influence on the film's stability on substrates.

The effects of different equilibration times at pH = 2 on the electrodes' charge storage properties have also been investigated. Figure 66(a) exhibits the CV curves comparison of MnO₂ nanosheet floccs equilibrated at pH = 2 for 8, 16 and 24 h, and the calculated capacitances are shown in Figure 66(b). Clearly it can be seen that with increasing the equilibration time from 8 to 24 hours, the specific capacitance increased from ~90 F/g to ~170 F/g. This could be explained by the fact that longer exposure to the acid environment leads to increased proton sorption at the MnO₂ surface, which expels more in-plane Mn and leading to the formation of more Mn vacancies. The formation of more surface Frenkel defects will thus promote alkali cation intercalation and the charge transfer process,²⁵ as discussed in Chapter II, which results in better electrochemical response. The above results also indicate that 24 h equilibration time is appropriate to introduce large quantity of Frenkel defects into the MnO₂ nanosheets on binder-free electrodes, thereby leading to optimized electrochemical charge storage properties.

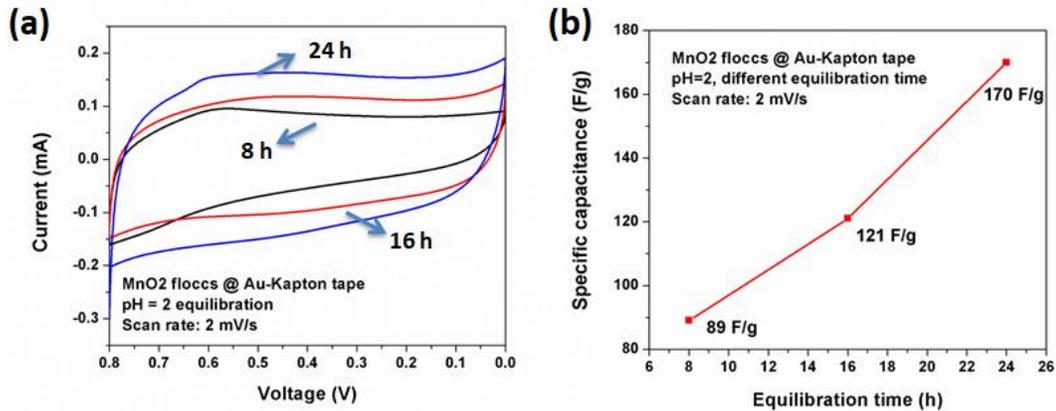


Figure 66. (a) Typical CV curves and (b) specific capacitance comparison of MnO₂ nanosheet floccs deposited on Au-coated Kapton[®] tapes and equilibrated at pH = 2 for different hours.

Finally, we have compared the specific capacitance of the EPD prepared binder-free MnO₂ nanosheet electrodes equilibrated in different pH solutions. The typical CV curves of MnO₂ nanosheet floccs deposited on Au-coated Kapton[®] tapes and equilibrated at pH = 2 & 4 solutions are shown in Figure 67(a-b), with the calculated specific capacitances shown in Figure 67(c). It is shown that at 2 mV/s scan rate, the specific capacitance is 162 F/g for the pH = 2 equilibrated electrode, and is 114 F/g for the pH = 4 treated electrode. Thus the pH = 2 sample exhibits 42 % higher capacitance than the pH = 4 sample, which is consistent with the results obtained by directly equilibrating the MnO₂ nanosheet floccs in different pH environment (as shown in Chapter II, the sample treated at pH = 2 has 50 % higher capacitance than the sample treated at pH = 4. The electrodes are prepared by mixing the active materials with carbon black and binder), and thus confirms that equilibrating the EPD prepared binder-free MnO₂ nanosheet electrodes in lower pH solution can also introduces more surface Frenkel defects and thereby enhanced charge storage properties.

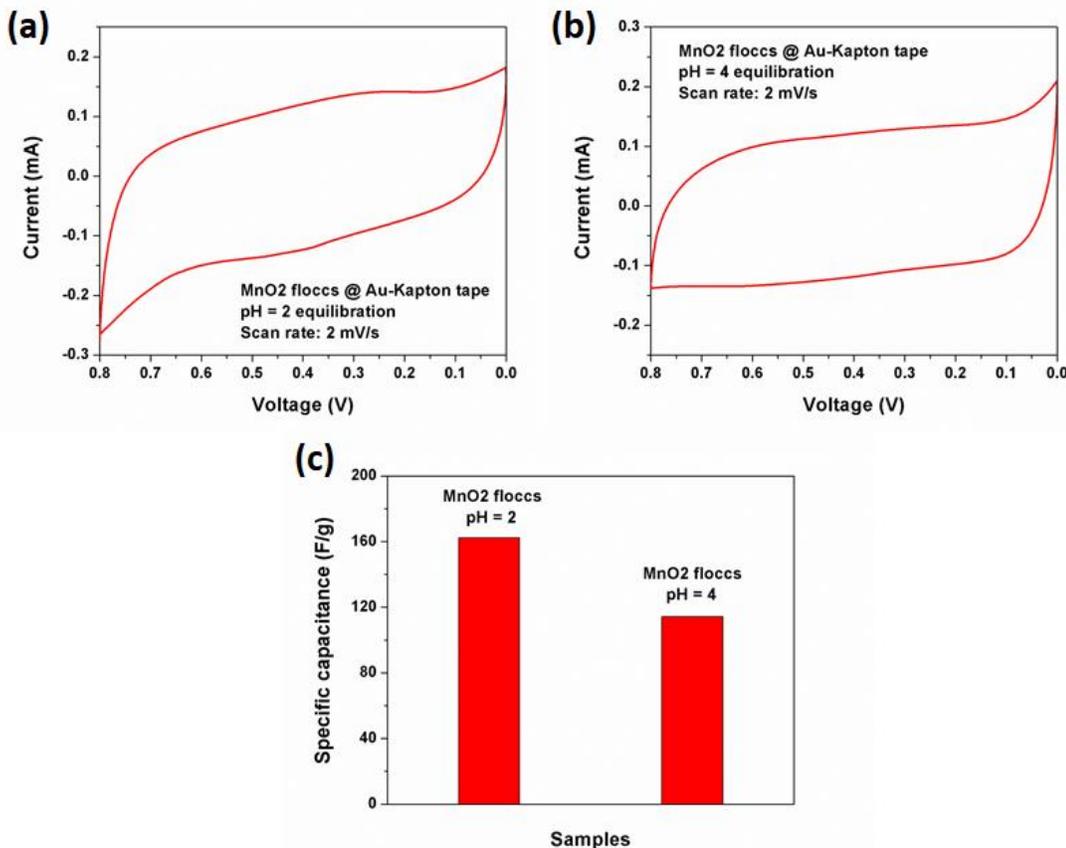


Figure 67. Typical CV curves of the MnO₂ nanosheet floccs deposited on Au-coated Kapton[®] tapes and equilibrated at (a) pH = 2, and (b) pH = 4 solution for 24 h. (c) Specific capacitance comparison of the two samples.

3.3.4 *Ex-situ* Raman spectroscopy of charge/discharged δ -MnO₂ nanosheet electrodes equilibrated in different pH environment

The charge storage mechanism of defective δ -MnO₂ nanosheets were first probed by *ex-situ* Raman spectroscopy, which can provide valuable information on local structural variation upon charge/discharge, and has been successfully applied to investigate the structural changes of MnO₂ in many recent studies.^{141,201,202} Since the spectral features (such as band position and intensity) are closely correlated with the local environment, thus it can be predicted that the potassium ions intercalation/sorption during the charge process will lead to varied local structures and consequently different Raman spectra, which can help get a better understanding of the cation incorporation mechanism into the interlayers of δ -MnO₂ nanosheets.

Figure 68 shows the typical Raman spectra of δ -MnO₂ nanosheet floccs deposited on glassy carbon foils, equilibrated at pH = 2 and 4 solution for 24 h and then interrupted at different charge states (fully discharged, half discharged and fully charged) during electrochemical cycling. It can be clearly seen that two major Raman bands (labelled as ν_1 and ν_2) within 500-700 cm⁻¹ are observed for all samples, which belong to the intrinsic vibrational modes of MnO₂. According to Julien *et al.*,²⁰³⁻²⁰⁵ the ν_1 band (620 – 650 cm⁻¹) was assigned to the symmetric stretching vibration of Mn-O bond in the MnO₆ octahedral, whereas the ν_2 band (570 – 590 cm⁻¹) was considered as the Mn-O vibration in the basal plane of [MnO₆] sheets in δ -MnO₂. Typical Raman scattering spectra of various MnO₂ polymorphs are also shown in Figure 69 for comparison with our data. The properties of both bands are sensitive to the intercalated species during the charge process (the intercalated alkali cations are usually absorbed onto the nanosheet surface, which affect the ν_1 band; the intercalation process is also accompanied with reduction of Mn⁴⁺ to Mn³⁺, thus may influence the in-plane Mn-O vibration mode), which offers the possibility to investigate the cation incorporation mechanism from the effects of electrochemical charging on Raman spectra.

Based on the spectra shown in Figure 68 (a) and (b), several clear trends and changes in spectroscopic features can be observed for both samples. First, no new bands were observed, indicating that no new phases were generated during the charge process. This is in agreement with previous operando Raman studies.¹⁴¹ Second, with increasing charge states, the ν_1 band was broadened gradually, which can be ascribed to the increased Jahn-Teller distortion upon cation intercalation during the cathodic process with the formation of more Mn³⁺,^{206,207} and may also be due to the formation of more Mn surface Frenkel defects that leads to more distorted local structures. The ν_1 band corresponds to the symmetric stretching vibration of Mn-O bond in the MnO₆ octahedra, which is very likely to be affected by the interlayer species and therefore becomes smeared during the charge process with the incorporation of large amount of potassium ions. It was also observed that the band broadening effect with increasing charge states is more pronounced in pH = 2 equilibrated MnO₂ nanosheets, compared with the pH = 4 treated samples. This could be attributed to its more defective structure, which leading to the incorporation of more potassium ions and the formation of more Mn³⁺, and thereby a

more distorted local structures when charging. Third, the positions of ν_2 band experienced no apparent shift during the cathodic process for both samples. Based on the empirical fact that the ν_2 band has negative correlation with interlayer spacing, the unchanged position of this band indicates that the incorporation of potassium ions during the charge process in the defective δ -MnO₂ nanosheets may have little influence on the interlayer distance. However, the *in-situ* or operando Raman measurements are still needed to unambiguously correlate the structural variation with different charge states.

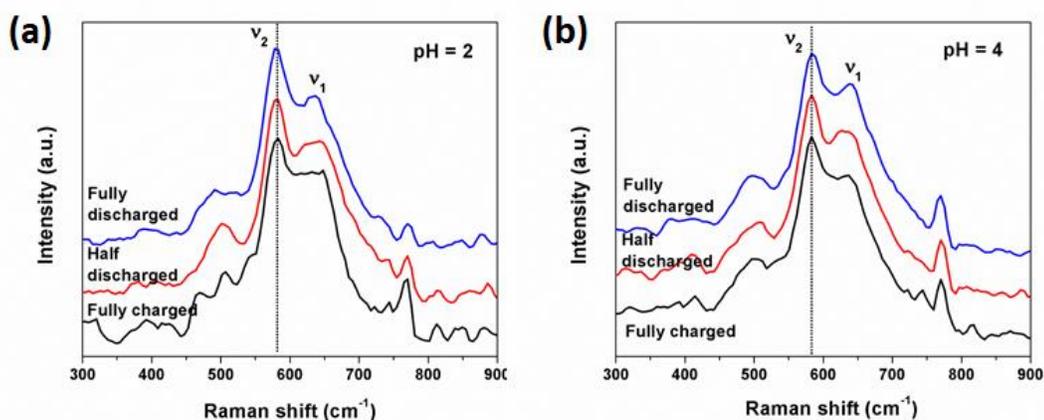


Figure 68. *Ex-situ* Raman spectroscopy of the MnO₂ nanosheet floccs deposited on glassy carbon foils, equilibrated at (a) pH = 2, and (b) pH = 4 solution for 24 h and interrupted at different charge states during electrochemical cycling.

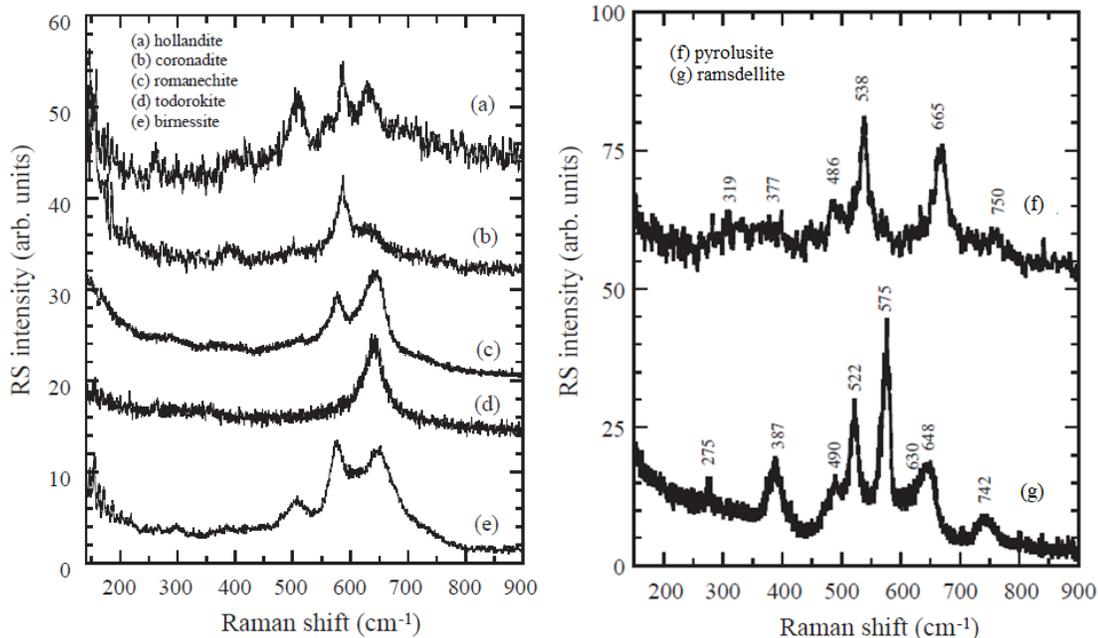


Figure 69. Raman scattering spectra of (a) hollandite MnO_2 , (b) coronadite MnO_2 , (c) romanechite MnO_2 , (d) todorokite MnO_2 , (e) birnessite MnO_2 , (f) pyrolusite MnO_2 , and (g) ramsdellite MnO_2 . From Julien, *et al.*²⁰⁵

3.3.5 *In-situ* XANES spectroscopy of $\delta\text{-MnO}_2$ nanosheet electrodes equilibrated in different pH environment

In order to unambiguously correlate the Mn oxidation states to different charge states, we have performed *in-situ* XANES measurements at beamline C1 at Cornell High Energy Synchrotron Source (CHESS, Cornell University) using our custom electrochemical cell. Three full consecutive CV cycles at 1 mV/s scan rate were applied to the working electrodes, and then stopped at 0.8 and 0 V (representing fully discharged and fully charged states) for XANES data collection. Figure 70(a) shows the XANES spectra of standard materials including MnO , Mn_3O_4 , LiMn_2O_4 and MnO_2 , and a linear relationship between their K-edge energy and Mn oxidation state has been plotted in Figure 70(b). This linear fitting was used to determine the oxidation states of Mn in the nanosheet electrodes upon charge/discharge based on their absorption edge.

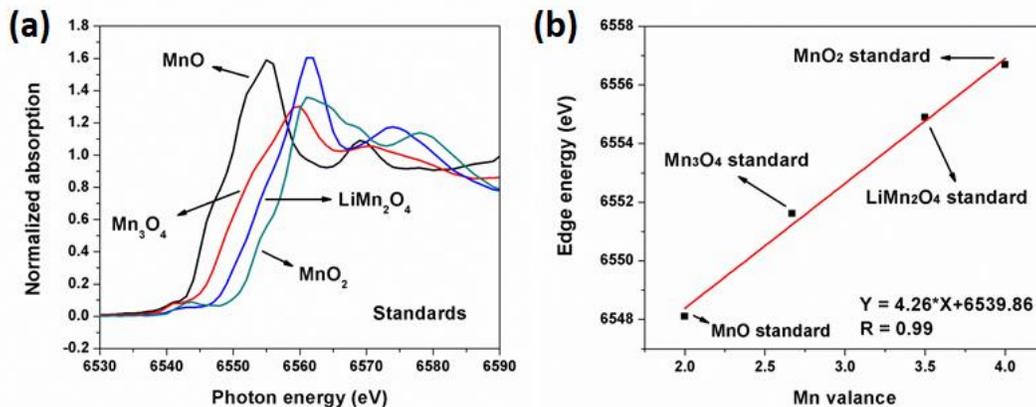


Figure 70. (a) XANES spectra of reference materials MnO, Mn₃O₄, LiMn₂O₄ and MnO₂. (b) Relationship between K-edge energy and Mn oxidation state (standards) for determining oxidation state of Mn in the samples.

The pH = 2, 4 and 9 treated δ -MnO₂ nanosheet on glassy carbon electrodes were studied via *in-situ* XANES measurements at fully discharged and fully charged states in two consecutive CV cycles, with the obtained spectra shown in Figure 71 (a, c, and e). Each spectrum was obtained by averaging nine independently measured spectra at two different spots on the MnO₂ nanosheet surface. The *in-situ* spectra showed that all MnO₂ nanosheets exhibit same XANES features compared to the pH = 2 and 4 equilibrated MnO₂ powders (data shown in Figure 48), indicating similar structural characteristics of Mn under different pH equilibrations and various applied potentials. However, a definitive shift of the absorption edge to lower energies has been observed for all the three samples when decreasing the applied potentials (charging the MnO₂ electrodes). The shifting of the absorption edge to a lower energy is related to a decrease in binding energy of the core electrons due to a decreasing oxidation state, thus representing the K⁺ intercalation Faradaic redox reaction as shown in Equation (9), as well as the formation of Mn³⁺. It is also observed that when re-discharging the electrode, the absorption edge of the XANES spectra moves back to almost the same position for all three samples, indicating high reversibility of the Faradaic redox reaction and K⁺ intercalation process. The observed decrease of Mn oxidation states when charging the electrode is consistent with most literature, and confirms that the Faradaic redox reaction is the main charge storage mechanism in the defective MnO₂ nanosheet system.

In order to further investigate the effect of defects on the charge storage process, we have plotted the variation of the Mn oxidation state upon charging for all three samples, and compared the trend obtained from XANES data to the values expected from the CV loop, with the results shown in Figure 71 (b, d, and f) and Figure 72. The EC calculated data is plotted based on the assumption that the potassium ion insertion is accompanied with the reduction of one Mn ion, and the value is calculated from the specific capacitance (determined from the CV loop). First, it can be clearly seen that with decreasing the pH equilibration value, the change of Mn oxidation state obtained from XANES data becomes more pronounced, indicating that more Mn^{4+} has been reduced to Mn^{3+} with the presence of more surface Frenkel defects. This is likely because the defects can help promote the ion intercalation and charge transfer process, thus facilitating the Faradaic redox reactions and reduction of Mn. This is also consistent with our previous results shown in Chapter II and further confirms that the Mn surface Frenkel defects in $\delta\text{-MnO}_2$ nanosheets can help increase the alkali cation intercalation properties.²⁵

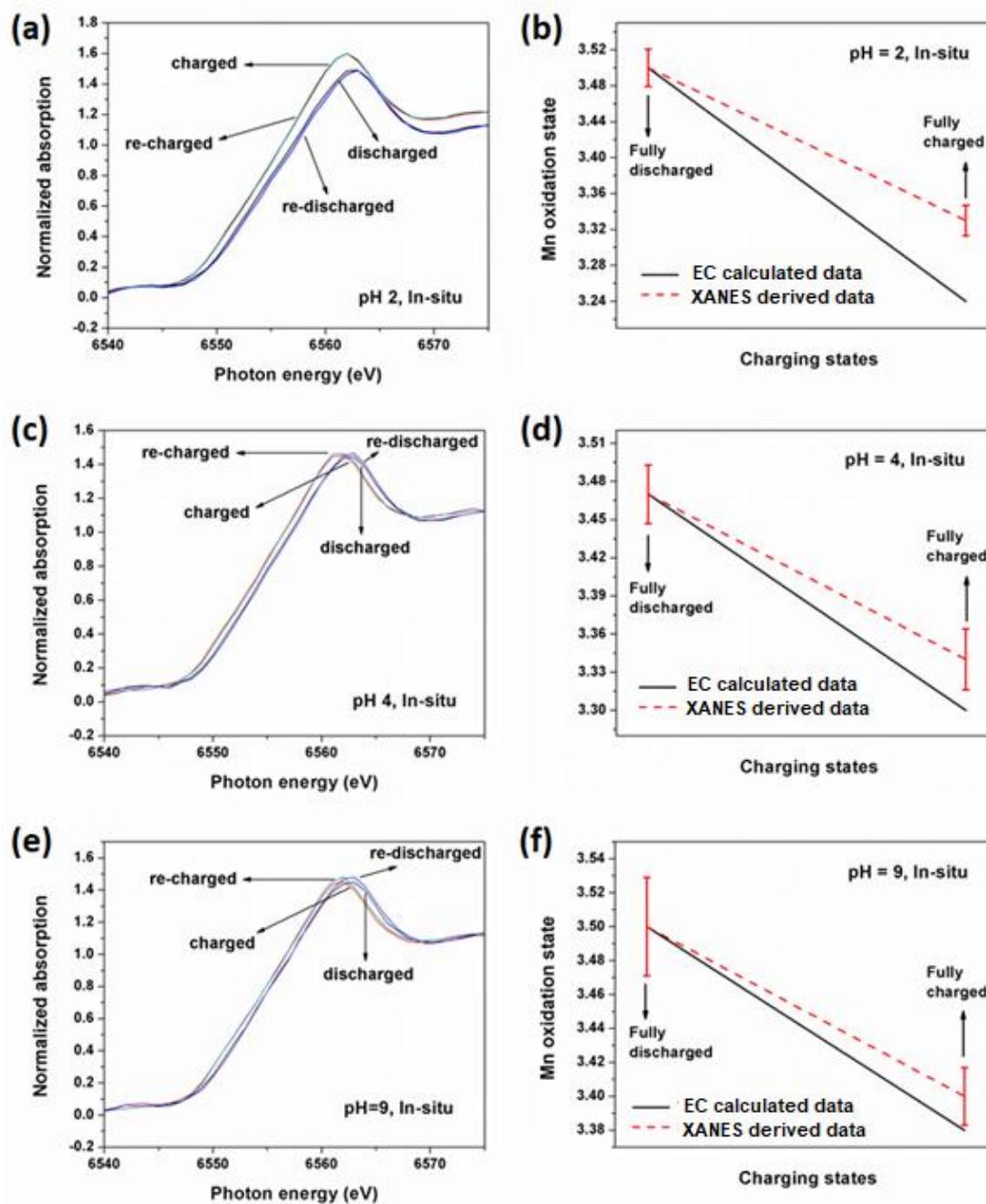


Figure 71. *In-situ* XANES spectra and calculated Mn oxidation states obtained at fully discharged and fully charged states for (a, b) pH = 2, (c, d) pH = 4, and (e, f) pH = 9 equilibrated MnO₂ nanosheet electrodes. Figures (b, d, and f) also show the comparison of Mn oxidation states variation measured from XANES data and predicted from electrochemical CV loop.

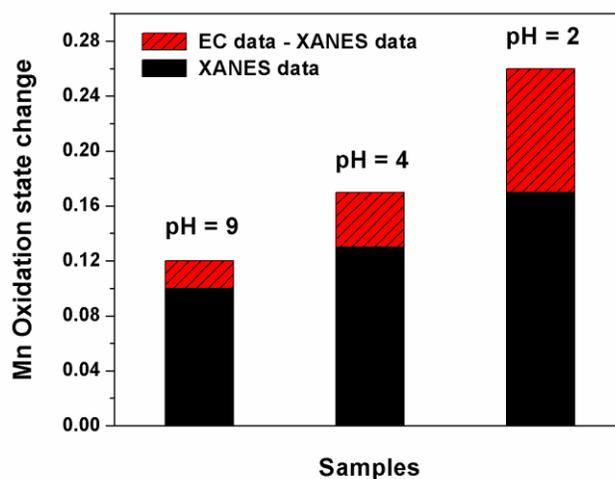


Figure 72. Mn oxidation state change comparison upon charge/discharge of pH = 2, 4 and 9 equilibrated MnO₂ nanosheet electrodes.

Further investigation of the pH = 9 treated electrodes shows that the oxidation state change obtained from XANES data (0.10 electrons) is close to that calculated from the specific capacitance (0.12 electrons). The difference between these two values might be attributed to the double-layer capacitance, since the reassembled nanosheets typically exhibit large surface area. However, when decreasing the pH equilibration value to 4 and 2, the discrepancy between measured data and theoretical line increases to 0.04 and 0.09 electrons, respectively. Thus, a smaller change of Mn oxidation states as compared to the CV loops determined values has been observed for the MnO₂ nanosheets with higher defect content. Since lower pH equilibration leading to the formation of more surface Frenkel defects, the above results imply that the potassium ions can be inserted without reduction of Mn cations, assuming a large amount of Mn vacancies in the MnO₂ nanosheets can serve as new intercalation sites for potassium ions without change of Mn oxidation state. The observed extra capacitance cannot be all attributed to the double-layer capacitance, since the three samples exhibit similar surface area.

Recently, it has been reported that the surface hydroxyl groups can serve as charge storage sites, which results in extra capacity without affecting the oxidation state of host cations.^{124,208,209} According to Cross *et al.*,²⁰⁸ when the electrode is underwent cathodic electrochemical scan, the surface hydroxyl groups on the MnO₂ can be polarized, and

they can attract a proton or metal ion from the electrolyte for charge balance. Thus, the surface hydroxyl groups can serve as extra charge storage sites. Their calculations based on the γ -MnO₂ crystal structure and 0.8 V voltage window result a capacitance of ~2750 F/g, which shows the potential that the surface hydroxyl groups can greatly contribute to the overall capacitance. Direct observation of more surface hydroxyls on pH = 2 equilibrated MnO₂ nanosheets has been obtained by de-convoluting the O 1s XPS spectra, with the results shown in Figure 73. Generally speaking, the peak located in between 529-530 eV is attributed to Mn-O-Mn (the lattice oxygen), and the peak located in between 530-531 eV is originated from Mn-OH (surface hydroxyls).²¹⁰⁻²¹² The relative ratios of surface hydroxyls and lattice oxygen in both samples have been obtained through fitting the O 1s spectra, and the results indicate that the surface hydroxyl concentration in pH = 2 equilibrated MnO₂ nanosheet floccs (43%) is much higher than that in the pH = 4 equilibrated sample (22%). Thus, we assume that hydroxyls or protonated oxygen sites around Mn vacancies in our defective MnO₂ nanosheet system may also help accumulate the charges upon K⁺ ions intercalation without affecting the oxidation state of Mn, which may explain the observed extra capacitance. In general, the *in-situ* XANES studies revealed that although the Faradaic redox reaction is still the main charge storage mechanism, a large amount of potassium ions can still intercalate into the defective MnO₂ nanosheets without reduction of Mn cations due to the presence of extra Mn vacancies that are surrounded by hydroxyls and protonated oxygen groups.

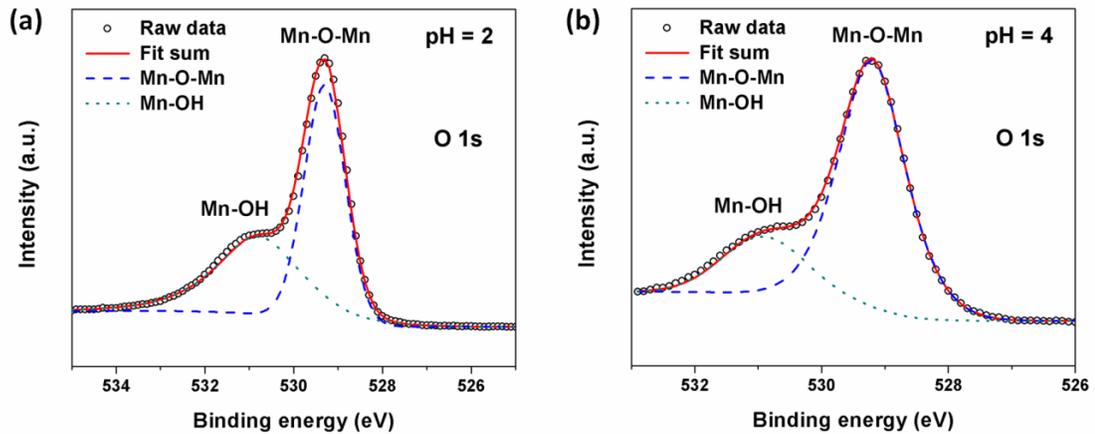


Figure 73. Curve fitting of O 1s XPS spectra of MnO₂ nanosheet floccs equilibrated at (a) pH = 2, and (b) pH = 4 solution for 24 h.

3.3.6 *In-situ* X-ray diffraction, scattering and PDF analysis of pH = 2 equilibrated δ -MnO₂ nanosheet electrodes

In order to further understand the effects of electrochemical charge/discharge on structural variation of the most defective MnO₂ nanosheets (pH = 2 equilibrated), we have performed the high energy XRD, X-ray scattering and PDF analysis at beamline 11-ID-B of APS at the Argonne National Laboratory by using our custom electrochemical cell. The data were collected by Rob Koch and Scott Misture, and analyzed by Rob Koch. The detailed description of the *in-situ* experiment can be found in section 3.2.4. Figure 74 (a-c) shows the X-ray diffraction patterns of pH = 2 equilibrated MnO₂ nanosheet electrodes in two consecutive CV cycles, with the data collected at fully discharged and fully charged states. From Figure 74 (a) it can be seen that the basal reflections (*00l* peaks) in all diffraction patterns are absent/overbroadened. In contrast, as shown in Figure 40, these peaks are well defined in the protonated and reassembled samples. Thus, the absence/overbroadening of these peaks suggest that the EPD prepared electrodes may contain nano-assemblies with a few re-stacked individual sheets, and the MnO₂ nanosheets are arranged with very little lattice coherence from stack to stack.

Further evaluation of Figure 74 (b-c) unambiguously show reversible shifting of the (100) and (110) diffraction peaks upon charge/discharge. Both peaks shifted to a longer d-spacing upon charging, indicating reversible in-plane expansion of the MnO₂ layers. The observed expansion upon charging could be related to the formation of more Mn³⁺, which usually accompanied with Jahn-Teller distortion (leading to lattice expansion) and has been confirmed from the *in-situ* XANES spectra. Upon discharging, both peaks shifted back to almost the same position, indicating reversible in-plane contraction and high reversibility. The same trend has also been observed from the X-ray scattering and PDF data, which is shown in Figure 74 (d). It can be clearly observed that the extracted PDFs reversibly shifted to lower *r* (shorter lattice spacings) on discharging and to higher *r* (longer lattice spacings) on charging, which further confirms the structural changes that are consistent with the *in-situ* XRD and XANES results. Interestingly, it was also found that although the samples aren't really crystalline, the (102) peak, which has some c-axis layer-to-layer character, does not shift appreciably during charge/discharge, suggesting that the interlayer spacing may not vary.

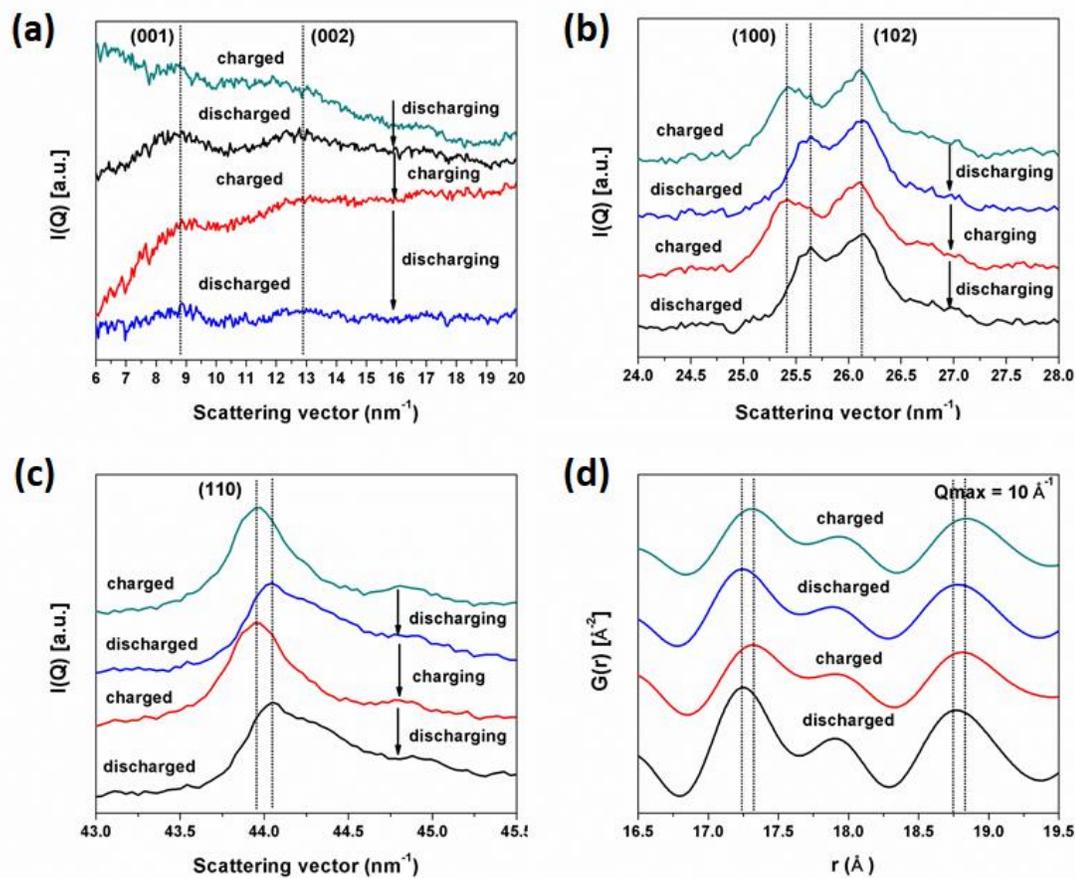


Figure 74. (a-c) *In-situ* X-ray diffraction and (d) PDF data of pH = 2 equilibrated MnO₂ nanosheet electrodes upon repeated charge/discharge.

3.4 Summary: investigation of the charge storage mechanism of defective δ -MnO₂

As shown in Chapter II, a clear correlation between the quantity of defects in our 2-D δ -MnO₂ nanosheet electrode system and the quantity of Na⁺ electrochemically inserted has been established. These correlations unambiguously imply that the defects/cation vacancies in δ -MnO₂ nanosheets can promote alkali cation intercalation and faradaic charge storage process. Therefore, understanding this link will help to enable rational design of pseudocapacitive materials with larger specific energy density.

In this part of the research work, first we have developed the electrophoretic deposition method to prepare carbon- and binder-free electrodes, which is necessary for the *in-situ* X-ray scattering measurements. The optimal deposition condition has been obtained by varying the amount of MnO₂ flocs in suspension, the pH, deposition voltage, substrate-electrode distance, and time, in order to obtain firmly attached films, well-maintained porous nanostructures, and appropriate mass loading of MnO₂. K⁺ ion was chosen as an alternative electrolyte to replace Na⁺ ion, which is a stronger X-ray scatterer and can give rise to the same charge storage process and similar capacitance. The effects of different equilibration time at pH = 2 on the electrodes' capacitance have been discussed, with the results showing that 24 h equilibration time is appropriate to result in large enough surface Frenkel defect content for optimized charge storage properties. The electrode equilibrated at pH = 2 also exhibits 42 % higher capacitance than pH = 4 treated electrode, which confirms that equilibrating the EPD prepared binder-free MnO₂ nanosheet electrodes in lower pH solution can introduce more surface Frenkel defects and thereby enhance charge storage properties.

The *ex-situ* Raman spectroscopy shows that with increasing the charge states, one characteristic Raman band (ν_1 , which is assigned to the symmetric stretching vibration of Mn-O bond in the MnO₆ octahedra) was broadened gradually. This is speculated to originate from the increased Jahn-Teller distortion upon cation intercalation during the cathodic process with the formation of more Mn³⁺ and may also due to the formation of more Mn surface Frenkel defects that leads to more distorted local structures, The band broadening effect is more pronounced in pH = 2 equilibrated MnO₂ nanosheet, which may attributed to its more defective structure. The *in-situ* XANES spectra exhibit a

reversible shift of the absorption edge to lower energies for all the three samples (pH = 2, 4 and 9 equilibrated nanosheets) when decreasing the applied potentials, indicating the reduction of Mn^{4+} to Mn^{3+} and confirms that the Faradaic redox reaction is the main charge storage mechanism in the defective MnO_2 nanosheet system. The electrodes equilibrated at lower pH exhibit larger Mn oxidation state changes, according to the XANES data, indicating that the defects can help promote the ion intercalation and charge transfer, thus facilitating the Faradaic redox reactions and reduction of Mn. When comparing the data derived from XANES and calculated from CV loops, a smaller change of Mn oxidation states upon charging has been observed for the MnO_2 nanosheets with higher defect content, implying that a large amount of Mn vacancies in the MnO_2 nanosheets can serve as new intercalation sites for potassium ions intercalation without change of Mn oxidation state. Other than a small fraction of double-layer capacitance, hydroxyls or protonated oxygen sites around Mn vacancies may also help accumulate the charges upon K^+ ion intercalation without affecting the oxidation state of Mn, according to several recently published papers,^{124,125,208,209} which may explain the observed extra capacitance. The *in-situ* XRD and PDF data also reveal reversible expansion/contraction of the nanosheet layers upon charge/discharge, as well as unchanged interlayer spacing during cycling, which are consistent with the *in-situ* XANES data.

CHAPTER IV. MN DOPED VO₂(B) NANOSHEETS

4.1 Introduction

Other than birnessite δ -MnO₂, which has been proven an effective supercapacitor electrode material, various other transition metal oxides with 2-D layered nanostructures have also been reported to as supercapacitor electrodes recently, including RuO₂,^{24,213} Co₃O₄,^{27,214} MoO₃,^{191,215} VO₂,^{216,217} etc. Among them, vanadium oxides are considered one of the most promising pseudocapacitor electrode materials due to their various vanadium oxidation states (II-V) that can provide a much wider potential window and much higher capacities, along with other advantages such as low cost, abundant resources, and easy synthesis.^{71,72} Among the various known vanadium oxides, VO₂(B), a metastable monoclinic polymorph, is a promising electrode material for pseudocapacitors. The crystal structure of VO₂(B) is comprised of distorted VO₆ octahedra that are edge sharing. Each sheet is linked to adjacent sheets by corner sharing along the c-direction, and it possesses perovskite-like cavities (see Figure 15).⁷⁸ The cation diffusion is usually parallel to the [010] crystal orientation. Since cation insertion usually leads to uniaxial expansion of the perovskite-like cavities, and the edge sharing of the octahedra in VO₂(B) is along the lattice expansion direction, thus, unlike the other polymorphs (the most stable phase VO₂(R) with rutile structure, the monoclinic VO₂(R) with a slightly distorted rutile structure, and the tetragonal phase VO₂(A)), there is an increased resistance to V-O bond cleavage during cation intercalation in VO₂(B), which leads to a stable structure during electrochemical cycling.

To date, most efforts for obtaining the VO₂(B) nanosheets have been focused on hydrothermal methods,^{101,216} although some papers also reported using exfoliation processes.^{81,116} Unlike the exfoliation method, which typically needed to ultrasonicate or age for several days in various solutions to get the 2-D nanosheets from their bulk counterpart, the hydrothermal process can be very fast and ease realization of mass production. Through adjusting the hydrothermal reaction conditions, ultra large and thin

VO₂(B) nanosheets²¹⁸ can be easily obtained, thus making it an excellent method for fabricating the VO₂(B) nanosheets.

Like many other transition metal oxides, the VO₂(B) nanosheets also suffer from low electrical conductivity, which inevitably limits their charge storage capability. However, the hydrothermal reactions often lead to the formation of densely packed bulk VO₂(B) instead of 3-D porous nanostructures, which results in less surface adsorption sites during electrochemical cycling. One effective strategy to resolve these problems is doping with other transition metal ions, which commonly introduces structural defects and tunes electrochemical properties. The replacement of host cations/anions with aliovalent dopants will not only increase the cation/anion vacancy content, but may also increase the cell volume of the host lattice, thus can help provide new intercalation sites, facilitate the diffusion of alkali cations, and also improve the electronic conductivity.

Li *et al*²¹⁹ have prepared Sn-doped V₂O₅ by sol-gel method and fabricated films using a drop-casting process. Their XPS results indicate that Sn doping facilitates the formation of lower valence state vanadium in V₂O₅ films, thus may enhance the electrical conductivity of the film and thereby facilitate Li⁺ ion intercalation/deintercalation. The electrochemical measurements also indicate that the Sn-doped V₂O₅ films show much enhanced lithium-ion storage capacity, faster kinetics, and improved cyclic stability. Yu *et al*¹²⁸ have synthesized Mn-doped V₂O₅ by a sol-gel process with Mn²⁺ directly added during sol preparation. The films were fabricated by dip-coating method. The XPS results show co-existence of V⁴⁺ and V⁵⁺ in a Mn-doped sample, and the oxygen vacancies have been formed due to Mn²⁺ substitution. Both the lower valence vanadium ions and oxygen vacancies can help increase the film's conductivity. The electrochemical results also indicate enhanced discharge capacities with much improved cyclic stability for the Mn-doped samples. Zeng *et al*¹³⁰ prepared Mn-doped V₂O₅ lithium-ion battery cathode material by using a layered compound, vanadium (III) jarosite, as the precursor, and Mn²⁺ as dopant. The uniform aliovalent doping of the larger Mn²⁺ cations in the V₂O₅ structure increases the cell volume, which facilitates Li⁺ ion diffusion, and introduces oxygen vacancies that improve the electronic conductivity. Cousteir *et al*⁷⁶ have prepared Cu and Ag doped V₂O₅. They found that the electrical conductivity of V₂O₅ increased by two to three orders of magnitude with increasing doping content. The

doped sample exhibits high intercalation rate performance and almost no capacity fading after more than 450 cycles. Although several works have been done investigating the electrochemical performance of transition metal ion doped vanadium oxide, there have been no papers discussing the effect of Mn-doping on hydrothermally prepared VO₂(B) nanosheets and their supercapacitor properties until now.

In this chapter, pure and Mn-doped VO₂(B) nanosheets have been successfully prepared via a simple one-step hydrothermal reaction. The hydrothermal reaction conditions have been studied, in order to obtain the desired nanosheet morphologies. The surface morphologies, chemical and crystal structures, as well as sodium ion intercalation properties of the pure and Mn-doped VO₂(B) nanosheets have been investigated systematically. The as-prepared Mn-doped VO₂(B) nanosheet sample exhibits much enhanced capacitance, charge transfer resistance, and cyclic stability compared with the pure VO₂(B), demonstrating great potential for the application in pseudocapacitor electrode materials.

4.2 Materials and Methods

4.2.1 Chemicals and reagents

Vanadium pentoxide (V_2O_5) and N-methyl-2-pyrrolidone (NMP) were purchased from Sigma-Aldrich. Manganese acetate ($Mn(CH_3COO)_2 \cdot 4H_2O$), isopropanol alcohol (IPA), sodium sulfate (Na_2SO_4), acetylene black, poly (vinylidene fluoride) (PVDF) and nickel foil (Ni foil) were obtained from Alfa Aesar. Hydrogen peroxide (H_2O_2), 6N hydrochloric acid (HCl) solution and sodium hydroxide (NaOH) were purchased from Fisher Scientific. All reagents were used as received without further purification.

4.2.2 Preparation of $VO_2(B)$ and Mn-doped $VO_2(B)$ nanosheets

The pure $VO_2(B)$ nanosheets were prepared by using the hydrothermal method. We have systematically investigated the hydrothermal reaction conditions, including different amount of starting materials, hydrothermal reaction temperatures and time, in order to optimize the reaction procedures and obtain samples with sheet-like morphology and $VO_2(B)$ crystal structure. In a typical synthesis procedure, 50 mg V_2O_5 powder (Sigma-Aldrich) was dissolved in 5 mL de-ionized water and 10 mL 30% H_2O_2 solution at room temperature. The suspension was stirred vigorously until V_2O_5 dissolved completely and a clear bright yellow solution was obtained. Then 10 mL IPA was added into the solution and stirred vigorously for another 5 min. For the purpose of making Mn-doped samples, 16 mg $Mn(CH_3COO)_2 \cdot 4H_2O$ was added into above-mentioned V_2O_5 solution to obtain the Mn-doped vanadium oxide sol and stirred for 5 min until it was totally dissolved. Finally, the as-prepared precursor solutions (both pure and Mn-doped) were transferred into a 50 mL Teflon-lined stainless steel autoclave. The autoclave was sealed, maintained at 180 °C for 6 h, and then cooled down to room temperature naturally. The obtained precipitates were washed thoroughly with distilled water and ethanol several times and then dried in an oven overnight. Figure 75 shows a typical synthesis procedure for making the pure and Mn-doped $VO_2(B)$ nanosheets. Other than employing doping as an effective method to introduce defects into the $VO_2(B)$ nanosheets, we have also tried equilibrating the as-obtained pure $VO_2(B)$ nanosheets in different pH solutions (as what

we did for the δ -MnO₂ nanosheets), in order to see if that can also help improving the charge storage properties.

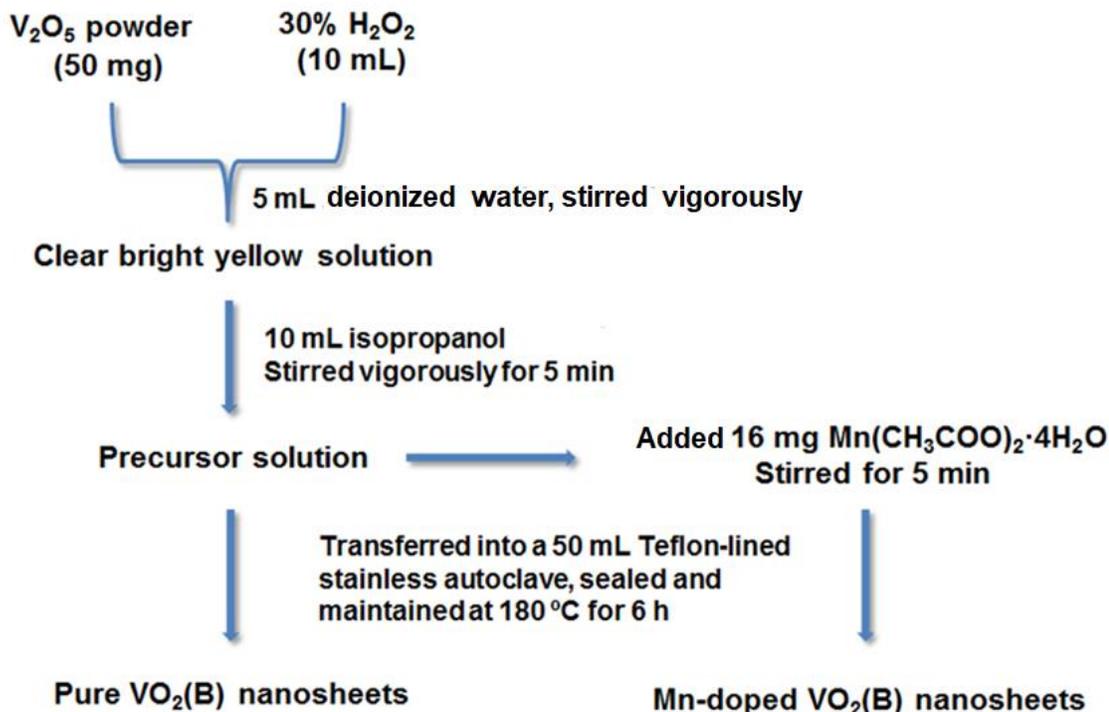


Figure 75. Typical synthesis procedure for making pure and Mn-doped VO₂(B) nanosheets.

4.2.3 Preparation of VO₂(A) nanobelts

The typical synthesis procedure for making VO₂(A) nanobelts is as follows. 0.751 g V₂O₅ powder and 1.0395 g H₂C₂O₄ were dispersed in 33 mL DI-H₂O under vigorous magnetic stirring for 10 min at room temperature. Then the mixed suspension was transferred into a 50 mL Teflon-lined stainless autoclave. The autoclave was sealed, maintained at 280 °C for 48 h, and then cooled down to room temperature naturally. The obtained precipitates were washed with distilled water and ethanol several times and then dried in oven overnight.

4.2.4 Characterization of the samples

As-prepared samples were characterized by powder X-ray diffraction (XRD) using a Bruker D8 diffractometer with Lynxeye detector and Cu K α radiation ($\lambda = 0.15418$ nm)

over 5-80° 2 θ range. Surface morphologies were studied using scanning electron microscopy (SEM, FEI Quanta 200) operating at 20 and 5 kV, respectively. The composition of the specimens was characterized by energy-dispersive spectroscopy (EDS) using a FEI EDAX system equipped with a silicon-drift detector (SEM integrated). Thermogravimetric analysis (TGA) was performed using a TA Instruments SQT-Q600 DTA/TGA under flowing air with a heating rate of 10 °C/min. The local chemical environment of the samples was probed using a PHI Quantera X-ray photoelectron spectrometer (XPS) equipped with Al K α radiation.

The *ex-situ* X-ray total scattering and PDF measurements were carried out at the F2 station of the Cornell High Energy Synchrotron Source (CHESS), Cornell University, with an X-ray energy of 61.33 KeV ($\lambda = 0.20215 \text{ \AA}$) at room temperature. Data sets were collected using standard 1 mm Kapton capillaries. 2-D X-ray diffraction data were integrated to 1-D using FIT2D,^{162,220} after appropriately calibrating detector deviations from orthogonality and masking invalid pixels. LaB₆ was used as the calibration standard for detector geometry. The reduced pair distribution function (PDF) spectrum was obtained by Fourier transformation of the measured structure factor in a Q range of 0.57 - 18.2 \AA^{-1} using software PDFgetX3,¹⁹⁵ which includes the appropriate corrections for inelastic scattering and energy-dependent detector response, in addition to experimental background and absorption corrections, amongst others. Structural modelling with fitting of the G(r) function over 0-90 \AA r range was carried out using the PDFgui software.²²¹

4.2.5 Electrochemical measurements

The working electrode slurry was prepared by mixing 80 wt.% active material (30 mg), 15 wt.% acetylene black (5.625 mg) and 5 wt.% PVDF (1.875 mg) in NMP solution. After stirring for 6 h, the homogeneous slurry was spread onto a Ni foil (pre-treated by ultrasonication in 1M HNO₃ and deionized water for 10 min, respectively) substrate with an area of 1 cm² by hand with a blade (three pieces of scotch tape were covered on the edges of the substrate to control the film thickness), and then heated at 100 °C for 2 h in oven to evaporate the solvent and obtain the electrode. The loading of the active material on the working electrode was typically in the range of 0.4-0.5 mg/cm².

The capacitive performance was measured using a CHI 650E electrochemical analyzer (CHI, USA) with a conventional three-electrode cell. Ag/AgCl and platinum wire were used as the reference and auxiliary electrodes, respectively, with 1 M Na₂SO₄ aqueous electrolyte. Cyclic voltammetry scans were carried out from 0 to 0.8 V at various scan rates from 2 to 100 mV/s. Galvanostatic charge-discharge was measured at different constant current densities from 0.2 to 10 A/g. Electrochemical impedance spectroscopy (EIS) was performed in the frequency range of 0.01 Hz - 100 kHz at an open circuit potential of 5 mV, with the same set-up as discussed in section 2.2.4 and 2.3.8. EIS data was fitted to an electrical equivalent circuit model using ZsimpWin (Version 3.21, EChem Software) software. The electrical equivalent circuit was chosen according to the obtained EIS spectra, and the combination of different elements with best fitting is used as the model to extract the charge transfer resistance.

4.3 Results and discussion

4.3.1 Investigation of the hydrothermal reaction conditions to prepare the VO₂(B) nanosheets

In order to prepare the VO₂(B) nanosheets with desired crystal structure and morphology, we have systematically investigated the hydrothermal reaction conditions, which include different amount of starting materials, the hydrothermal reaction temperatures and time. The detailed information of the varied hydrothermal reaction parameters has been summarized in Table III.

Table III. Various Hydrothermal Reaction Conditions that have been Investigated to Prepare VO₂(B) Nanosheets.

Sample ID	Starting materials	Temperature (°C)	Time (h)
VO1	0.2 g V ₂ O ₅ + 25 mL H ₂ O + 5 mL 30 wt.% H ₂ O ₂	180	9
VO2	0.2 g V ₂ O ₅ + 25 mL H ₂ O + 5 mL 30 wt.% H ₂ O ₂	180	12
VO3	0.2 g V ₂ O ₅ + 25 mL H ₂ O + 5 mL 30 wt.% H ₂ O ₂	180	18
VO4	0.36 g V ₂ O ₅ + 30 mL H ₂ O + 5 mL 30 wt.% H ₂ O ₂	190	12
VO5	0.18 g V ₂ O ₅ + 10 mL H ₂ O + 10 mL 30 wt.% H ₂ O ₂ + 10 mL IPA	170	24
VO6	0.09 g V ₂ O ₅ + 5 mL H ₂ O + 5 mL 30 wt.% H ₂ O ₂ + 5 mL IPA	180	6
VO7	0.05 g V ₂ O ₅ + 5 mL H ₂ O + 10 mL 30 wt.% H ₂ O ₂ + 10 mL IPA	180	6

Generally speaking, it has been observed that the opaque V₂O₅ suspension with orange color will turn to a transparent bright yellow solution when H₂O₂ was added under vigorous stirring, which is attributed to the reaction between V₂O₅ powder and H₂O₂ to form a V₂O₅ sol.²²² Addition of isopropanol will not causes apparent color change at room temperature; however, it plays an important role for the formation of VO₂(B) phase and acts as reducing agent for the reduction of V₂O₅ to form VO₂(B) during the

hydrothermal reaction process.²²³ Although the observed colors for the samples prepared with different hydrothermal reaction conditions varied from brown to blue, the VO₂(B) nanosheets typically exhibits dark blue color, which corresponds well with reports in the literature.²¹⁸

Figure 76 shows the typical XRD patterns of the hydrothermally prepared vanadium oxide nanostructures, and Figure 77 exhibits their corresponding SEM images. First, it should be demonstrated that although the samples VO1-VO3 have the same starting materials and hydrothermal reaction temperature, the powders can be formed during the hydrothermal process only when the reaction time is 12 h, whereas longer and shorter reaction times lead to the clear solution after reaction without any powders that can be collected. Thus, it can be concluded that the appropriate reaction time is crucial for the formation of vanadium oxide powders during the hydrothermal processes.

The important role of IPA in the formation of VO₂(B) phase has also been confirmed through comparing the XRD patterns of the as-prepared samples, as shown in Figure 76. Although the (00*l*) basal diffraction peaks can be clearly observed for the samples VO2 and VO4, and the SEM images (shown in Figure 77(a-b)) also indicate the formation of layered structures, none of their diffraction peaks can be indexed to the VO₂(B) crystal structure. In contrast, for the samples VO5 to VO7, which were synthesized with addition of IPA during the hydrothermal processes, all of the diffraction peaks can be indexed to the monoclinic structure of VO₂(B) (ICDD Card No. 00-031-1438), indicating that the starting V₂O₅ has been completely transformed to VO₂(B) phase during the hydrothermal reaction.

Although the samples VO5 to VO7 exhibit same crystal structure, there still exists apparent difference in their morphologies. As shown in Figure 77(c-e), the sample VO5 exhibits belt-like morphology, with typical length of ~500 nm and width of ~100 nm. In contrast, the sample VO7 exhibits typical sheet-like morphology, with lateral dimensions in the range of several hundred nanometers and thickness approximately 20-30 nm. Thus, the relative ratio of starting materials and hydrothermal reaction conditions also lead to the formation of different morphologies. Since our research is mainly focused on preparing the VO₂(B) nanosheets, therefore we have chosen the sample VO7, with the starting materials 0.05 g V₂O₅ + 5 mL H₂O + 10 mL 30 wt.% H₂O₂ + 10 mL IPA, and

hydrothermally reacted at 180 °C for 6 h, for further structure modification and electrochemical charge storage performance measurements.

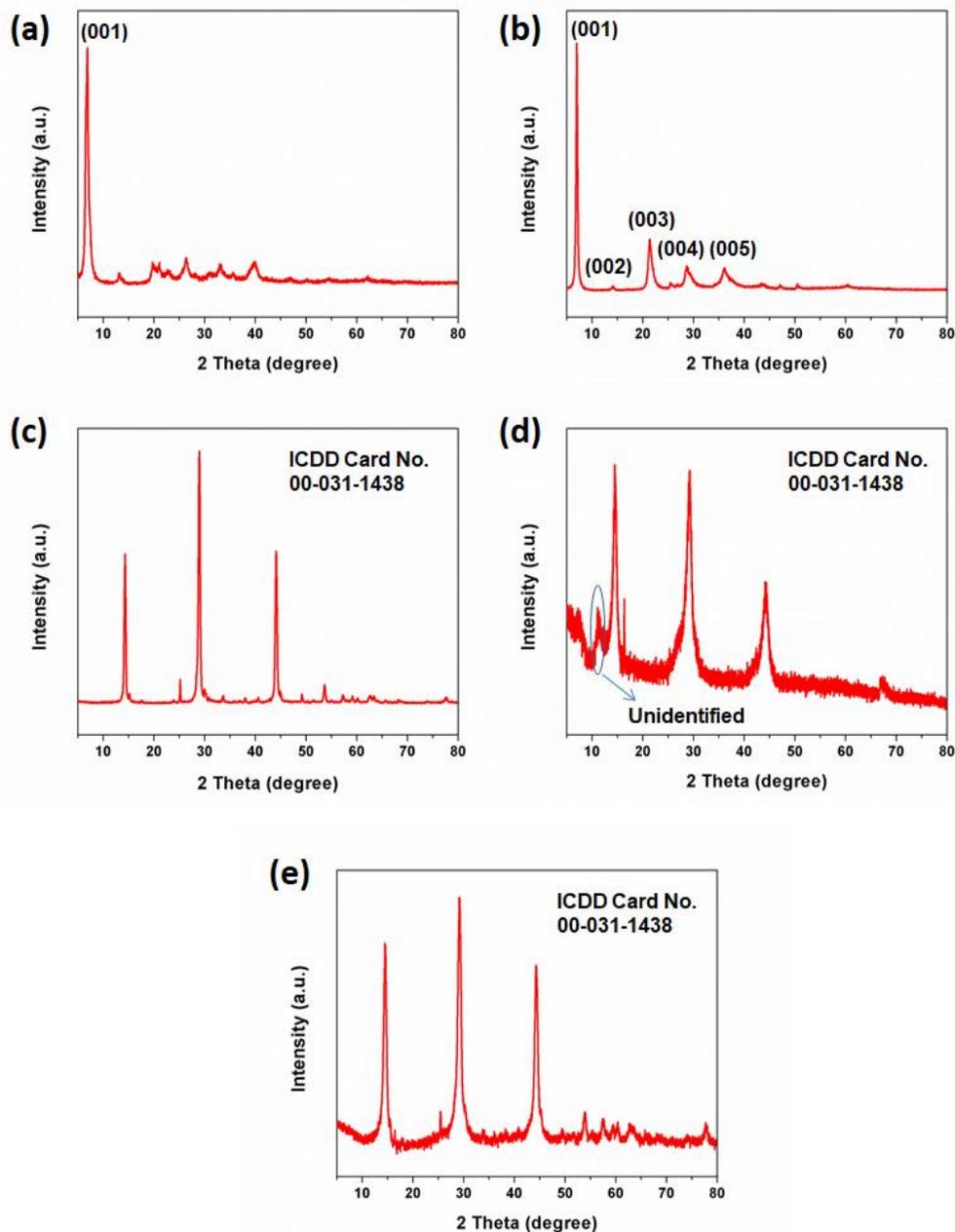


Figure 76. Typical XRD patterns of the hydrothermally prepared vanadium oxide nanostructures. (a) 0.2 g V_2O_5 + 25 mL H_2O + 5 mL 30 wt.% H_2O_2 , 180 °C, 12 h; (b) 0.36 g V_2O_5 + 30 mL H_2O + 5 mL 30 wt.% H_2O_2 , 190 °C, 12 h; (c) 0.18 g V_2O_5 + 10 mL H_2O + 10 mL 30 wt.% H_2O_2 + 10 mL IPA, 170 °C, 24 h; (d) 0.09 g V_2O_5 + 5 mL H_2O + 5 mL 30 wt.% H_2O_2 + 5 mL IPA, 180 °C, 6 h; (e) 0.05 g V_2O_5 + 5 mL H_2O + 10 mL 30 wt.% H_2O_2 + 10 mL IPA, 180 °C, 6 h.

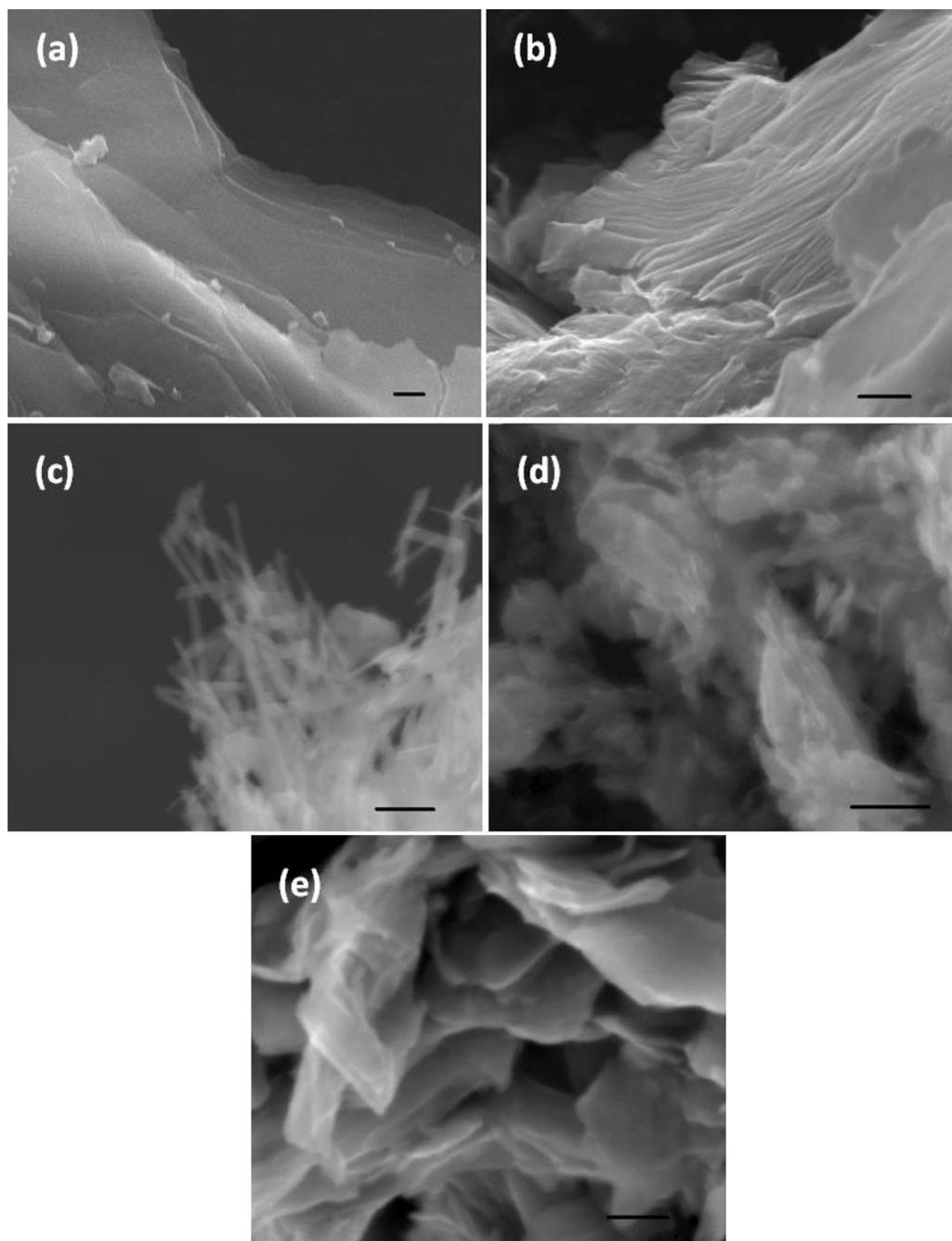


Figure 77. SEM images of the hydrothermally prepared vanadium oxide nanostructures. (a) 0.2 g V_2O_5 + 25 mL H_2O + 5 mL 30 wt.% H_2O_2 , 180 °C, 12 h; (b) 0.36 g V_2O_5 + 30 mL H_2O + 5 mL 30 wt.% H_2O_2 , 190 °C, 12 h; (c) 0.18 g V_2O_5 + 10 mL H_2O + 10 mL 30 wt.% H_2O_2 + 10 mL IPA, 170 °C, 24 h; (d) 0.09 g V_2O_5 + 5 mL H_2O + 5 mL 30 wt.% H_2O_2 + 5 mL IPA, 180 °C, 6 h; (e) 0.05 g V_2O_5 + 5 mL H_2O + 10 mL 30 wt.% H_2O_2 + 10 mL IPA, 180 °C, 6 h. Scale bar, 2 μ m (a), 1 μ m (b), 500 nm (c-d), 200 nm (e).

4.3.2 Effects of different pH equilibration on structures, morphologies and charge storage properties of the hydrothermally prepared VO₂(B) nanosheets

As discussed in Chapter II, the 3-D porous δ -MnO₂ nanostructures reassembled from 2-D δ -MnO₂ nanosheets equilibrated at different pH values exhibit different concentrations of Mn point defects and Mn^{3+/4+} ratios. The electrochemical measurements provide direct evidence that intentional Mn ion defects and Mn reduction synergistically improve supercapacitor performance. In order to investigate the possibility of using a similar pH equilibration method to introduce defects into the hydrothermally obtained VO₂(B) nanosheets, we have equilibrated the as-prepared VO₂(B) nanosheets in pH = 2 and 9 solutions for 24 h. We have also equilibrated the VO₂(B) nanosheets in deionized water for 24 h under stirring, which represents an intermediate pH environment (the pH value of deionized water is ~ 6, due to the absorption of CO₂ in the surrounding atmosphere which forms carbonic acid) and can be used as a reference.

The typical XRD patterns of the hydrothermally prepared VO₂(B) nanosheets equilibrated at pH = 2, 6, and 9 for 24 h are shown in Figure 78. Although most diffraction peaks can be indexed to the monoclinic structure of VO₂(B) (ICDD Card No. 00-031-1438), a broad peak located in the 2θ range between 5 and 10° (marked with the asterisk) has emerged for all the three samples after 24 h equilibration in different pH solutions. This is an indication of the incorporation of water molecules into the layered structures in VO₂(B), which leads to the partial hydration of the nanosheet and thereby an expansion of the interlayer distance.²²⁴ Except the presence of a broad peak in the low 2θ range, no other obvious differences can be found for the three samples, indicating their similar crystal structures after different pH equilibration. Figure 79 also shows similar SEM morphologies for all the three samples, indicating that equilibration at different pH values have no apparent influence on their morphologies. However, compared with the original VO₂(B) shown in Figure 77(e), the pH equilibrated samples look more fluffy and exhibit more porous nanostructures composed of thinner and less rigid nanosheets, with some scrolling at the edges, which is probably because of water incorporation and expansion of the interlayer distance.

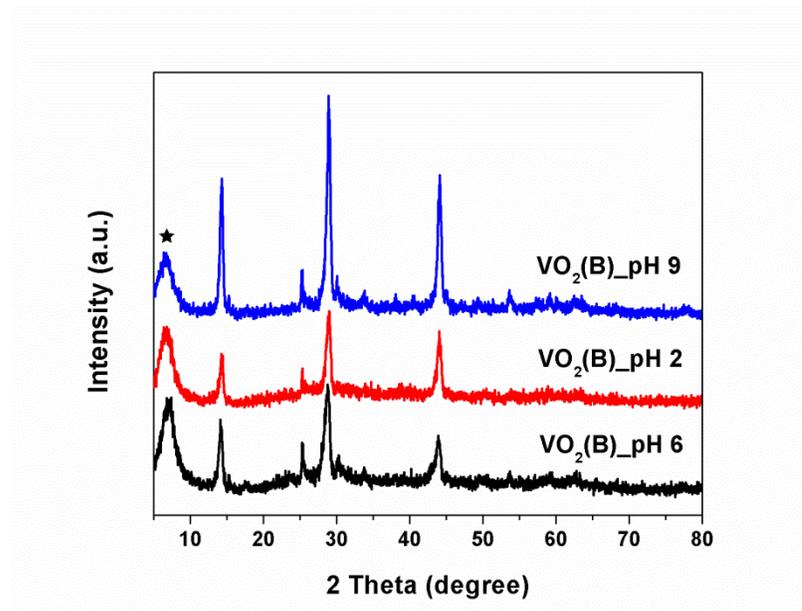


Figure 78. Typical XRD patterns of the hydrothermally prepared VO₂(B) nanosheets equilibrated at pH = 2, 6 and 9 solution for 24 h.

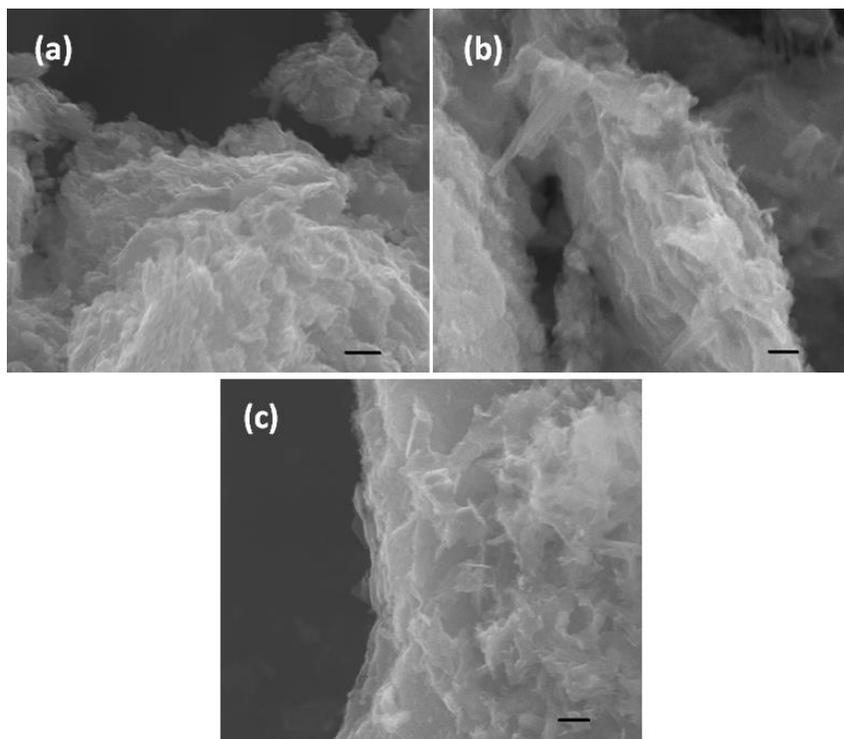


Figure 79. Typical SEM images of the hydrothermally prepared VO₂(B) nanosheets equilibrated at (a) pH = 2, (b) pH = 6, and (c) pH = 9 solution for 24 h. Scale bar, 200 nm (a), 500 nm (b-c).

In order to evaluate the effects of equilibration at different pH values on the charge storage properties of the VO₂(B) nanosheets, we have performed electrochemical measurements on the three samples. Figure 80(a) exhibits the galvanostatic charge-discharge curves measured at 0.5 A/g current density, and the comparison of calculated specific capacitance as a function of current density is shown in Figure 80(b). Clearly it can be seen that the specific capacitances for all the three samples are almost the same, especially at low current densities. This may be due to their similar morphologies and crystal structures. At 0.5 A/g current density, the specific capacitance is 163 F/g for pH = 2 treated VO₂(B) nanosheets, 162 F/g for pH = 6 treated VO₂(B) nanosheets, and 161 F/g for pH = 9 treated VO₂(B) nanosheets. With increasing the current density, the specific capacitance for all samples decreases gradually. However, at each applied current density, the difference of specific capacitance for all samples less than 15 F/g, which indicates that equilibration at different pH values has almost no influence on the charge storage properties of the VO₂(B) nanosheets. This is probably because the different crystal structure of VO₂(B) compared with the δ -MnO₂ makes it difficult to form point defects by using the low pH equilibration method. Thus, other approaches are investigated to modify the structure and introduce defects into the VO₂(B) nanosheets, in order to improve its charge storage properties.

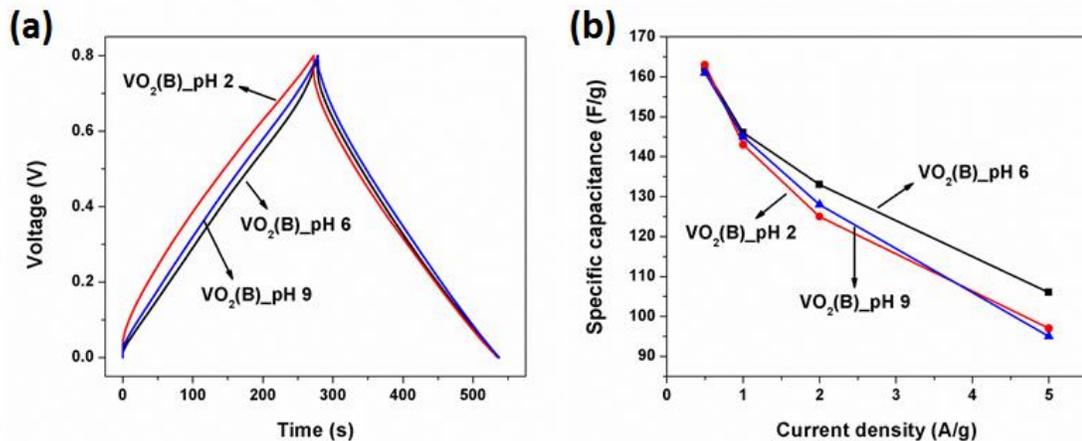


Figure 80. (a) Galvanostatic charge-discharge curves of the pH = 2, 6 and 9 equilibrated VO₂(B) nanosheets at 0.5 A/g current density; (b) Comparison of specific capacitance for the samples as a function of current density.

4.3.3 Phases and microstructures of the hydrothermally prepared pure and Mn-doped VO₂(B) nanosheets

Doping, an effective and commonly used way to tune the defect structure and enhance the oxide properties, has been investigated as an alternative method to modify the structure of VO₂(B) nanosheets. In this research, manganese acetate has been introduced during the hydrothermal reactions to study the effects of Mn-doping on structures and charge storage properties of VO₂(B) nanosheets. Although several works have been done investigating the electrochemical performance of transition metal ions doped into V₂O₅,^{76,128,219} to the best of our knowledge, there have been no papers discussing the effect of Mn-doping on hydrothermally prepared VO₂(B) nanosheets and their supercapacitor properties.

The SEM images of hydrothermally prepared pure and Mn-doped VO₂(B) nanosheets are shown in Figure 81. It can be seen that most pure VO₂(B) exhibits typical sheet-like morphology, with lateral dimensions in the range of several hundred nanometers and the thickness is approximately 20-30 nm. The magnified image (Figure 81(c)) demonstrates that the sheets are generally flat and smooth, with some scrolling at the edges as has been reported in other nanosheet studies.^{25,167} However, the as-prepared large VO₂(B) nanosheets are tended to simply stack together, which is more likely forming a dense and less open structure.

In contrast to the pure sample, the Mn-doped VO₂(B) exhibits different morphology. From Figure 81(b) it can be seen that the sample is formed by the house-of-cards type stacking of nanosheets which has smaller lateral dimensions, which may provide more accessible surface absorption sites. From the magnified SEM image (Figure 81(d)), we can see obvious ripples and corrugations instead of flat surface, and some sheets on the edges of the agglomerates look transparent, which indicate that the doped samples may contain thinner and less rigid nanosheets. The apparent observed difference in morphologies may due to the effect of Mn doping, which impedes the growth of VO₂(B) nanosheets in the lateral dimension and also introduces more lattice distortion during hydrothermal process. The EDS spectra (Fig. 82(b)) reveals 8.7% molar content of Mn in the doped samples, demonstrating that not all Mn in the starting material is incorporated into the VO₂(B) nanosheets during hydrothermal reactions. Thus, the SEM

images indicate that the Mn doping can promote the formation of thinner and smaller nanosheets, as well as the house-of-cards restacked morphology, which may lead to more accessible surface area and facilitate the Na^+ ion intercalation when used as supercapacitor electrodes.

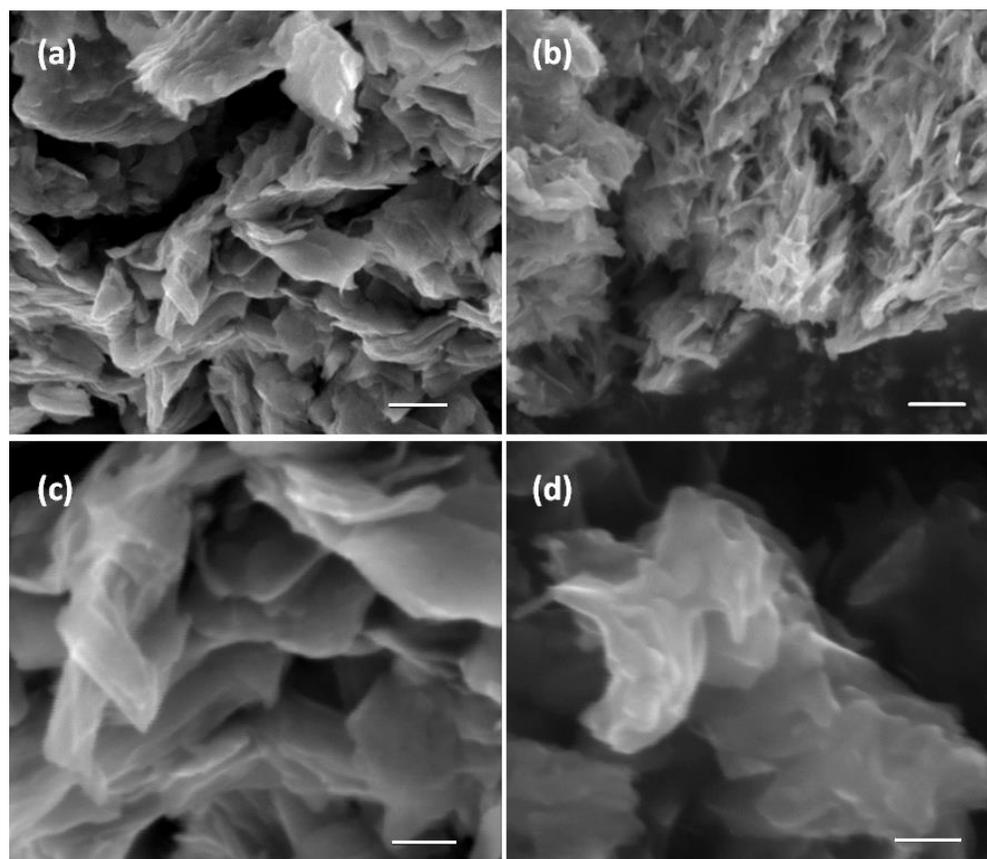


Figure 81. Typical SEM images of the pure $\text{VO}_2(\text{B})$ (a, c) and Mn-doped $\text{VO}_2(\text{B})$ (b, d) nanosheets prepared by hydrothermal method and dried in oven overnight. Scale bar, 500 nm (a-b), 200 nm (c-d).

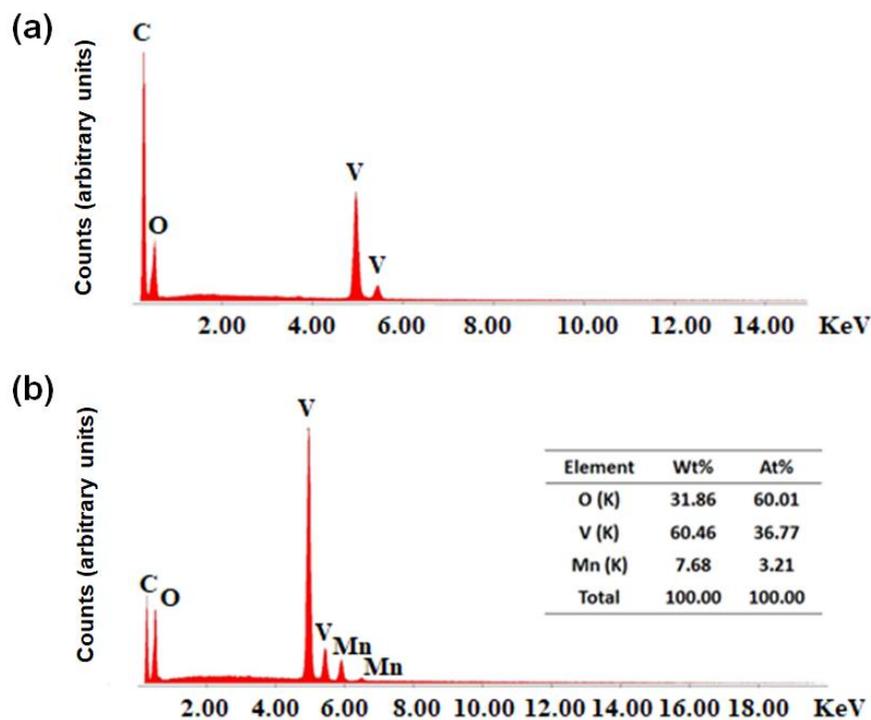


Figure 82. The energy dispersive spectrum of (a) VO₂(B) and (b) Mn-doped VO₂(B) nanosheets. The inset table shows the quantification of each element present in Mn-doped VO₂(B) nanosheets.

Figure 83 shows the synchrotron XRD patterns and the Rietveld refinement results of as-prepared pure and Mn-doped VO₂(B) nanosheets. For the pure sample, all diffraction peaks can be indexed to the monoclinic structure of VO₂(B) (ICDD Card No. 00-031-1438), indicating that the starting V₂O₅ has been transformed to the VO₂(B) crystal structure during hydrothermal reactions with no detectable secondary phases formed. For the Mn-doped sample, except the monoclinic VO₂(B), our Rietveld refinement result also indicates the presence of another polymorph, the tetragonal phase VO₂(A) (ICDD Card No. 04-007-2428). The refined results indicate the presence of 68 mol% VO₂(B) and 32 mol% VO₂(A). Such partial crystal structure transformation from VO₂(B) to VO₂(A) is likely due to the Mn doping, which distorts the VO₆ octahedra and introduces a local structural perturbation, thus giving rise to the changes of lattice structure. Similar phenomenon has also been reported by Wu *et al* on Ti doped VO₂.²²⁵ It is worthwhile noting that no manganese related phases have been found for the Mn-doped samples, implying that all Mn ions are likely to incorporate into the vanadium sites

in the lattice during the hydrothermal process. This is in accordance with the results reported by Zeng *et al.*¹³⁰ They found that the saturation limit for Mn ions is around 10 mol%, where Mn ions can be incorporated into the vanadium oxide lattice without forming the other undesired phases.

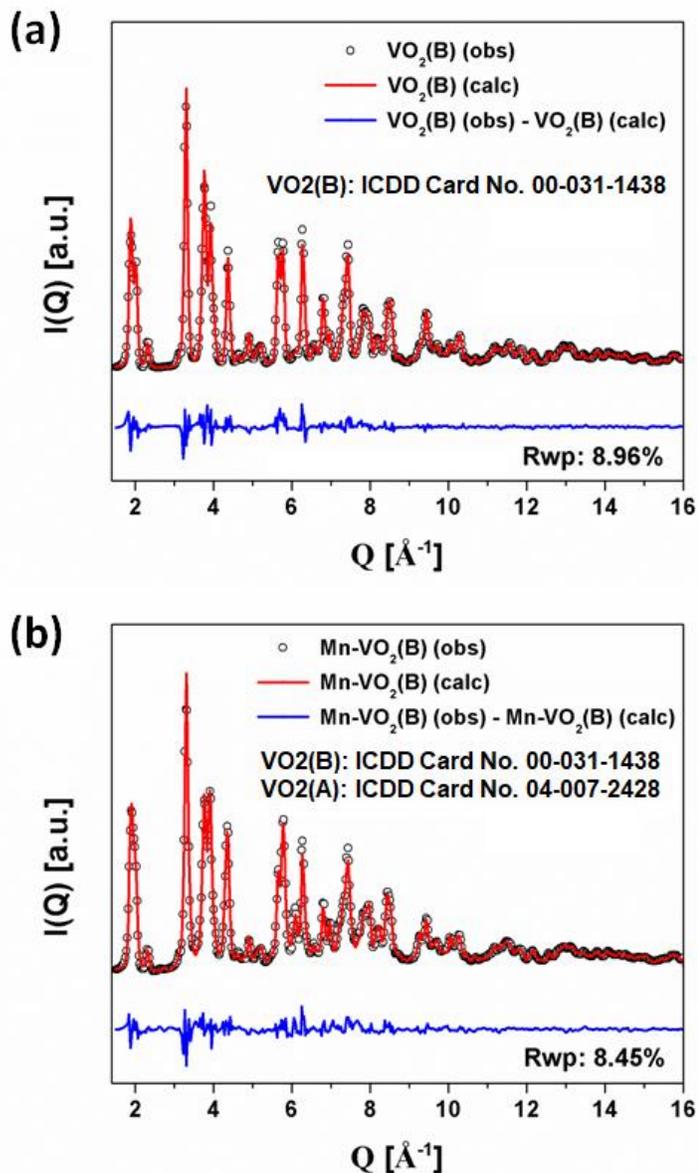


Figure 83. XRD patterns of (a) pure VO₂(B) and (b) Mn-doped VO₂(B) nanosheets (the Rietveld refinement of the diffraction pattern reveals a mixture of monoclinic (C2/m, 68 %) and tetragonal (P42/ncm, 32 %) polytypes). Data collected on CHESS F2 station.

The thermogravimetric analysis of pure and Mn-doped VO₂(B) nanosheets was carried out in air, and is shown in Figure 84. Both samples were dried in oven at 65 °C before performing the TGA measurements, in order to minimize the surface absorbed water content. It can be seen that both samples exhibit a mass loss up to around 340 °C (2.6 wt% for pure VO₂(B) and 3.4 wt% for Mn-doped sample), which can be attributed to the removal of adsorbed water and structural hydroxyl ions.¹⁷³ Above 340 °C, both samples exhibit a rapid mass increase up until ~450 °C, which could be attributed to the oxidation of VO₂(B) to V₂O₅. Interestingly, the mass increase for Mn-doped VO₂(B) in this temperature range is 6.4 wt%, which is slightly smaller (0.5 wt% difference) than that of pure VO₂(B) (6.9 wt% mass increase). This is considered to originate from the effect of Mn doping. We have measured the XRD patterns for both samples after TGA analysis, which is shown in Figure 85. It can be seen that only V₂O₅ was found after TGA for the pure VO₂(B). However, a second phase, MnV₂O₆, was also observed after TGA analysis for the Mn-doped sample. Thus it indicates that the doped Mn ions can react with V₂O₅ and leading to the formation of MnV₂O₆. Since the initial amount of VO₂ that can be oxidized at high temperature is smaller for Mn-doped VO₂(B) compared with the pure sample because of the Mn doping, and the formation of MnV₂O₆ will not result in any mass change, so it could be well predicted that the mass increase for Mn-doped samples at temperatures above 340 °C should be smaller than that of undoped samples. The theoretical calculation based on the total conversion of VO₂ to V₂O₅ and the formation of MnV₂O₆ using the Mn-doping content (8.7 mol% as determined by EDS) indicates a mass change difference of ~0.6 wt% between the Mn-doped and pure VO₂(B), which coincides with the experimental data. The above results also indicate successful incorporation of Mn ions into the VO₂(B) crystal lattice.

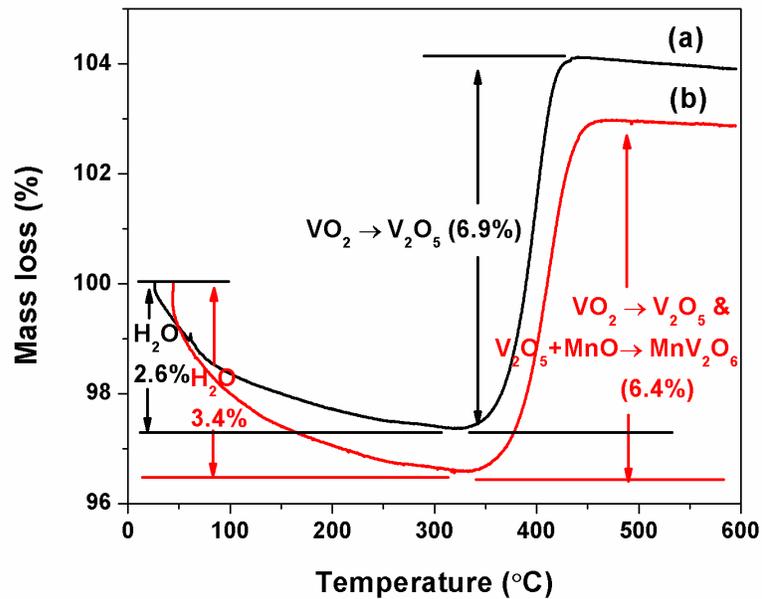


Figure 84. TGA curves of (a) pure and (b) Mn-doped VO₂(B) nanosheets.

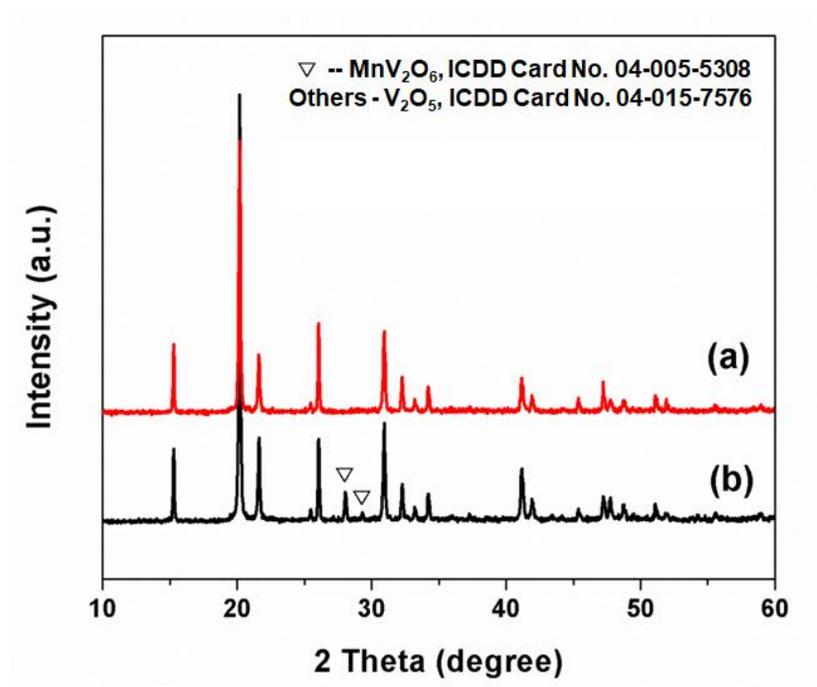


Figure 85. XRD patterns of (a) VO₂(B) and (b) Mn-doped VO₂(B) nanosheets after TGA in air to 600 °C.

4.3.4 Determination of oxidation states of the hydrothermally prepared pure and Mn-doped VO₂(B) nanosheets

In order to determine the oxidation states of vanadium and manganese in the as-prepared samples, we have performed XPS measurements on both pure and Mn-doped VO₂(B) nanosheets. Figure 86 (a) and (b) exhibit typical XPS survey scans. For pure VO₂(B) all peaks are assigned to V, O and C, whereas for Mn-doped VO₂(B) the Mn peaks can be clearly observed, thus, further confirming the existence of Mn ions in the doped samples.

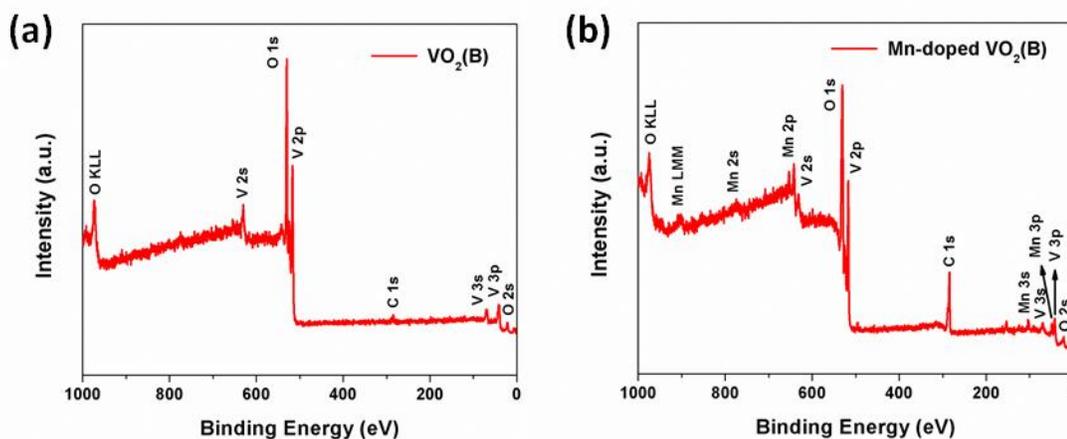


Figure 86. XPS survey scans of (a) pure and (b) Mn-doped VO₂(B) nanosheets.

From Figure 87 (a) and (b) we can see that both the V 2p_{3/2} spectra for the pure and Mn-doped VO₂(B) nanosheets are composed of two components located at ~517.5 and ~516.4 eV respectively, which can be associated with two formal oxidation states, V⁵⁺ and V⁴⁺.^{217,219,226} Typically speaking, the binding energies of V⁵⁺, V⁴⁺, and V³⁺ fall between 517-518 eV, 516-517 eV, and 514-516 eV respectively.²²⁷ Thus it indicates that not all the V⁵⁺ can be reduced to V⁴⁺ due to the hydrothermal reaction conditions, and both V⁵⁺ and V⁴⁺ ions coexist in pure and Mn-doped VO₂(B) nanosheets, although the crystal structure has been changed from V₂O₅ to VO₂(B) during hydrothermal process. Figure 87 (c) shows the relative ratio of V⁵⁺ and V⁴⁺ ions in both samples obtained through fitting V 2p_{3/2} spectra. Clearly it can be seen that the V⁴⁺ concentration in the

Mn-doped VO₂(B) is much higher than that in the pure VO₂(B). In the Mn-doped sample, the molar ratio of V⁴⁺/ (V⁴⁺ + V⁵⁺) is 54%, which is 13% higher than that in pure VO₂(B) (41%). Therefore, Mn doping facilitates the formation of lower valance state vanadium in the as-prepared VO₂(B). The presence of more lower valance state vanadium in Mn-doped VO₂(B) may enhance the sample's electrical conductivity and thus facilitate Na⁺ ion intercalation/deintercalation processes.²¹⁹ The mixed-valance states also suggest the existence of defects, such as vacancies, which may facilitate charge transfer and formation of more open structure for intercalation.^{25,130}

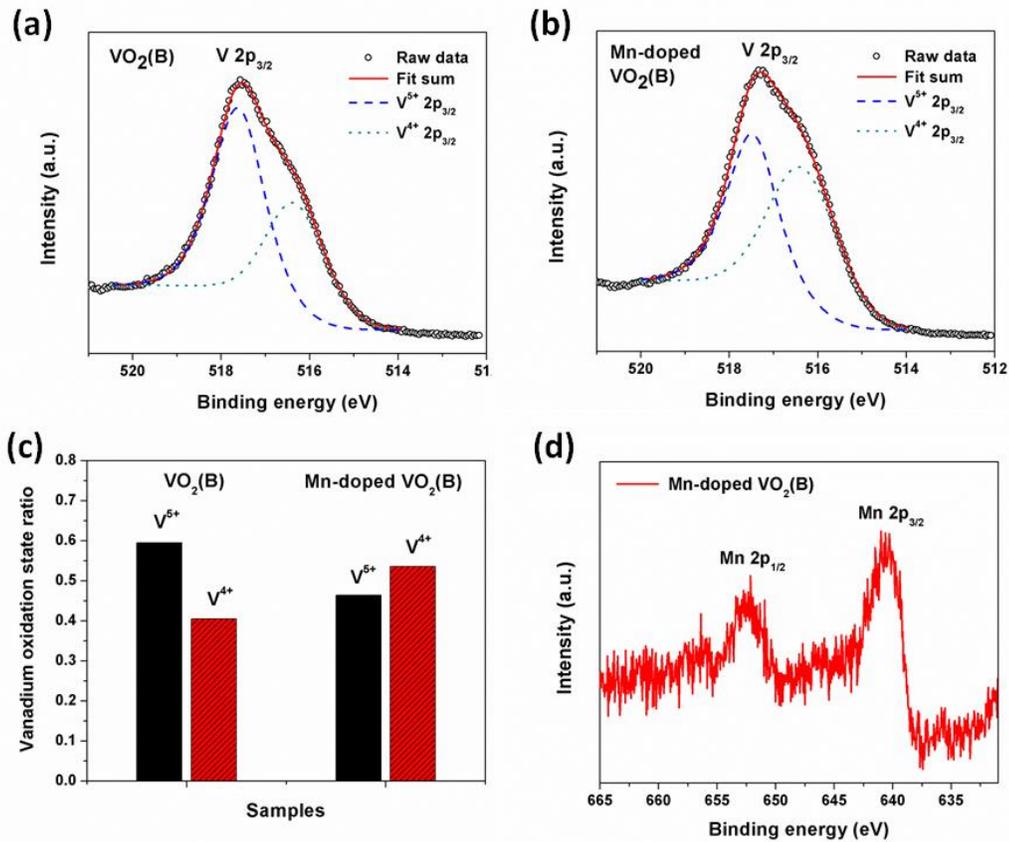
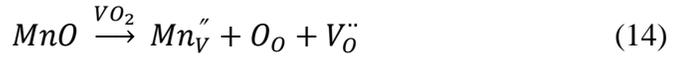


Figure 87. Curve fitting of the V 2p_{3/2} XPS spectra of (a) pure VO₂(B) and (b) Mn-doped VO₂(B) nanosheets; (c) comparison of the relative ratio of V⁵⁺ and V⁴⁺ in pure and Mn-doped VO₂(B) nanosheets; (d) XPS spectra in the Mn 2p regions of Mn-doped VO₂(B).

Figure 87 (d) shows the Mn 2p spectra and the binding energy of Mn 2p_{3/2} is located at approximately 640.3 eV, which can be assigned to Mn²⁺.^{25,180} According to the literature, binding energy values of 642.0 eV are usually assigned to Mn⁴⁺, 641.0 eV to

Mn^{3+} , and 640.0 eV to Mn^{2+} .^{179,180} Thus it indicates that the Mn in the doped samples is still remaining Mn^{2+} . Based on the similarity in ionic radii between $\text{V}^{5+}/\text{V}^{4+}$ and Mn^{2+} in the same coordination, it can be presumed that Mn^{2+} ions entered into the $\text{VO}_2(\text{B})$ crystal lattice during the hydrothermal process and partially substituted $\text{V}^{5+}/\text{V}^{4+}$, leading to the formation of oxygen vacancies. The defect reaction can be written as follows (assume Mn^{2+} substituted V^{4+} sites):



Where Mn_V'' is the manganese substitutional defect, and V_O'' represents oxygen vacancies. Thus, the aliovalent Mn^{2+} doping into the V^{4+} sites may lead to the formation of oxygen vacancies. The presence of oxygen vacancies will result in more open structure, which can promote ease access for Na^+ ions intercalation and diffusion, as well as alleviation of the electrochemical strains. It can also help increase the sample's electrical conductivity and thus facilitate the charge transfer process.¹²⁸

4.3.5 Phase composition and local structure characterization of the hydrothermally prepared pure and Mn-doped $\text{VO}_2(\text{B})$ nanosheets

To get further insight into the phase composition and local structure variation of $\text{VO}_2(\text{B})$ nanosheets with Mn doping, we have performed high-energy X-ray scattering and pair distribution function analysis. The PDF analysis can probe not only the local atomic bonding motifs but also intermediate and long-range order, thus making it an effective tool for investigating the phase composition and local structure distortions induced by metal ion doping.

The PDF data, $G(r)$, collected on both pure and Mn-doped $\text{VO}_2(\text{B})$ nanosheets, have been refined in the range of 1.34 – 90 Å, which are shown in Figure 88 (the data was collected by Rob Koch and Peng Gao at CHESS, and analyzed by Rob Koch). The experimental data of pure $\text{VO}_2(\text{B})$ was fitted by simply using the monoclinic $\text{VO}_2(\text{B})$ crystal structure as starting model, while that of Mn-doped $\text{VO}_2(\text{B})$ was fitted by using both monoclinic $\text{VO}_2(\text{B})$ and tetragonal $\text{VO}_2(\text{A})$ structures, and introduces manganese at the vanadium site. From the fitting results, we observed that the as-prepared pure sample

can be well fitted with single monoclinic VO₂(B) crystal structure, indicating successful formation of VO₂(B) crystal structure during hydrothermal process. In contrast, the best fit of Mn-doped sample needs inclusion of both monoclinic VO₂(B) and tetragonal VO₂(A), which is consistent with the XRD data and further confirms the partial phase transformation from VO₂(B) to VO₂(A) caused by Mn doping. The refined results indicate the presence of 76 mol% VO₂(B) and 24 mol% VO₂(A). No Mn related compounds are needed to improve the fit quality, indicating the complete incorporation of Mn ions into the vanadium oxide lattice without forming undesired phases. Furthermore, an increase of the lattice parameters with Mn-doping has been observed from our refinement data, which can be ascribed to the larger ionic radius of Mn²⁺ compared to V⁵⁺/V⁴⁺.

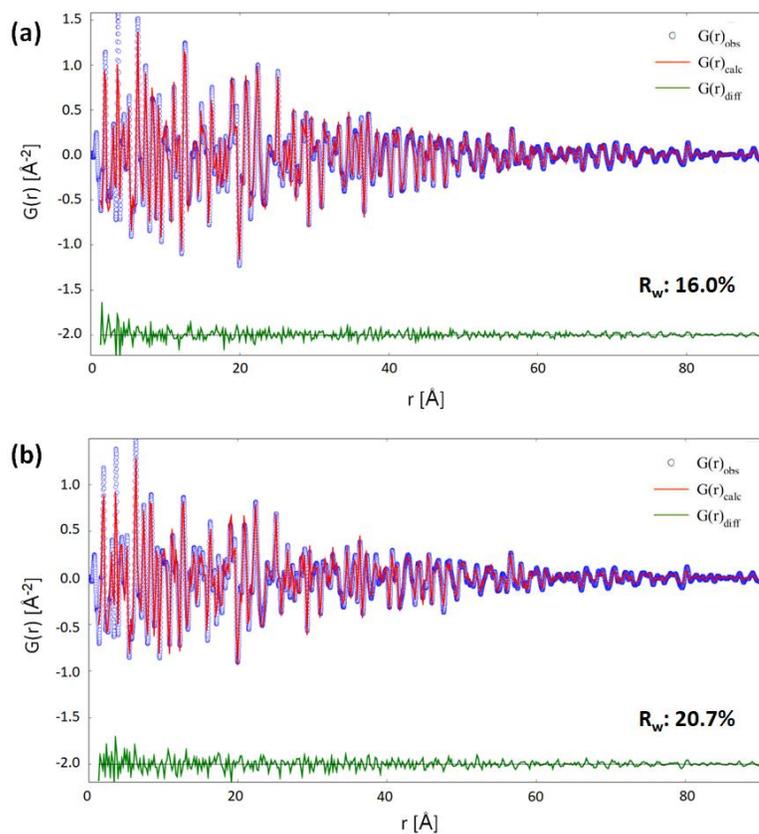


Figure 88. Pair distribution functions (PDFs or $G(r)$ s) of (a) pure VO₂(B) and (b) Mn-doped VO₂(B) nanosheets over 1.34 – 90 \AA r range. The experimental data of pure VO₂(B) was fitted only with monoclinic VO₂(B), while that of Mn-doped VO₂(B) was fitted by using both monoclinic VO₂(B) and tetragonal VO₂(A) structures. (Blue dots are experimental data, red lines are fitted data and the green lines are differences).

In order to get a better understanding of the local structure variation of the pure and Mn-doped VO₂(B) nanosheets, we have qualitatively compared their PDFs, G(r), over low r regions (1 – 7 Å), with the result shown in Figure 89. The first strong peak just below 2 Å (V-O2) and the shoulder at ~1.5-1.7 Å (V-O1) contains the contribution from two adjacent V-O pairs, while the other two strong peaks observed at ~3 Å (V-V1) and ~3.6 Å (V-V2) correspond to the two adjacent V-V bond lengths.

Generally speaking, both pure and Mn-doped VO₂(B) show similar features in extracted PDFs, indicating that the local structures of both samples are similar. However, clear differences can still be observed for both samples. First, with Mn doping several PDF peaks (such as the peaks between 4-4.5 Å and the peak around 6 Å) become slightly broadened, reflecting some minor local structure disorder and distribution of bond lengths.¹⁴⁰ Second, an obvious shift of the V-O1 and V-V1 bonds toward longer distances are observed, which may be related to the incorporation of larger radius Mn²⁺ ions into the V⁴⁺/V⁵⁺ sites. The apparent decrease of peak intensity (V-V2) for the Mn-doped samples also indicates the replacement of Mn on V sites and increased local structural distortion.²²⁸ Third, a shoulder is appear in 2.7-2.9 Å r range for the Mn-doped sample, which is not present in the pure VO₂(B). It is possibly originated from adjacent Mn-Mn or Mn-V bond distances, the V-V bond distances in VO₂(A) phase, or compressed V-V bond length due to the presence of larger adjacent Mn²⁺ ions. Its broad nature also indicates a distribution of bond lengths and thus may attributes to several possible different bond distances.

In general, the above refined PDF data over large r range and qualitative comparison of the experimental PDF data over small r range clearly demonstrates the incorporation of Mn²⁺ into V⁴⁺/ V⁵⁺ sites, the extension of adjacent bond length/unit cell parameters due to larger radius cation substitution, as well as the distortion of the local structure, which we believe will lead to a more defective structures and therefore promote the electrochemical intercalation properties.

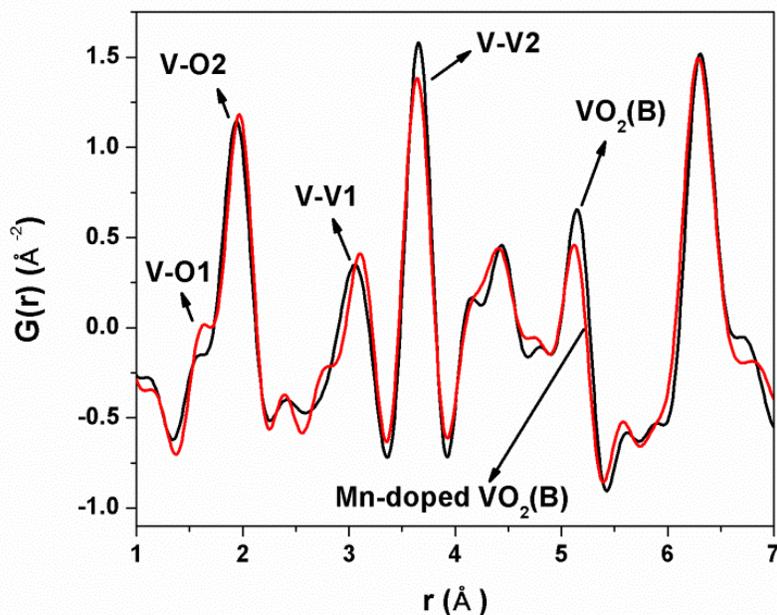


Figure 89. Comparison of the experimental Pair Distribution Functions (PDF) $G(r)$ over low r regions (1 – 7 Å) of pure and Mn-doped $\text{VO}_2(\text{B})$ nanosheets.

4.3.6 Electrochemical measurements of the hydrothermally prepared pure and Mn-doped $\text{VO}_2(\text{B})$ nanosheets

The capacitive properties of the pure and Mn-doped $\text{VO}_2(\text{B})$ nanosheets as supercapacitor electrode materials are evaluated by cyclic voltammetry and galvanostatic charge-discharge measurements in 1M Na_2SO_4 electrolyte solution. Figure 90(a) shows the typical CV curves comparison for both samples at 20 mV/s scan rate. It can be seen that the shape of both CV curves deviates from the ideal rectangular, with broad redox peaks in the potential range of 0.1-0.6 V, indicating the Faradic pseudocapacitive behavior of both electrodes.²²⁹ The CV integral area for Mn-doped $\text{VO}_2(\text{B})$ is obviously larger than that of pure $\text{VO}_2(\text{B})$ at the same scan rate, demonstrating that the Mn-doped $\text{VO}_2(\text{B})$ nanosheets possess a higher specific capacitance. The scan rate dependent CV curves for both samples are shown in Figure 91. With increasing the scan rate from 2 to 100 mV/s, both samples keep their original quasi-rectangular shape, indicating fast redox kinetics and good reversibility. The variation of specific capacitance with scan rate is

shown in Figure 90(b), by which the specific capacitance is calculated by using the following equation:²²⁶

$$C = \frac{1}{mv(V_a - V_c)} \int_{V_c}^{V_a} I(V) dV \quad (15)$$

Where C (F/g) is the specific capacitance, m (g) is the mass of active materials on electrodes, v (V/s) is the scan rate, $(V_a - V_c)$ (V) is the potential window, and $\int_{V_c}^{V_a} I(V) dV$ is the integrated area of each curve. At 2 mV/s scan rate, the specific capacitance of Mn-doped VO₂(B) nanosheets calculated from the CV curve is 203 F/g, which is ~80% higher than that of pure VO₂(B) nanosheets (113 F/g). With increasing scan rate, the specific capacitance decreases gradually for both samples, which is typically observed for pseudocapacitor electrodes due to the kinetic limitation associated with the diffusion of Na⁺ ions.²³⁰ However, even at the highest scan rate employed (100 mV/s), the specific capacitance of Mn-doped VO₂(B) nanosheets (125 F/g) is still ~50% higher than that of pure VO₂(B) nanosheets (84 F/g), indicating its good capacitive performance.

The electrochemical properties of pure and Mn-doped VO₂(B) nanosheets were further evaluated by galvanostatic charge-discharge measurements. Figure 90(c) shows the galvanostatic charge-discharge profiles for both samples at a current density of 0.2 A/g. All the discharge curves are nearly symmetrical to their charge counterparts, demonstrating good capacitive properties of these electrodes.²³¹ The potential does not linearly change with time, a behavior typical for pseudocapacitive materials that involve redox reactions.²⁵ The galvanostatic charge-discharge curves for both samples at different current densities (0.2-10 A/g) are shown in Figure 92, and the specific capacitances obtained by using Equation (13) are summarized in Figure 90(d). At 0.2 A/g, the specific capacitance is calculated to be 201 F/g for the Mn-doped VO₂(B) nanosheets, which is much higher than that of pure VO₂(B) (125 F/g). This is consistent with the results obtained from CV measurements. Also, the specific capacitance decreases gradually for both samples with increasing current density, similar to the results shown in Figure 90(b).

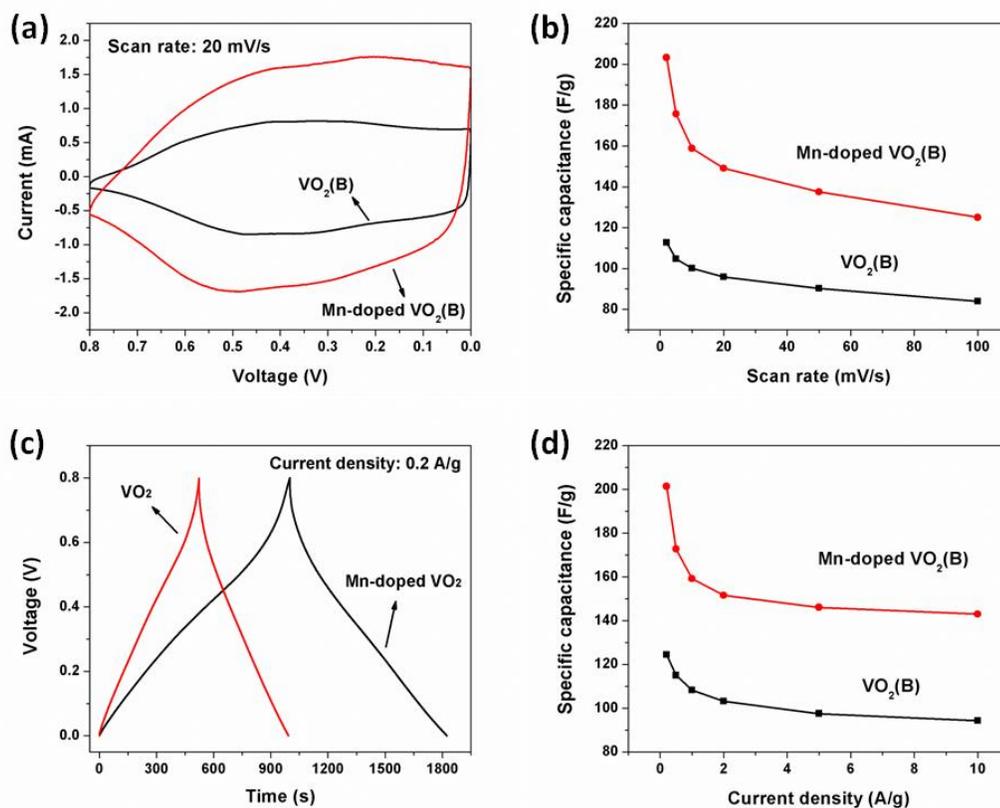


Figure 90. (a) Cyclic voltammogram comparison of the pure and Mn-doped VO₂(B) nanosheets measured in 1M Na₂SO₄ electrolyte solution at a potential window of 0-0.8 V with 20 mV/s scan rate; (b) variation of specific capacitance as a function of scan rate for both samples; (c) Galvanostatic charge-discharge curves of pure and Mn-doped VO₂(B) nanosheets in 1M Na₂SO₄ electrolyte solution at 0.2 A/g current density; (d) comparison of specific capacitance for both samples as a function of current density.

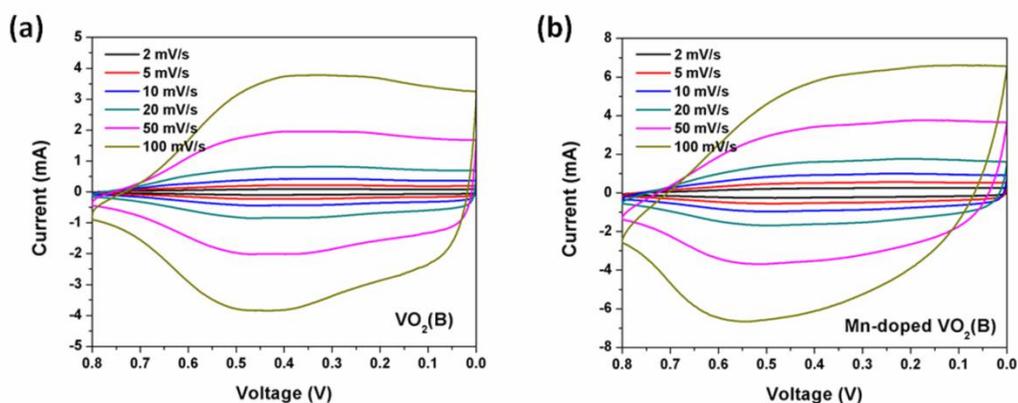


Figure 91. Cyclic voltammogram curves for (a) VO₂(B) and (b) Mn-doped VO₂(B) nanosheets in 1M Na₂SO₄ electrolyte at various scan rates.

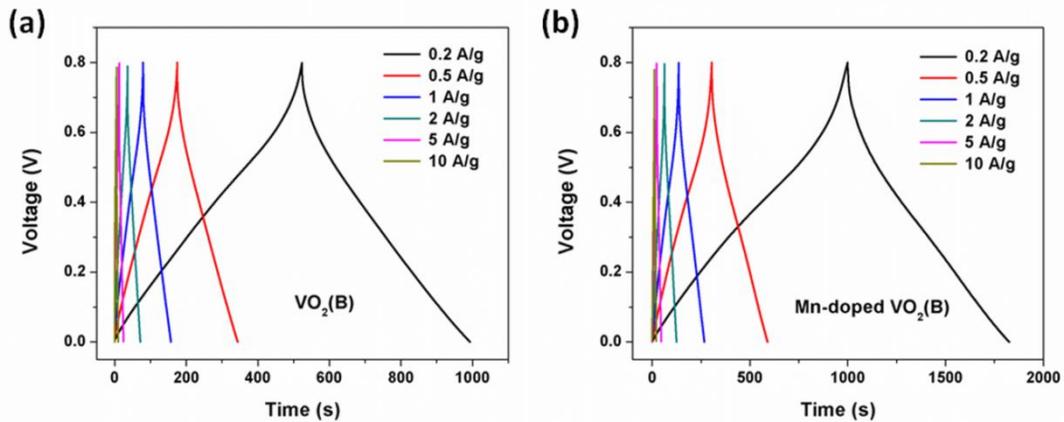


Figure 92. Galvanostatic charge-discharge curves for (a) VO₂(B) and (b) Mn-doped VO₂(B) nanosheets in 1M Na₂SO₄ electrolyte solution at different current densities.

The above electrochemical results obtained from CV and GCD measurements indicate a dramatic increase of the charge storage capacitance of VO₂(B) nanosheets with Mn doping. A possible reason is the formation of the house-of-cards type stacking with smaller nanosheets induced by Mn doping, may provide more accessible surface adsorption sites for alkali cations. However, except the morphology change, other influencing factors are also evaluated. From XRD data and the high energy X-ray scattering and PDF analysis, we observed the presence of 20-30 mol% VO₂(A) phase that is induced by Mn doping. Thus, in order to elucidate the contribution of VO₂(A) to the charge storage, we have synthesized VO₂(A) nanobelts by using a similar hydrothermal method and measured its specific capacitance.

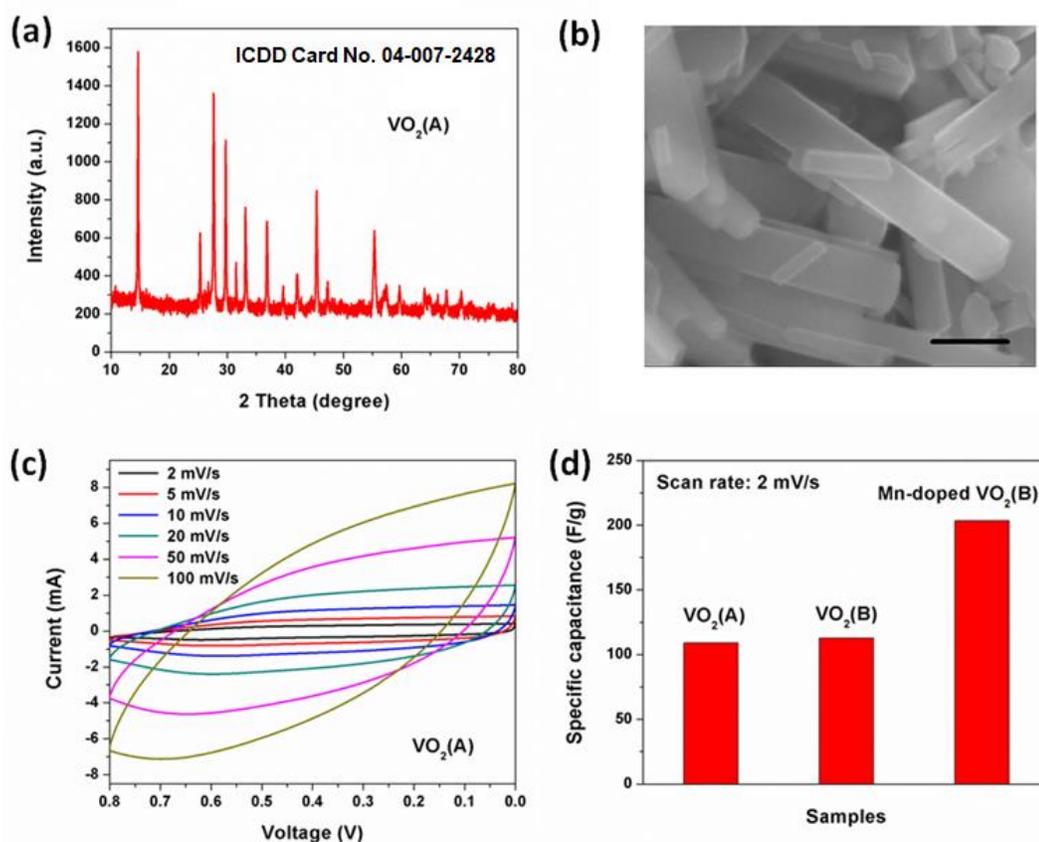


Figure 93. (a) The XRD pattern and (b) SEM image of the hydrothermally prepared VO₂(A). Scale bar, 500 nm. (c) Cyclic voltammety curves for VO₂(A) in 1M Na₂SO₄ electrolyte at various scan rates. (d) Specific capacitance comparison of VO₂(A), VO₂(B) and Mn-doped VO₂(B) at 2 mV/s scan rate.

The typical XRD pattern and SEM image of the as-prepared VO₂(A) are shown in Figure 93(a-b), and the cyclic voltammety curves measured in 1M Na₂SO₄ electrolyte at various scan rates are shown in Figure 93(c). The specific capacitance of VO₂(A) measured at 2 mV/s scan rate is similar to that of pure VO₂(B), but is 46 % smaller than that of the Mn-doped sample, with the results shown in Figure 93(d). Thus, it can be concluded that the formation of VO₂(A) is not a main reason for the dramatic increase of the capacitance of Mn-doped samples.

Generally speaking, the total current response from the CV curves can be described as a combination of both capacitive and intercalation/de-intercalation currents. Accordingly, the total electrochemical stored charge in the electrodes originates from

both capacitive and intercalation mechanism. Besides, the capacitive mechanism consists of two different processes, including faradic contribution from the fast surface redox or pseudocapacitive process, as well as the nonfaradic contribution from the fast electric double layer at the electrode/electrolyte interface due to ion adsorption/desorption.^{230,232,233} Whereas the capacitive processes are usually occur at the electrode surface without diffusion limit, the intercalation mechanism is mainly controlled by the diffusion of electrolyte cations into the interior of electrode materials' microstructures. The capacitive effects (including both surface pseudocapacitance and electric double layer capacitance) and diffusion controlled process (intercalation mechanism) can be identified by analyzing the CV curves at various scan rates according to:^{234,235}

$$i = av^b \quad (16)$$

Where the measured current i (A) obeys a power law relationship with the scan rate v (V/s). Both a and b are adjustable parameters, and b -values can be determined from the slope of linear fit of $\log(i)$ vs. $\log(v)$ plot at a fixed potential (V). Typically, there are two well-defined conditions for the b value. When $b = 0.5$, the electrode kinetics are controlled by the diffusion process, which indicates a Faradic process that is accompanied with intercalation/de-intercalation of the electrolyte ions into/from the electrode. When $b = 1.0$, the current response is representative of a capacitive process or non-diffusion controlled process.^{236,237} Thus, the charge storage mechanism of the electrodes can be identified by evaluating b -values at fixed potentials.

A plot of $\log(i)$ vs. $\log(v)$ for pure and Mn-doped VO₂(B) nanosheets at different potentials are shown in Figure 94(a-b). The corresponding b -values obtained at various potentials for both samples are compared in Figure 94(c). It clearly shows that the value of b for pure VO₂(B) is very close to 1.0 at different potential (except at 0.6 V), demonstrating that its current response is primarily capacitive in nature. In contrast, the b -values at different potentials for Mn-doped VO₂(B) are much smaller than that of pure VO₂(B), indicating both capacitive and intercalation mechanisms are involved in the charge storage process. The involvement of intercalation pseudocapacitance is another

important contributing factor for the significantly enhanced charge storage capability of the samples with Mn-doping.

The observed difference of b-value is also consistent with the capacitance comparison as shown in Figure 90(b, d). At low scan rate (such as 2 mV/s), the Mn doping leads to much improved capacitance, which is mainly attributed to the intercalation charge storage mechanism. With increasing scan rate, the capacitance of Mn-doped VO₂(B) decreases a little faster than that of pure VO₂(B) (62% capacitance retention for Mn-doped VO₂(B), vs. 74% capacitance retention for pure VO₂(B), with scan rate increased from 2 to 100 mV/s). This is because the intercalation mechanism is a diffusion-controlled process, thus the Na⁺ ion insertion is limited at high scan rate and thereby results in faster decay of the intercalation pseudocapacitance when increasing scan rates. However, we still observed much higher capacitance of Mn-doped VO₂(B) at 100 mV/s scan rate, which clearly indicates the advantages of using Mn doping as an effective way to modify the morphology and structures of VO₂(B) nanosheets and further increase their charge storage properties.

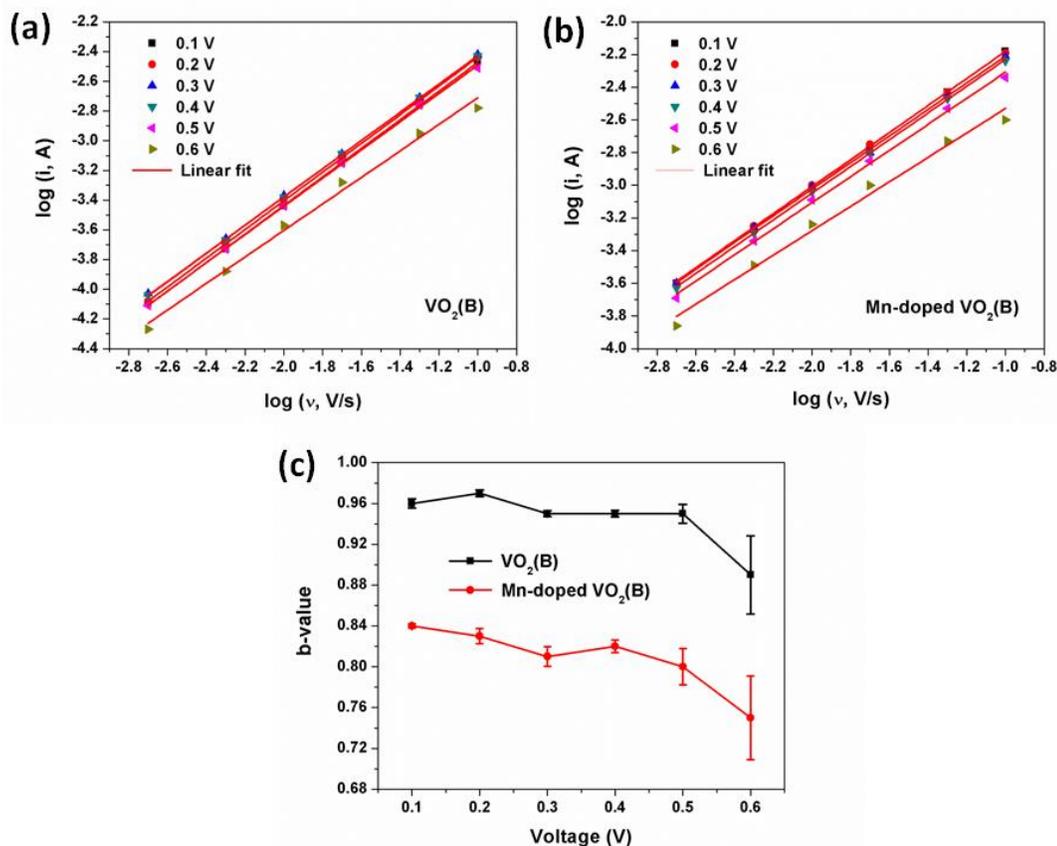


Figure 94. Variation of $\log(i)$ vs. $\log(v)$ for power law fitted at various potentials for (a) $VO_2(B)$ and (b) Mn-doped $VO_2(B)$ nanosheets; (c) b-value for the pure and Mn-doped $VO_2(B)$ nanosheets plotted as a function of potentials for cathodic scans.

Electrochemical impedance spectroscopy (EIS) was also employed to measure the charge transfer resistance of each electrode, with the results shown in Figure 95(a). Both plots exhibit a straight line in the low-frequency region and a single semicircle in the high-frequency region, indicating a diffusion-limited step in the low frequency region and a charge transfer limited step in the high-frequency region.^{190,238} The Nyquist plots were further modelled and interpreted by using an appropriate electrical equivalent circuit, which is shown in the inset in Figure 95(a). R_s , R_f and R_{ct} are ohmic resistance (total resistance of the electrolyte and electrical contacts), film resistance, and charge transfer resistance respectively. Z_w is the Warburg resistance which is related to ion diffusion in the electrolyte, and CPE is the constant phase element.^{191,239} The calculated charge transfer resistance (R_{ct}) extracted from the high-frequency range of the Mn-doped $VO_2(B)$

is 5.5Ω , which is only about half of that of the pure $\text{VO}_2(\text{B})$ nanosheets (10.3Ω). This result indicates an increased electrical conductivity and improved electrode kinetics for Mn-doped $\text{VO}_2(\text{B})$ nanosheets, which will facilitate the charge transfer process and makes the electrochemical reaction proceed more easily than that of pure $\text{VO}_2(\text{B})$ nanosheets.

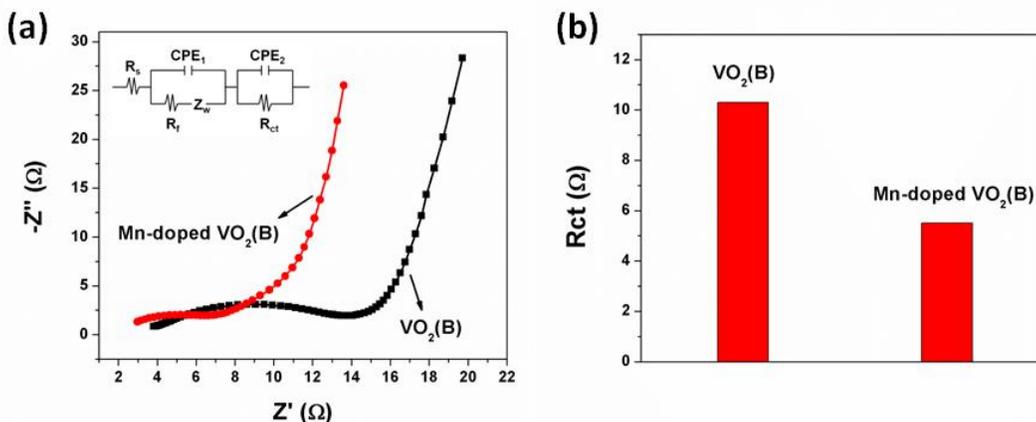


Figure 95. (a) Nyquist plots of pure and Mn-doped $\text{VO}_2(\text{B})$ nanosheets in the frequency range of 0.01 Hz-100 kHz at an open circuit potential of 5 mV (inset shows the electrical equivalent circuit used for fitting the impedance spectra); (b) comparison of the charge transfer resistance of the as-prepared two samples (values obtained from the fitted data).

Excellent cycling stability is also required for electrochemical supercapacitor electrode materials. Therefore, we have measured the cycling performance of pure and Mn-doped $\text{VO}_2(\text{B})$ nanosheets by repeating the galvanostatic charge-discharge test at a current density of 5 A/g, with the results shown in Figure 96. Surprisingly, we found out that after 1000 consecutive cycles at very high current density, the Mn-doped $\text{VO}_2(\text{B})$ can still retain 67% of its initial specific capacitance, which is much higher than that of pure $\text{VO}_2(\text{B})$ (only retains 32% of its initial capacitance). The capacitance retention for Mn-doped $\text{VO}_2(\text{B})$ nanosheets is even better than several vanadium oxide based composite electrodes reported in literature, such as $\text{VO}_2(\text{B})$ -multiwalled carbon nanotubes,²⁴⁰ graphene/ VO_2 hybrid electrode,²⁴¹ and the VO_2 /polyaniline coaxial nanobelts.²³¹ The improved cycling performance of Mn-doped $\text{VO}_2(\text{B})$ nanosheets is obviously related to the doping effects of Mn ions in the $\text{VO}_2(\text{B})$ crystal lattice. The house-of-cards stacking of flexible 2-D $\text{VO}_2(\text{B})$ nanosheets results in more accessible surface areas and thus

promotes the fast diffusion of Na^+ ions when cycling. The aliovalent doping of larger Mn^{2+} cations into $\text{V}^{4+}/\text{V}^{5+}$ sites also increases local distortion and the number of defects, which may help facilitate the insertion of Na^+ ions in the electrode materials. Besides, the formation of oxygen vacancies may help alleviate the stress and strain accompanied by fast Na^+ ion intercalation/de-intercalation process, thus improving the long-term cycling stability.

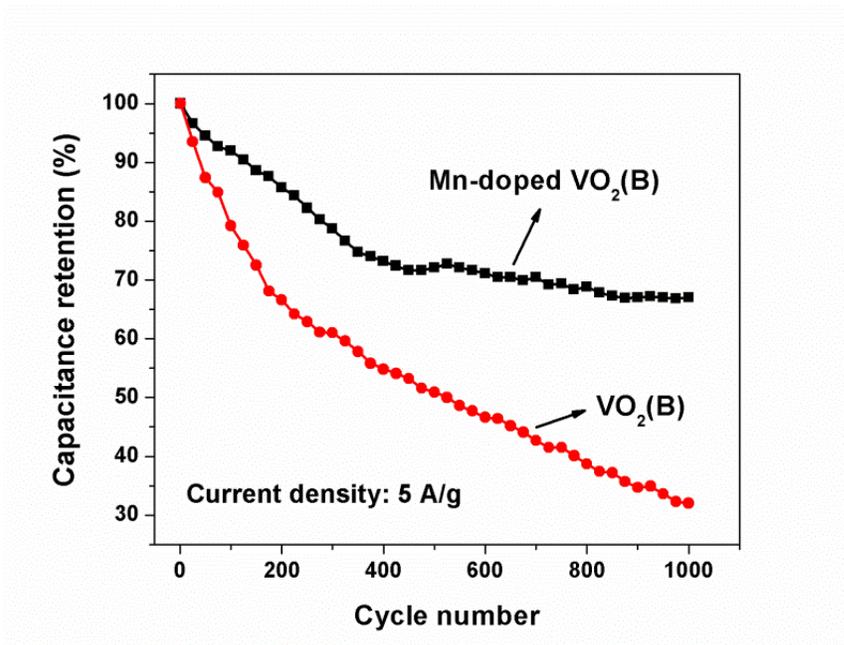


Figure 96. Cycling stability of pure and Mn-doped $\text{VO}_2(\text{B})$ nanosheets at constant current density of 5 A/g between 0 and 0.8 V.

4.4 Summary: Mn doped VO₂(B) nanosheets

VO₂(B) nanosheets, one of the promising electrode materials for pseudocapacitors, has attracted much attention in recent years due to its various vanadium oxidation states (II-V) that can provides much wider potential window and higher capacities. Its corner and edge sharing structure also leads to an increased resistance to V-O bond cleavage during cation intercalation, which results in a stable structure during electrochemical cycling.

In this research, we have prepared the VO₂(B) nanosheets by using the hydrothermal method. The hydrothermal reaction conditions have been investigated systematically, in order to obtain the VO₂(B) nanosheets with desired morphology. Equilibration of the hydrothermally obtained VO₂(B) nanosheets in different pH environments has been used as the first attempt to introduce defects into the VO₂(B) structures, a similar way that has been discussed in Chapter II and confirmed effective for δ -MnO₂ nanosheets. However, it was found that although the pH equilibrated samples exhibit more porous nanostructures and higher capacitance compared with the as-prepared VO₂(B) nanosheets, no apparent difference in charge storage properties of the three different pH equilibrated samples was observed. Thus it indicates that the different crystal structure of VO₂(B) and redox stability of vanadium compared with the δ -MnO₂ makes it difficult to form the similar point defects by using the low pH equilibration method.

Another effective and commonly used way to tune the defect structure and enhance the oxide properties, doping, has been further investigated as an alternative method to modify the structure of VO₂(B) nanosheets. The Mn-doped VO₂(B) nanosheets have been successfully prepared by a simple one-step hydrothermal reaction with the direct addition of the manganese salt. 3-D porous nanostructures built from 2-D nanosheets have been obtained, without the formation of undesired Mn precipitates. Compared with pure VO₂(B) nanosheets, 8.7 mol% Mn-doping results in 80 % higher specific capacitance, $\times 2$ smaller charge transfer resistance, as well as $\times 2$ improvement in cyclic stability. The improved electrochemical charge storage properties of the Mn-doped samples can be attributed to enhanced mass transfer kinetics due to the formation of house-of-cards stacking with thinner nanosheets, the incorporation of larger Mn²⁺ cations

that leads to a more defective structures, as well as the formation of more V^{4+} and oxygen vacancies that increase the electrical conductivity and also help alleviate the electrochemical strains, which promotes the charge transfer process and improves the cyclic stability. Therefore, with these advantages, we believe such aliovalent doping based on Mn-doped $VO_2(B)$ nanosheets prototype shown in this research is an effective strategy to tune the defect structure (other than the pH equilibration method for δ - MnO_2 nanosheets), and can be extended to synthesize other transition metal doped nanostructures. It will also benefit other application fields such as photocatalysis, gas/bio sensors, etc., other than charge storage devices.

SUMMARY AND CONCLUSIONS

This project provides the first quantitative assessment of the electrochemical effects of intentional cation defects on ion intercalation in layered δ -MnO₂ nanosheet systems for Faradaic electrochemical supercapacitors. We also aimed to determine the atomic-scale charge/discharge mechanisms in the defective nanosheets by using advanced characterization tools. Further extension of the defect studies to other similar model systems, such as VO₂(B) nanosheets, by using doping, confirms the feasibility and effectiveness of improving the charge storage capability of layered metal oxide nanosheets through tuning their defect structures.

First, we have successfully prepared δ -MnO₂ nanosheets by exfoliation of the crystalline K_xMnO₂. The subsequent flocculation/reassembly processes have been systematically investigated, in order to get desired 3-D porous nanostructures with large surface area. Equilibrating the reassembled nanosheets in varied pH controls the extent of Mn⁴⁺→Mn³⁺ reduction as well as creating charged defect pairs we term “surface Frenkel defects” comprising a Mn vacancy within the sheet and a six-fold coordinated Mn³⁺ site on the surface of the nanosheet. The XANES data indicate an increase of the Mn³⁺/Mn⁴⁺ ratio with decreasing pH equilibration values, and the X-ray scattering and PDF analysis shows that equilibration at low pH leads to the formation of more Mn vacancies in the reassembled δ -MnO₂ nanostructures. Further electrochemical measurements show the first quantitative links of Mn defects to electrochemical capacitance and charge transfer resistance, indicating that Mn surface Frenkel defects in δ -MnO₂ nanosheets increase Na⁺ ion intercalation capacities.

Second, we take a further step to understand the correlations between the defects/cation vacancies and the charge storage process. An optimized electrophoretic deposition approach has been developed to prepare carbon and binder-free electrodes, which is necessary for the *in-situ* X-ray scattering measurements. K⁺ ion was chosen as an alternative electrolyte to replace Na⁺ ion, which is a stronger X-ray scatterer and can give rise to the same charge storage behavior. The *ex-situ* Raman spectroscopy suggests (although not clearly) increased Jahn-Teller distortion upon cation intercalation during

the cathodic process, which is more pronounced in pH = 2 equilibrated MnO₂. The *in-situ* XRD and PDF data also reveals reversible in-plane expansion/contraction of the nanosheet layers upon charge/discharge, as well as unchanged interlayer spacing during cycling. The *in-situ* XANES spectra shows that the Mn undergoes a reversible shift of the absorption edge to lower energies when decreasing the applied potentials, indicating the formation of Mn³⁺ and confirms that the Faradaic redox reaction is the main charge storage mechanism. A smaller change of Mn oxidation states as compared to the CV loops determined values has been observed for the MnO₂ nanosheets with higher defect content, implying that a large amount of Mn vacancies in the MnO₂ nanosheets can serve as new intercalation sites for potassium ions without change of Mn oxidation state.

Finally, we investigated the effects of doping defects on the structural and charge storage properties of another layered oxide, VO₂(B) nanosheets. Pure and Mn-doped VO₂(B) nanosheets have been successfully prepared by a simple one-step hydrothermal reaction. Compared with pure VO₂(B) nanosheets, 8.7 mol% Mn-doping results in 80 % higher specific capacitance, ×2 smaller charge transfer resistance, as well as ×2 improvement in cyclic stability. The improved charge storage capability can be attributed to enhanced mass transfer kinetics due to the formation of house-of-cards stacking that provides more accessible surface absorption sites, the incorporation of larger substituted cations that leads to a more defective structure and thereby facilitates the Na⁺ ion intercalation, as well as the formation of more V⁴⁺ and oxygen vacancies that increase the electrical conductivity and also help alleviate the electrochemical strains. With these advantages, we believe the aliovalent doping is also an effective strategy to tune the defect structures (other than the pH equilibration method for δ-MnO₂ nanosheets), and can be extended to synthesize other transition metal doped nanostructures. In summary, this research work provides a new way for the design of next generation electrochemical supercapacitors through controlling the defect structures of layered transition metal oxide nanosheets.

FUTURE WORK

As stated previously, a correlation between the quantity of defects in our 2-D δ -MnO₂ nanosheet system and the quantity of alkali cations electrochemically inserted has been established. Our preliminary *in-situ* data also indicates reversible structural variation and Mn oxidation state change upon charge/discharge, as well as slower reduction rate of Mn, which are all shed light on understanding the charge storage mechanism. However, more works are still needed to get a deeper insight of the whole picture.

First, the *in-situ* X-ray PDF analysis and Raman spectroscopy of the MnO₂ nanosheets with different defect content are needed, in order to investigate the local structure variation as a function of both charge states and defect content. The operando studies that collecting the data without stopping the electrochemical cycling will also need to be done in the future, which can help elucidating the charge storage process more accurately. Second, in order to understand the influence of surface and intercalated water species/hydroxyls on alkali cation sorption and insertion in δ -MnO₂ nanosheets, we have conducted inelastic neutron scattering and neutron PDF (NPDF) experiments on samples with different defect content and charge states. The data needs to be further analyzed and we believe it can help elucidate the alkali cation sorption sites. Third, high-resolution NMR spectroscopy of Mn and alkali cations may also performed in the future, which can give rise to their local coordination environments and thereby assist clarifying the alkali cation intercalation sites. Fourth, DFT calculations could also be performed in the future, which can provide greater insight into the alkali cations intercalation sites and diffusion energy barriers in the defective MnO₂ nanosheets, thus complementing our experimental results. Finally, exploratory studies of preparing other defective layered transition metal oxide nanosheets will also be conducted in the future, which can help further investigate the feasibility and effectiveness of improving their charge storage properties by controlling their defect structures.

REFERENCES

1. B. E. Conway, *Electrochemical Supercapacitors: Scientific Fundamentals and Technological Applications*. Springer Science & Business Media, New York, 2013.
2. W. Wei, X. Cui, W. Chen, and D. G. Ivey, "Manganese Oxide-Based Materials as Electrochemical Supercapacitor Electrodes," *Chem. Soc. Rev.*, **40** [3] 1697-721 (2011).
3. P. Simon, Y. Gogotsi, and B. Dunn, "Where Do Batteries End and Supercapacitors Begin?" *Science*, **343** [6176] 1210-1 (2014).
4. G. Wang, L. Zhang, and J. Zhang, "A Review of Electrode Materials for Electrochemical Supercapacitors," *Chem. Soc. Rev.*, **41** [2] 797-828 (2012).
5. S. Oh and K. Kim, "Synthesis of a New Mesoporous Carbon and Its Application to Electrochemical Double-Layer Capacitors," *Chem. Commun.*, [21] 2177-8 (1999).
6. C. Meng, C. Liu, L. Chen, C. Hu, and S. Fan, "Highly Flexible and All-Solid-State Paperlike Polymer Supercapacitors," *Nano Lett.*, **10** [10] 4025-31 (2010).
7. S. Chen, J. Zhu, X. Wu, Q. Han, and X. Wang, "Graphene Oxide-MnO₂ Nanocomposites for Supercapacitors," *ACS Nano*, **4** [5] 2822-30 (2010).
8. B. Conway, V. Birss, and J. Wojtowicz, "The Role and Utilization of Pseudocapacitance for Energy Storage by Supercapacitors," *J. Power Sources*, **66** [1-2] 1-14 (1997).
9. B. Conway and W. Pell, "Double-Layer and Pseudocapacitance Types of Electrochemical Capacitors and Their Applications to the Development of Hybrid Devices," *J. Solid State Electrochem.*, **7** [9] 637-44 (2003).
10. E. Frackowiak, K. Jurewicz, S. Delpeux, and F. Béguin, "Nanotubular Materials for Supercapacitors," *J. Power Sources*, **97**, 822-5 (2001).
11. S. C. Pang, M. A. Anderson, and T. W. Chapman, "Novel Electrode Materials for Thin-Film Ultracapacitors: Comparison of Electrochemical Properties of Sol-Gel-Derived and Electrodeposited Manganese Dioxide," *J. Electrochem. Soc.*, **147** [2] 444-50 (2000).

12. M. Toupin, T. Brousse, and D. Bélanger, "Charge Storage Mechanism of MnO₂ Electrode Used in Aqueous Electrochemical Capacitor," *Chem. Mater.*, **16** [16] 3184-90 (2004).
13. C. M. Chuang, C. W. Huang, H. Teng, and J. M. Ting, "Effects of Carbon Nanotube Grafting on the Performance of Electric Double Layer Capacitors," *Energy Fuels*, **24** [12] 6476-82 (2010).
14. V. Augustyn, J. Come, M. A. Lowe, J. W. Kim, P. L. Taberna, S. H. Tolbert, H. D. Abruña, P. Simon, and B. Dunn, "High-Rate Electrochemical Energy Storage through Li⁺ Intercalation Pseudocapacitance," *Nat. Mater.*, **12** [6] 518-22 (2013).
15. V. Augustyn, P. Simon, and B. Dunn, "Pseudocapacitive Oxide Materials for High-Rate Electrochemical Energy Storage," *Energy Environ. Sci.*, **7** [5] 1597-614 (2014).
16. M. Okubo, E. Hosono, J. Kim, M. Enomoto, N. Kojima, T. Kudo, H. Zhou, and I. Honma, "Nanosize Effect on High-Rate Li-Ion Intercalation in LiCoO₂ Electrode," *J. Am. Chem. Soc.*, **129** [23] 7444-52 (2007).
17. A. Balducci, R. Dugas, P.-L. Taberna, P. Simon, D. Plee, M. Mastragostino, and S. Passerini, "High Temperature Carbon-Carbon Supercapacitor Using Ionic Liquid as Electrolyte," *J. Power Sources*, **165** [2] 922-7 (2007).
18. M. Zhi, F. Yang, F. Meng, M. Li, A. Manivannan, and N. Wu, "Effects of Pore Structure on Performance of an Activated-Carbon Supercapacitor Electrode Recycled from Scrap Waste Tires," *ACS Sustain. Chem. Eng.*, **2** [7] 1592-8 (2014).
19. C. Liu, M. Liu, F. Li, and H. Cheng, "Frequency Response Characteristic of Single-Walled Carbon Nanotubes as Supercapacitor Electrode Material," *Appl. Phys. Lett.*, **92** [14] 143108 3pp. (2008).
20. D. N. Futaba, K. Hata, T. Yamada, T. Hiraoka, Y. Hayamizu, Y. Kakudate, O. Tanaike, H. Hatori, M. Yumura, and S. Iijima, "Shape-Engineerable and Highly Densely Packed Single-Walled Carbon Nanotubes and Their Application as Super-Capacitor Electrodes," *Nat. Mater.*, **5** [12] 987-94 (2006).
21. G. A. Snook, P. Kao, and A. S. Best, "Conducting-Polymer-Based Supercapacitor Devices and Electrodes," *J. Power Sources*, **196** [1] 1-12 (2011).
22. Y. Shi, L. Peng, Y. Ding, Y. Zhao, and G. Yu, "Nanostructured Conductive Polymers for Advanced Energy Storage," *Chem. Soc. Rev.*, **44** [19] 6684-96 (2015).

23. K. Wang, H. Wu, Y. Meng, and Z. Wei, "Conducting Polymer Nanowire Arrays for High Performance Supercapacitors," *Small*, **10** [1] 14-31 (2014).
24. C. C. Hu, K. H. Chang, M. C. Lin, and Y. T. Wu, "Design and Tailoring of the Nanotubular Arrayed Architecture of Hydrated RuO₂ for Next Generation Supercapacitors," *Nano Lett.*, **6** [12] 2690-5 (2006).
25. P. Gao, P. Metz, T. Hey, Y. Gong, D. Liu, D. D. Edwards, J. Y. Howe, R. Huang, and S. T. Misture, "The Critical Role of Point Defects in Improving the Specific Capacitance of δ -MnO₂ Nanosheets," *Nat. Commun.*, **8**, 14559 10pp. (2017).
26. S. I. Kim, J. S. Lee, H. J. Ahn, H. K. Song, and J. H. Jang, "Facile Route to an Efficient NiO Supercapacitor with a Three-Dimensional Nanonetwork Morphology," *ACS Appl. Mater. Interfaces*, **5** [5] 1596-603 (2013).
27. S. K. Meher and G. R. Rao, "Ultralayered Co₃O₄ for High-Performance Supercapacitor Applications," *J. Phys. Chem. C*, **115** [31] 15646-54 (2011).
28. R. K. Selvan, I. Perelshtein, N. Perkas, and A. Gedanken, "Synthesis of Hexagonal-Shaped SnO₂ Nanocrystals and SnO₂@C Nanocomposites for Electrochemical Redox Supercapacitors," *J. Phys. Chem. C*, **112** [6] 1825-30 (2008).
29. B. Saravanakumar, K. K. Purushothaman, and G. Muralidharan, "Interconnected V₂O₅ Nanoporous Network for High-Performance Supercapacitors," *ACS Appl. Mater. Interfaces*, **4** [9] 4484-90 (2012).
30. J. Rajeswari, P. S. Kishore, B. Viswanathan, and T. K. Varadarajan, "One-Dimensional MoO₂ Nanorods for Supercapacitor Applications," *Electrochem. Commun.*, **11** [3] 572-5 (2009).
31. S. Shivakumara, T. R. Penki, and N. Munichandraiah, "Synthesis and Characterization of Porous Flowerlike α -Fe₂O₃ Nanostructures for Supercapacitor Application," *ECS Electrochem. Lett.*, **2** [7] A60-2 (2013).
32. Y. Zhang, H. Feng, X. Wu, L. Wang, A. Zhang, T. Xia, H. Dong, X. Li, and L. Zhang, "Progress of Electrochemical Capacitor Electrode Materials: A Review," *Int. J. Hydrogen Energy*, **34** [11] 4889-99 (2009).
33. Q. Y. Li, Z. S. Li, L. Lin, X. Wang, Y. F. Wang, C. H. Zhang, and H. Q. Wang, "Facile Synthesis of Activated Carbon/Carbon Nanotubes Compound for Supercapacitor Application," *Chem. Eng. J.*, **156** [2] 500-4 (2010).
34. C. Du and N. Pan, "High Power Density Supercapacitor Electrodes of Carbon Nanotube Films by Electrophoretic Deposition," *Nanotechnology*, **17** [21] 5314-8 (2006).

35. C. Lee, X. Wei, J. W. Kysar, and J. Hone, "Measurement of the Elastic Properties and Intrinsic Strength of Monolayer Graphene," *Science*, **321** [5887] 385-8 (2008).
36. S. Park and R. S. Ruoff, "Chemical Methods for the Production of Graphenes," *Nat. Nanotechnol.*, **4** [4] 217-24 (2009).
37. C. Liu, Z. Yu, D. Neff, A. Zhamu, and B. Z. Jang, "Graphene-Based Supercapacitor with an Ultrahigh Energy Density," *Nano Lett.*, **10** [12] 4863-8 (2010).
38. P. Sharma and T. Bhatti, "A Review on Electrochemical Double-Layer Capacitors," *Energy Convers. Manag.*, **51** [12] 2901-12 (2010).
39. L. Z. Fan and J. Maier, "High-Performance Polypyrrole Electrode Materials for Redox Supercapacitors," *Electrochem. Commun.*, **8** [6] 937-40 (2006).
40. Y. K. Zhou, B. L. He, W. J. Zhou, J. Huang, X. H. Li, B. Wu, and H. L. Li, "Electrochemical Capacitance of Well-Coated Single-Walled Carbon Nanotube with Polyaniline Composites," *Electrochim. Acta*, **49** [2] 257-62 (2004).
41. V. Gupta and N. Miura, "High Performance Electrochemical Supercapacitor from Electrochemically Synthesized Nanostructured Polyaniline," *Mater. Lett.*, **60** [12] 1466-9 (2006).
42. K. R. Prasad, K. Koga, and N. Miura, "Electrochemical Deposition of Nanostructured Indium Oxide: High-Performance Electrode Material for Redox Supercapacitors," *Chem. Mater.*, **16** [10] 1845-7 (2004).
43. H. Li, J. Wang, Q. Chu, Z. Wang, F. Zhang, and S. Wang, "Theoretical and Experimental Specific Capacitance of Polyaniline in Sulfuric Acid," *J. Power Sources*, **190** [2] 578-86 (2009).
44. R. Sharma, A. Rastogi, and S. Desu, "Pulse Polymerized Polypyrrole Electrodes for High Energy Density Electrochemical Supercapacitor," *Electrochem. Commun.*, **10** [2] 268-72 (2008).
45. C. Arbizzani, M. Mastragostino, and F. Soavi, "New Trends in Electrochemical Supercapacitors," *J. Power Sources*, **100** [1] 164-70 (2001).
46. A. Laforgue, P. Simon, C. Sarrazin, and J. F. Fauvarque, "Polythiophene-Based Supercapacitors," *J. Power Sources*, **80** [1] 142-8 (1999).

47. W. Li, J. Chen, J. Zhao, J. Zhang, and J. Zhu, "Application of Ultrasonic Irradiation in Preparing Conducting Polymer as Active Materials for Supercapacitor," *Mater. Lett.*, **59** [7] 800-3 (2005).
48. K. Lota, V. Khomenko, and E. Frackowiak, "Capacitance Properties of Poly (3, 4-Ethylenedioxythiophene)/Carbon Nanotubes Composites," *J. Phys. Chem. Solids*, **65** [2] 295-301 (2004).
49. D. D. Zhao, S. J. Bao, W. J. Zhou, and H. L. Li, "Preparation of Hexagonal Nanoporous Nickel Hydroxide Film and Its Application for Electrochemical Capacitor," *Electrochem. Commun.*, **9** [5] 869-74 (2007).
50. Q. Jia, S. Song, X. Wu, J. Cho, S. Foltyn, A. Findikoglu, and J. Smith, "Epitaxial Growth of Highly Conductive RuO₂ Thin Films on (100) Si," *Appl. Phys. Lett.*, **68** [8] 1069-71 (1996).
51. I. H. Kim and K. B. Kim, "Electrochemical Characterization of Hydrous Ruthenium Oxide Thin-Film Electrodes for Electrochemical Capacitor Applications," *J. Electrochem. Soc.*, **153** [2] A383-9 (2006).
52. C. C. Hu, C. H. Lee, and T. C. Wen, "Oxygen Evolution and Hypochlorite Production on Ru-Pt Binary Oxides," *J. Appl. Electrochem.*, **26** [1] 72-82 (1996).
53. M. Ramani, B. S. Haran, R. E. White, and B. N. Popov, "Synthesis and Characterization of Hydrous Ruthenium Oxide-Carbon Supercapacitors," *J. Electrochem. Soc.*, **148** [4] A374-80 (2001).
54. S. Ferro and A. De Battisti, "Electrocatalysis and Chlorine Evolution Reaction at Ruthenium Dioxide Deposited on Conductive Diamond," *J. Phys. Chem. B*, **106** [9] 2249-54 (2002).
55. J. Zheng, P. Cygan, and T. Jow, "Hydrous Ruthenium Oxide as an Electrode Material for Electrochemical Capacitors," *J. Electrochem. Soc.*, **142** [8] 2699-703 (1995).
56. R. Fu, Z. Ma, and J. P. Zheng, "Proton NMR and Dynamic Studies of Hydrous Ruthenium Oxide," *J. Phys. Chem. B*, **106** [14] 3592-6 (2002).
57. W. Sugimoto, K. Yokoshima, Y. Murakami, and Y. Takasu, "Charge Storage Mechanism of Nanostructured Anhydrous and Hydrous Ruthenium-Based Oxides," *Electrochim. Acta*, **52** [4] 1742-8 (2006).
58. H. Kim and B. N. Popov, "Characterization of Hydrous Ruthenium Oxide/Carbon Nanocomposite Supercapacitors Prepared by a Colloidal Method," *J. Power Sources*, **104** [1] 52-61 (2002).

59. F. Pico, E. Morales, J. A. Fernández, T. Centeno, J. Ibáñez, R. M. Rojas, J. M. Amarilla, and J. M. Rojo, "Ruthenium Oxide/Carbon Composites with Microporous or Mesoporous Carbon as Support and Prepared by Two Procedures. A Comparative Study as Supercapacitor Electrodes," *Electrochim. Acta*, **54** [8] 2239-45 (2009).
60. L. Z. Fan, Y. S. Hu, J. Maier, P. Adelhelm, B. Smarsly, and M. Antonietti, "High Electroactivity of Polyaniline in Supercapacitors by Using a Hierarchically Porous Carbon Monolith as a Support," *Adv. Funct. Mater.*, **17** [16] 3083-7 (2007).
61. H. Y. Lee and J. B. Goodenough, "Supercapacitor Behavior with KCl Electrolyte," *J. Solid State Chem.*, **144** [1] 220-3 (1999).
62. M. Toupin, T. Brousse, and D. Bélanger, "Influence of Microstructure on the Charge Storage Properties of Chemically Synthesized Manganese Dioxide," *Chem. Mater.*, **14** [9] 3946-52 (2002).
63. J. K. Chang, M. T. Lee, and W. T. Tsai, "In Situ Mn K-Edge X-Ray Absorption Spectroscopic Studies of Anodically Deposited Manganese Oxide with Relevance to Supercapacitor Applications," *J. Power Sources*, **166** [2] 590-4 (2007).
64. S. Devaraj and N. Munichandraiah, "High Capacitance of Electrodeposited MnO₂ by the Effect of a Surface-Active Agent," *Electrochem. Solid State Lett.*, **8** [7] A373-7 (2005).
65. M. W. Xu, W. Jia, S. J. Bao, Z. Su, and B. Dong, "Novel Mesoporous MnO₂ for High-Rate Electrochemical Capacitive Energy Storage," *Electrochim. Acta*, **55** [18] 5117-22 (2010).
66. S. Devaraj and N. Munichandraiah, "Effect of Crystallographic Structure of MnO₂ on Its Electrochemical Capacitance Properties," *J. Phys. Chem. C*, **112** [11] 4406-17 (2008).
67. H. Kim and B. N. Popov, "Synthesis and Characterization of MnO₂-Based Mixed Oxides as Supercapacitors," *J. Electrochem. Soc.*, **150** [3] D56-62 (2003).
68. Y. Li and H. Xie, "Mechanochemical-Synthesized Al-Doped Manganese Dioxides for Electrochemical Supercapacitors," *Ionics*, **16** [1] 21-5 (2010).
69. X. Pang, Z. Q. Ma, and L. Zuo, "Sn Doped MnO₂ Electrode Material for Supercapacitors," *Acta Phys.-Chim. Sin.*, **25** [12] 2433-7 (2009).
70. A. E. Fischer, K. A. Pettigrew, D. R. Rolison, R. M. Stroud, and J. W. Long, "Incorporation of Homogeneous, Nanoscale MnO₂ within Ultraporous Carbon

- Structures Via Self-Limiting Electroless Deposition: Implications for Electrochemical Capacitors," *Nano Lett.*, **7** [2] 281-6 (2007).
71. C. Zhang, Z. Chen, Z. Guo, and X. W. D. Lou, "Additive-Free Synthesis of 3D Porous V_2O_5 Hierarchical Microspheres with Enhanced Lithium Storage Properties," *Energy Environ. Sci.*, **6** [3] 974-8 (2013).
 72. Y. Yang, D. Kim, M. Yang, and P. Schmuki, "Vertically Aligned Mixed V_2O_5 - TiO_2 Nanotube Arrays for Supercapacitor Applications," *Chem. Commun.*, **47** [27] 7746-8 (2011).
 73. M. S. Whittingham, "The Role of Ternary Phases in Cathode Reactions," *J. Electrochem. Soc.*, **123** [3] 315-20 (1976).
 74. X. Rui, Z. Lu, H. Yu, D. Yang, H. H. Hng, T. M. Lim, and Q. Yan, "Ultrathin V_2O_5 Nanosheet Cathodes: Realizing Ultrafast Reversible Lithium Storage," *Nanoscale*, **5** [2] 556-60 (2013).
 75. J. Zhu, L. Cao, Y. Wu, Y. Gong, Z. Liu, H. E. Hoster, Y. Zhang, S. Zhang, S. Yang, and Q. Yan, "Building 3D Structures of Vanadium Pentoxide Nanosheets and Application as Electrodes in Supercapacitors," *Nano Lett.*, **13** [11] 5408-13 (2013).
 76. F. Coustier, J. Hill, B. B. Owens, S. Passerini, and W. H. Smyrl, "Doped Vanadium Oxides as Host Materials for Lithium Intercalation," *J. Electrochem. Soc.*, **146** [4] 1355-60 (1999).
 77. Z. Chen, V. Augustyn, J. Wen, Y. Zhang, M. Shen, B. Dunn, and Y. Lu, "High-Performance Supercapacitors Based on Intertwined CNT/ V_2O_5 Nanowire Nanocomposites," *Adv. Mater.*, **23** [6] 791-5 (2011).
 78. E. Baudrin, G. Sudant, D. Larcher, B. Dunn, and J.-M. Tarascon, "Preparation of Nanotextured $VO_2[B]$ from Vanadium Oxide Aerogels," *Chem. Mater.*, **18** [18] 4369-74 (2006).
 79. J. Wang, X. Zhang, Y. Zhang, A. Abas, X. Zhao, Z. Yang, Q. Su, W. Lan, and E. Xie, "Lightweight, Interconnected VO_2 Nanoflowers Hydrothermally Grown on 3D Graphene Networks for Wide-Voltage-Window Supercapacitors," *RSC Adv.*, **7** [56] 35558-64 (2017).
 80. M. Rahman, J. Z. Wang, N. H. Idris, Z. Chen, and H. Liu, "Enhanced Lithium Storage in a $VO_2(B)$ -Multiwall Carbon Nanotube Microsheet Composite Prepared Via an in Situ Hydrothermal Process," *Electrochim. Acta*, **56** [2] 693-9 (2010).

81. Q. Wang, J. Pan, M. Li, Y. Luo, H. Wu, L. Zhong, and G. Li, "VO₂(B) Nanosheets as a Cathode Material for Li-Ion Battery," *J. Mater. Sci. Technol.*, **31** [6] 630-3 (2015).
82. S. Ren, M. Wang, M. Xu, Y. Yang, C. Jia, and C. Hao, "Fabrication of High-Performance Supercapacitors Based on Hollow SnO₂ Microspheres," *J. Solid State Electrochem.*, **18** [4] 909-16 (2014).
83. S. C. Pang and M. A. Anderson, "Novel Electrode Materials for Electrochemical Capacitors: Part II. Material Characterization of Sol-Gel-Derived and Electrodeposited Manganese Dioxide Thin Films," *J. Mater. Res.*, **15** [10] 2096-106 (2000).
84. M. W. Xu, D. D. Zhao, S. J. Bao, and H. L. Li, "Mesoporous Amorphous MnO₂ as Electrode Material for Supercapacitor," *J. Solid State Electrochem.*, **11** [8] 1101-7 (2007).
85. H. Xia, J. Feng, H. Wang, M. O. Lai, and L. Lu, "MnO₂ Nanotube and Nanowire Arrays by Electrochemical Deposition for Supercapacitors," *J. Power Sources*, **195** [13] 4410-3 (2010).
86. L. Besra and M. Liu, "A Review on Fundamentals and Applications of Electrophoretic Deposition (EPD)," *Prog. Mater. Sci.*, **52** [1] 1-61 (2007).
87. J. Li and I. Zhitomirsky, "Cathodic Electrophoretic Deposition of Manganese Dioxide Films," *Colloids Surf. A*, **348** [1] 248-53 (2009).
88. M. Cheong and I. Zhitomirsky, "Electrophoretic Deposition of Manganese Oxide Films," *Surf. Eng.*, **25** [5] 346-52 (2009).
89. J. Li and I. Zhitomirsky, "Electrophoretic Deposition of Manganese Oxide Nanofibers," *Mater. Chem. Phys.*, **112** [2] 525-30 (2008).
90. C. Y. Chen, S. C. Wang, C. Y. Lin, F. S. Chen, and C. K. Lin, "Electrophoretically Deposited Manganese Oxide Coatings for Supercapacitor Application," *Ceram. Int.*, **35** [8] 3469-74 (2009).
91. K. S. Novoselov, A. K. Geim, S. V. Morozov, D. Jiang, Y. Zhang, S. V. Dubonos, I. V. Grigorieva, and A. A. Firsov, "Electric Field Effect in Atomically Thin Carbon Films," *Science*, **306** [5696] 666-9 (2004).
92. M. Choi, K. Na, J. Kim, Y. Sakamoto, O. Terasaki, and R. Ryoo, "Stable Single-Unit-Cell Nanosheets of Zeolite MFI as Active and Long-Lived Catalysts," *Nature*, **461** [7261] 246-9 (2009).

93. S. Wu, Z. Zeng, Q. He, Z. Wang, S. J. Wang, Y. Du, Z. Yin, X. Sun, W. Chen, and H. Zhang, "Electrochemically Reduced Single-Layer MoS₂ Nanosheets: Characterization, Properties, and Sensing Applications," *Small*, **8** [14] 2264-70 (2012).
94. J. Fan, S. Liu, and J. Yu, "Enhanced Photovoltaic Performance of Dye-Sensitized Solar Cells Based on TiO₂ Nanosheets/Graphene Composite Films," *J. Mater. Chem.*, **22** [33] 17027-36 (2012).
95. E. Yoo, J. Kim, E. Hosono, H.-s. Zhou, T. Kudo, and I. Honma, "Large Reversible Li Storage of Graphene Nanosheet Families for Use in Rechargeable Lithium Ion Batteries," *Nano Lett.*, **8** [8] 2277-82 (2008).
96. H. Zhu, J. Luo, H. Yang, J. Liang, G. Rao, J. Li, and Z. Du, "Birnessite-Type MnO₂ Nanowalls and Their Magnetic Properties," *J. Phys. Chem. C*, **112** [44] 17089-94 (2008).
97. R. Ma, Y. Bando, L. Zhang, and T. Sasaki, "Layered MnO₂ Nanobelts: Hydrothermal Synthesis and Electrochemical Measurements," *Adv. Mater.*, **16** [11] 918-22 (2004).
98. M. S. Song, K. M. Lee, Y. R. Lee, I. Y. Kim, T. W. Kim, J. L. Gunjaker, and S. J. Hwang, "Porously Assembled 2D Nanosheets of Alkali Metal Manganese Oxides with Highly Reversible Pseudocapacitance Behaviors," *J. Phys. Chem. C*, **114** [50] 22134-40 (2010).
99. O. Ghodbane, J. L. Pascal, and F. Favier, "Microstructural Effects on Charge-Storage Properties in MnO₂-Based Electrochemical Supercapacitors," *ACS Appl. Mater. Interfaces*, **1** [5] 1130-9 (2009).
100. T. Chirayil, P. Y. Zavalij, and M. S. Whittingham, "Hydrothermal Synthesis of Vanadium Oxides," *Chem. Mater.*, **10** [10] 2629-40 (1998).
101. C. Nethravathi, C. R. Rajamathi, M. Rajamathi, U. K. Gautam, X. Wang, D. Golberg, and Y. Bando, "N-Doped Graphene-VO₂(B) Nanosheet-Built 3D Flower Hybrid for Lithium Ion Battery," *ACS Appl. Mater. Interfaces*, **5** [7] 2708-14 (2013).
102. C. Tsang and A. Manthiram, "Synthesis of Nanocrystalline VO₂ and Its Electrochemical Behavior in Lithium Batteries," *J. Electrochem. Soc.*, **144** [2] 520-4 (1997).
103. Z. Chen, S. Gao, L. Jiang, M. Wei, and K. Wei, "Crystalline VO₂(B) Nanorods with a Rectangular Cross-Section," *Mater. Chem. Phys.*, **121** [1] 254-8 (2010).

104. G. Armstrong, J. Canales, A. R. Armstrong, and P. G. Bruce, "The Synthesis and Lithium Intercalation Electrochemistry of VO₂(B) Ultra-Thin Nanowires," *J. Power Sources*, **178** [2] 723-8 (2008).
105. H. Liu, Y. Wang, K. Wang, E. Hosono, and H. Zhou, "Design and Synthesis of a Novel Nanothorn VO₂(B) Hollow Microsphere and Their Application in Lithium-Ion Batteries," *J. Mater. Chem.*, **19** [18] 2835-40 (2009).
106. Y. Omomo, T. Sasaki, L. Wang, and M. Watanabe, "Redoxable Nanosheet Crystallites of MnO₂ Derived Via Delamination of a Layered Manganese Oxide," *J. Am. Chem. Soc.*, **125** [12] 3568-75 (2003).
107. Z. H. Liu, K. Ooi, H. Kanoh, W. P. Tang, and T. Tomida, "Swelling and Delamination Behaviors of Birnessite-Type Manganese Oxide by Intercalation of Tetraalkylammonium Ions," *Langmuir*, **16** [9] 4154-64 (2000).
108. T. W. Kim, T. S. Jung, S. H. Hyun, and S. J. Hwang, "Mesoporous Assembly of 2D Manganate Nanosheets Intercalated with Cobalt Ions," *Mater. Lett.*, **64** [5] 565-8 (2010).
109. K. Kai, Y. Yoshida, H. Kageyama, G. Saito, T. Ishigaki, Y. Furukawa, and J. Kawamata, "Room-Temperature Synthesis of Manganese Oxide Monosheets," *J. Am. Chem. Soc.*, **130** [47] 15938-43 (2008).
110. X. Zhang, P. Yu, H. Zhang, D. Zhang, X. Sun, and Y. Ma, "Rapid Hydrothermal Synthesis of Hierarchical Nanostructures Assembled from Ultrathin Birnessite-Type MnO₂ Nanosheets for Supercapacitor Applications," *Electrochim. Acta*, **89** 523-9 (2013).
111. M. Kundu and L. Liu, "Direct Growth of Mesoporous MnO₂ Nanosheet Arrays on Nickel Foam Current Collectors for High-Performance Pseudocapacitors," *J. Power Sources*, **243** 676-81 (2013).
112. A. K. Sinha, M. Pradhan, and T. Pal, "Morphological Evolution of Two-Dimensional MnO₂ Nanosheets and Their Shape Transformation to One-Dimensional Ultralong MnO₂ Nanowires for Robust Catalytic Activity," *J. Phys. Chem. C*, **117** [45] 23976-86 (2013).
113. S. Liang, Y. Hu, Z. Nie, H. Huang, T. Chen, A. Pan, and G. Cao, "Template-Free Synthesis of Ultra-Large V₂O₅ Nanosheets with Exceptional Small Thickness for High-Performance Lithium-Ion Batteries," *Nano Energy*, **13**, 58-66 (2015).
114. L. Mai, Q. Wei, Q. An, X. Tian, Y. Zhao, X. Xu, L. Xu, L. Chang, and Q. Zhang, "Nanoscroll Buffered Hybrid Nanostructural VO₂(B) Cathodes for High-Rate and Long-Life Lithium Storage," *Adv. Mater.*, **25** [21] 2969-73 (2013).

115. S. Zhang, Y. Li, C. Wu, F. Zheng, and Y. Xie, "Novel Flowerlike Metastable Vanadium Dioxide (B) Micronanostructures: Facile Synthesis and Application in Aqueous Lithium Ion Batteries," *J. Phys. Chem. C*, **113** [33] 15058-67 (2009).
116. L. Liu, T. Yao, X. Tan, Q. Liu, Z. Wang, D. Shen, Z. Sun, S. Wei, and Y. Xie, "Room-Temperature Intercalation–Deintercalation Strategy Towards VO₂(B) Single Layers with Atomic Thickness," *Small*, **8** [24] 3752-6 (2012).
117. M. Huang, Y. Zhang, F. Li, L. Zhang, R. S. Ruoff, Z. Wen, and Q. Liu, "Self-Assembly of Mesoporous Nanotubes Assembled from Interwoven Ultrathin Birnessite-Type MnO₂ Nanosheets for Asymmetric Supercapacitors," *Sci. Rep.*, **4** 3878 8pp. (2014).
118. L. Peng, X. Peng, B. Liu, C. Wu, Y. Xie, and G. Yu, "Ultrathin Two-Dimensional MnO₂/Graphene Hybrid Nanostructures for High-Performance, Flexible Planar Supercapacitors," *Nano Lett.*, **13** [5] 2151-7 (2013).
119. D. R. Rolison and L. F. Nazar, "Electrochemical Energy Storage to Power the 21st Century," *MRS Bull.*, **36** [7] 486-93 (2011).
120. P. Ruetschi, "Cation-Vacancy Model for MnO₂," *J. Electrochem. Soc.*, **131** [12] 2737-44 (1984).
121. P. Ruetschi, "Influence of Cation Vacancies on the Electrode Potential of MnO₂," *J. Electrochem. Soc.*, **135** [11] 2657-63 (1988).
122. P. Ruetschi and R. Giovanoli, "Cation Vacancies in MnO₂ and Their Influence on Electrochemical Reactivity," *J. Electrochem. Soc.*, **135** [11] 2663-9 (1988).
123. M. Pernet, P. Strobel, B. Bonnet, P. Bordet, and Y. Chabre, "Structural and Electrochemical Study of Lithium Insertion into γ -Fe₂O₃," *Solid State Ionics*, **66** [3-4] 259-65 (1993).
124. B. Koo, H. Xiong, M. D. Slater, V. B. Prakapenka, M. Balasubramanian, P. Podsiadlo, C. S. Johnson, T. Rajh, and E. V. Shevchenko, "Hollow Iron Oxide Nanoparticles for Application in Lithium Ion Batteries," *Nano Lett.*, **12** [5] 2429-35 (2012).
125. B. Koo, S. Chattopadhyay, T. Shibata, V. B. Prakapenka, C. S. Johnson, T. Rajh, and E. V. Shevchenko, "Intercalation of Sodium Ions into Hollow Iron Oxide Nanoparticles," *Chem. Mater.*, **25** [2] 245-52 (2013).
126. W. Li, D. Corradini, M. Body, C. Legein, M. Salanne, J. Ma, K. W. Chapman, P. J. Chupas, A. L. Rollet, and C. Julien, "High Substitution Rate in TiO₂ Anatase Nanoparticles with Cationic Vacancies for Fast Lithium Storage," *Chem. Mater.*, **27** [14] 5014-9 (2015).

127. H. S. Kim, J. B. Cook, H. Lin, J. S. Ko, S. H. Tolbert, V. Ozolins, and B. Dunn, "Oxygen Vacancies Enhance Pseudocapacitive Charge Storage Properties of MoO_{3-x} ," *Nat. Mater.*, **16** [4] 454-60 (2017).
128. D. Yu, S. Zhang, D. Liu, X. Zhou, S. Xie, Q. Zhang, Y. Liu, and G. Cao, "Effect of Manganese Doping on Li-Ion Intercalation Properties of V_2O_5 Films," *J. Mater. Chem.*, **20** [48] 10841-6 (2010).
129. B. P. Hahn, J. W. Long, A. N. Mansour, K. A. Pettigrew, M. S. Osofsky, and D. R. Rolison, "Electrochemical Li-Ion Storage in Defect Spinel Iron Oxides: The Critical Role of Cation Vacancies," *Energy Environ. Sci.*, **4** [4] 1495-502 (2011).
130. H. Zeng, D. Liu, Y. Zhang, K. A. See, Y. S. Jun, G. Wu, J. A. Gerbec, X. Ji, and G. D. Stucky, "Nanostructured Mn-Doped V_2O_5 Cathode Material Fabricated from Layered Vanadium Jarosite," *Chem. Mater.*, **27** [21] 7331-6 (2015).
131. K. E. Swider-Lyons, C. T. Love, and D. R. Rolison, "Improved Lithium Capacity of Defective V_2O_5 Materials," *Solid State Ionics*, **152**, 99-104 (2002).
132. J. Y. Shin, J. H. Joo, D. Samuelis, and J. Maier, "Oxygen-Deficient $\text{TiO}_{2-\delta}$ Nanoparticles Via Hydrogen Reduction for High Rate Capability Lithium Batteries," *Chem. Mater.*, **24** [3] 543-51 (2012).
133. S. Grangeon, A. Manceau, J. Guilhermet, A. C. Gaillot, M. Lanson, and B. Lanson, "Zn Sorption Modifies Dynamically the Layer and Interlayer Structure of Vernadite," *Geochim. Cosmochim. Acta*, **85**, 302-13 (2012).
134. A. Manceau, M. A. Marcus, S. Grangeon, M. Lanson, B. Lanson, A. C. Gaillot, S. Skanthakumar, and L. Soderholm, "Short-Range and Long-Range Order of Phyllosulfate Nanoparticles Determined Using High-Energy X-Ray Scattering," *J. Appl. Crystallogr.*, **46** [1] 193-209 (2013).
135. L. Abdulaeva, O. Silyukov, Y. V. Petrov, and I. Zvereva, "Low-Temperature Transformations of Protonic Forms of Layered Complex Oxides HLnTiO_4 and $\text{H}_2\text{Ln}_2\text{Ti}_3\text{O}_{10}$ (Ln= La, Nd)," *J. Nanomater.*, **2013**, 514781 8pp. (2013).
136. H. Li, P. He, Y. Wang, E. Hosono, and H. Zhou, "High-Surface Vanadium Oxides with Large Capacities for Lithium-Ion Batteries: From Hydrated Aerogel to Nanocrystalline $\text{VO}_2(\text{B})$, V_6O_{13} and V_2O_5 ," *J. Mater. Chem.*, **21** [29] 10999-1009 (2011).
137. H. Adelkhani, "Functionalized Electrolytic Manganese Dioxide Nanostructure Prepared at Fixed pH for Electrochemical Supercapacitor," *J. Electrochem. Soc.*, **156** [10] A791-5 (2009).

138. H. Adelkhani, M. Ghaemi, and S. Jafari, "Cycle Life Improvement of Alkaline Batteries Via Optimization of Pulse Current Deposition of Manganese Dioxide under Low Bath Temperatures," *J. Power Sources*, **163** [2] 1091-104 (2007).
139. T. Egami and S. J. Billinge, *Underneath the Bragg Peaks: Structural Analysis of Complex Materials*, Vol. 16. Elsevier, Oxford, 2003.
140. B. Jiang and S. M. Selbach, "Local and Average Structure of Mn-and La-Substituted BiFeO₃," *J. Solid State Chem.*, **250**, 75-82 (2017).
141. D. Chen, D. Ding, X. Li, G. H. Waller, X. Xiong, M. A. El-Sayed, and M. Liu, "Probing the Charge Storage Mechanism of a Pseudocapacitive MnO₂ Electrode Using in Operando Raman Spectroscopy," *Chem. Mater.*, **27** [19] 6608-19 (2015).
142. S. Cheng, L. Yang, D. Chen, X. Ji, Z. J. Jiang, D. Ding, and M. Liu, "Phase Evolution of an Alpha MnO₂-Based Electrode for Pseudo-Capacitors Probed by in Operando Raman Spectroscopy," *Nano Energy*, **9**, 161-7 (2014).
143. T. Koketsu, J. Ma, B. J. Morgan, M. Body, C. Legein, W. Dachraoui, M. Giannini, A. Demortière, M. Salanne, and F. Dardoize, "Reversible Magnesium and Aluminium Ions Insertion in Cation-Deficient Anatase TiO₂," *Nat. Mater.*, **16** [11] 1142-8 (2017).
144. M. J. Ariza, D. J. Jones, J. Rozière, R. Chitrakar, and K. Ooi, "Probing the Local Structure and the Role of Protons in Lithium Sorption Processes of a New Lithium-Rich Manganese Oxide," *Chem. Mater.*, **18** [7] 1885-90 (2006).
145. T. Brousse, D. Bélanger, and J. W. Long, "To Be or Not to Be Pseudocapacitive?" *J. Electrochem. Soc.*, **162** [5] A5185-9 (2015).
146. O. Ghodbane, F. Ataherian, N. L. Wu, and F. Favier, "In Situ Crystallographic Investigations of Charge Storage Mechanisms in MnO₂-Based Electrochemical Capacitors," *J. Power Sources*, **206**, 454-62 (2012).
147. O. Vargas, A. Caballero, L. Hernán, and J. Morales, "Improved Capacitive Properties of Layered Manganese Dioxide Grown as Nanowires," *J. Power Sources*, **196** [6] 3350-4 (2011).
148. S. Komaba, A. Ogata, and T. Tsuchikawa, "Enhanced Supercapacitive Behaviors of Birnessite," *Electrochem. Commun.*, **10** [10] 1435-7 (2008).
149. J. Zhu and J. He, "Facile Synthesis of Graphene-Wrapped Honeycomb MnO₂ Nanospheres and Their Application in Supercapacitors," *ACS Appl. Mater. Interfaces*, **4** [3] 1770-6 (2012).

150. L. Hu, W. Chen, X. Xie, N. Liu, Y. Yang, H. Wu, Y. Yao, M. Pasta, H. N. Alshareef, and Y. Cui, "Symmetrical MnO₂-Carbon Nanotube-Textile Nanostructures for Wearable Pseudocapacitors with High Mass Loading," *ACS Nano*, **5** [11] 8904-13 (2011).
151. S. W. Lee, J. Kim, S. Chen, P. T. Hammond, and Y. Shao-Horn, "Carbon Nanotube/Manganese Oxide Ultrathin Film Electrodes for Electrochemical Capacitors," *ACS Nano*, **4** [7] 3889-96 (2010).
152. Y. Luo, J. Jiang, W. Zhou, H. Yang, J. Luo, X. Qi, H. Zhang, Y. Denis, C. M. Li, and T. Yu, "Self-Assembly of Well-Ordered Whisker-Like Manganese Oxide Arrays on Carbon Fiber Paper and Its Application as Electrode Material for Supercapacitors," *J. Mater. Chem.*, **22** [17] 8634-40 (2012).
153. Y. C. Chen, Y. K. Hsu, Y. G. Lin, Y. K. Lin, Y. Y. Horng, L. C. Chen, and K. H. Chen, "Highly Flexible Supercapacitors with Manganese Oxide Nanosheet/Carbon Cloth Electrode," *Electrochim. Acta.*, **56** [20] 7124-30 (2011).
154. D. Kong, J. Luo, Y. Wang, W. Ren, T. Yu, Y. Luo, Y. Yang, and C. Cheng, "Three-Dimensional Co₃O₄@MnO₂ Hierarchical Nanoneedle Arrays: Morphology Control and Electrochemical Energy Storage," *Adv. Funct. Mater.*, **24** [24] 3815-26 (2014).
155. S. Zhao, T. Liu, D. Hou, W. Zeng, B. Miao, S. Hussain, X. Peng, and M. S. Javed, "Controlled Synthesis of Hierarchical Birnessite-Type MnO₂ Nanoflowers for Supercapacitor Applications," *Appl. Surf. Sci.*, **356**, 259-65 (2015).
156. R. Jiang, T. Huang, J. Liu, J. Zhuang, and A. Yu, "A Novel Method to Prepare Nanostructured Manganese Dioxide and Its Electrochemical Properties as a Supercapacitor Electrode," *Electrochim. Acta*, **54** [11] 3047-52 (2009).
157. F. F. Marafatto, M. L. Strader, J. Gonzalez-Holguera, A. Schwartzberg, B. Gilbert, and J. Peña, "Rate and Mechanism of the Photoreduction of Birnessite (MnO₂) Nanosheets," *Proc. Natl. Acad. Sci.*, **112** [15] 4600-5 (2015).
158. A. C. Gaillot, B. Lanson, and V. A. Drits, "Structure of Birnessite Obtained from Decomposition of Permanganate under Soft Hydrothermal Conditions. 1. Chemical and Structural Evolution as a Function of Temperature," *Chem. Mater.*, **17** [11] 2959-75 (2005).
159. A. C. Gaillot, V. A. Drits, A. Manceau, and B. Lanson, "Structure of the Synthetic K-Rich Phyllosulfate Birnessite Obtained by High-Temperature Decomposition of KMnO₄: Substructures of K-Rich Birnessite from 1000 °C Experiment," *Microporous Mesoporous Mater.*, **98** [1] 267-82 (2007).

160. B. Ravel and M. Newville, "Athena, Artemis, Hephaestus: Data Analysis for X-Ray Absorption Spectroscopy Using IFEFFIT," *J. Synchrotron Radiat.*, **12** [4] 537-41 (2005).
161. P. J. Chupas, X. Qiu, J. C. Hanson, P. L. Lee, C. P. Grey, and S. J. Billinge, "Rapid-Acquisition Pair Distribution Function (RA-PDF) Analysis," *J. Appl. Crystallogr.*, **36** [6] 1342-7 (2003).
162. A. Hammersley, S. Svensson, M. Hanfland, A. Fitch, and D. Hausermann, "Two-Dimensional Detector Software: From Real Detector to Idealised Image or Two-Theta Scan," *Int. J. High Pressure Res.*, **14** [4-6] 235-48 (1996).
163. X. Qiu, J. W. Thompson, and S. J. Billinge, "PDFgetX2: A Gui-Driven Program to Obtain the Pair Distribution Function from X-Ray Powder Diffraction Data," *J. Appl. Crystallogr.*, **37** [4] 678 (2004).
164. P. C. Metz, "Total Scattering Analysis of Disordered Nanosheet Materials"; Ph.D. Thesis. Alfred University, Alfred, NY, 2017.
165. P. Metz, R. Koch, B. Cladek, K. Page, J. Neuefeind, and S. Misture, "X-Ray and Neutron Total Scattering Analysis of $\text{Hy} \cdot (\text{Bi}_{0.2}\text{Ca}_{0.55}\text{Sr}_{0.25})(\text{Ag}_{0.25}\text{Na}_{0.75})\text{Nb}_3\text{O}_{10} \cdot x\text{H}_2\text{O}$ Perovskite Nanosheet Booklets with Stacking Disorder," *Powder Diffr.*, **31** [2] 126-34 (2016).
166. R. Ma, Y. Bando, and T. Sasaki, "Directly Rolling Nanosheets into Nanotubes," *J. Phys. Chem. B*, **108** [7] 2115-9 (2004).
167. Z. Sun, T. Liao, Y. Dou, S. M. Hwang, M. S. Park, L. Jiang, J. H. Kim, and S. X. Dou, "Generalized Self-Assembly of Scalable Two-Dimensional Transition Metal Oxide Nanosheets," *Nat. Commun.*, **5**, 3813 9pp. (2014).
168. M. Zhu, C. L. Farrow, J. E. Post, K. J. Livi, S. J. Billinge, M. Ginder-Vogel, and D. L. Sparks, "Structural Study of Biotic and Abiotic Poorly-Crystalline Manganese Oxides Using Atomic Pair Distribution Function Analysis," *Geochim. Cosmochim. Acta*, **81**, 39-55 (2012).
169. S. M. Paek, H. Jung, Y. J. Lee, M. Park, S. J. Hwang, and J. H. Choy, "Exfoliation and Reassembling Route to Mesoporous Titania Nanohybrids," *Chem. Mater.*, **18** [5] 1134-40 (2006).
170. C. M. Lew, Z. Li, S. Li, S. J. Hwang, Y. Liu, D. I. Medina, M. Sun, J. Wang, M. E. Davis, and Y. Yan, "Pure-Silica-Zeolite MFI and MEL Low-Dielectric-Constant Films with Fluoro-Organic Functionalization," *Adv. Funct. Mater.*, **18** [21] 3454-60 (2008).

171. L. Mao, K. Zhang, H. S. O. Chan, and J. Wu, "Surfactant-Stabilized Graphene/Polyaniline Nanofiber Composites for High Performance Supercapacitor Electrode," *J. Mater. Chem.*, **22** [1] 80-5 (2012).
172. Y. R. Lee, I. Y. Kim, T. W. Kim, J. M. Lee, and S. J. Hwang, "Mixed Colloidal Suspensions of Reduced Graphene Oxide and Layered Metal Oxide Nanosheets: Useful Precursors for the Porous Nanocomposites and Hybrid Films of Graphene/Metal Oxide," *Chem. Eur. J.*, **18** [8] 2263-71 (2012).
173. J. Wang, P. Zhang, J. Li, C. Jiang, R. Yunus, and J. Kim, "Room-Temperature Oxidation of Formaldehyde by Layered Manganese Oxide: Effect of Water," *Environ. Sci. Technol.*, **49** [20] 12372-9 (2015).
174. M. I. Burguete, R. Gavara, F. Galindo, and S. V. Luis, "New Polymer-Supported Photocatalyst with Improved Compatibility with Polar Solvents. Synthetic Application Using Solar Light as Energy Source," *Catal. Commun.*, **11** [13] 1081-4 (2010).
175. R. Argazzi, G. Larramona, C. Contado, and C. A. Bignozzi, "Preparation and Photoelectrochemical Characterization of a Red Sensitive Osmium Complex Containing 4, 4', 4''-Tricarboxy-2, 2': 6', 2''-Terpyridine and Cyanide Ligands," *J. Photochem. Photobiol. A.*, **164** [1-3] 15-21 (2004).
176. L. Medvecky, J. Briancin, and J. Durisin, "Nanohydroxyapatite Prepared by Rapid Precipitation Method in the Presence of Tetrabutylammonium Hydroxide," *Powder Metall. Prog.*, **10** [4] 213-22 (2010).
177. Â. L. Andrade, J. D. Fabris, J. D. Ardisson, M. A. Valente, and J. M. Ferreira, "Effect of Tetramethylammonium Hydroxide on Nucleation, Surface Modification and Growth of Magnetic Nanoparticles," *J Nanomater.*, **2012**, 15 10pp. (2012).
178. M. Matsuoka, S. Isotani, R. D. Mansano, W. Sucasaire, R. A. Pinto, J. C. Mittani, K. Ogata, and N. Kuratani, "X-Ray Photoelectron Spectroscopy and Raman Spectroscopy Studies on Thin Carbon Nitride Films Deposited by Reactive RF Magnetron Sputtering," *World J. Nano Sci. Eng.*, **2** [2] 92-102 (2012).
179. M. Nakayama, A. Tanaka, S. Konishi, and K. Ogura, "Effects of Heat-Treatment on the Spectroscopic and Electrochemical Properties of a Mixed Manganese/Vanadium Oxide Film Prepared by Electrodeposition," *J. Mater. Res.*, **19** [5] 1509-15 (2004).
180. M. Nakayama, S. Konishi, H. Tagashira, and K. Ogura, "Electrochemical Synthesis of Layered Manganese Oxides Intercalated with Tetraalkylammonium Ions," *Langmuir*, **21** [1] 354-9 (2005).

181. M. C. Biesinger, B. P. Payne, A. P. Grosvenor, L. W. Lau, A. R. Gerson, and R. S. C. Smart, "Resolving Surface Chemical States in XPS Analysis of First Row Transition Metals, Oxides and Hydroxides: Cr, Mn, Fe, Co and Ni," *Appl. Surf. Sci.*, **257** [7] 2717-30 (2011).
182. M. Chigane and M. Ishikawa, "Manganese Oxide Thin Film Preparation by Potentiostatic Electrolyses and Electrochromism," *J. Electrochem. Soc.*, **147** [6] 2246-51 (2000).
183. J. Carver, G. Schweitzer, and T. A. Carlson, "Use of X-Ray Photoelectron Spectroscopy to Study Bonding in Cr, Mn, Fe, and Co Compounds," *J. Chem. Phys.*, **57** [2] 973-82 (1972).
184. M. Oku, K. Hirokawa, and S. Ikeda, "X-Ray Photoelectron Spectroscopy of Manganese-Oxygen Systems," *J. Electron. Spectrosc. Relat. Phenom.*, **7** [5] 465-73 (1975).
185. S. L. Kuo and N. L. Wu, "Investigation of Pseudocapacitive Charge-Storage Reaction of $\text{MnO}_2 \cdot n\text{H}_2\text{O}$ Supercapacitors in Aqueous Electrolytes," *J. Electrochem. Soc.*, **153** [7] A1317-24 (2006).
186. S. J. Hwang, C. W. Kwon, J. Portier, G. Campet, H. S. Park, J. H. Choy, P. V. Huong, M. Yoshimura, and M. Kakihana, "Local Crystal Structure around Manganese in New Potassium-Based Nanocrystalline Manganese Oxyiodide," *J. Phys. Chem. B*, **106** [16] 4053-60 (2002).
187. H. W. Wang, M. Naguib, K. Page, D. J. Wesolowski, and Y. Gogotsi, "Resolving the Structure of $\text{Ti}_3\text{C}_2\text{T}_x$ Mxenes through Multilevel Structural Modeling of the Atomic Pair Distribution Function," *Chem. Mater.*, **28** [1] 349-59 (2015).
188. M. Oku, K. Hirokawa, and S. Ikeda, "X-Ray Photoelectron Spectroscopy of Manganese-Oxygen Systems," *J. Electron. Spectrosc. Relat. Phenom.*, **7** [5] 465-73 (1975).
189. M. Wojdyr, "Fityk : A General-Purpose Peak Fitting Program," *J. Appl. Crystallogr.*, **43**, 1126-8 (2010).
190. P. Gao and D. Liu, "Facile Synthesis of Copper Oxide Nanostructures and Their Application in Non-Enzymatic Hydrogen Peroxide Sensing," *Sens. Actuators, B*, **208**, 346-54 (2015).
191. J. Chang, M. Jin, F. Yao, T. H. Kim, V. T. Le, H. Yue, F. Gunes, B. Li, A. Ghosh, and S. Xie, "Asymmetric Supercapacitors Based on Graphene/ MnO_2 Nanospheres and Graphene/ MoO_3 Nanosheets with High Energy Density," *Adv. Funct. Mater.*, **23** [40] 5074-83 (2013).

192. Z. Fan, J. Yan, T. Wei, L. Zhi, G. Ning, T. Li, and F. Wei, "Asymmetric Supercapacitors Based on Graphene/MnO₂ and Activated Carbon Nanofiber Electrodes with High Power and Energy Density," *Adv. Funct. Mater.*, **21** [12] 2366-75 (2011).
193. Y. Shao, H. Wang, Q. Zhang, and Y. Li, "High-Performance Flexible Asymmetric Supercapacitors Based on 3D Porous Graphene/MnO₂ Nanorod and Graphene/Ag Hybrid Thin-Film Electrodes," *J. Mater. Chem. C*, **1** [6] 1245-51 (2013).
194. P. Umek, A. Gloter, M. Pregelj, R. Dominko, M. Jagodic, Z. Jaglicic, A. Zimina, M. Brzhezinskaya, A. Potocnik, C. Filipic, A. Levstik and D. Arcon, "Synthesis of 3D Hierarchical Self-Assembled Microstructures Formed from α -MnO₂ Nanotubes and Their Conducting and Magnetic Properties," *J. Phys. Chem. C*, **113** [33] 14798-803 (2009).
195. P. Juhás, T. Davis, C. L. Farrow, and S. J. Billinge, "PDFgetX3: A Rapid and Highly Automatable Program for Processing Powder Diffraction Data into Total Scattering Pair Distribution Functions," *J. Appl. Crystallogr.*, **46** [2] 560-6 (2013).
196. A. Paravannoor, R. Ranjusha, A. Asha, R. Vani, S. Kalluri, K. Subramanian, N. Sivakumar, T. Kim, S. V. Nair, and A. Balakrishnan, "Chemical and Structural Stability of Porous Thin Film Nio Nanowire Based Electrodes for Supercapacitors," *Chem. Eng. J.*, **220**, 360-6 (2013).
197. Y. Huang, H. Liu, Y. C. Lu, Y. Hou, and Q. Li, "Electrophoretic Lithium Iron Phosphate/Reduced Graphene Oxide Composite for Lithium Ion Battery Cathode Application," *J. Power Sources*, **284**, 236-44 (2015).
198. C. J. Hung, P. Lin, and T. Y. Tseng, "High Energy Density Asymmetric Pseudocapacitors Fabricated by Graphene/Carbon Nanotube/MnO₂ Plus Carbon Nanotubes Nanocomposites Electrode," *J. Power Sources*, **259**, 145-53 (2014).
199. M. S. Wu and Y. H. Fu, "Tubular Graphene Nanoribbons with Attached Manganese Oxide Nanoparticles for Use as Electrodes in High-Performance Supercapacitors," *Carbon*, **60**, 236-45 (2013).
200. A. S. Pillai, R. Rajagopalan, A. Amruthalakshmi, J. Joseph, A. Ajay, I. Shakir, S. V. Nair, and A. Balakrishnan, "Mesoscopic Architectures of Co(OH)₂ Spheres with an Extended Array of Microporous Threads as Pseudocapacitor Electrode Materials," *Colloids Surf., A*, **470**, 280-9 (2015).
201. S. Cheng, L. Yang, D. Chen, X. Ji, Z. J. Jiang, D. Ding, and M. Liu, "Phase Evolution of an Alpha MnO₂-Based Electrode for Pseudo-Capacitors Probed by in Operando Raman Spectroscopy," *Nano Energy*, **9**, 161-7 (2014).

202. Y. K. Hsu, Y. C. Chen, Y. G. Lin, L. C. Chen, and K. H. Chen, "Reversible Phase Transformation of MnO₂ Nanosheets in an Electrochemical Capacitor Investigated by in Situ Raman Spectroscopy," *Chem. Commun.*, **47** [4] 1252-4 (2011).
203. C. Julien, M. Massot, R. Baddour-Hadjean, S. Franger, S. Bach, and J. Pereira-Ramos, "Raman Spectra of Birnessite Manganese Dioxides," *Solid State Ionics*, **159** [3-4] 345-56 (2003).
204. C. Julien and M. Massot, "Lattice Vibrations of Materials for Lithium Rechargeable Batteries III. Lithium Manganese Oxides," *Mater. Sci. Eng., B*, **100** [1] 69-78 (2003).
205. C. Julien, M. Massot, and C. Poinignon, "Lattice Vibrations of Manganese Oxides: Part I. Periodic Structures," *Spectrochim. Acta, Part A*, **60** [3] 689-700 (2004).
206. C. Julien and M. Massot, "Spectroscopic Studies of the Local Structure in Positive Electrodes for Lithium Batteries," *Phys. Chem. Chem. Phys.*, **4** [17] 4226-35 (2002).
207. M. Inaba, Y. Iriyama, Z. Ogumi, Y. Todzuka, and A. Tasaka, "Raman Study of Layered Rock-Salt LiCoO₂ and Its Electrochemical Lithium Deintercalation," *J. Raman Spectrosc.*, **28** [8] 613-7 (1997).
208. A. Cross, A. Morel, A. Cormie, T. Hollenkamp, and S. Donne, "Enhanced Manganese Dioxide Supercapacitor Electrodes Produced by Electrodeposition," *J. Power Sources*, **196** [18] 7847-53 (2011).
209. Y. Liu, F. Zhou, and V. Ozolins, "Ab Initio Study of the Charge-Storage Mechanisms in RuO₂-Based Electrochemical Ultracapacitors," *J. Phys. Chem. C*, **116** [1] 1450-7 (2011).
210. J. Liu, X. Ge, X. Ye, G. Wang, H. Zhang, H. Zhou, Y. Zhang, and H. Zhao, "3D Graphene/ δ -MnO₂ Aerogels for Highly Efficient and Reversible Removal of Heavy Metal Ions," *J. Mater. Chem. A*, **4** [5] 1970-9 (2016).
211. C. Tangarnjanavalukul, N. Phattharasupakun, J. Wuthiprom, P. Kidkhunthod, and M. Sawangphruk, "Charge Storage Mechanisms of Birnessite-Type MnO₂ Nanosheets in Na₂SO₄ Electrolytes with Different pH Values: In Situ Electrochemical X-Ray Absorption Spectroscopy Investigation," *Electrochim. Acta*, **273**, 17-25 (2018).
212. G. Wang, Q. Tang, H. Bao, X. Li, and G. Wang, "Synthesis of Hierarchical Sulfonated Graphene/MnO₂/Polyaniline Ternary Composite and Its Improved Electrochemical Performance," *J. Power Sources*, **241**, 231-8 (2013).

213. J. Zang, S. J. Bao, C. M. Li, H. Bian, X. Cui, Q. Bao, C. Q. Sun, J. Guo, and K. Lian, "Well-Aligned Cone-Shaped Nanostructure of Polypyrrole/RuO₂ and Its Electrochemical Supercapacitor," *J. Phys. Chem. C*, **112** [38] 14843-7 (2008).
214. Q. Yang, Z. Lu, X. Sun, and J. Liu, "Ultrathin Co₃O₄ Nanosheet Arrays with High Supercapacitive Performance," *Sci. Rep.*, **3** 3537 7pp. (2013).
215. D. Hanlon, C. Backes, T. M. Higgins, M. Hughes, A. O'Neill, P. King, N. McEvoy, G. S. Duesberg, B. Mendoza Sanchez, and H. Pettersson, "Production of Molybdenum Trioxide Nanosheets by Liquid Exfoliation and Their Application in High-Performance Supercapacitors," *Chem. Mater.*, **26** [4] 1751-63 (2014).
216. R. Rakhi, D. H. Nagaraju, P. Beaujuge, and H. N. Alshareef, "Supercapacitors Based on Two Dimensional VO₂ Nanosheet Electrodes in Organic Gel Electrolyte," *Electrochim. Acta*, **220**, 601-8 (2016).
217. L. Deng, G. Zhang, L. Kang, Z. Lei, C. Liu, and Z. H. Liu, "Graphene/VO₂ Hybrid Material for High Performance Electrochemical Capacitor," *Electrochim. Acta*, **112**, 448-57 (2013).
218. S. Liang, Y. Hu, Z. Nie, H. Huang, T. Chen, A. Pan, and G. Cao, "Template-Free Synthesis of Ultra-Large V₂O₅ Nanosheets with Exceptional Small Thickness for High-Performance Lithium-Ion Batteries," *Nano Energy*, **13**, 58-66 (2015).
219. Y. Li, J. Yao, E. Uchaker, M. Zhang, J. Tian, X. Liu, and G. Cao, "Sn-Doped V₂O₅ Film with Enhanced Lithium-Ion Storage Performance," *J. Phys. Chem. C*, **117** [45] 23507-14 (2013).
220. A. Hammersley, S. Svensson, and A. Thompson, "Calibration and Correction of Spatial Distortions in 2D Detector Systems," *Nucl. Instrum. Methods Phys. Res., Sect. A*, **346** [1-2] 312-21 (1994).
221. C. Farrow, P. Juhas, J. Liu, D. Bryndin, E. Božin, J. Bloch, T. Proffen, and S. Billinge, "PDFfit2 and PDFgui: Computer Programs for Studying Nanostructure in Crystals," *J. Phys. Condens. Matter*, **19** [33] 335219 7pp. (2007).
222. B. Alonso and J. Livage, "Synthesis of Vanadium Oxide Gels from Peroxovanadic Acid Solutions: A 51V NMR Study," *J. Solid State Chem.*, **148** [1] 16-9 (1999).
223. A. Q. Pan, H. B. Wu, L. Zhang, and X. W. D. Lou, "Uniform V₂O₅ Nanosheet-Assembled Hollow Microflowers with Excellent Lithium Storage Properties," *Energy Environ. Sci.*, **6** [5] 1476-9 (2013).

224. S. R. Popuri, M. Miclau, A. Artemenko, C. Labrugere, A. Villesuzanne, and M. I. Pollet, "Rapid Hydrothermal Synthesis of VO₂(B) and Its Conversion to Thermochromic VO₂(M1)," *Inorg. Chem.*, **52** [9] 4780-5 (2013).
225. Y. Wu, L. Fan, Q. Liu, S. Chen, W. Huang, F. Chen, G. Liao, C. Zou, and Z. Wu, "Decoupling the Lattice Distortion and Charge Doping Effects on the Phase Transition Behavior of VO₂ by Titanium (Ti⁴⁺) Doping," *Sci. Rep.*, **5** 9328 8pp. (2015).
226. X. Xiao, S. Li, H. Wei, D. Sun, Y. Wu, G. Jin, F. Wang, and Y. Zou, "Synthesis and Characterization of VO₂(B)/Graphene Nanocomposite for Supercapacitors," *J. Mater. Sci. Mater. Electron.*, **26** [6] 4226-33 (2015).
227. M. C. Biesinger, L. W. M. Lau, A. R. Gerson, and R. S. C. Smart, "Resolving Surface Chemical States in XPS Analysis of First Row Transition Metals, Oxides and Hydroxides: Sc, Ti, V, Cu and Zn," *Appl. Surf. Sci.*, **257** [3] 887-98 (2010).
228. M. Dapiaggi, F. Maglia, L. Pagliari, I. G. Tredici, and N. Rotiroti, "The Role of Local Structural Distortions in the Stabilisation of Undoped Nanocrystalline Tetragonal Zirconia," *Mater. Chem. Phys.*, **147** [3] 395-402 (2014).
229. J. Shao, X. Li, Q. Qu, and H. Zheng, "One-Step Hydrothermal Synthesis of Hexangular Starfruit-Like Vanadium Oxide for High Power Aqueous Supercapacitors," *J. Power Sources*, **219**, 253-7 (2012).
230. D. McNulty, D. N. Buckley, and C. O'Dwyer, "Comparative Electrochemical Charge Storage Properties of Bulk and Nanoscale Vanadium Oxide Electrodes," *J. Solid State Electrochem.*, **20** [5] 1445-58 (2016).
231. G. Nie, X. Lu, Y. Zhu, M. Chi, M. Gao, S. Chen, and C. Wang, "Reactive Template Synthesis of Inorganic/Organic VO₂@Polyaniline Coaxial Nanobelts for High-Performance Supercapacitors," *ChemElectroChem*, **4** [5] 1095-100 (2017).
232. P. Yang, P. Sun, L. Du, Z. Liang, W. Xie, X. Cai, L. Huang, S. Tan, and W. Mai, "Quantitative Analysis of Charge Storage Process of Tungsten Oxide That Combines Pseudocapacitive and Electrochromic Properties," *J. Phys. Chem. C*, **119** [29] 16483-9 (2015).
233. K. V. Sankar, S. Surendran, K. Pandi, A. Allin, V. Nithya, Y. Lee, and R. K. Selvan, "Studies on the Electrochemical Intercalation/De-Intercalation Mechanism of NiMn₂O₄ for High Stable Pseudocapacitor Electrodes," *RSC Adv.*, **5** [35] 27649-56 (2015).

234. M. Sathiya, A. Prakash, K. Ramesha, J. M. Tarascon, and A. Shukla, "V₂O₅-Anchored Carbon Nanotubes for Enhanced Electrochemical Energy Storage," *J. Am. Chem. Soc.*, **133** [40] 16291-9 (2011).
235. J. Duay, S. A. Sherrill, Z. Gui, E. Gillette, and S. B. Lee, "Self-Limiting Electrodeposition of Hierarchical MnO₂ and M(OH)₂/MnO₂ Nanofibril/Nanowires: Mechanism and Supercapacitor Properties," *ACS Nano*, **7** [2] 1200-14 (2013).
236. H. Yin, C. Song, Y. Wang, S. Li, M. Zeng, Z. Zhang, Z. Zhu, and K. Yu, "Influence of Morphologies and Pseudocapacitive Contributions for Charge Storage in V₂O₅ Micro/Nano-Structures," *Electrochim. Acta*, **111**, 762-70 (2013).
237. T. Brezesinski, J. Wang, S. H. Tolbert, and B. Dunn, "Ordered Mesoporous α -MoO₃ with Iso-Oriented Nanocrystalline Walls for Thin-Film Pseudocapacitors," *Nat. Mater.*, **9** [2] 146-51 (2010).
238. P. Gao, Y. Gong, N. P. Mellott, and D. Liu, "Non-Enzymatic Amperometric Detection of Hydrogen Peroxide Using Grass-Like Copper Oxide Nanostructures Calcined in Nitrogen Atmosphere," *Electrochim. Acta*, **173**, 31-9 (2015).
239. P. Gao and D. Liu, "Petal-Like CuO Nanostructures Prepared by a Simple Wet Chemical Method, and Their Application to Non-Enzymatic Amperometric Determination of Hydrogen Peroxide," *Microchim. Acta*, **182** [7-8] 1231-9 (2015).
240. L. Liang, H. Liu, and W. Yang, "Fabrication of VO₂(B) Hybrid with Multiwalled Carbon Nanotubes to Form a Coaxial Structure and Its Electrochemical Capacitance Performance," *J. Alloys Compd.*, **559**, 167-73 (2013).
241. L. Deng, G. Zhang, L. Kang, Z. Lei, C. Liu, and Z. H. Liu, "Graphene/VO₂ Hybrid Material for High Performance Electrochemical Capacitor," *Electrochim. Acta*, **112**, 448-57 (2013).

APPENDIX I. CUSTOM ELECTROCHEMICAL CELL FOR IN-SITU MEASUREMENTS

In order to perform the *in-situ*/operando measurements from pseudocapacitors with a liquid electrolyte, we have designed and fabricated a housing device (custom electrochemical cell) which is shown in Figure 97. The 2-part housing is made from plates of stainless steel. The two plates mate together with a pin-and-hole system, and are secured by four M3 hex bolts that thread into the steel. Six 300-micron shims maintain a gap between the faces of the plates when fastened down. The total dimensions of the cell are shown in Figure 98. The total height is ~15.5 cm. The distance from base to center of beam is ~8.4 and 7.9 cm. The width of the cell is ~6.5 cm.

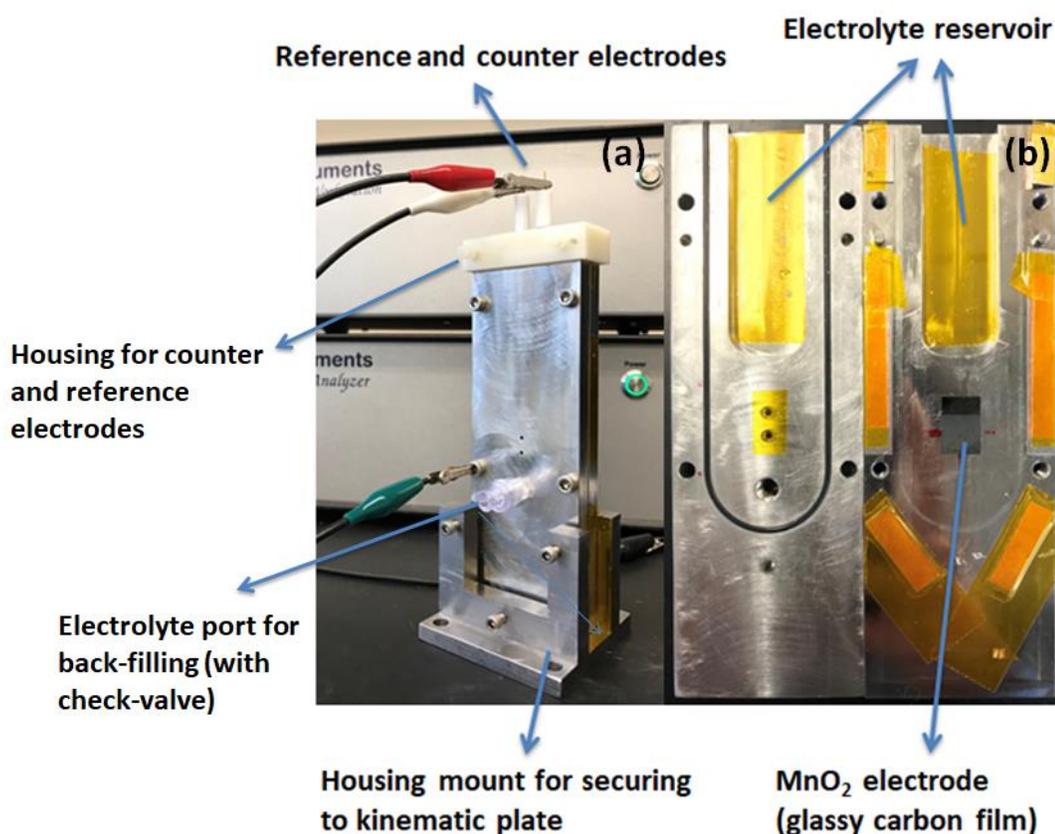


Figure 97. Photo images of the custom electrochemical cell for *in-situ* measurements.

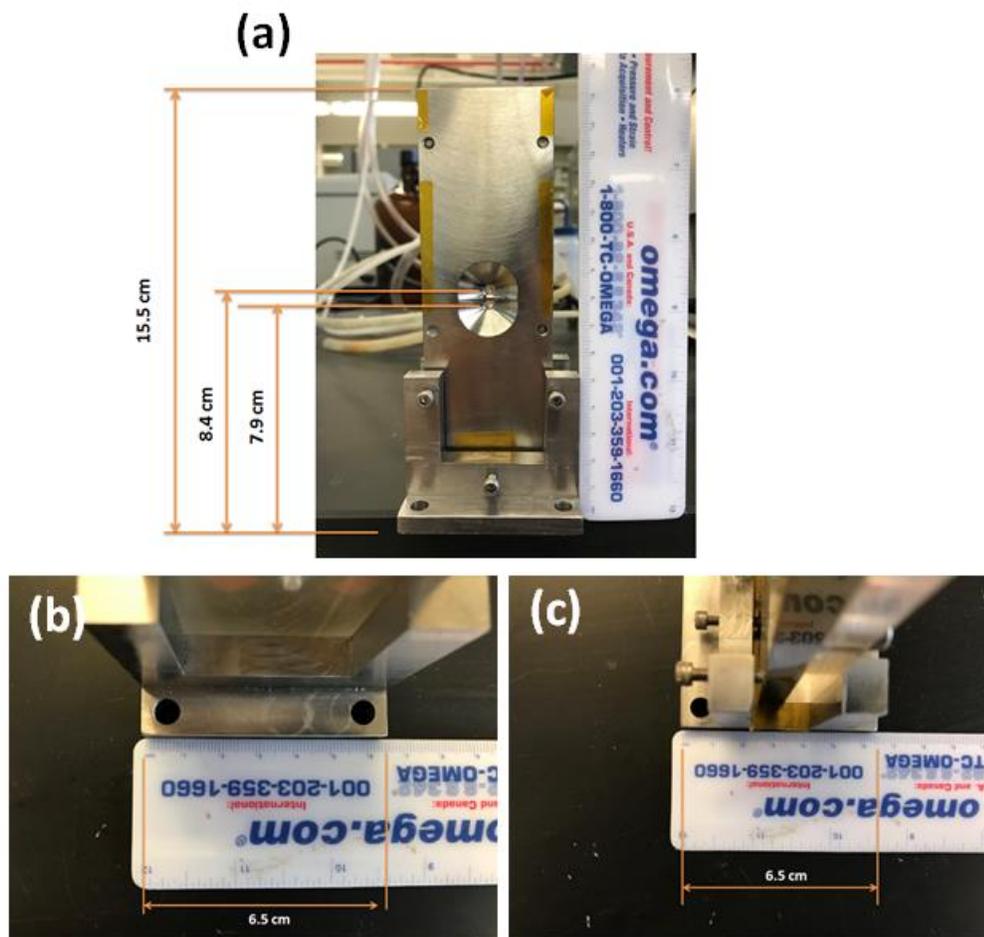


Figure 98. Dimensions of the custom electrochemical cell.

The cell contains a top reservoir which accommodates both the reference and counter electrodes, and the two sides in the bottom parts were perforated in order to allow the X-ray beam passing through the cell. The Kapton[®] foil was used as the window for the X-ray beam entrance port, and the glassy carbon working electrode acted as the window for the beam exit port which is secured with Kapton[®] tapes. The steel plate also acts as the current collector for the working electrode. One steel plate (right one in Figure 97(b)) is designed to be downstream of the sample with respect to the X-ray beam, and features twin ports with 50-degree bevels to transmit the scattered signal (see Figure 98(a)). The other plate (left one in Figure 97(b)) is set with a 1/16" O-ring to prevent leakage of the electrolyte. It also has a 1/4" UNF Luer socket port affixed, with a check valve. This allows us to fill the electrolyte chamber from the bottom up, encouraging

wetting of the electrode without trapped bubbles. We also have a top piece to close off the electrolyte port and hold our electrodes during testing, as well as a mounting bracket designed for the kinematic mounting plates. Both affix to the electrode housing via set screws.

The configuration and thickness of the glassy carbon electrode, the active material, the electrolyte and the Kapton[®] window in the cell are shown in Figure 99. The MnO₂ nanosheets are electrophoretically deposited onto the glassy carbon electrode (1 cm width, 1.5 cm length, 100 μm thickness), with a typical thickness of ~10 μm. The total mass of MnO₂ on electrodes is ~0.5 mg, covering a surface area of ~1 cm², and the mass of nanosheets in the beam is ~1-2 μg.

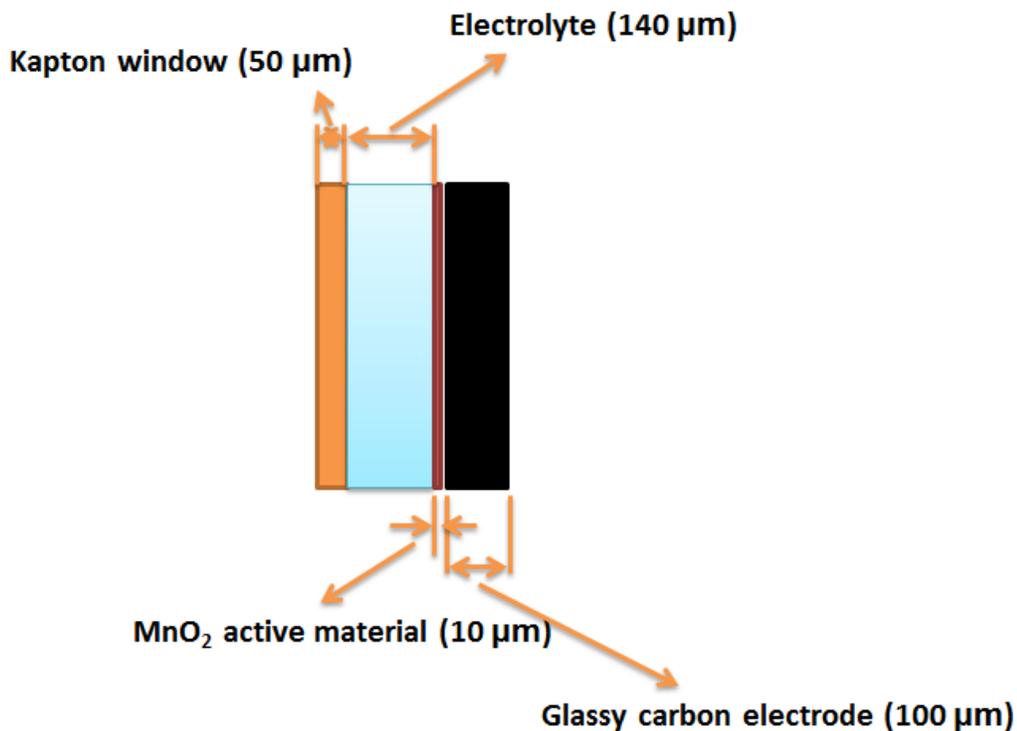


Figure 99. The configuration and thickness of the glassy carbon electrode, the active material, the electrolyte and the Kapton[®] window in the cell.